Control of Spin Wave Flow and Its Application to Magnonic Devices using Yttrium Iron Garnet

(イットリウム鉄ガーネットを用いたスピン波制御およびそのマグノニック素子への応用)

January 2017

Doctor of Engineering

Naoki Kanazawa

Toyohashi University of Technology

2017.1.10

Dpt. of Electrical and Electronic Information Engineering	ID	103313
Name	Naoki Kanazawa	

Supervisor	Yuichi Nakamura Hiroyuki Takagi

Abstract (Doctor)

Title	Control of Spin Wave Flow and Its Application to Magnonic Devices using Yttrium Iron Garnet

Integrated circuits have been advanced by miniaturization of complementary metal oxide semiconductor (CMOS) devices, but the thickness of gate oxide films is reaching to the ultimate limit. Thus beyond CMOS devices becomes a primary interest of science. Spin waves (SWs) transmit information even in the insulators, since they transport spin momentum rather than electron. Wavelength ranging from tens of nanometers to millimeters gives easy access to magnonic band with arbitrarily structures, thus positive utilization of wave nature is expected to yield of another possibility in operations. In this work, yttrium iron garnet, one of notable insulating magnet, was employed as waveguide material. Based on this material, several waveguide structures were investigated to control wave flows, and their potential applications were explored.

First, performance of SWs as magnetic field sensors was studied with artificial magnetic lattices (AMLs). Copper stripes covering the waveguide surface act as AML. When defect layer with extra periodicity was added, a localized mode was observed. Contrary to the optical counterpart, demagnetizing effect caused incoherence of interference. By considering this factor, calculation showed reasonable agreement with experimental results. Large slope of transmission intensity in the vicinity of the localized mode was used for sensors together with the sharp magnetic field dependence of magnonic band. Nevertheless, minimum resolution of the sensor was only about 10^{-4} Oe. Limitation was due to temperature drift, and thus differential circuit was applied to magnonic devices. By using this circuit, phase rotation induced by magnetic field and temperature drift can be separated, yielding in suppression of temperature sensitivity from -20 deg./°C to $-9.5 \times 10-3$ deg./°C.

Next, interferometers were studied for the 3-input majority function. Boolean sum and product can be also represented by a majority gate. Since data was encoded in the phase of propagating waves, forward volume SWs with isotropic dispersion was used. In advance, basic properties were investigated with 2 wave interferometry in the linear waveguide. The contributions of backscattered waves from waveguide ends gave rise in instability of operation, and which was terminated by thin gold layer with the thickness of tens of nanometers. In these thicknesses, two SW modes with different wavenumber were generated. Attenuation was strongly enhanced at thicknesses of mode hybridization. Terminated waveguide exhibited stable performance to a magnetic field deviation over 30 Oe. This is the first experimental report of the interferometer using forward volume SWs. This principle was expanded in the 3 wave interferometry with the Ψ-shaped interferometer. Obliquely incident SWs to the junction caused mode transition. Thus waveguide width was limited in order to be single mode. With this interferometer, control of Boolean sum and product by majority function was achieved. Stability of the operation to the magnetic field, and wave flow at the junction area were further investigated.

In this study, several waveguides to control SW flow were studied on AMLs and interferometers. Controllability of magnonic band holds promise of extremely short wavelength and high speed clocking in the future, expecting a prospect as beyond CMOS device.

Contents

Chapter 1

Introduction

1.1 Spin Waves for Beyond CMOS Devices

Complementary metal oxide semiconductor (CMOS) underlies integrated circuits, and high-performance CMOS devices cannot be separated from the sustainability of modern information technology. So called *More Moore* describes one of the basic strategies of the development, in which the operational speed has been accelerated and the element size has been miniaturized over a half century. So far CMOS devices have adopted technological breakthroughs, high-K metal gate or FinFET (3-D tri-gate) for example, to steadily extend More Moore strategy.[1] Nevertheless, this strategy is facing to the ultimate limit, financially or physically in near future.[2] Therefore CMOS devices are taking equivalent scaling called *More than Moore*. Integration of multi-functionalities such like sensors and actuators, namely system on chip (SoC), improves a total performance of integrated circuits.[3] On the other hand, another viewpoint of the development called *beyond CMOS* have attracted the interest of researchers to alternate the concept of CMOS devices.[4,5] One promising direction may be the replacement of semiconductors by carbon nanotubes or graphene nanoribbons. Utilization of their unique band structures are expected to dramatically advance a mobility of electron, enabling further miniaturization and high speed switching.[6,7] However, a leakage current while switching generates wasted heat, and the wasted heat increases the heat density as accelerating the switching speed or integration. This unavoidable issue is the fundamental drawback of the transistor, as long as information is transported by electrons.

Spin waves (SWs) are the collective excitation of magnetic moments in ferromagnets, in which microwave signals are transmitted in GHz region. Unlike to the electronic devices, spin wave devices (SWDs) transport spin momentum, yielding in free of electron transport. Thus SWDs are expected to overcome the drawback of leakage current. In addition, formalism of minibands and tunability of dispersion characteristic are totally differ from their optical and acoustic counterparts, and of course semiconductors.[8,9] This enables to control of microwave signals in various situations. Such advantage had accepted in the telecommunication market in 1980's.[10–12] GHz filters, delay lines and

signal to noise enhancers had been investigated, and resulted in production of commercial microwave devices. Most of these analogue technologies had been replaced in recent years by digital signal processing. On the other hand, development of nanotechnology enabled downscaling of SWDs. This technological advancement shifted paradigms. So called *magnonics* is aiming at manipulation, transportation and storage information with SWDs.[13–15] Since SWs are free of electron transport, SWDs can be integrated even in the magnetic insulators, e.g. yttrium iron garnet (YIG).[16] Joule loss and accompanying heating are expected to be minimized in this system. Moreover, small spin orbit interaction in this material enables long distance transport of the spin momentum. Fabrication of μm-thick YIG films with bulk-like magnetic properties was achieved by using liquid phase epitaxy around 1970's.[17–19] This breakthrough had greatly contributed to the realization of practical microwave devices in the past. The renaissance of the SWD was started by the introduction of pulsed laser deposition technique on state of art.[20,21] Resulting ultra-thin films are approaching to the thickness of several nanometers.[22] The shortest wavelength reported in the YIG thin film is comparable to that of soft X-ray.[23] The availability of such short wavelengths holds great promise on the downscaling and integration of SWDs into nanoscale, without increasing the heat density.

Notable benefit to use SWs instead of CMOS devices is the capability for the positive utilization of wave phenomena. Since the wavelengths of de Broglie waves are too short to manipulate, application of wave phenomena in the CMOS devices is limited to the specific technologies such as tunnel FET and such wave nature is rather suppressed for the synchronization of the distributed constant circuits. In contrast, wavelengths of SWs are ranging in tens of nanometer to several millimeters, depending on types of the dominant magnetic interaction. This wide tunability removes technical barriers to operate rich wave phenomena in SWDs. For example, a superposition of waves easily implements a majority function, which excels at realizing full adder circuits.[24] Orthogonal frequency-division multiplexing may be available in the system, yielding in a possibility of parallel data transmission.[25] Since SWs are dominated by nonlinear magnetic interactions, a strong excitation of the ferromagnetic system induces various nonlinear phenomena.[26] Such parallelism and nonlinearity would underlie the architecture of neural networks.[27] These potentials of the wave-oriented logic elements will show enough prospectives as beyond CMOS devices. With this in mind, a control of wave flow in the ferromagnetic system is essential to pave the way for exploring potential of SWDs.

1.2 Magnetic Field Sensors

One of the the notable features of waves is interference, which can be controlled by periodic modulation of propagation constants of the waveguide. Such artificial lattice have been extensively studied especially in the field of optics, as known as photonic crystals.[29] The magnonic counterpart of photonic crystals is called magnonic crystals (MCs), which is a key component of SW flow control. The primitive application of MCs is microwave filters, in which a stop band prohibits a propagation of microwave signals at

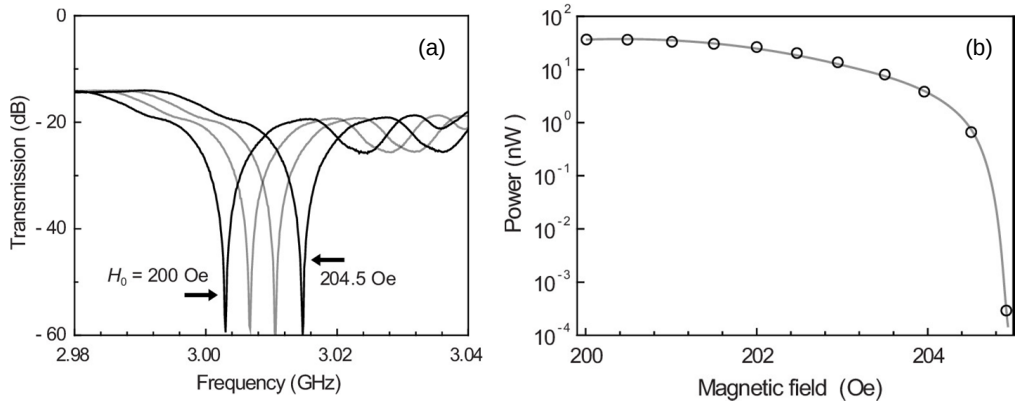

Figure 1.1 Application of MCs to a magnetic field sensor. (a) Frequency shift in the stop band corresponding to the change in the bias field from 200.0 Oe to 204.5 Oe with an interval of 1.5 Oe. (b) Change in the transmission power of the SW at 3.02 GHz with respect to the change in a bias magnetic field of +0.5 Oe from 204.5 Oe.[28]

the Bragg frequency. Furthermore MCs yield of rich functionality such as power limiter,[30] generator,[31] temporal memory[32] and so on. Such extensive potential is quite interest from the view point of SoC. In this manner, very unique application was demonstrated by M. Inoue *et al.*, in which MCs is capable of sensing the magnetic field as shown in Fig.1.1. In this report, the magnetic field tunability of the wavenumber was incorporated with the band edge of MCs. Since the transmission intensity in the vicinity of the Bragg frequency strongly depends on the excitation frequency, the shift of the Bragg frequency due to the magnetic field is drastically presented in the transmission intensity. The author reported a gigantic change in the intensity of 9,336%/Oe, and this was greater than that of GMI sensors, e.g. 600%/Oe.[33] Thus a possibility of another application of MCs was opened.

Nevertheless, a specific magnetic field resolution of the MC-based sensor was not mentioned in the report. Thus in this study, the specific magnetic filed resolution was evaluated by the homemade testing system, and prospectives as a magnetic field sensor are reviewed. Since in Fig.1.1b, transmission power become very weak in the sensitive area due to the use of stop band spectra, a localized mode is rather employed, in which a convex transmission spectra is obtained at the Bragg frequency. Obtained knowledge about magnetic field dependence and the related experimental technique will be utilized in the later investigations about logic elements.

1.3 Wave-oriented Logic Elements

In the past decade, the main target of SWDs has been changed to the computation rather than analogue signal processing at microwave frequency. Waves, including SWs, excel at encoring information in their phase, and providing a logic output via superposition. Therefore varieties of SW interferometers have been demonstrated as a key component of

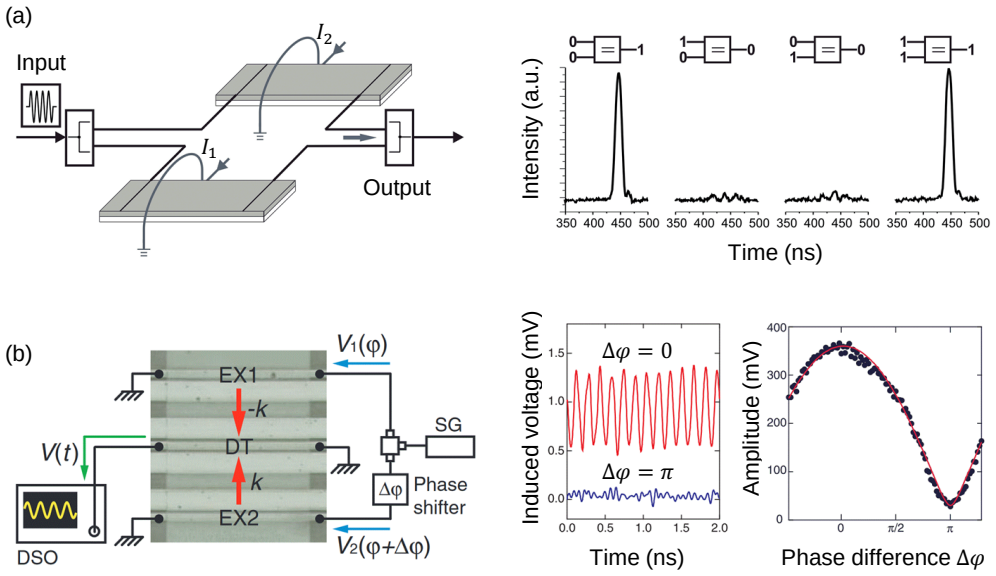

Figure 1.2 Demonstrated wave-oriented logic elements. (a) XNOR gate. Phase shift of SWs in the YIG waveguides are controlled by current inputs I_1 and I_2. The resulting waves are superposed at the output multiplexer, in which the interference is carried out by electromagnetic waves.[34] (b) Solid state SW interferometer. Input SWs are injected from EX1 and EX2, and interfered beneath DT antenna. Constructive and destructive interference by SWs are clearly visible.[35]

wave-oriented logic elements. In 2005, M. P. Kostylev *et al.* reported a phase controller incorporated with a pulse current modulating the magnetic field of the waveguide.[36] Based on the result, they demonstrated a XNOR logic gate as shown in Fig.1.2a. In this experiment, the SWs were only used in the purpose of controlling the phase of electromagnetic waves, and superposition was done by a microwave multiplexer. Magnonic counterpart of the multiplexer, namely SW interferometer, was separately demonstrated by N. Sato *et al.*, in which clear constructive and destructive superposition of SWs are displayed as shown in Fig.1.2b. Such elemental technologies have been enthusiastically studied by several research groups, nevertheless presented elements in proof-of-principle-type form do not overcome the CMOS technology in operational efficiency, element size, and speed. However, fundamental studies on the field of spintronics are rapidly advancing the potential of SWDs.[15]

Apart from the studies of elemental technologies, there are prospects of functionalities provided by SW networks. Constructive and destructive superposition of waves excel at implementing the majority function rather than the simple XNOR gate. One of the well-known applications of majority gates is the full adder circuit. In the case of full adder circuit, a specific topology of SW network was proposed as shown in Fig.1.3. In the conventional logic circuit, a sum and carry out of 1 bit full adder circuit can be

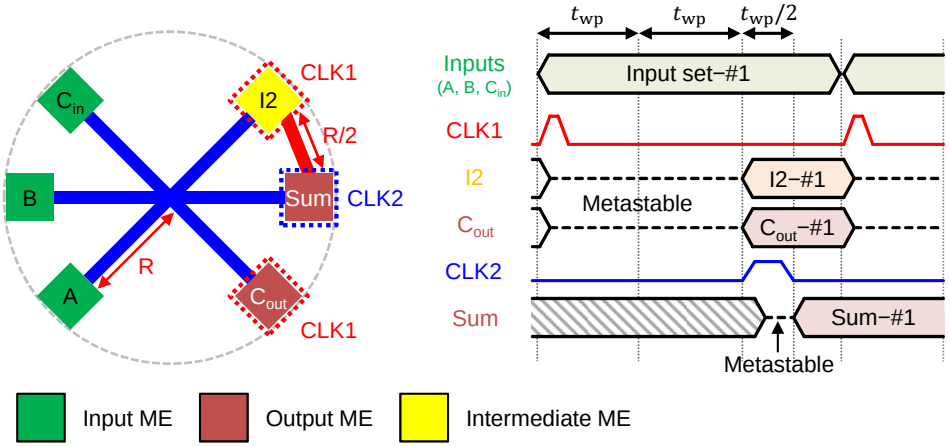

Figure 1.3 Concept of 1 bit magnonic full adder circuit. ME denotes magneto electric cell which to convert electrical signals to SWs and vice versa. After receiving clock (CLK) signals, each ME cell transit to the metastable state to accept superposed signal of SWs. A and B represent input signals. C_{in} and C_{out} are carry in and carry output, respectively. I2 is the intermediate ME, in which the received signal is amplified to double. A time duration t_{wp} represent a delay of propagation in the distance R.[24]

represented by a following logic formula:[37]

$$\mathrm{Sum} = (\mathrm{A} \oplus \mathrm{B}) \oplus \mathrm{C_{in}}, \tag{1.1}$$

$$\mathrm{C_{out}} = \mathrm{A} \cdot \mathrm{B} + \mathrm{C_{in}} \cdot (\mathrm{A} \oplus \mathrm{B}). \tag{1.2}$$

To realize this functionality, typically over 28 transistors are required in the conventional logic circuit, yielding in a large delay, element size, and power consumption. Thus such 1 bit full adder circuit is often used as an index of performance of Beyond CMOS devices. By using majority gates, Eq.1.1 and Eq.1.2 can be simplified by

$$\mathrm{Sum} = \mathrm{MAJ}(\mathrm{A}, \mathrm{B}, \mathrm{C_{in}}, -2\mathrm{MAJ}(\mathrm{A}, \mathrm{B}, \mathrm{C_{in}})), \tag{1.3}$$

$$\mathrm{C_{out}} = \mathrm{MAJ}(\mathrm{A}, \mathrm{B}, \mathrm{C_{in}}). \tag{1.4}$$

It should be noted that the sum and carry out can be implemented only by majority gates, yielding in the easy implementation. The benchmark of the SW network was also given by P. Shabadi *et al.* and compared with the 45 nm node CMOS implementation in Table1.1. The benchmark indicated the advantage of the SW network especially in

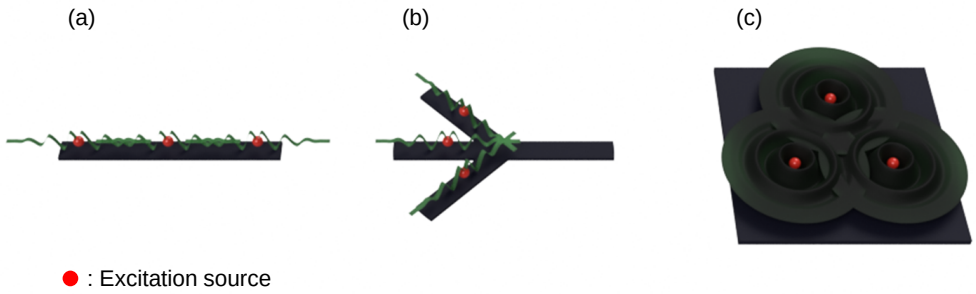

Figure 1.4 Classification of SW network topology. (a) Type-I. All sources are aligned in a single line.[35,39,40] (b) Type-II. Each source has dedicated waveguide, and wave superposition was mainly done at the junction area.[41–43] (c) Type-III. No waveguide is exist and superposition was done at the entire device plane. Connectivity was determined by the relative distance between each excitation source.[44–47] Red points represent excitation source of SWs, and green surfaces show propagating waves.

power consumption and element size. According to the above report, parallel counters can be also implemented in the same manner, which is used in a fast parallel multipliers. Furthermore, a majority function underlies various potential applications such as fault tolerant system, threshold logic, spectrum spread coding, and artificial neural networks and so on.[38]

Nevertheless, the fundamental study is still necessary to bridge conceptual SW networks and underling SWDs. In Fig.1.3, careful discussion on the SW flow between ME cells was still uncompleted, and such complicated networks have never experimentally shown. The 1 bit full adder requires a SW interferometer with 3 fan-in and 3 fan-out and its topology belongs to the type-II in Fig.1.4. So far the topology of experimentally demonstrated interferometers belonged to the type-I. The waveguide geometry is homogeneous in the propagation direction, and this situation argues to consider the waveguide as an 1-D transmission line, like a conventional electrical circuit. In contrast, in the type-II topology, a wave superposition is done at the junction area of the waveguides, and the 1-D approximation is no longer valid because of the change of waveguide shape at the junction area. Change of the waveguide shape affects the magnetic anisotropy, yielding in the magnetic field inhomogeneity. In addition, certain SW modes exhibit strong directivity. These realistic properties may induce an extra scattering at the junction area. Type-III topology may cancel the problem of shape magnetic anisotropy, but operational scheme is currently abstractive.

Table 1.1 Benchmark of 1 bit full adder circuit.[24]

Fabric	Delay (ps)	Power (μW)	Area (μm^2)	Elements
CMOS	250	36.5	20	32 Transistors
SW network	375	0.16	0.5	6 MEs

According to above discussion, the main challenge of this study is to show experimentally the SW interferometer belonging to the type-II topology, which has 3 fan-in to meet the requirement from the magnonic full adder circuit. To avoid the directivity of SWs, the waveguide was perpendicularly magnetized so that isotropic forward volume spin waves were excited. Throughout the study, the SW flow especially in the junction area were carefully analyzed and the feature of type-II topology were summarized.

1.4 Overview of Thesis

In chapter 1, orientation to the field of magnonics and motivation of this work are presented. This work is organized as follows: In chapter 2, the basis of ferromagnetism and SWs are presented together with the description of the aspect of yttrium iron garnet as the best material for SW application. In chapter 3, numerical models of SW propagation both in the bare surface and metalized surface are introduced, and MCs composed of metallic stripes are studied. In chapter 4, a prospectives of MCs as a magnetic field sensors is reviewed. Temperature sensitivity of devices is also investigated. In chapter 5, the first experimental demonstration of SW interferometer using forward voume spin waves is presented. In chapter 6, the SW interferometer with type-II topology with 3 fan-in is experimentally demonstrated and flow of SW at the junction area is intensively discussed. I finish this thesis with a summary and outlook in chapter 7.

Chapter 2

Magnetism and Spin Waves

In this chapter, the fundamentals of ferromagnetism and spin wave spectroscopy are explained. Beforehand, a simple picture of the origin of the magnetic moment is given in §2.1. Landau-Lifshitz-Gilbert equation and permeability tensor are derived with begging from the basis of magnetic moment. These bases describe behavior of the ferromagnetic system irradiated by microwave systems. Then, basic properties and operation principle of SWs under dipolar interaction are presented in §2.2. Since this study focuses on yttrium iron garnet (YIG) as the waveguide material, its magnetic properties and advantages are described from the viewpoint of SWDs in §2.3.

2.1 Dynamics of Magnetic Moment

2.1.1 Origin of Magnetic Moment

A circulating current gives rise to a magnetic dipole moment. In the classical Bohr model, an electron with an electronic mass m_e rotates around a nuclei with the momentum $\boldsymbol{P}$ and the orbital radius $\boldsymbol{r}$. Following to kinetics, this motion gives the orbital angular momentum $\boldsymbol{l}$ and the circulating current $\boldsymbol{i}$ by

$$\boldsymbol{l} = \boldsymbol{r} \times \boldsymbol{P} = \boldsymbol{r} \times (m_e \boldsymbol{v_0}) \,, \tag{2.1}$$

and

$$\boldsymbol{i} = -e \frac{\boldsymbol{v_0}}{2\pi |\boldsymbol{r}|}, \tag{2.2}$$

where $\boldsymbol{v_0}$ is velocity of the rotational motion. Then a magnetic dipole moment in the Gaussian-cgs unit system is given by

$$\boldsymbol{\mu_l} = \left(\frac{\boldsymbol{r}}{|\boldsymbol{r}|} \times \boldsymbol{i} \right) \frac{\pi |\boldsymbol{r}|^2}{c_0} = (\boldsymbol{r} \times \boldsymbol{i}) \frac{\pi |\boldsymbol{r}|}{c_0}, \tag{2.3}$$

where $c_0 = 3 \times 10^8$ m/s is the speed of light in a vacuum. Substitution of Eq.2.2 and Eq.2.1 into Eq.2.3 yielded

$$\boldsymbol{\mu_l} = -\frac{e}{2m_e c}\boldsymbol{l}. \tag{2.4}$$

Eq.2.4 indicates an electron has a magnetic dipole originated from its rotational motion. This is called orbital magnetic moment. The $\boldsymbol{l}$ of the electron and the induced $\boldsymbol{\mu_l}$ are oppositely directed due to the negative electronic charge. Eq.2.4 is also able to be

$$\boldsymbol{\mu_l} = \frac{e\hbar}{2m_e c}\frac{\boldsymbol{l}}{\hbar} = \mu_B \frac{\boldsymbol{l}}{\hbar}, \tag{2.5}$$

where $\hbar$ is reduced Planck (Dirac's) constant and

$$\mu_B = \frac{e\hbar}{2mc} = 9.2732 \times 10^{-21} \text{ erg/G}, \tag{2.6}$$

is called Bohr magneton, which is the minimum unit of magnetic moment. In addition to $\boldsymbol{\mu_l}$, an electron is also known to have a momentum called spin magnetic moment $\boldsymbol{\mu_s}$, which is different by factor of 2. Therefore $\boldsymbol{\mu_s}$ can be written as[9]

$$\boldsymbol{\mu_s} = -\frac{e}{m_e c}\boldsymbol{s} = \mu_B \frac{2\boldsymbol{s}}{\hbar}, \tag{2.7}$$

where $\boldsymbol{s}$ is spin angular momentum with a magnitude of $|\boldsymbol{s}| = \hbar/2$. In the presence of both spin and orbital angular momenta, a total magnetic moment $\boldsymbol{\mu}$ becomes a vector sum of $\boldsymbol{\mu_l}$ and $\boldsymbol{\mu_s}$, which can be written as

$$\boldsymbol{\mu} = \frac{\mu_B}{\hbar}\left(\boldsymbol{l} + 2\boldsymbol{s}\right). \tag{2.8}$$

On the other hand, a total angular momentum $\boldsymbol{j}$ of an electron can be obtained as

$$\boldsymbol{j} = \boldsymbol{l} + \boldsymbol{s}. \tag{2.9}$$

When comparing Eq.2.8 and Eq.2.9, it can be easily understood that $\boldsymbol{\mu}$ and $\boldsymbol{j}$ are no longer parallel due to the different contribution of $\boldsymbol{s}$. Projection of $\boldsymbol{\mu}$ along $\boldsymbol{j}$ gives

$$\begin{aligned}\boldsymbol{\mu}\cdot\boldsymbol{j} &= \frac{\mu_B}{\hbar}\left(\boldsymbol{l} + 2\boldsymbol{s}\right)\cdot\left(\boldsymbol{l} + \boldsymbol{s}\right) \\ &= \frac{\mu_B}{\hbar}\left(l^2 + 3\boldsymbol{l}\cdot\boldsymbol{s} + 2s^2\right).\end{aligned} \tag{2.10}$$

By using Eq.2.9, a scalar product of $\boldsymbol{l} \cdot \boldsymbol{s}$ can be represented as

$$\boldsymbol{l} \cdot \boldsymbol{s} = \frac{1}{2}\left(j^2 - l^2 - s^2\right). \tag{2.11}$$

Substitution of Eq.2.11 into Eq.2.10 gives

$$\boldsymbol{\mu} \cdot \boldsymbol{j} = \frac{\mu_B}{\hbar}\left(\frac{3}{2} + \frac{s^2 - l^2}{2j^2}\right) j^2. \tag{2.12}$$

This corresponds to a parallel component of $\boldsymbol{\mu}$ to $\boldsymbol{j}$. For comparing to this, an effective magnetic moment $\boldsymbol{\mu_j}$ directly caused by $\boldsymbol{j}$ is defined. Following to Eq.2.8, a factor γ is introduced to connect $\boldsymbol{\mu_j}$ and $\boldsymbol{j}$. Consequently, $\boldsymbol{\mu_j}$ is obtained as

$$\boldsymbol{\mu_j} = \gamma \boldsymbol{j}. \tag{2.13}$$

A projection of $\boldsymbol{\mu_j}$ along $\boldsymbol{j}$ gives

$$\boldsymbol{\mu_j} \cdot \boldsymbol{j} = \gamma j^2. \tag{2.14}$$

Comparing Eq.2.12 and Eq.2.14, an introduced factor γ can be defined as

$$\gamma = \left(\frac{3}{2} + \frac{s^2 - l^2}{2j^2}\right)\frac{\mu_B}{\hbar} = \mathrm{g}\frac{\mu_B}{\hbar}, \tag{2.15}$$

where the so-called g-factor is a measure of the strength of spin-orbit interaction, and the introduced γ is generally mentioned as gyromagnetic ratio, which determines a relationship between the magnetic moment and angular momentum.

This result was obtained by treating angular momentums as classical vectors. According to the quantum theory, the squared magnitude of $\boldsymbol{j}$ is $j(j+1)$ rather than j^2. In the same manner, those of $\boldsymbol{l}$ and $\boldsymbol{s}$ give $l(l+1)$ and $s(s+1)$, respectively. Thus g-factor is strictly defined as[9]

$$\mathrm{g} = \frac{3}{2} + \frac{s(s+1) - l(l+1)}{2j(j+1)}. \tag{2.16}$$

So far the magnetic moment caused in the single electron system was discussed. If there are several electrons in the system, angular momenta start interacting each other. In many-electron system, three types of coupling mechanism can be defined.

1. Spin-Spin coupling
2. Orbit-Orbit coupling

3. Spin-Orbit coupling

In the system with weak spin-orbit coupling, spin angular momentum $\boldsymbol{s}$ and orbital angular momentum $\boldsymbol{l}$ create macroscopic angular momentum independently. Then, the resulting momenta creates a total angular momentum. This can be written as

$$\boldsymbol{S} = \sum \boldsymbol{s_i}, \quad \boldsymbol{L} = \sum \boldsymbol{l_i}, \quad \boldsymbol{J} = \boldsymbol{L} + \boldsymbol{S}. \tag{2.17}$$

Hence results obtained for the single-electron system can be expanded to the many-electron system by replacing momenta by $\boldsymbol{L}$, $\boldsymbol{S}$ and $\boldsymbol{J}$. This coupling scheme is called Russel-Saunders coupling.

2.1.2 Landau-Lifshitz-Gilbert Equation

Previously, a relationship between magnetic moment and angular momentum was explained. Then the dynamics of magnetic moment $\boldsymbol{\mu_j}$ on time t is described here. When an effective magnetic field $\boldsymbol{H_{\text{eff}}}$ is applied to the system, and $\boldsymbol{\mu_j}$ is slightly tilted from the $\boldsymbol{H_{\text{eff}}}$. Since such non-equilibrium state increases an energy of the system, $\boldsymbol{\mu_j}$ receives torques to align $\boldsymbol{\mu_j}$ in the direction of $\boldsymbol{H_{\text{eff}}}$. And this torque drives precession of $\boldsymbol{\mu_j}$.

The configuration of the system is shown in Fig.2.1. A effective magnetic field H_{eff} is applied along w-axis. To express a rotational motion, the polar coordinate is convenient. In the polar coordinate, a position of $\boldsymbol{\mu_j}$ can be represented by (r, θ_a, θ_b). The potential energy E of $\boldsymbol{\mu_j}$ is given in the term of Zeeman energy. This yields

$$E = -\boldsymbol{\mu_j} \cdot \boldsymbol{H_{\text{eff}}} = \mu_j H_{\text{eff}} \cos\theta_a. \tag{2.18}$$

Eq.2.18 indicates E takes a minimum value when $\boldsymbol{\mu_j}$ and $\boldsymbol{H_{\text{eff}}}$ are collinear and a non-collinear location of them gives rise to E. The force experienced by $\boldsymbol{\mu_j}$ is given by

$$\begin{aligned} \boldsymbol{F} &= -\boldsymbol{\nabla} E \\ &= -\left(\hat{r}\frac{\partial}{\partial r} + \hat{\theta_a}\frac{1}{r}\frac{\partial}{\partial \theta_a} + \hat{\theta_b}\frac{1}{r\sin\theta_a}\frac{\partial}{\partial \theta_b} \right) E. \end{aligned} \tag{2.19}$$

This force exerts a torque $\boldsymbol{N}$ on $\boldsymbol{\mu_j}$. Following to kinetics, $\boldsymbol{N}$ is described as

$$\begin{aligned} \boldsymbol{N} &= \boldsymbol{r} \times \boldsymbol{F} \\ &= -\mu_j H_{\text{eff}} \frac{\partial \sin\theta_a}{\partial \theta_a} \left(\hat{r} \times \hat{\theta_a} \right) \\ &= \boldsymbol{\mu_j} \times \boldsymbol{H_{\text{eff}}}. \end{aligned} \tag{2.20}$$

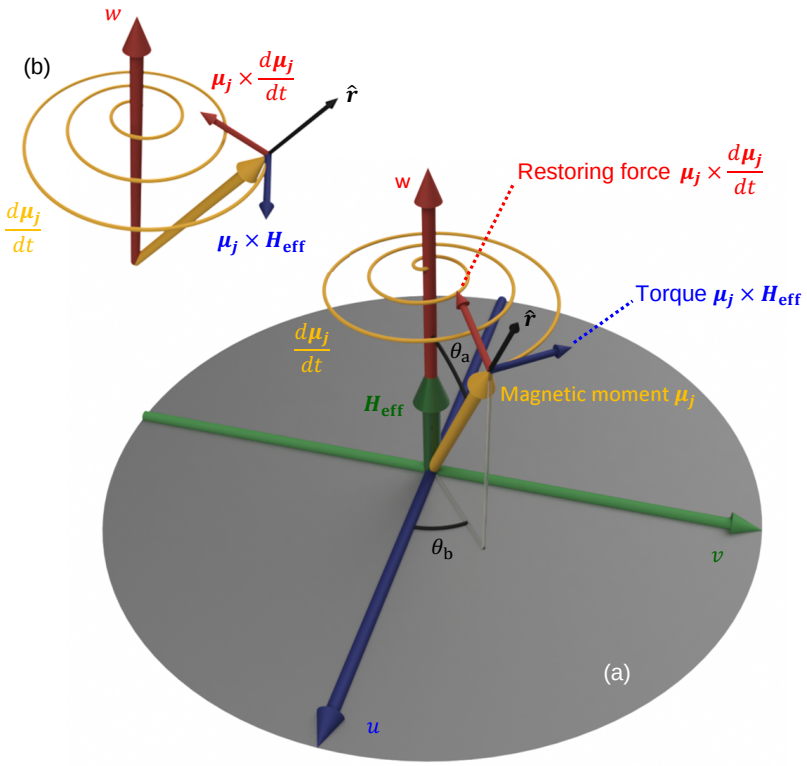

Figure 2.1 Precession of magnetic moment. (a) Schematic drawing. An effective magnetic field H_{eff} is applied along the mean direction (w-axis). A magnetic moment $\boldsymbol{\mu_j}$ precess around H_{eff}. (b) Relationship of torques on $\boldsymbol{\mu_j}$ from different angle. A yellow spiral represents a trajectory of movement.

From the equation of motion in kinetics, the torque $\boldsymbol{N}$ is also given by

$$\boldsymbol{N} = \frac{d\boldsymbol{J}}{dt}, \tag{2.21}$$

where $\boldsymbol{J}$ is the total angular momentum of the system, yielding magnetic moment $\boldsymbol{\mu_j}$ by a gyromagnetic ratio γ. By using Eq.2.20, Eq.2.21, and Eq.2.13, a dynamics of $\boldsymbol{\mu_j}$ is given by

$$\frac{d\boldsymbol{\mu_j}}{dt} = -\gamma \boldsymbol{\mu_j} \times \boldsymbol{H_{\mathrm{eff}}}. \tag{2.22}$$

Eq.2.22 describe a precession of $\boldsymbol{\mu_j}$ around $\boldsymbol{H_{\mathrm{eff}}}$ in the unit magnetic cell. It should be noted that the size of $\boldsymbol{\mu_j}$ is invariant on t. This is evidenced by taking inner product of $\boldsymbol{\mu_j}$ to Eq.2.22, yielding $d\boldsymbol{\mu_j}^2/dt = 0$. Therefore the precession of $\boldsymbol{\mu_j}$ dose not involve

demagnetization.

To expand Eq.2.22 to a bulk of magnetic material, a macroscopic magnetization $\boldsymbol{M} = \sum \boldsymbol{\mu_j}$ is assumed. Since the magnetic material is homogeneously magnetized by $\boldsymbol{H_{\mathbf{eff}}}$, the resulting $\boldsymbol{M}$ can be simply considered as a large vector composed of an integer multiple of $\boldsymbol{\mu_j}$. In addition, a restoring force is also take into account. This restoring force align $\boldsymbol{M}$ to $\boldsymbol{H_{\mathbf{eff}}}$ after an enough duration of time. Finally, a dynamics of magnetization can be written as[48]

$$\frac{d\boldsymbol{M}}{dt} = -\gamma \boldsymbol{M} \times \boldsymbol{H_{\mathbf{eff}}} + \frac{\alpha}{|\boldsymbol{M}|} \boldsymbol{M} \times \frac{d\boldsymbol{M}}{dt}, \tag{2.23}$$

where α denotes Gilbert damping, which is a measure of an attenuation of precession. The second term describes a restoring force on $\boldsymbol{M}$ and the direction is shown in Fig.2.1b. This equation is called Landau-Lifshitz-Gilbert (LLG) equation, describing the dynamics of magnetization in a ferromagnetic material.

2.1.3 Permeability Tensor

LLG equation was introduced to describe a dynamics of magnetization. However, this equation is represented in the term of time development, therefore it is not preferable to analyze magnetization behaviors in the frequency domain. Electromagnetic simulators are commonly used to design electronic devices used in frequencies in several GHz. Since a Maxwell equation is used as the dominant equation in commercial electromagnetic simulators, it is very convenient to model the magnetization dynamics in terms of the permeability $\bar{\mu}$.

In this part, a magnetization dynamics at specific frequency ω is described. As shown in Fig.2.1, The system is magnetized along w-axis. The dynamic magnetization can be decomposed to the components parallel and perpendicular to w-axis. When precession angle is small, the parallel component of the dynamic magnetization is comparable to the saturation magnetization M_S. Thus perturbation terms are perpendicular to the w-axis, and static terms are parallel to the w-axis. When monochromatic excitation is assumed, the time dependence is $\propto e^{i\omega t}$. In this situation, dynamic magnetic field $\boldsymbol{H}(t)$ and magnetization $\boldsymbol{M}(t)$ become

$$\boldsymbol{H}(t) = \nu H_{\mathrm{eff}} \hat{w} + \boldsymbol{h}(t), \tag{2.24}$$

$$\boldsymbol{M}(t) = \nu M_S \hat{w} + \boldsymbol{m}(t), \tag{2.25}$$

where $\nu = \pm 1$ is a direction of field vectors along mean direction $\hat{w}$. Both static components are parallel to the mean direction $\hat{w}$. The magnetization precession at frequency ω is considered by using Eq.2.23 in the Cartesian coordinate $O_M(u, v, w)$. Substitution of

Eq.2.24 and Eq.2.25 into Eq.2.23 yields

$$i\omega \boldsymbol{m} e^{i\omega t} = -\left\{ \nu\gamma M_S \hat{w}\boldsymbol{h} + (\nu\gamma H_{\text{eff}} + i\omega\alpha)\, \boldsymbol{m} \times \hat{w} \right\} e^{i\omega t}. \tag{2.26}$$

To obtain Eq.2.26, a cross product of dynamic terms $\boldsymbol{h} \times \boldsymbol{m}$ is neglected because of the small amplitude (small signal approximation is used). Then, solving Eq.2.26 for $\boldsymbol{m}$ yields

$$4\pi \boldsymbol{m} = \bar{\chi}\boldsymbol{h} = \begin{bmatrix} \chi & i\nu\kappa & 0 \\ -i\nu\kappa & \chi & 0 \\ 0 & 0 & 0 \end{bmatrix} \boldsymbol{h}, \tag{2.27}$$

where

$$\chi = \frac{\omega_H \omega_M}{{\omega_H}^2 - \omega^2}, \tag{2.28}$$

$$\kappa = \frac{\omega \omega_M}{{\omega_H}^2 - \omega^2}. \tag{2.29}$$

For convenience,

$$\omega_H = \gamma H_{\text{eff}} + i\omega\alpha, \tag{2.30}$$

$$\omega_M = \gamma 4\pi M_S. \tag{2.31}$$

are defined. Eq.2.30 is specially called Lamor frequency, which is associated with the frequency of magnetization precession. In Eq.2.27, the coefficient matrix $\bar{\chi}$ represents the magnetic susceptibility. Consequently, permeability tensor is obtained as

$$\bar{\mu} = \bar{\chi} + \bar{I} = \begin{bmatrix} \mu & i\nu\kappa & 0 \\ -i\nu\kappa & \mu & 0 \\ 0 & 0 & 1 \end{bmatrix}, \tag{2.32}$$

where,

$$\mu = \chi + 1 = \frac{\omega_H (\omega_H + \omega_M) - \omega^2}{{\omega_H}^2 - \omega^2}. \tag{2.33}$$

Magnetization dynamics at frequency ω is obtained in Eq.2.32. Since $\bar{\mu}$ is represented in the form of permeability, it can be directly used in the commercial electromagnetic simulators. More specifically, general electromagnetic simulators use electric field $\boldsymbol{E}$ as a state vector, $\bar{\mu}$ is taken into account as

$$\boldsymbol{\nabla} \times \bar{\mu}^{-1} (\boldsymbol{\nabla} \times \boldsymbol{E}) - k_0^2 \left(\varepsilon_r - \frac{i\sigma}{\omega \varepsilon_0} \right) \boldsymbol{E} = 0, \tag{2.34}$$

where ε_r is a relative dielectric constant, ε_0 is the dielectric constant in vacuum, k_0 is a wavenumber of electromagnetic wave in vacuum, and σ is a conductivity, respectively. By using Eq.2.34, a magnetization dynamics can be analyzed in commercial electromagnetic simulators.

2.2 Spin Waves

2.2.1 Magnetostatic Waves

In the previous section, we discussed magnetization dynamics homogeneously excited in the ferromagnet. When magnetic moments are locally excited, this local precession starts propagating accompanying with finite phase difference. In the long wave limit $kd \ll 1$, where k is wavenumber and d is the film thickness, magnetic interaction called dipolar interaction is dominant. In this situation, SWs are sensitive to the waveguide geometry, and three orthogonal modes are formed. Damon-Eshbach spin wave (DE-SW) is excited when the film is magnetized in-plane and when k is perpendicular to M. Forward volume spin wave (FV-SW) is excited in the perpendicularly magnetized films. In this FV-SW mode, since M is always perpendicular to k, this mode shows good symmetry in the device plane. Backward volume spin wave (BV-SW) is excited when the film is magnetized in-plane and when k is parallel to M. These are shown in Fig.2.2a-c. Each dispersion curves can be described as follows.[49]

DE-SW

$$\omega^2 = \omega_H (\omega_H + \omega_M) + \frac{\omega_M^2}{4} \left(1 - e^{-2kd} \right). \tag{2.35}$$

FV-SW

$$\omega^2 = \omega_H \left[\omega_H + \omega_M \left(1 - \frac{1 - e^{-kd}}{kd} \right) \right]. \tag{2.36}$$

BV-SW

$$\omega^2 = \omega_H \left[\omega_H + \omega_M \frac{1 - e^{-kd}}{kd} \right]. \tag{2.37}$$

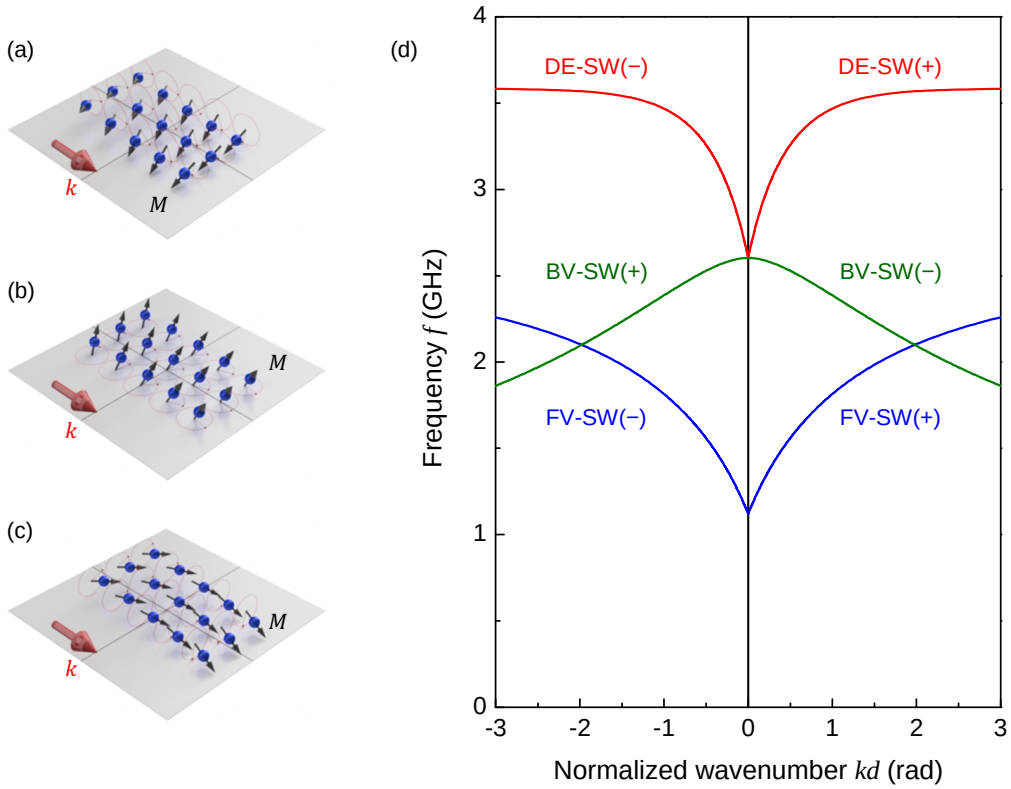

Figure 2.2 Propagation mode of magnetostatic waves. Schematic illustrations of (a) Damon-Eshbach spin wave, (b) forward volume spin wave, and (c) backward volume spin wave. In the figure, M denotes magnetic moments and k denotes wave vector. (d) Calculated dispersion curves for three orthogonal configuration. Calculated wavenumbers are normalized by film thickness d. The sign ($\pm$) represent the direction of energy flow from the source.

It should be noted that all dispersion curves $k(\omega)$ include the factor of d. This fact indicates the wavelengths of magnetostatic waves can be downscaled in thinner magnetic films. Typical dispersion curves are calculated with $H_0 = 200$ Oe, and $4\pi M_S = 1760$ G and are shown in Fig.2.2d.

All SWs formed transmission band, and $k = 0$ of each modes was appeared at GHz region. In contrast to electromagnetic waves, $k = 0$ corresponds to a frequency of the

Table 2.1 Comparison of magnetostatic modes. ✓ is available. ✗ is unavailable.

Mode	Isotropy	Termination	Nonreciprocity	Fast v_g	Negative v_p
DE-SW	✗	✓	✓	✓	✗
FV-SW	✓	✗	✗	✗	✗
BV-SW	✗	✓	✗	✗	✓

ferromagnetic resonance of the ferromagnet. In both cases, excitation is homogeneously spread in the entire space. Curvature of the dispersion curves is another interest, which yields in the discrepancy between the phase velocity v_p and group velocity v_g. Thus SWs are dispersive, which is a necessary condition of nonlinear excitation like solitons. FV-SW and BV-SW share the propagation frequency where the permeability $\mu < 0$, while DE-SW appears at frequencies where $\mu > 0$. As shown in Fig.2.2a and c, both DE-SW and BV-SW can be excited in the in-plane magnetized film with different direction of k. However, a cross over point of DE-SW and BV-SW is only at $k = 0$. When k orientation is changed in the film plane, e.g. scattering, these modes are strongly damped. In the viewpoint of SW termination, this relationship is useful to suppress backscattering.[50] Since DE-SW shows steep dispersion curve compared to other modes, the group velocity of this mode is slightly faster than others. BV-SW exhibited negative slope on its dispersion curve. Such anomalous dispersion properties are sometime mentioned as a meta-material, but it is noteworthy the group velocity is always positive and no backflow of injected energy occurs. This is noted as signs in bracket. This unique property have attracted interest of researchers for exploration of novel physics.[51–53] All dispersion curves are symmetric to $k = 0$, therefore no reciprocity exist on the dispersion curves. However, DE-SWs exhibit reciprocal property on the energy distribution. As DE-SWs are also mentioned as *magnetostatic surface wave*, the energy of the mode localized in the vicinity of the single waveguide surface and flows an opposite surface for $+k$ and $-k$ branches. Therefore DE-SWs show nonreciprocal property against to the surface structures, e.g. metalization.[54] These characteristics of magnetostatic modes are summarized in Table2.1. Since all of these modes have variety of merit and demerit, it is important to chose precise mode for the application.

2.2.2 Dipole-Exchange Spin Waves

When the wavenumber of spin waves is enough extended, a difference of precession phase between neighboring magnetic moments cannot be ignored. This phase difference give raise in the energy of the system to align magnetic moments, yielding of the exchange magnetic field give by

$$\boldsymbol{H}_{\mathbf{ex}} = \lambda_{\mathrm{ex}} \boldsymbol{\nabla}^2 \boldsymbol{M}, \tag{2.38}$$

where λ_{ex} is called exchange constant. Because such exchange interaction becomes quite strong in $kd \gg 1$, the dipolar interaction is rather minor in this situation and dipole-exchange SWs propagate. When magnetic moment $\boldsymbol{M}$ is oscillating with a wavenumber k, $\boldsymbol{H}_{\mathbf{ex}} = -\lambda_{\mathrm{ex}} k^2 \boldsymbol{M}$ is given. Propagation of dipole-exchange SWs was analyzed by B. A. Kalinikos *et al.* using the exchange boundary conditions.[55,56] According with their theory, Eq.2.35-Eq.2.37 can be rewritten to include the contribution of $\boldsymbol{H}_{\mathbf{ex}}$.

$$\omega_n^2 = \left(\omega_H + \omega_M \lambda_{\mathrm{ex}} k_n^2\right)\left(\omega_H + \omega_M \lambda_{\mathrm{ex}} k_n^2 + \omega_M F_{nn}\right) \tag{2.39}$$

where $k_n^2 = k^2 + \kappa_n^2$ is the full wavenumber of mode number n including the transverse wavenumber κ_n across the film thickness. When the surface magnetic moments are totally unpinned, $\kappa_n = n\pi/d$ is given. A parameter F_{nn} is wavenumber dependent and given to each magnetic field configuration.

DE-SW

$$F_{nn} = 1 - \omega_M \frac{P_{nn}\left(1 - P_{nn}\right)}{\omega_H + \omega_M \lambda_{\mathrm{ex}} k_n^2}, \tag{2.40}$$

FV-SW

$$F_{nn} = P_{nn}, \tag{2.41}$$

BV-SW

$$F_{nn} = 1 - P_{nn}, \tag{2.42}$$

where

$$P_{nn} = \frac{k^2}{k_n^2} - \frac{k^4}{k_n^4} \frac{2\left(1 - (-1)^n e^{-kd}\right)}{\left(1 + \delta_{0n}\right) kd}, \tag{2.43}$$

where δ_{0n} is Kronecker's delta.

Typical dispersion curves calculated with the parameters $H_0 = 200$ Oe, $4\pi M_S = 1760$ G, $\lambda_{\mathrm{ex}} = 3 \times 10^{-16}$ m^2, and $d = 10$ μm are shown in Fig.2.3. Dot lines represent results of magnetostatic modes, which are also shown in Fig.2.2d. By considering the exchange interaction, dispersion curves exhibited completely different behavior in large k region. Around $k \sim 10^7$ m^{-1}, dipole-exchange SWs show quadratic dispersion curves, yielding in the rapid wave transmission. On the other hand, magnetostatic modes show flat bands, indicating no capability of transmitting information. In this study, excitation of magnetization with k ranging in $\sim 10^4$ m^{-1} was treated because of the limit of excitation technique. In such small k region, the contribution of H_{ex} is usually negligible and dipole-exchange modes and magnetostatic modes are comparable as shown in Fig.2.3.

2.2.3 All Electrical Spin Wave Spectroscopy

To excite SWs, magnetic moments in the waveguide should be aligned in parallel by a magnetic field H_{eff}. When a part of magnetic moments is tilted from the equilibrium direction, SWs start propagating. Depending on how a torque for tilting magnetic moments is generated, there are different ways to excite SWs. The classical approach is the microwave induction, which is commonly used because of the simplicity of the setup

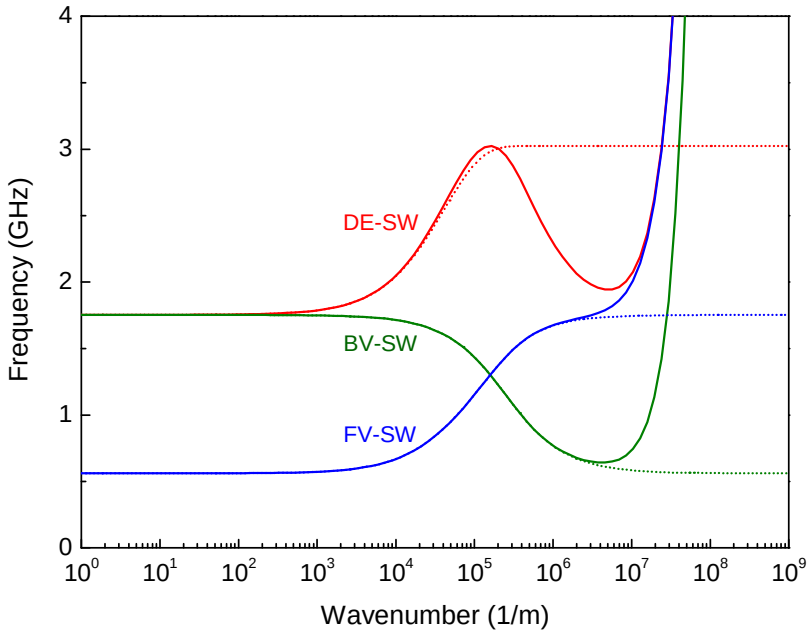

Figure 2.3 Dispersion curves of spin waves with different magnetic field configurations and magnetic interactions. Bold lines represent dispersion curves of dipole-exchange modes, while dot lines represent those of magnetostatic modes. Magnetic film thickness $d = 10$ μm and exchange constant $\lambda_{\mathrm{ex}} = 3 \times 10^{-16}$ m^2 are used.

and capability of controlling of the frequency, wavelength, and phase of the SWs. Nevertheless, an inductive coupling between antennas becomes a serious issue for the further miniaturization. Apart from this, the optical pump techniques using the inverse Faraday effect,[57] magneto electric (ME) cells composed of multiferroic structure,[58] and spin torque nano-oscillators using the spin transfer torque[59] are emerging research topics on the state of art. These techniques are focusing on the point excitation SWs, but the excitation efficiency is rather low.

In this research, the microwave induction was employed to excite SWs using microstrip line (MSL), because of the controllability of excited SWs and the affinity with the equipment, e.g. vector network analyzer. This technique is also known as *all electrical spin wave spectroscopy* (AESWS). A schematic picture is illustrated in Fig.2.4. In this setup, magnetic moments are aligned along y-axis, and a leakage field h_x from the planar antennas inductively couples to the magnetic moments. Among various planar antenna structures, MSLs are used due to the capability of broad excitation. Two MSLs are placed with separation by a distance L, to observe a propagation of SWs. Since a typical value of k_{EMW} is ranging in $\sim 10^2$ m^{-1}, k_{SW} and k_{EMW} cannot directory couple due to the large discrepancy of wavenumbers. Instead of using a crossover of dispersion curves, these waves coupled laterally via leakage magnetic field $h_x(x)$. Thus the excitation spectrum depends on the width of MSLs. From the microwave circuit, the magnetic

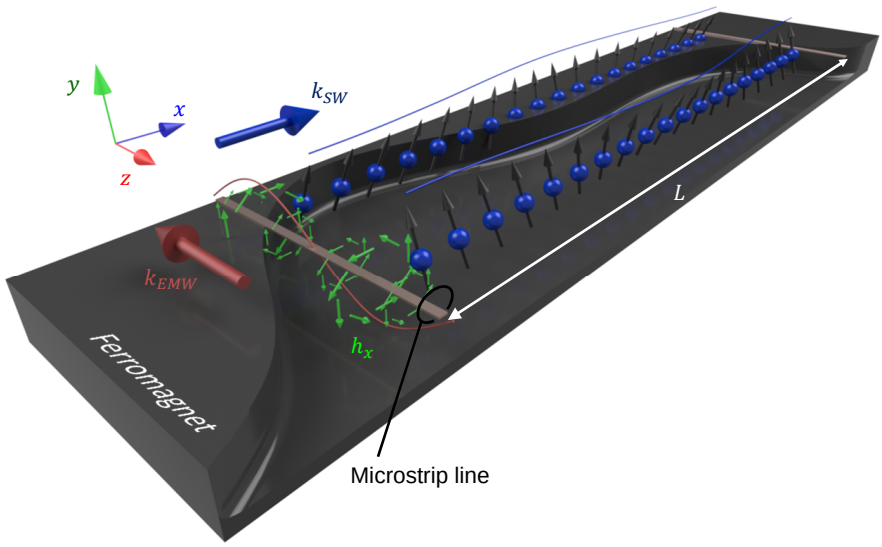

Figure 2.4 Schematization of AESWS. k_{SW} and k_{EMW} represent the wave vectors of SWs and electromagnetic waves, respectively. Lateral leakage field h_x from the microstrip line excites precession of magnetization and SW propagates along x direction.

susceptibility of the ferromagnet at certain frequency ω is derived as[60]

$$\chi(\omega) = \int dk \chi_k(\omega, k) \rho(k) e^{-ikL}, \tag{2.44}$$

where $\chi_k(\omega, k)$ is a contribution to $\chi(\omega)$ from the specific wavenumber k, and $\rho(k)$ is the efficiency of excitation, i.e. Fourier component of $h_x(x)$. It is noteworthy that Eq.2.44 indicates a convolution of the Fourier component of excitation field h_x and k_{SW}.

Typical antenna structure used in this work is shown in Fig.2.5a. L1 is the impedance matched antenna cascaded by narrower L2 without matching. The width of L2 was 50 μm, which was the minimum line and space resolution of a commercial printed circuit board process. The end of L2 was short terminated by the thru-hole to suppress an extra radiation. Lateral magnetic field h_x from L1 and L2 are calculated by using the electromagnetic simulator (ANSYS HFSS ver.15.0). The calculated h_x profiles on the surface of MSLs are graphed in Fig.2.5b. The intensity of h_x is enhanced at the edge of MSLs because of the skin effect. Fourier spectra of h_x are shown in Fig.2.5c. As a result, L1 exhibits the periodic droppings of k for example $\sim 5 \times 10^3$ m^{-1}, and its primary excitation is ranging in 10^3 m^{-1}. On the other hand, L2 covers wider k up to 10^5 m^{-1}. Thus a MSL with such a narrow width is essential to observe SWs with higher k_{SW}, though an impedance mismatch between L1 and L2 increases the insertion loss of the device (typically 10 $\sim$ 20 dB). In the experiment, magnetic waveguides are

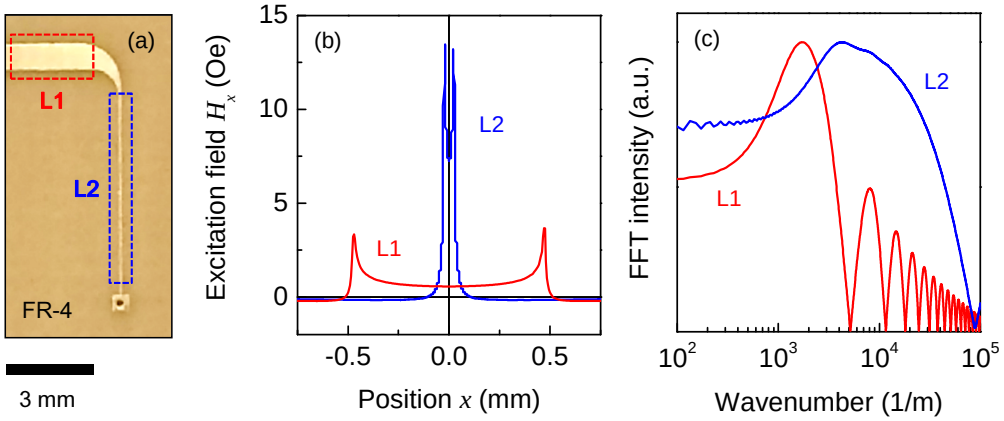

Figure 2.5 Excitation spectra of MSLs. (a) Top view of typical excitation antenna used in this study. L1 labels a part of MSL with the width of 952 μm, L2 labels the rest with the width of 50 μm. Characteristic impedances of L1 and L2 are 50 Ω and 139 Ω, respectively. (b) Distribution of lateral magnetic field $h_x(x)$ from the middle of L1 and L2. Excitation power of 1 mW is assumed. (c) Corresponding Fourier spectra.

placed on the L2 part, and L1 is used to interface with external equipment. Finally, the benefit of MSLs is emphasized in the viewpoint of fundamental investigations. Thanks to such broad excitation spectrum, almost the entire magnonic band can be excited by single measurement, while other planar antennas exhibit strong k selectivity, e.g. coplanar waveguide, meander lines, or inter digital transducers.[61–63]

Typical excitation spectra measured by AESWS are shown in Fig.2.6a. Spectra were measured by using the vector network analyzer, and intensity of SW was displayed in the term of S-parameter. DE-SW was excited under various bias magnetic field H_0. Strong excitation was visualized as brighter line. Measured DE-SWs exhibited the strong excitation with wide frequency bandwidth of nearly 1 GHz (see yellow region), and the maximum transmission intensity of over −20 dB. Propagation band was strongly depends on H_0, and the spectra are slightly differ on each H_0. To understand such H_0 dependence, combined color plot is often used as shown in Fig.2.6b. In the combined color plot, intensity S_{21} was expressed in the brightness. By using this format, H_0 dependence of SWs can be visually understood.

2.3 Yttrium Iron Garnet

2.3.1 Magnetic Properties

YIG was discovered in 1956 by a research group in Grenoble.[64] This material is belong to a magnetic garnet in the group of $R_3Fe_5O_{12}$, where R is from a series of rare earths. There are different types of coordination: dodecahedral {c} site, two octahedral (a) site, and three tetrahedral [d] site. Iron garnet has Fe^{3+} ions on the (a) and [d] sites. And a

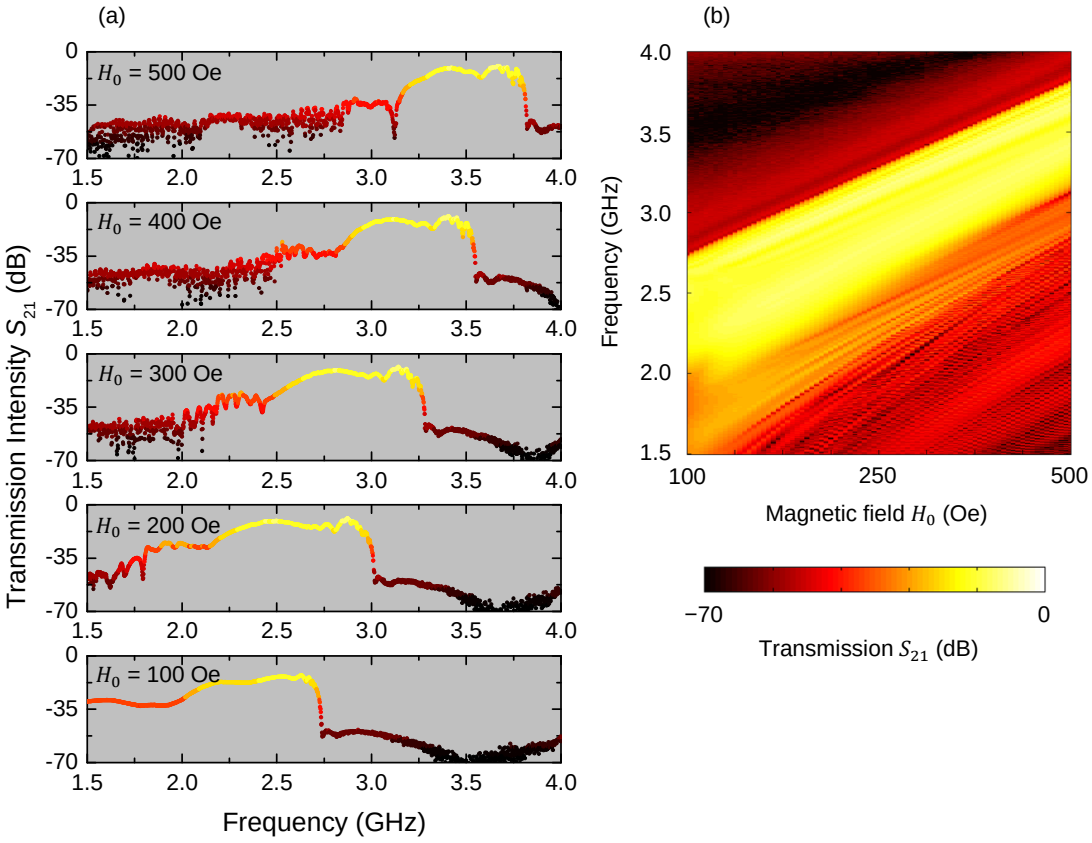

Figure 2.6 Typical SW transmission spectra in 110 μm-thick YIG. (a) Transmission spectra obtained by vector network analyzer with variety of bias magnetic field H_0. (b) Combined color plot with the H_0 resolution of 5 Oe. Color represents intensity of transmission.

Y^{3+} iron occupies the remaining {c} site: $\{Y_3^{3+}\}(Fe_2^{3+})[Fe_3^{3+}]O_{12}$. Fe^{3+} ions give rise to ferromagnetism, but (a) site and [d] site is antiferromagnetically coupled to each other. This yields in a ferromagnetic state with a net magnetic moment comparable to just one Fe^{3+} ($= 5\ \mu_B$). This small net magnetization is advantage to obtain perpendicular magnetization configuration, e.g. FV-SWs. In Fig.2.7, typical magnetic hysteresis of 10 μm-thick YIG is graphed. Saturation field for the in-plane magnetization is about 10 Oe, and measured $4\pi M_S$ is about 2 kG. In the case of out of plane magnetization, saturation field is increased to 2 kOe due to the shape magnetic anisotropy. However, this magnetic field is still able to be applied by usual permanent magnets.

In addition, Fe^{3+} ions are surrounded by oxygen ions, in which an orbital angular momentum is quenched due to a covalent bond with oxygen ions. This yields in a weak spin-orbit coupling.[48] Therefore, orbital angular momentum does not contribute to the

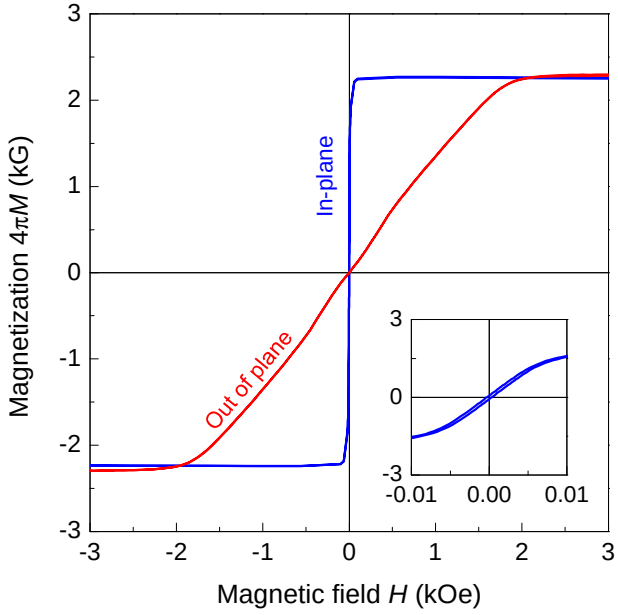

Figure 2.7 Typical magnetic hysteresis of 10 μm-thick YIG. Blue and red line represent in-plane and out of plane magnetic hysteresis loop, respectively. Inset graph shows the detail in the small magnetic field region of the in-plane loop.

magnetism of YIG. Resulting g-factor become 2, and gyromagnetic ratio γ is given by

$$\gamma = \frac{2\mu_B}{\hbar} = 2.8 \text{ MHz/Oe}. \tag{2.45}$$

2.3.2 Potential for Spin Wave Application

The requirements for modern SWDs are downscaling and low power consumption. Therefore affinity to the thin-film technology and smaller magnetic relaxation are required for the ferromagnet. There parameters were extracted for various ferromagnets from earlier reports, and summarized in Fig.2.8. A degree of the magnetic relaxation can be expressed in two physical parameters, namely the Gilbert damping α and resonance field linewidth ΔH. Once the measured frequency ω_{FMR} is given, values of α and ΔH can be converted by the following relation:

$$\Delta H = \Delta H_0 + \frac{2\omega_{\text{FMR}}\alpha}{\gamma}, \tag{2.46}$$

where ΔH_0 is called extrinsic damping, which is given by the inhomogeneity of the magnetic anisotropy or the imperfection of the measurement setup. A value of ΔH was often employed in previous papers using electron spin resonance technique.[65] However, ΔH_0

Table 2.2 Gilbert damping α and thickness d of various reported ferromagnets.

#	Material	Technique	Gilbert damping	thickness (nm)	Ref.
1	Fe_3O_4	MBE	2.0×10^{-1}	5	[66]
1	Fe_3O_4	MBE	3.7×10^{-2}	100	[66]
2	Fe_3O_4	Sputtering	2.0×10^{-2}	50	[67]
3	$Y_3Fe_5O_{12}$	LPE	2.0×10^{-4}	200	[68]
4	$Y_3Fe_5O_{12}$	LPE	2.8×10^{-4}	100	[69]
5	$Y_3Fe_5O_{12}$	LPE	6.7×10^{-5}	1300	[70]
6	$Y_3Fe_5O_{12}$	PLD	7.0×10^{-4}	17	[21]
7	$Y_3Fe_5O_{12}$	PLD	2.3×10^{-4}	20	[22]
7	$Y_3Fe_5O_{12}$	PLD	1.6×10^{-3}	7	[22]
7	$Y_3Fe_5O_{12}$	PLD	3.8×10^{-3}	4	[22]
8	$Y_3Fe_5O_{12}$	PLD	6.2×10^{-5}	56	[71]
8	$Y_3Fe_5O_{12}$	PLD	7.4×10^{-5}	20	[71]
9	$Y_3Fe_5O_{12}$	Sputtering	8.6×10^{-5}	22.3	[72]
10	$Y_3Fe_5O_{12}$	Sputtering	1.0×10^{-3}	10.2	[73]
11	Bi:YIG	MOD	1.4×10^{-3}	27	[74]
12	Ce:YIG	PLD	2.0×10^{-2}	111	[75]
13	EuGa:YIG	LPE	3.0×10^{-2}	8000	[76]
13	SmGa:YIG	LPE	1.3×10^{-1}	3900	[76]
13	EuLuGa:YIG	LPE	2.0×10^{-2}	4400	[76]
13	SmLuGa:YIG	LPE	1.8×10^{-1}	7700	[76]
14	$Co_2MnFeSi$	Sputtering	5.0×10^{-3}	30	[77]
14	Co_2MnSi	Sputtering	2.0×10^{-2}	30	[77]
14	Co_2FeSi	Sputtering	3.0×10^{-3}	30	[77]
15	NiFe	MBE	6.0×10^{-3}	10	[78]
16	NiFe	Sputtering	7.0×10^{-3}	50	[79]
16	NiFe	Sputtering	7.0×10^{-3}	100	[79]
17	CoFeB	Sputtering	8.0×10^{-3}	5	[80]
17	CoFeB	Sputtering	6.0×10^{-3}	40	[80]

is generally unknown. In contrast, α represents pure physical property. Thus α was employed as an index for comparison, and accordingly several reports using only ΔH were omitted.

In Fig.2.8 and Table2.2, potential for SW application is shown for different material systems: magnetites ([1],[2]), garnets ([3]-[13]), Heusler alloys ([14]), and transition metal alloys ([15]-[17]). YIG films exhibit quite low α values in the thicknesses from 10 nm to several micrometers. YIG films with thicknesses over 100 nm have good affinity with liquid phase epitaxy (LPE). Below the thickness of 100 nm, YIG is fabricated by using pulsed laser deposition (PLD) or sputtering. PLD and sputtering techniques pro-

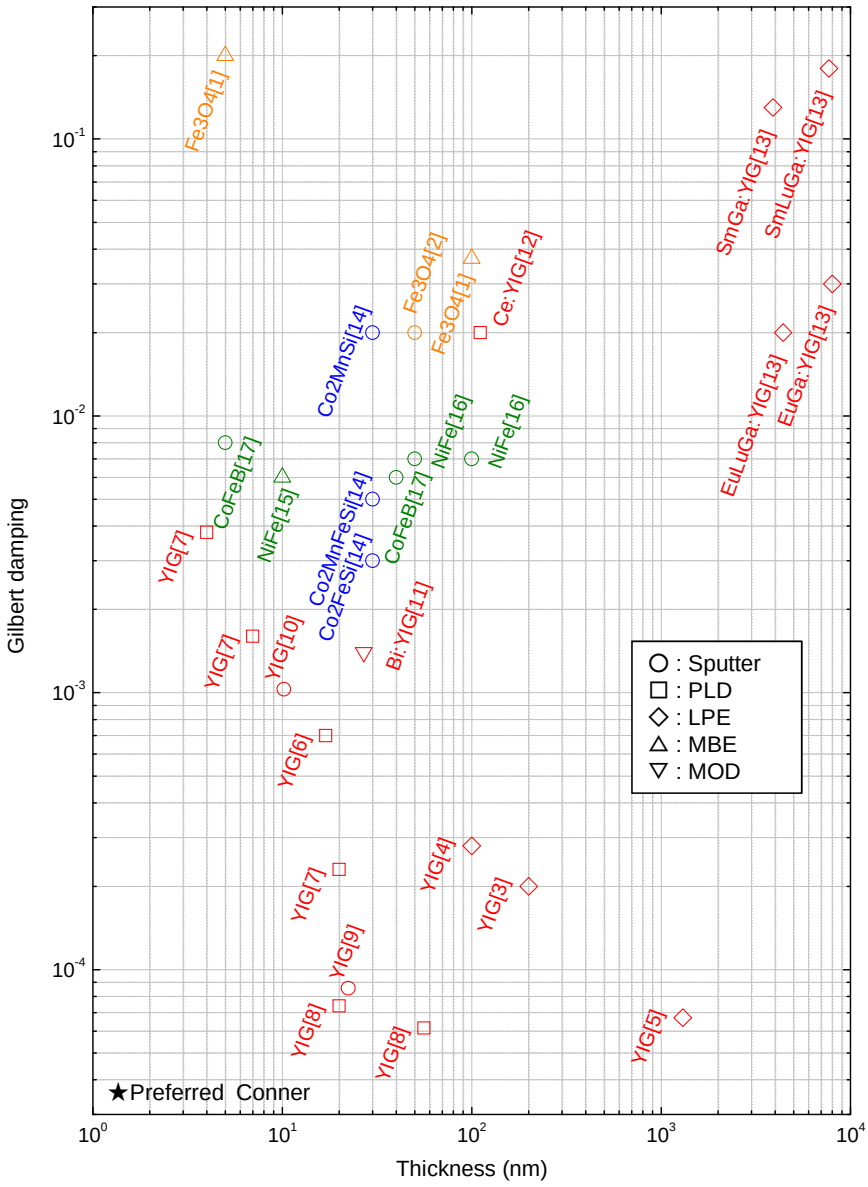

Figure 2.8 Gilbert damping α and thickness of various reported ferromagnets so far.Orange group is magnetite, red group is garnet, blue group is Heusler alloy, and green group is transition metal alloy. Detail is shown in Table2.2.

ceed the growth of high quality thin films. However, the crystal growth in those situation is in a thermodynamically non-equilibrium state, and fabrication of high quality single crystalline garnet was challenging matter. Recent progress on the fabrication technique, e.g. improvement of heat treatment and oxygen partial pressure, enables to make stoichiometric and low defect density YIG films in 10 nm-thick region. Substituted YIG films can enhance other physical properties, e.g. Faraday effect, but α is also increased by the substitution. Therefore, such the substituted garnets are not suitable for the use of waveguides in the view point of this study, i.e. low propagation loss. Several transition metal alloys, e.g. Permalloy (Ni-Fe) and CoFeB, are commonly used in recent SWDs because of the workability, and affinity with technologies from spintronics on the state of art. However, the reported α values are one order of magnitude larger than that of YIG films. Thus these materials require amplification for long distance propagation. Heusler alloys, which are half metals, exhibit slightly better α values than those of transition metal alloys, but α is still larger than those of YIG. However, in the thicknesses of only a few nanometers, α values are almost comparable with YIG films. Relaxation mechanism is sensitive to the surface morphology because of the two-magnon scattering at the interface. Since an unit cell of YIG is 12.376 Å, such ultra-thin YIG films are composed of only a few unit layers. In this limit, the scattering process would be strongly induced. The minimum limit of α might be explained by Kasuya-LeCraw mechanism, in which the fine structure, e.g. crystallographic anisotropies, is dominant for three-magnon scattering or magnon-phonon scattering.[81,82]

From the discussion on earlier works, it can be mentioned that YIG films have advantages both on the thin-film fabrication and lower spin relaxation. According to its perfectly small magnetic relaxation, its position in the field of magnonics is the same as the that of silicon in semiconductor technology. Recently, a long SW decay length reaching to 600 μm was achieved in the 20 nm-thick YIG film.[83] This could enable to integrate SWDs in monolithic YIG substrate. Furthermore, YIG exhibits a huge charge gap of 2.7 eV, yielding in the resistivity of $\sim 10^{12}$ Ωcm at R.T., which is greater than that of air.[70] Such nature further benefits YIG to be exposed by a strong electric field, e.g. capability of further integration of planar antennas, or the voltage control of SWs by ME cells. Considering these potential, YIG films were adopted to the core material of this study. Specifically, prepared YIG films were fabricated on (111) gadolinium gallium garnet substrate by LPE technique, yielding in α in order of 10^{-4}, and thicknesses ranging from 10 to 100μm.

2.4 Summary

In this chapter, theoretical background covering from the origin of ferromagnetism to SWs was presented. The LLG equation was derived from the analogy of classical equation of motion. By considering monochromatic excitation at frequency ω, permeability tensor was derived from the LLG equation. These numerical models underlie the important framework to describe magnetization dynamics in the following chapters. Properties

of SWs under the dipolar interaction were also explained together with the basis of AESWS. Important feature is classification of SWs with respect to the relative direction between k_{SW} and magnetization, i.e. DE-SW, FV-SW, and BV-SW. There modes are orthogonal each other, and exhibit unique properties. Therefore selection of proper mode is necessary. Finally, aspects of YIG were given from the viewpoint of SWDs. YIG films have a possibility of thin-film fabrication with small magnetization relaxation. This is the motivation of this work to investigate SWDs based YIG films.

Chapter 3

Spin Waves in Periodic Structures

In this chapter, general propagation characteristics of SWs are mathematically analyzed, and the control of SW flows by periodic structures, namely artificial magnetic lattices (AMLs), is demonstrated. In §3.1, dispersion curves of SWs in a ferromagnetic thin film with arbitrary magnetization is analyzed. It is shown that the dispersion curve can be modulated by covering the surface with high conductive material. This situation is also calculated for following investigations. In §3.2, AMLs composed of metallic stripes covering the waveguide surface are introduced. Capability of propagation control is numerically analyzed by using the transfer matrix approach, and proved by the experiment. Differences between calculation and experiment is also discussed.

3.1 Spin Waves in Arbitrary Magnetization Direction

3.1.1 Permeability Tensor in Arbitrary Coordinates

In §2.1, a permeability tensor $\bar{\mu}$ was given at specific coordinate $O_M(u, v, w)$, in which an effective field $\boldsymbol{H}_{\mathbf{eff}}$ was applied along w-axis. It is also interesting to investigate magnetization dynamics in other systems with $\boldsymbol{H}_{\mathbf{eff}}$ pointing an arbitrarily direction. To obtain permeability tensor $\bar{\mu}$ in such situation, rotational transforms were employed with following steps:

1. O_M was converted to $O'_M(u', v', w')$ by rotating around u-axis with θ_u.
2. O'_M was converted to $O_G(x, y, z)$ by rotating around v'-axis with θ_v.

The rotating angle θ_u and θ_v were defined in the range of $-\pi/2 \leq \theta_u \leq \pi/2$, and $-\pi \leq \theta_v \leq \pi$, respectively. This operation allowed dynamic magnetic field $\boldsymbol{H}$ and magnetization $\boldsymbol{M}$ to be in any direction in the transformed coordinate $O_G(x, y, z)$. This is schematically displayed in Fig.3.1. A transformation matrix $\mathcal{H}$ corresponding to above

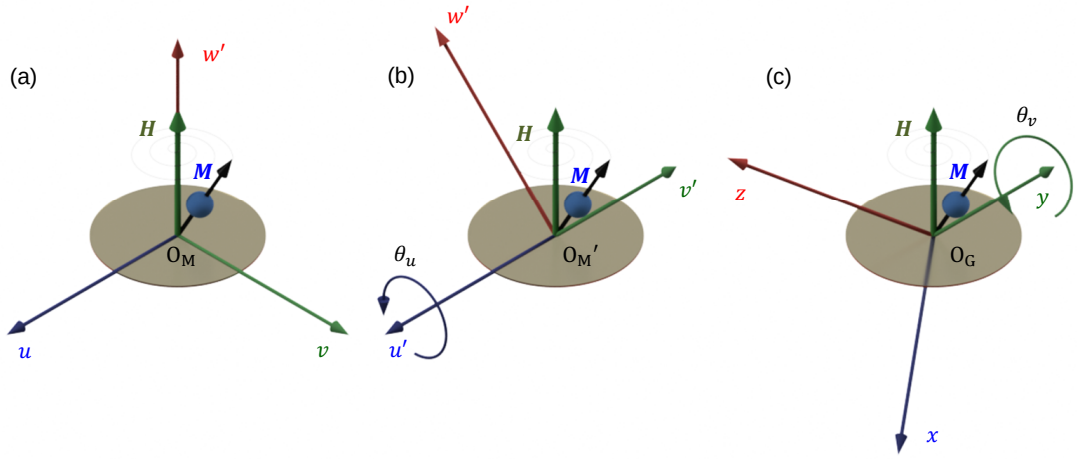

Figure 3.1 Rotational transforms of coordinate. (a) Original coordinate O_M. Effective field $\boldsymbol{H}_{\mathbf{eff}}$ is applied along w-axis. (b) First transform from O_M to O'_M. Rotation around u-axis with θ_u. (c) First transform from O'_M to O_G. Rotation around v'-axis with θ_v.

rotational transform is given by

$$\mathcal{H} = \begin{bmatrix} \mathrm{C}\theta_v & 0 & \mathrm{S}\theta_v \\ 0 & 1 & 0 \\ -\mathrm{S}\theta_v & 0 & \mathrm{C}\theta_v \end{bmatrix} \begin{bmatrix} 1 & 0 & 0 \\ 0 & \mathrm{C}\theta_u & -\mathrm{S}\theta_u \\ 0 & \mathrm{S}\theta_u & \mathrm{C}\theta_u \end{bmatrix}$$

$$= \begin{bmatrix} \mathrm{C}\theta_v & \mathrm{S}\theta_u\mathrm{S}\theta_v & \mathrm{C}\theta_u\mathrm{S}\theta_v \\ 0 & \mathrm{C}\theta_u & -\mathrm{S}\theta_u \\ -\mathrm{S}\theta_v & \mathrm{S}\theta_u\mathrm{C}\theta_v & \mathrm{C}\theta_u\mathrm{C}\theta_v \end{bmatrix}, \tag{3.1}$$

where $\cos\theta_u = C\theta_u$, $\sin\theta_u = S\theta_u$, $\cos\theta_v = C\theta_v$ and $\sin\theta_v = S\theta_v$ are abbreviated forms, respectively. This transform matrix $\mathcal{H}$ satisfies an orthogonality condition, which is given by

$$\sum_i \mathcal{H}_{ij}\mathcal{H}_{jk} = \delta_{jk} \qquad ;\ i,j,k \in \{1,2,3\}, \tag{3.2}$$

where δ_{jk} is the delta function. Since Eq.3.1 satisfies Eq.3.2, $\mathcal{H}$ is ensured to be an orthogonal transformation. The resulting $O_G(x, y, z)$ become an orthogonal coordinate system as long as $O_M(u, v, w)$ is orthogonal. This arrows us to write

$$\mathcal{H}^{-1} = \mathcal{H}^T, \tag{3.3}$$

where the superscript T represents a transposed matrix. A magnetic flux, magnetic field and permeability tensor in the O_G-coordinate system were defined as $\boldsymbol{b}_G$, $\boldsymbol{h}_G$ and $\bar{\mu}_G$, respectively. Likewise, $\boldsymbol{b}_M$, $\boldsymbol{h}_M$ and $\bar{\mu}_M$ were defined for the O_M-coordinate. A coordinate transform of magnetic flux is given by

$$\boldsymbol{b}_G = \mathcal{H}\boldsymbol{b}_M = \mathcal{H}\left(\bar{\mu}_M \boldsymbol{h}_M\right) = \left(\mathcal{H}\bar{\mu}_M\mathcal{H}^T\right)\boldsymbol{h}_G. \tag{3.4}$$

Substitution of Eq.2.33 into Eq.3.4, transformed permeability tensor $\bar{\mu}_G$ is given by

$$\bar{\mu}_G = \mathcal{H}\bar{\mu}_M\mathcal{H}^T = \begin{bmatrix} \mu_{11} & \mu_{21} & \mu_{31} \\ \mu_{12} & \mu_{22} & \mu_{32} \\ \mu_{13} & \mu_{23} & \mu_{33} \end{bmatrix}, \tag{3.5}$$

where

$$\begin{cases} \mu_{11} &= \mu \mathrm{C}^2\theta_v + \mu \mathrm{S}^2\theta_u \mathrm{S}^2\theta_v + \mathrm{C}^2\theta_u \mathrm{S}^2\theta_v \\ \mu_{12} &= i\nu\kappa \mathrm{C}\theta_u \mathrm{C}\theta_v + (\mu - 1)\mathrm{C}\theta_u \mathrm{S}\theta_u \mathrm{S}\theta_v \\ \mu_{13} &= i\nu\kappa \mathrm{S}\theta_u - (\mu - 1)\mathrm{C}^2\theta_u \mathrm{C}\theta_v \mathrm{S}\theta_v \\ \mu_{21} &= -i\nu\kappa \mathrm{C}\theta_u \mathrm{C}\theta_v + (\mu - 1)\mathrm{C}\theta_u \mathrm{S}\theta_u \mathrm{S}\theta_v \\ \mu_{22} &= \mu \mathrm{C}^2\theta_u + \mathrm{S}^2\theta_u \\ \mu_{23} &= i\nu\kappa \mathrm{C}\theta_u \mathrm{S}\theta_v + (\mu - 1)\mathrm{C}\theta_u \mathrm{S}\theta_u \mathrm{C}\theta_v \\ \mu_{31} &= -i\nu\kappa \mathrm{S}\theta_u - (\mu - 1)\mathrm{C}^2\theta_u \mathrm{C}\theta_v \mathrm{S}\theta_v \\ \mu_{32} &= -i\nu\kappa \mathrm{C}\theta_u \mathrm{S}\theta_v + (\mu - 1)\mathrm{C}\theta_u \mathrm{S}\theta_u \mathrm{C}\theta_v \\ \mu_{33} &= \mu \mathrm{S}^2\theta_v + \mu \mathrm{S}^2\theta_u \mathrm{S}^2\theta_v + \mathrm{C}^2\theta_u \mathrm{C}^2\theta_v \end{cases} . \tag{3.6}$$

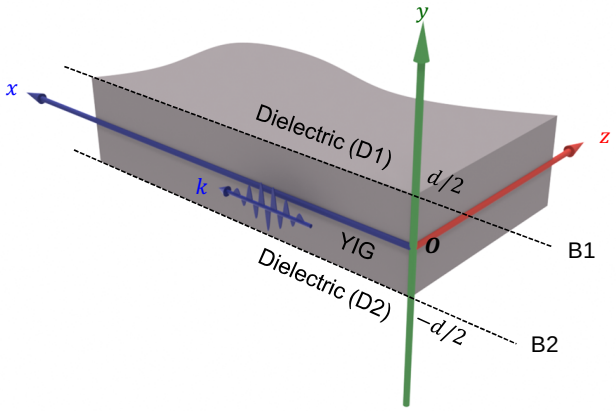

Figure 3.2 Model of bare surface slab. From the top, there are dielectric (D1) layer, YIG layer, and dielectric (D2) layer. SW propagates along x-axis. Boundary B1 is at $y = d/2$, and B2 is at $y = -d/2$, where d is the thickness of YIG slab. No boundary on z-axis, yielding in $\partial/\partial z = 0$.

3.1.2 Bare Surface Waveguides

So far we discussed magnetization dynamics homogeneously excited in the ferromagnet. Thus there was no phase difference among precession at excitation frequency ω, namely wavenumber $k = 0$. This state is often mentioned as ferromagnetic resonance (FMR). In this part, other magnetization dynamics with $k > 0$ are analyzed. The origin of inhomogeneous excitation may be, e.g. inhomogeneous inductive field caused by planar antennas, or scattering due to defects or impurities.[84] Such excitations with non-zero k are called SWs. The contribution of exchange interaction can be ignored, since operated wavelengths were below $k < 10^{-6}$ m^{-1} in this study. Beforehand, the dominant equations are given as follows:

$$\boldsymbol{\nabla} \times \boldsymbol{h} = 0, \tag{3.7}$$

$$\boldsymbol{\nabla} \cdot \boldsymbol{b} = \boldsymbol{\nabla} \cdot (\bar{\mu}_G \boldsymbol{h}) = 0, \tag{3.8}$$

where $\boldsymbol{h}$ is a radio frequency magnetic field, and $\boldsymbol{b}$ is a radio frequency magnetic flux. These time dependences are supposed to be $\propto e^{-i\omega t}$. In Eq.3.7, the conduction current and displacement current on the right hand side are ignored. This is called magnetostatic

approximation, and usually valid in insulating ferromagnets like YIG.[85,86] From Eq.3.7, a potential of the system is given by

$$\boldsymbol{h} = -\boldsymbol{\nabla}\phi(\boldsymbol{r}, t), \tag{3.9}$$

where $\phi(\boldsymbol{r}, t)$ is the scalar potential at specific coordinate $\boldsymbol{r} = (x, y, z)$ and time t. The purpose of this part is to obtain the dispersion curve for ϕ, which is defined in the O_G-coordinate. The configuration around the YIG slab is shown in Fig.3.2, where the saturation magnetization $4\pi\boldsymbol{M_S}$ and the magnetic field $\boldsymbol{H}_{\mathbf{eff}}$ point an arbitrarily direction. The ferromagnetic waveguide (YIG) is sandwiched by two dielectric materials (D1, D2). Both boundaries B1 and B2 are not electromagnetically grounded. Hereby this type of slab is called bare surface (BS) slab. It should be noted that the slab is homogeneous along z-axis, yielding $\partial/\partial z = 0$.

When $\phi(\boldsymbol{r}, t)$ forms periodic oscillation, namely $\phi(\boldsymbol{r}, t) = \phi(\boldsymbol{r} + \boldsymbol{R}, t)$, this function can be expanded in the term of Bloch function. In Fig.3.2, the SW propagates along x-axis, and its time dependence is assumed to be $\propto e^{-i\omega t}$. Therefore $\phi(\boldsymbol{r}, t)$ is simply given as

$$\phi(\boldsymbol{r}, t) = \phi_0(y)e^{i(\omega t - k_x x)}, \tag{3.10}$$

where $\phi_0(y)$ is the profile of scalar potential along y-axis. Since $\phi_0(y)$ is undetermined function, this should be determined in such a way as to satisfy the electromagnetic nature at boundaries B1 and B2. Substitution of Eq.3.10 into Eq.3.9 and Eq.3.8 yields

$$\begin{aligned}\boldsymbol{\nabla} \cdot (-\bar{\mu}_G \boldsymbol{\nabla}\phi) &= -\boldsymbol{\nabla} \cdot \begin{bmatrix} \mu_{11} & \mu_{12} & \mu_{13} \\ \mu_{21} & \mu_{22} & \mu_{23} \\ \mu_{31} & \mu_{32} & \mu_{33} \end{bmatrix} \begin{pmatrix} \nabla_x\phi \\ \nabla_y\phi \\ 0 \end{pmatrix} \\ &= \mu_{11}{k_x}^2\phi + ik_x\left(\mu_{12} + \mu_{21}\right)\frac{\partial\phi}{\partial y} - \mu_{22}\frac{\partial^2\phi}{\partial y^2} = 0. \end{aligned} \tag{3.11}$$

From Eq.3.11, a differential equation of $\phi_0(y)$ is given as

$$\frac{\partial^2}{\partial y}\phi_0(y) - ik_x\frac{\mu_{12} + \mu_{21}}{\mu_{22}}\frac{\partial}{\partial y}\phi_0(y) - {k_x}^2\frac{\mu_{11}}{\mu_{22}}\phi_0(y) = 0. \tag{3.12}$$

To assume a general solution of $\phi_0(y)$, a characteristic equation of Eq.3.12 is investigated. This is given by

$$\zeta^2 - ik_x\frac{\mu_{12} + \mu_{21}}{\mu_{22}}\zeta - {k_x}^2\frac{\mu_{11}}{\mu_{22}} = 0, \tag{3.13}$$

where ζ is solution of this equation. From Eq.3.13 and Eq.3.6, its discriminant yields

$$\mu\left(\frac{{k_x}^2}{\mu \mathrm{C}^2\theta_u + \mathrm{S}^2\theta_u}\right)\left\{\mathrm{C}^2\theta_v\left(\mu \mathrm{C}^2\theta_u + \mathrm{S}^2\theta_u\right) + \mathrm{S}^2\theta_v\right\} \neq 0. \tag{3.14}$$

This is because $k_x \neq 0$ and $\mu \neq 0$ in frequencies where SWs propagate. Therefore the general solution is given by a linear sum of two independent solutions.

$$\phi_0(y) = \phi_{01}e^{\zeta_+ y} + \phi_{02}e^{\zeta_- y}, \tag{3.15}$$

where exponents $\zeta_\pm$ allows complex numbers. The solutions $\zeta_\pm$ of the characteristic equation Eq.3.13 is given by

$$\begin{aligned}\zeta_\pm &= ik_x\frac{\mu_{12}+\mu_{21}}{\mu_{22}} \pm \frac{k_x}{\mu_{22}}\sqrt{4\mu_{11}\mu_{22} - (\mu_{12}+\mu_{21})^2} \\ &= \frac{2i\left(\mu-1\right)\mathrm{C}\theta_u\mathrm{S}\theta_u\mathrm{S}\theta_v \pm \sqrt{\mu \mathrm{C}^2\theta_v\left(\mu \mathrm{C}^2\theta_u + \mathrm{S}^2\theta_u\right) + \mu \mathrm{S}^2\theta_v}}{\mu \mathrm{C}^2\theta_u + \mathrm{S}^2\theta_u}\ k_x.\end{aligned} \tag{3.16}$$

The solution implies the given wavenumber for $\phi_0(y)$ is proportional to k_x. For specific coordinate, e.g. $\theta_v = 0$, the solution $\zeta_\pm = \pm k_x$, in which $|\nabla_x\phi| = |\nabla_y\phi|$. This situation is also predicted by Walker's equation.[49] For simplicity, k_x is redefined as k, and $\phi_0(y)$ is specified. Now Eq.3.10 can be written with obtained $\phi_0(y)$, which yields

$$\phi(\boldsymbol{r}, t) = \left(\phi_{01}e^{\tilde{\zeta}_+ ky} + \phi_{02}e^{\tilde{\zeta}_- ky}\right)e^{i(\omega t - kx)}, \tag{3.17}$$

where

$$\tilde{\zeta}_\pm = \frac{2i\left(\mu-1\right)\mathrm{C}\theta_u\mathrm{S}\theta_u\mathrm{S}\theta_v \pm \sqrt{\mu \mathrm{C}^2\theta_v\left(\mu \mathrm{C}^2\theta_u + \mathrm{S}^2\theta_u\right) + \mu \mathrm{S}^2\theta_v}}{\mu \mathrm{C}^2\theta_u + \mathrm{S}^2\theta_u}. \tag{3.18}$$

A general form of the scalar potential $\phi(\boldsymbol{r}, t)$ was obtained in Eq.3.17, but this equation is available only $-d/2 \leq y \leq d/2$ because permeability tensor $\bar{\mu}_G$ of YIG was supposed. In Fig.3.2, boundaries B1 and B2 are not grounded, there are other finite potential $\psi^{(N)}(\boldsymbol{r}, t)$ in the dielectric layer DN.

$$\psi^{(N)}(\boldsymbol{r}, t) = \psi_0^{(N)}(y)e^{i(\omega t - kx)}, \tag{3.19}$$

where $\psi_0^{(N)}(y)$ is the unknown function to represent the profile along y-axis. This is also specified by using Eq.3.8. Since, DN is composed of the dielectric material, a permeability

tensor becomes $\bar{\mu}_G = \bar{I}$ (unit matrix) in this case. This gives a simple Laplace equation for $\psi_0^{(N)}(y)$ instead of the complicated differential equation.

$$\frac{\partial^2}{\partial y^2}\psi_0^{(N)}(y) - k^2\psi_0^{(N)}(y) = 0 \tag{3.20}$$

A general solution of $\psi_0^{(N)}(y)$ can be easily obtained as

$$\psi_0^{(N)}(y) = \psi_{01}^{(N)}e^{ky} + \psi_{02}^{(N)}e^{-ky}. \tag{3.21}$$

In the system, ground is given at infinite-point, therefore Eq.3.21 should be converged at $y \to \infty$. This condition yields

$$\begin{cases} \psi_{01}^{(N)} = 0 & ;\ D1 : y > 0 \\ \psi_{02}^{(N)} = 0 & ;\ D2 : y < 0 \end{cases}. \tag{3.22}$$

Finally, Eq.3.19 can be written as

$$\psi^{(N)}(\boldsymbol{r}, t) = \left(\psi_{01}^{(N)}e^{ky} + \psi_{02}^{(N)}e^{-ky}\right)e^{i(\omega t - kx)}. \tag{3.23}$$

Now scalar potentials $\psi^{(1)}(\boldsymbol{r}, t)$, $\phi(\boldsymbol{r}, t)$, and $\psi^{(2)}(\boldsymbol{r}, t)$ were specified in the all domains, i.e. D1, YIG, and D2. To specify the character of propagating SWs, unknown coefficients $\psi_{02}^{(1)}$, ϕ_{01}, ϕ_{02}, and $\psi_{01}^{(2)}$ in Eq.3.17 and Eq.3.23 should be determined. These parameters are determined by following boundary conditions.

1. Continuity of scalar potentials at B1 and B2.
2. Continuity of the normal component of magnetic fluxes b_y at B1 and B2.

Normal component of the magnetic flux can be derived by $(-\bar{\mu}_G\boldsymbol{\nabla}\phi)\cdot\hat{y}$ for YIG layer and $-\nabla_y\psi^{(N)}$ for dielectric layers. These boundary condition yields following simultaneous equations.

$$\psi_{02}^{(1)}e^{-kd/2} = \phi_{01}e^{\tilde{\zeta}_+ kd/2} + \phi_{02}e^{\tilde{\zeta}_- kd/2}, \tag{3.24}$$

$$\psi_{01}^{(2)}e^{-kd/2} = \phi_{01}e^{-\tilde{\zeta}_+ kd/2} + \phi_{02}e^{-\tilde{\zeta}_- kd/2}, \tag{3.25}$$

$$-\psi_{02}^{(1)}e^{-kd/2} = \left(\tilde{\zeta_+}\mu_{22} - i\mu_{21}\right)\phi_{01}e^{\tilde{\zeta_+}kd/2} + \left(\tilde{\zeta_-}\mu_{22} - i\mu_{21}\right)\phi_{02}e^{\tilde{\zeta_-}kd/2}, \tag{3.26}$$

$$\psi_{01}^{(2)}e^{-kd/2} = \left(\tilde{\zeta_+}\mu_{22} - i\mu_{21}\right)\phi_{01}e^{-\tilde{\zeta_+}kd/2} + \left(\tilde{\zeta_-}\mu_{22} - i\mu_{21}\right)\phi_{02}e^{-\tilde{\zeta_-}kd/2}. \tag{3.27}$$

Solving Eq.3.24-Eq.3.27 for the state vector $(\phi_{01}, \phi_{02})^T$, a secular equation for $(\phi_{01}, \phi_{02})^T$ is obtained. This equation can be written in the matrix form as

$$\begin{bmatrix} \left(\tilde{\zeta_+}\mu_{22} - i\mu_{21} + 1\right)e^{\tilde{\zeta}_+kd/2} & \left(\tilde{\zeta_-}\mu_{22} - i\mu_{21} + 1\right)e^{\tilde{\zeta}_-kd/2} \\ \left(\tilde{\zeta_+}\mu_{22} - i\mu_{21} - 1\right)e^{-\tilde{\zeta}_+kd/2} & \left(\tilde{\zeta_-}\mu_{22} - i\mu_{21} - 1\right)e^{-\tilde{\zeta}_-kd/2} \end{bmatrix} \begin{pmatrix} \phi_{01} \\ \phi_{02} \end{pmatrix} = 0. \tag{3.28}$$

Solving Eq.3.28 for the nontrivial solution of $(\phi_{01}, \phi_{02})^T$, the eigenfunction gives dispersion curve of the propagating SWs. This can be obtained by making the determinant to be zero.

$$k = \frac{1}{(\tilde{\zeta}_+ - \tilde{\zeta}_-)d} \ln\left\{ \frac{\tilde{\zeta_+}\mu_{22} - i\mu_{21} - 1}{\tilde{\zeta_+}\mu_{22} - i\mu_{21} + 1} \frac{\tilde{\zeta_-}\mu_{22} - i\mu_{21} + 1}{\tilde{\zeta_-}\mu_{22} - i\mu_{21} - 1} \right\} \tag{3.29}$$

By using Eq.3.29, a wavenumber k in the BS slab can be calculated. In the obtained dispersion curve, SW propagation is expressed in the O_G-coordinate and k is pointing x-axis based on the definition in Fig.3.2. During the transformation, O_M-coordinate is rotated against O_G-coordinate. It is noteworthy that O_G-coordinate can be observed from O_M-coordinate, since the relative direction of these coordinates is remained because of the orthogonality of transformation matrix $\mathcal{H}$. In this case, it is also possible to fix $\boldsymbol{H}_{\mathbf{eff}}$ and $4\pi\boldsymbol{M_S}$ in certain direction in the O_G-coordinate, and rotate k in the film plane. Fig.3.3a shows dispersion relation of (k_x, k_z) with the magnetic field applied along z-axis (in-plane magnetization). On the other hand, Fig.3.3b shows those of (k_x, k_z) with the magnetic field applied along y-axis (out of plane magnetization).

In the case of in-plane magnetization, SWs exhibited two dispersion branches. At lower frequencies, SWs preferred to propagate along z-axis (BV-SWs was calculated). Obtained dispersion branch was symmetric to x-axis. In this frequency region, no dispersion branch was appeared along x-axis. At higher frequencies, SWs preferred to propagate along x-axis (DE-SWs was calculated). In this frequency region, no dispersion branch was appeared along z-axis. Obtained dispersion branch was symmetric to z-axis. Dispersion curve at specific frequencies are also shown. Red and blue lines on the bottom represent iso-dispersion surfaces of the BV-SW at 2 GHz and DE-SW at 3 GHz, respectively. All iso-dispersion curves are symmetric to their symmetric axis, therefore

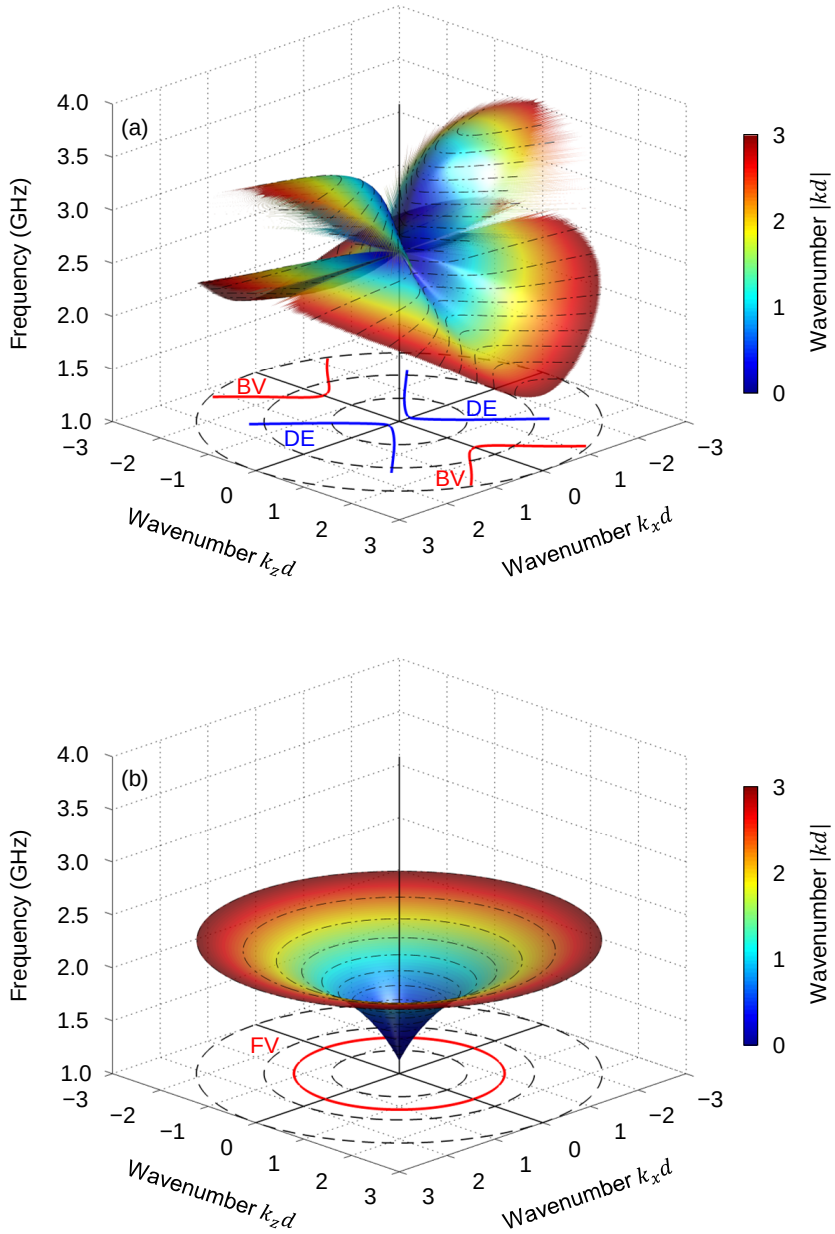

Figure 3.3 Dispersion curve of SWs within BS slab lying in $x-z$ plane. Normalized wavenumber $k_x d$ and $k_z d$ denote x component and z component of wave vector of SWs normalized by slab thickness d. Magnetic field $\boldsymbol{H}_{\mathbf{eff}} = 400$ Oe is applied along (a) z-axis and (b) y-axis. A 3-D contour plot represent k at certain frequency and orientation. Color represents the size of $|kd| = (k_x d + k_z d)^{1/2}$. In the plot, $|kd| < 3$ is displayed. Red and blue bold lines on the bottom show typical $(k_x d, k_z d)$ at 2.00 GHz and 3.00 GHz, respectively. Labels DE, BV, and FV indicate corresponding SW modes of DE-SW, BV-SW, and FV-SW.

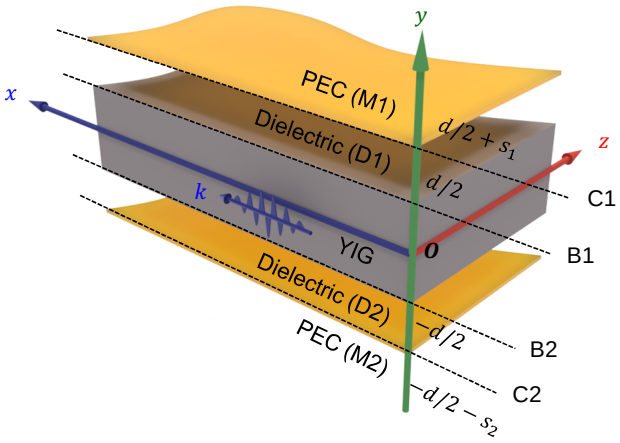

Figure 3.4 Model of metalized surface slab. From the top, there are PEC (M1) layer, dielectric (D1) layer, YIG layer, dielectric (D2) layer, and PEC (M2) layer. SW propagates along x-axis. Boundary B1 is at $y = d/2$, and B2 is at $y = -d/2$, where d is the thickness of slab. Boundary C1 is at $y = d/2 + s_1$, and C2 is at $y = -d/2 - s_2$, where s_i is the gap between YIG and PEC. No boundary on z-axis, yielding in $\partial/\partial z = 0$.

no non-reciprocity can be seen on dispersion branches.

When out of plane magnetization was assumed, SWs exhibited a single dispersion branch (FV-SW is calculated). This mode exhibited perfect point symmetry in all frequencies in the band. This symmetric dispersion curve was completely different to that of the in-plane magnetization. Iso-dispersion curves also gave a perfect symmetry, yielding in $k_x^2 + k_z^2 = k^2$. This graph ensured that FV-SWs can propagate every direction in the film plane, without changing the size of wavenumber k. This is why the FV-SWs show good affinity with device integration, from the viewpoint of phase-conservation.

3.1.3 Metalized Surface Waveguides

In the previous part, SW dispersion was obtained for the BS slab. In this slab, a ground was assumed at infinite-point. This ground can be replaced by conductive layers, e.g. perfect electric conductor (PEC). Therefore locating PEC layers near the YIG layer gives change in the boundary condition, yielding in the modulation of dispersion curve. This modulation of dispersion curves provides an opportunity to control SW flow, as discussed in the following section.

Slab structure with PEC layers is shown in Fig.3.4. The ferromagnet layer (YIG) is sandwiched by two dielectric layers D1 and D2. This slab structure is further sandwiched

by two perfect electric conductor (PEC) layers M1 and M2. The gap between YIG and M1 is defined as s_1, and that between YIG and M2 is defined as s_2. Hereby this type of slab is called metalized surface (MS) slab. The dispersion curve of this slab was analyzed by the same procedure as previous part except for the boundary condition. New boundary condition was given as follows:

1. Continuity of scalar potentials at B1 and B2.
2. Continuity of the normal component of magnetic fluxes b_y at B1 and B2.
3. Zero normal component of magnetic fluxes b_y at C1 and C2.

In the MS slab, the boundary condition #3 was introduced. When the conductivity is infinite, the electromagnetic field cannot penetrate into the PEC layers because of the zero skin depth against the variable magnetic field. Thus b_y is vanished at C1 and C2. These boundary conditions gives following secure equation.

$$\begin{bmatrix} \left(\tilde{\zeta_+}\mu_{22} - i\mu_{21} + \delta_1\right) e^{\tilde{\zeta_+}kd/2} & \left(\tilde{\zeta_-}\mu_{22} - i\mu_{21} + \delta_1\right) e^{\tilde{\zeta_-}kd/2} \\ \left(\tilde{\zeta_+}\mu_{22} - i\mu_{21} - \delta_2\right) e^{-\tilde{\zeta_+}kd/2} & \left(\tilde{\zeta_-}\mu_{22} - i\mu_{21} - \delta_2\right) e^{-\tilde{\zeta_-}kd/2} \end{bmatrix} \begin{pmatrix} \phi_{01} \\ \phi_{02} \end{pmatrix} = 0, \quad (3.30)$$

where

$$\delta_i = \tanh(ks_i). \quad (3.31)$$

Solving Eq.3.30 for the nontrivial solution of $(\phi_{01}, \phi_{02})^T$, the eigenfunction gives dispersion curve of the propagating SWs. This can be obtained by making the determinant to be zero.

$$k = \frac{1}{(\tilde{\zeta_+} - \tilde{\zeta_-})d} \ln \left\{ \frac{\tilde{\zeta_+}\mu_{22} - i\mu_{21} - \delta_2}{\tilde{\zeta_+}\mu_{22} - i\mu_{21} + \delta_1} \frac{\tilde{\zeta_-}\mu_{22} - i\mu_{21} + \delta_1}{\tilde{\zeta_-}\mu_{22} - i\mu_{21} - \delta_2} \right\}. \quad (3.32)$$

By considering $s_i \to \infty$ in Eq.3.31, $\delta_i \to 1$ is obtained. In this limit, Eq.3.32 becomes same as Eq.3.29 of BS slab. This is quite reasonable. More specifically, $\tanh(x)$ takes a value of 0.76 at $x = 1$, and 0.96 at $x = 2$. Therefore the gap heights of $s_i = 2/k$ are enough to suppress the effect of PEC layer. On the other hand, the waveguide with the gap heights of $s_i = 0$ yields

$$k = \frac{1}{(\tilde{\zeta_+} - \tilde{\zeta_-})d} \ln(1) = 0. \quad (3.33)$$

This implies the waveguide sandwiched by the PEC layers without gap does not allow propagation of any SW modes. Thus the most interesting structure for applications is combination of $s_1 = 0$ and $s_2 \to \infty$, in which only a single side is covered by the high conductive layer. This slab exhibit the dispersion curve of

$$k = \frac{1}{(\tilde{\zeta_+} - \tilde{\zeta_-})d} \ln \left\{ \frac{\tilde{\zeta_+}\mu_{22} - i\mu_{21} - 1}{\tilde{\zeta_+}\mu_{22} - i\mu_{21}} \frac{\tilde{\zeta_-}\mu_{22} - i\mu_{21}}{\tilde{\zeta_-}\mu_{22} - i\mu_{21} - 1} \right\}. \tag{3.34}$$

Following to the previous part, dispersion curves within the slab were calculated by using Eq.3.34 and were shown in Fig.3.5. As shown in the case of the BS slab, the in-plane magnetization configuration exhibited anisotropic dispersion curves, and the out of plane magnetization configuration exhibited isotropic dispersion curve. Comparing to the BS slab, $|kd|$ takes smaller values in all magnetization configurations. Especially in the FV-SWs, the $|kd|$ value of MS slab is decreased to about a half of that of BS slab in all frequencies. This indicates metalization of the single surface controls the wavenumber. This change of the wavenumber can control the SW reflection at the interface, like an interface of materials with different refractive indexes for optical waves.

In the case of DE-SWs, the dispersion branch of $k_x < 0$ side was remarkably modulated. Since the scalar potential of DE-SWs is localized at the either surface of the slab, DE-SWs are sensitive to the surface environment. In this calculation, DE-SW with $k_x < 0$ supposed to be concentrated beneath the boundary B1 (metalized side). In contrast, one with $k_x > 0$ supposed to be concentrated beneath the boundary B2 (dielectric side). Therefore the metalization gave remarkable non-reciprocity, and the large modulation of the wavenumber at the same time. Not only in the DE-SW branches, but this non-reciprocity can be also seen in BV-SW branches. As obviously in the iso-dispersion surface in Fig.3.5a (seen red lines), calculated dispersion curves showed a small offset along k_x direction, and became asymmetric to x-axis. This is caused by the contribution of mixing of non-reciprocal DE-SWs to BV-SWs. This accompanying non-reciprocity would invest a weak isolation property for BV-SWs with oblique incidence.

3.1.4 Evidence of Dispersion Curve Modulation

In previous parts, SW dispersion curves were calculated both for the BS and MS slabs. Modulation of the dispersion curve by the surface metalization was numerically proved. In Fig.3.5, the DE-SW dispersion branch with $k_x < 0$ was strongly affected by the metalization. To confirm this by experiment, the following experiments were carried out. The experimental setups for the BS slab and MS slabs are shown in Fig.3.6a and b, respectively. A 110 μm-thick YIG was employed for the experiment. The waveguide ends were cut with the cutting angle of 45° to suppress SW backscattering from the waveguide end. This is reasonable from the dispersion curve shown in Fig.3.3a. Such tapered waveguide ends usually scatters DE-SWs into orthogonal direction, but there is no dispersion branch in the scattered direction. In this manner, DE-SWs were strongly damped at the tapered waveguide ends. This waveguide was placed on the transducer

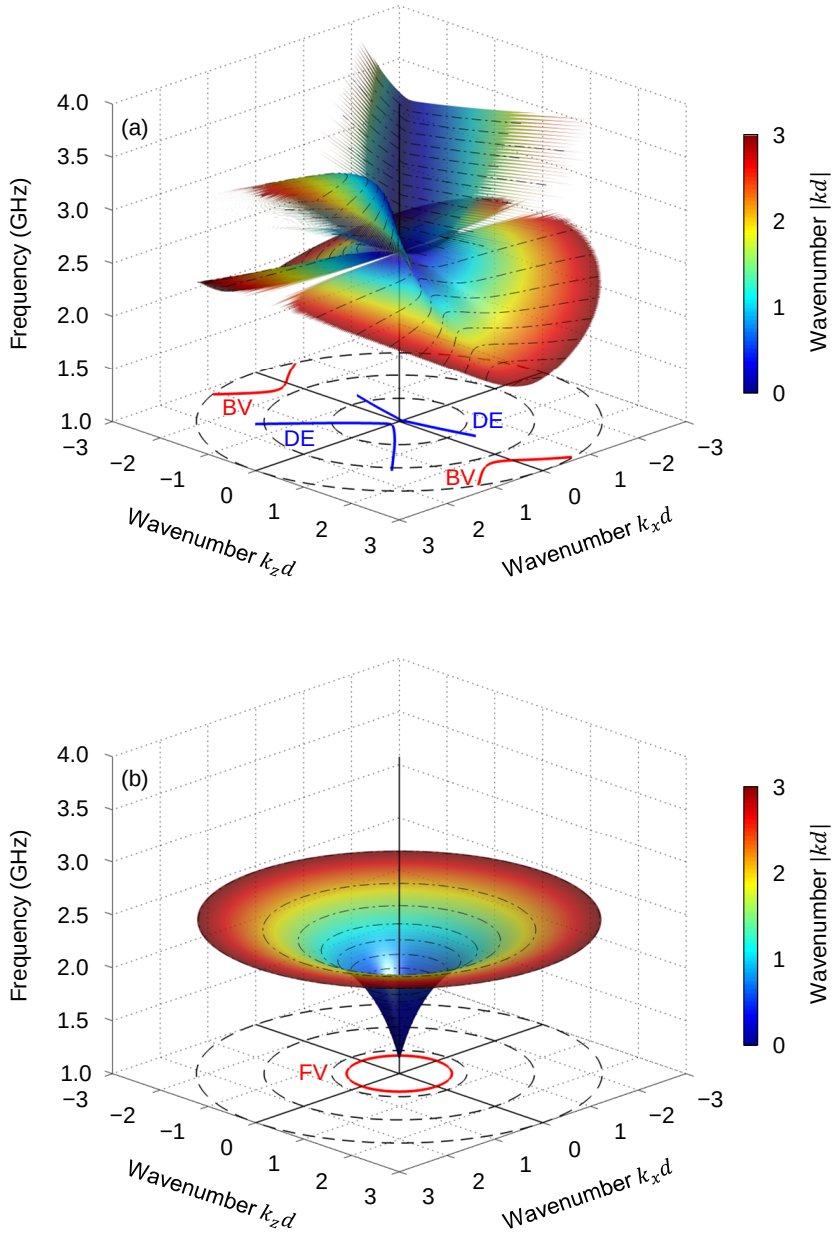

Figure 3.5 Dispersion curve of SWs within MS slab lying in $x-z$ plane. Normalized wavenumber $k_x d$ and $k_z d$ denote x component and z component of wave vector of SWs normalized by slab thickness d. Magnetic field $\boldsymbol{H}_{\mathbf{eff}} = 400$ Oe is applied along (a) z-axis and (b) y-axis. A 3-D contour plot represent k at certain frequency and orientation. Color represents the size of $|kd| = (k_x d + k_z d)^{1/2}$. In the plot, $|kd| < 3$ is displayed. Red and blue bold lines on the bottom show typical $(k_x d, k_z d)$ at 2.00 GHz and 3.00 GHz, respectively. Labels DE, BV, and FV indicate corresponding SW modes of DE-SW, BV-SW, and FV-SW.

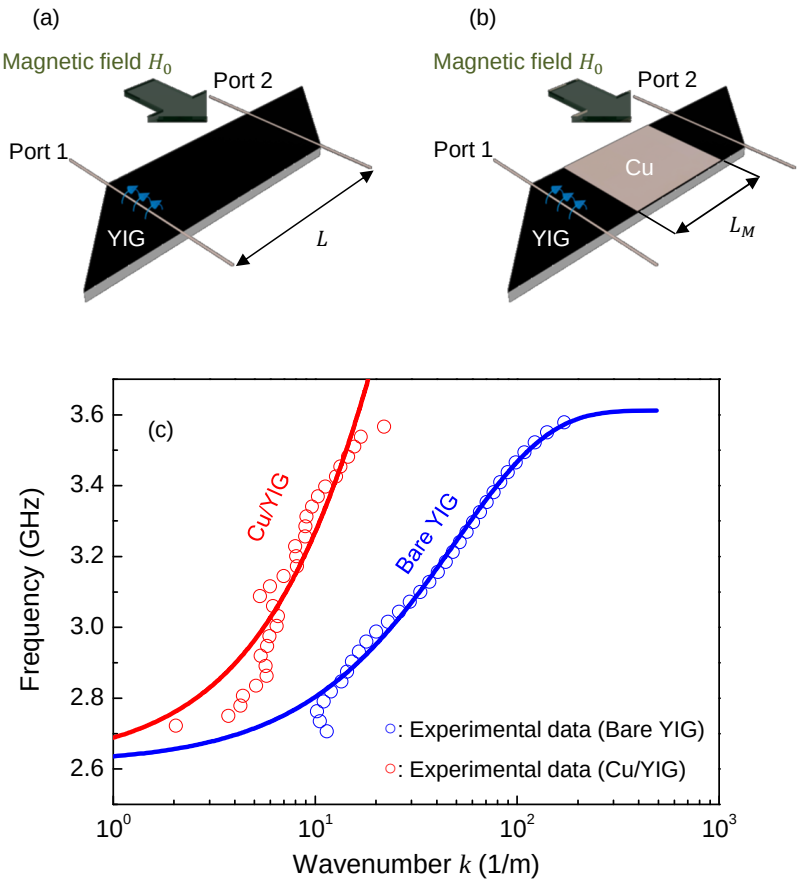

Figure 3.6 Schematics of experimental setups for (a) BS slab and (b) MS slab, and (c) dispersion curve of each waveguides transmitting DE-SWs. Red circles and blue circles represent dispersion curves of the MS slab and BS slab, respectively. Bold lines are the theoretical fit by using Eq.3.34 and Eq.3.29 for MS and BS slabs, respectively. In the experiment, $L = 10$ mm and $L_M = 6$ mm, and $H_0 = 400$ Oe. A 110 μm-thick YIG was used for all experiment.

with the interval of MSLs $L = 10$ mm. Magnetic field H_0 was applied in-plane so that DE-SWs propagated from the port 1 to port 2. The phase θ of transmited SW was evaluated by using the vector network analyzer (KEYSIGHT, 8753ES).

Since excited SWs were assumed to be a plan wave $\propto e^{i(\omega t - kx)}$, the resulting phase rotation at certain time t_0 with the wavenumber k can be derived as

$$\theta = -kL. \tag{3.35}$$

Therefore by measuring transmission phase θ, the wavenumber k can be estimated. In the actual experiment, measured data usually include following two errors.

- Extra phase shift due to MSL antennas.
- Uncertainty of 2π in the measured phase θ.

The first error can be easily compensated because the extra phase rotation was caused by the electromagnetic waves (EMWs) propagating along MSLs. A dispersion curve of EMWs is linear against frequency, therefore this phase rotation can be subtracted by the linear fitting of the phase rotation at the frequencies without SW propagation. After subtraction, the phase rotation θ due to SWs was extracted.

The second error was compensated by using the unwrapping technique. Since MSLs have wider excitation spectra including $k \sim 0$, the obtained phase rotation θ at the lowest frequency represents the contribution of SWs with very-low k region satisfying $|kL| < \pi$. When the phase shift $|kL|$ exceeded 2π with the increase of frequency, a value of θ was automatically wrapped within $-\pi \leq \theta \leq \pi$. This discontinuous point due to the wrapping was recovered by adding the corresponding phase shift 2π on the post-processing. By repeating this unwrapping procedure at each discontinuous point, a continuous dispersion curve from $k \sim 0$ was obtained. If coplanar waveguide or meander waveguide are used for the transducer, this technique is no longer valid because these antennas cannot excite very-low k region, yielding in the unknown 2π phase shifting. In such cases, a slope of $d\theta/d\omega$, namely the group delay (velocity), might give an information of k because the group delay (velocity) is uniquely specified for the certain k, thanks to the dispersion of SWs. Similar technique can be seen in several literatures.[87,88] In this study, conventional unwrapping technique provided good estimation of the dispersion curve.

The estimation of the dispersion curves in the MS slab required further tricks. Fig.3.6b is the schematic image of the setup. A 8 μm-thick copper layer was deposited on the YIG waveguide with a 60 nm-thick titanium buffer layer by using the magnetron sputtering. The Cu layer thickness was enough thicker than the skin depth so that the magnetic flux can not penetrate entire Cu thickness. Length of the deposition area was limited to $L_M = 6$ mm, to ensure the electric isolation of two MSLs. The single crystalline YIG layer was grown directly on the GGG substrate, thus insertion of the conductive layer impossible on this side. In this situation, the measured θ is expressed as

$$\theta = 2\theta_{\mathrm{BS}} + \theta_{\mathrm{MS}} = -2k_{\mathrm{BS}}\frac{L - L_M}{2} - k_{\mathrm{MS}}L_M, \tag{3.36}$$

where k_{BS} is the wavenumber of the BS slab, and k_{MS} is that of the MS slab. To separate these contributions, a curve of k_{BS} obtained from the setup shown in Fig.3.6a was referred. YIG waveguides were cut from the same wafer to assure the film quality between two measurements. The evaluated results based on Eq.3.35 and Eq.3.36 are shown in Fig.3.6c. The experimental results and theoretical curves exhibited reasonable agreement. In the experimental result of MS slab (Cu/YIG), a notable fluctuation on the data point was observed probably because the wavenumber was evaluated by the model of Eq.3.36, in which the contribution of the reflection at the interfaces of the BS slab and the MS slab was ignored. However, the dispersion curves of the BS slab and MS slab are

obviously different, and the experimental results are enough to evidence the calculations of this section.

3.2 Artificial Magnetic Lattice

3.2.1 Introduction

Propagation of waves, including SWs, can be controlled by periodically modulated structures. The most recognized example may be a wave function of an electron. The energy of a free electron at certain wavenumber k shows quadratic dispersion curve. And the dispersion curve forms a band gap at $k = \pi/a$, when the electron is exposed by the periodic potential V with periodicity a. Since electrons are the representative energy carrier in materials, such band structures determine various physical properties, e.g. conductivity, mobility, spin polarization, reflection or transmission of light, etc.[89–91] Band structure is also important to characterize a propagation of other waves, e.g. photon, phonon, plasmon, and also in magnon.[92–95]

Band engineering of optical waves has been widely investigated in past centuries, namely photonic crystals (PhCs). Confinement of optical waves have been attracted interests of researchers since E. Yablonovitch and coworker proposed a full-bandgap formation in the 3-D PhCs.[96,97] Researches in NTT Basic Research Laboratory recently demonstrated a large optical delay over 1 ns in 2-D PhCs.[98] These so called slow light is expected to take an important role in the optical computing. Simple 1-D periodic structure is also known as Bragg mirrors. This type of PhCs shows a strong wavelength selectivity on reflectivity. This benefits to minimize an error of operating wavelengths, e.g. a distributed feedback (DFB) laser can provide a stable wavelength for the optical communication.[99] Such flow controls of optical waves are one of the important applications of PhCs. On the other hand, the interaction of optical waves with magnetic materials is known as magneto-optic (MO) effect. A Faraday effect, which was discovered by M. Faraday in 1845, is one of the well-known phenomena, in which a magnetic material rotates optical polarization. Even though MO effects are observed in conventional magnetic materials, those effects can be enhanced by controlling optical flow with PhCs. This idea was introduced by M. Inoue and coworkers, and the proposed structure is called magneto photonic crystals (MPCs).[100,101] MPCs provided an option to control optical waves by magnetic field.[102–104] Such scheme of the combination of artificial periodic structure and magnetic interaction have been studied also in other fields, e.g. magnetoplasmonic crystals.[105,106] Hereby these schemes are called artificial magnetic lattices (AMLs).

Magnonic crystal (MCs) are the magnonic counterpart of AMLs, in which a periodically modulated waveguide exhibits a potential to control the flow of SWs. Studies on so called magnetic waves in periodically modulated media, becoming the origin of MCs, were first reported in 1970's. In 1975, C. Elachi carried out the theoretical investigation on magnetic waves in periodically modulated media.[107] In 1976, C. Sykes *et al.* reported the experimental observation of DE-SWs in corrugated YIG slabs.[108] In 1978, J. Owens

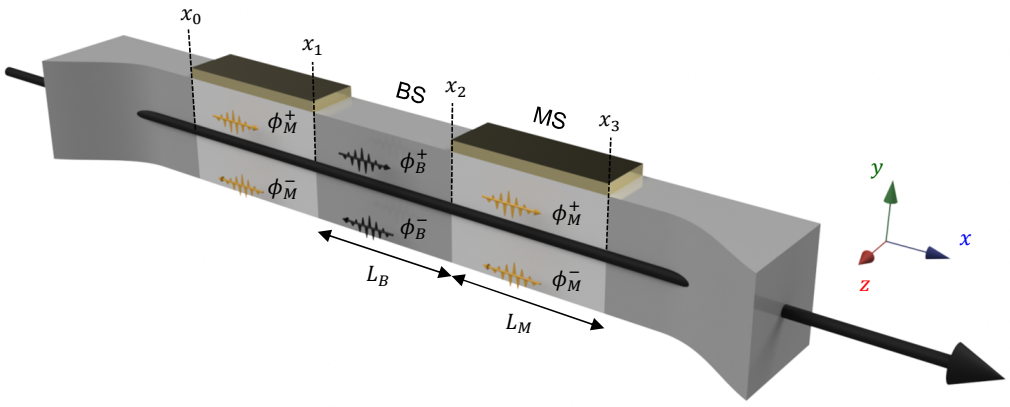

Figure 3.7 Model of 1D periodic structure in x-axis. Dark gray area denotes BS slab, and light gray area denotes MS slab.

et al. reported that in metallic gratings.[109] At the same time, Japanese researchers strongly contributed in this field. Two years before the theoretical work by C. Elachi,[107] dispersion analysis of periodically magnetized YIG rod was reported by M. Tsutsumi and Y. Yuki.[110] According to their argument, this is one of the origins of MCs. Following to this report, behavior of SWs in periodically modulated YIG films with various situations were extensively investigated in Japan.[111–115] Thanks to the development of microfabrication technique, there has been a rebirth of magnetic periodic structures around the year 2000, together with the new scientific term. MCs have been intensively investigated including ferromagnetic metal system in the past decade.[88,95,116–119] Dispersion curves of SWs relying various physical parameters, therefore there are several ways to form MCs. Apart from corrugation or metallic stripes reported in the past,[120,121] shape magnetic anisotropy,[122] Oersted field,[123] and even laser heating[124] can form MCs. Such capabilities have attracted the attention of scientists. In this work, MCs are included in a class of AML, and differences of design from other AMLs, e.g. MPCs, are discussed. In the latter half of this chapter, MCs composed of metallic stripes with inclusion of a defect layer are specially investigated, since metallic stripes have an advantage of easy fabrication.

3.2.2 Transfer Matrix Approach

In the past study, the transfer matrix approach has been used to analyze wave propagation in AMLs.[100,125] Comparing to the other techniques, e.g. plane wave method,[126] this technique benefits to calculate wave dynamics within a structure with finite periodicity. Accordingly, the transfer matrix approach was employed to design AMLs composed of the realistic number of periodic structure. In this part, the essence of transfer matrix approach is explained.

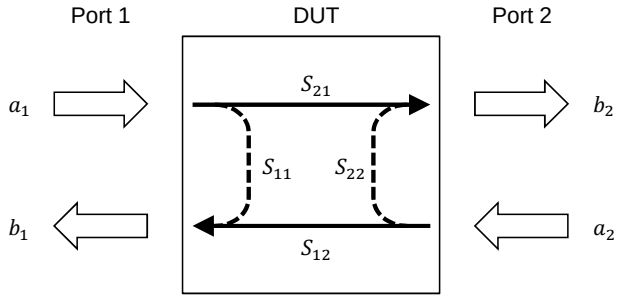

Figure 3.8 Schematization of the relation between input and output waves to the device under test (DUT). Waves a_i denote input to the DUT, and b_i denote output from the DUT. Flow of S_{ij} represents corresponding S-parameters.

In the AML, a propagation of scalar potential $\Phi_X(\boldsymbol{r})$ is considered. Since the entire waveguide is composed of the periodic cascading of BS slabs (B) and MS slabs (M), the subscript of the scalar potential become $X \in (B, M)$. At the interface of the BS slab and MS slab, certain amount of energy is backscattered due to the mismatch of the wavenumber of slabs. The model for the analysis is shown in Fig.3.7. The scalar potential $\Phi_X(\boldsymbol{r})$ can be represented by the linear sum of forward and backward wave.

$$\Phi_X(x) = \phi_X^+ e^{-ik_X^+ x} + \phi_X^- e^{-ik_X^- x} = \begin{pmatrix} \Phi_X^+(x) \\ \Phi_X^-(x) \end{pmatrix}, \tag{3.37}$$

where ϕ_X^+ (ϕ_X^-) denotes the amplitude of forward (backward) wave, and k_X^+ (k_X^-) denotes the wavenumber of forward (backward) wave, respectively. SW propagates in the x direction, and the information of thickness direction (y-axis) is included in the $k_X^{\pm}$, therefore the model can be handled as a 1-D system. In this case, $\boldsymbol{r} = x$ is enough. A propagation of SWs from x_1 to x_3 can be described as follows.

1. Φ_M is reflected at x_1. Some Φ_M enters to the BS slab and becomes Φ_B.
2. Φ_B propagates in the BS slab from x_1 to x_2.
3. Φ_B is reflected at x_2. Some Φ_B enters to the MS slab and becomes Φ_M.
4. Φ_M propagates in the MS slab from x_2 to x_3.

These procedure are repeated N times during SW propagation within the waveguide with the periodic number N. This behavior can be easily expressed by using T-parameters, which is commonly used to analyze electronic circuits. A schematic drawing of the signal

flow in a single device under test (DUT) is shown in Fig.3.8. For this signal flow, T-parameter was defined as follows.

$$\begin{pmatrix} a_1 \\ b_1 \end{pmatrix} = \begin{bmatrix} T_{11} & T_{12} \\ T_{21} & T_{22} \end{bmatrix} \begin{pmatrix} b_2 \\ a_2 \end{pmatrix}. \tag{3.38}$$

Since directions of the signal flow of vector $(a_1, b_1)^T$ is consistent with $(b_2, a_2)^T$, the resulting vector on the left hand side of Eq.3.38 can be multiplied to the another T matrix. Therefore by using T matrices describing the propagation of $\Phi_X(x)$ at each point, the wave propagation in the entire structure can be expressed.

$$\Phi_M(x_1) = \left[\bar{T}_{\mathrm{BM}}\bar{T}_{\mathrm{B}}\bar{T}_{\mathrm{MB}}\bar{T}_{\mathrm{M}}\right]\Phi_M(x_3) = \bar{T}_{\mathrm{uni}}\Phi_M(x_3), \tag{3.39}$$

where $\bar{T}_{\mathrm{XY}}$ denotes interface scattering from the X side to Y side, and $\bar{T}_{\mathrm{X}}$ denotes wave propagation in the structure X. The total product of T matrices in the blanket corresponds to the transmission matrix $\bar{T}_{\mathrm{uni}}$ of the unit cell composed of a single cascade of the BS slab and MS slab. It should be noted that direction of multiplication is inverted to the direction of the signal flow, because of the definition in Eq.3.38.

SW scattering at the interface was considered by the boundary conditions similar to that used in the analysis of dispersion of slabs (§3.1). Since interfaces appears on the x-axis, following boundary conditions are given.

1. Continuity of scalar potentials at the interface x_n.
2. Continuity of the normal component of magnetic fluxes b_x at the interface x_n.

The magentic flux can be obtained by $b_x = (-\bar{\mu}_G\boldsymbol{\nabla}\Phi_X(x)) \cdot \hat{x}$. Thus these boundary conditions yielded following simultaneous equations.

$$\phi_X^+ e^{-ik_X^+ x_n} + \phi_X^- e^{-ik_X^- x_n} = \phi_Y^+ e^{-ik_Y^+ x_n} + \phi_Y^- e^{-ik_Y^- x_n}, \tag{3.40}$$

$$\mu_{11}^X \left(k_X^+\phi_X^+ e^{-ik_X^+ x_n} + k_X^-\phi_X^- e^{-ik_X^- x_n}\right) = \mu_{11}^Y \left(k_Y^+\phi_Y^+ e^{-ik_Y^+ x_n} + k_Y^-\phi_Y^- e^{-ik_Y^- x_n}\right), \tag{3.41}$$

where μ_{11}^X (μ_{11}^Y) is the component of permeability tensor of the structure X (Y), as given by Eq.3.6. Solving Eq.3.40 and Eq.3.41 for the scalar potential $\phi_Y(x)$, the transmission

matrix $\bar{T}_{\mathrm{XY}}$ is obtained.

$$\bar{T}_{\mathrm{XY}} = \begin{bmatrix} \dfrac{\mu_{11}^X k_X^+ - \mu_{11}^Y k_Y^-}{\mu_{11}^Y \left(k_Y^+ - k_Y^-\right)} & \dfrac{\mu_{11}^X k_X^- - \mu_{11}^Y k_Y^-}{\mu_{11}^Y \left(k_Y^+ - k_Y^-\right)} \\ \dfrac{\mu_{11}^X k_X^+ - \mu_{11}^Y k_Y^+}{\mu_{11}^Y \left(k_Y^- - k_Y^+\right)} & \dfrac{\mu_{11}^X k_X^- - \mu_{11}^Y k_Y^+}{\mu_{11}^Y \left(k_Y^- - k_Y^+\right)} \end{bmatrix}. \tag{3.42}$$

When the waveguide is composed of MS slabs and BS slabs, $\mu_{11}^X = \mu_{11}^Y$ is valid because the surface metalization does not change the permeability. In this case, $\bar{T}_{\mathrm{XY}}$ can be simplified as

$$\bar{T}_{\mathrm{XY}} = \begin{bmatrix} \dfrac{k_X^+ - k_Y^-}{k_Y^+ - k_Y^-} & \dfrac{k_X^- - k_Y^-}{k_Y^+ - k_Y^-} \\ \dfrac{k_X^+ - k_Y^+}{k_Y^- - k_Y^+} & \dfrac{k_X^- - k_Y^+}{k_Y^- - k_Y^+} \end{bmatrix}. \tag{3.43}$$

Propagation of the SW just causes the rotation of phase on forward and backward waves, therefore the transmission matrix $\bar{T}_{\mathrm{X}}$ can be written as

$$\bar{T}_{\mathrm{X}} = \begin{bmatrix} e^{ik_X^+ L_X} & 0 \\ 0 & e^{ik_X^- L_X} \end{bmatrix}, \tag{3.44}$$

where L_X is the length of the structure X. From Eq.3.43 and Eq.3.44, the transmission matrix of unit cell $\bar{T}_{\mathrm{uni}}$ is obtained. In addition, the wavelengths $k_B^{\pm}$ and $k_M^{\pm}$ have been already solved in Eq.3.29 and Eq.3.34, respectively. The entire transmission property $\bar{T}_0$ with the perioic number N is then obtained as

$$\bar{T}_0 = \bar{T}_{\mathrm{uni}} \bar{T}_{\mathrm{uni}} \bar{T}_{\mathrm{uni}} ... = \bar{T}_{\mathrm{uni}}^N. \tag{3.45}$$

In usual radio frequency circuit analysis, S-parameter is preferably used instead of T-parameters. Therefore it is convenient to transform Eq.3.45 into S-parameter format. By using the same circuit shown in Fig.3.8, S-parameters were defined as

$$\begin{pmatrix} b_1 \\ b_2 \end{pmatrix} = \begin{bmatrix} S_{11} & S_{12} \\ S_{21} & S_{22} \end{bmatrix} \begin{pmatrix} a_1 \\ a_2 \end{pmatrix}. \tag{3.46}$$

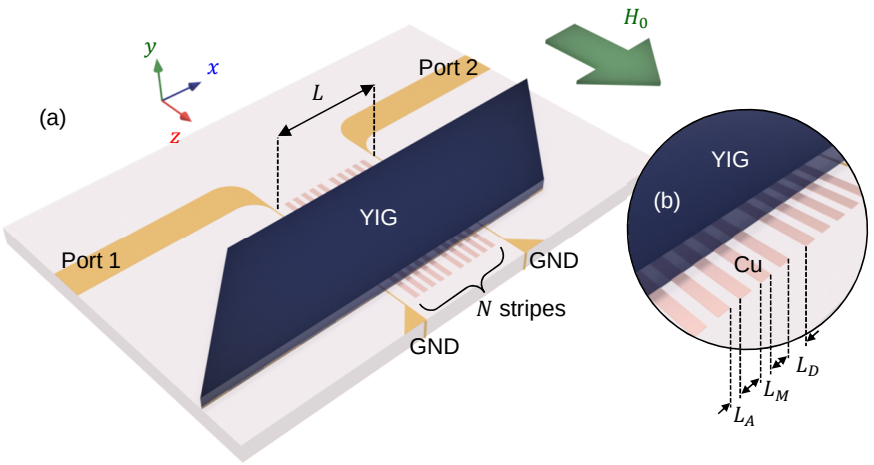

Figure 3.9 Schematization of the magnonic microcavity. (a) entire view and (b) enlarged view of metalization. YIG is placed on the SW transducer with 2 ports. Between port 1 and port 2, Cu stripes are sandwiched. A gap of Cu stripes is L_A, width of Cu stripe is L_M, and the gap of a defect layer is L_D which is introduced at the center of stripes.

Comparing Eq.3.46 to Eq.3.38, S-parameter can be derived by T-parameter with the mathematical calculation.[127]

$$\begin{bmatrix} S_{11} & S_{12} \\ S_{21} & S_{22} \end{bmatrix} = \begin{bmatrix} T_{21}/T_{11} & (T_{11}T_{22} - T_{12}T_{21})/T_{11} \\ 1/T_{11} & -T_{12}/T_{11} \end{bmatrix}. \tag{3.47}$$

Hereby a transmission spectra denotes S_{21} in logarithmic scale.

$$S_{21} = -20 \log_{10} T_{11}. \tag{3.48}$$

3.2.3 Magnonic Microcavity

In MPCs, a Faraday effect is enhanced at a transparent magnetic layer which is sandwiched by Bragg mirrors. The thickness of the magnetic layer is usually designed to localize optical waves at this position. MPCs can be regarded as a kind of Fabri-Perot resonator, and the localization can enhance the interaction with the host matrix. In the

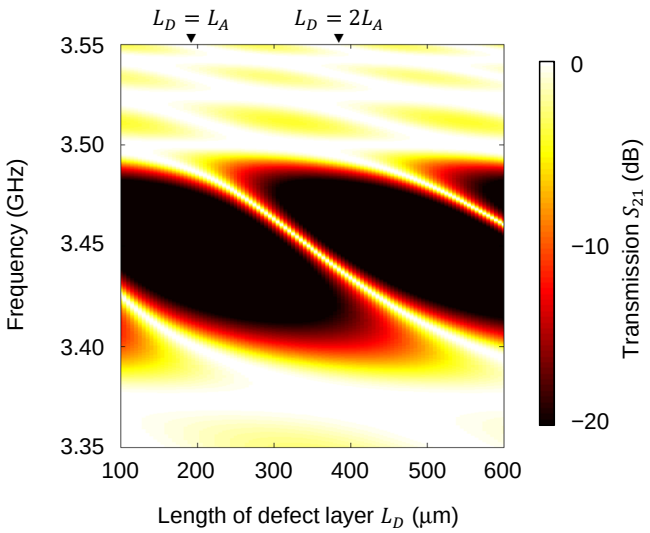

Figure 3.10 Transmission property dependence of the defect layer gap L_D. Color represents intensity of transmission.

case of SWs, such the wave localization is also expected to appear in the microcavity composed of surface metalization. Such trapped wave exhibits unique physical properties, e.g. slow wave, increase of energy density and accompanying nonlinear effect, existence of an extended transmission mode within the stop band, and so on. These properties may provide an another option to control a SW flow.

Hereby microcavities for SWs is called *magnonic microcavity*. A schematic drawing of a magnonic microcavity used in the experiment is shown in Fig.3.9a. Cu stripes were directly formed on the dielectric substrate, and the 90 μm-thick YIG waveguide was placed by flip-chip. The both ends of waveguide were cut with the cutting angle of 45° to suppress SW reflection. A bias magnetic field H_0 was applied to z-axis so that DE-SWs propagated. As discussed in §3.1, DE-SWs were expected to show a significant change on its wavelength beneath Cu stripes. From Eq.3.31, an extra dielectric gap between the Cu stripes and the YIG surface attenuate the modulation effect. Therefore YIG substrate was tightly fixed on the dielectric substrate, to obtain a good contact to the surface of Cu stripes. Fortunately, the wavelengths of DE-SWs were several hundred micrometers under this setup, the resulting gap hight might be ignorable. This flip-chip mounting is convenient to compare the transmission properties of several microcavities with the consistent YIG waveguide.

Parameters to build the magnonic microcavity are listed in Table3.1. The parameter of interest was L_D, which was the gap width of the defect layer (see Fig.3.9b). The defect layer was composed of a gap layer rather than the Cu stripe, because of avoiding the eddy current loss due to the localization. This gives periodic number N in an even number. Parameters of L_A and L_M were determined to realize the Bragg frequency at

higher frequency within the transmission band, in which the excitation efficiency of the MSL antenna was almost maximized. Transmission properties of the waveguide were calculated by transfer matrix approach, with various L_D values. The result is shown in Fig.3.10. Horizontal positions of $L_D = L_A$ and $2L_A$ are indicated by triangles. A notable stop band was formed at frequencies from 3.4 GHz to 3.5 GHz, and oblique lines (extended modes) can be seen within the stop band. When $L_D = L_A$, no extended mode exists. It should be noted that the condition of $L_D = L_A$ no longer forms a defect layer, in which the Cu stripes aligned with an uniform periodicity. This situation yields of the stop band in the k_x direction. On the other hand, $L_D = 2L_A$ exhibited the extended mode at almost the center of the stop band. The position of the extended mode was strongly depended on the L_D, and wider L_D down-shifted the frequency of the extended mode. This pattern showed a periodicity on L_D because of the periodicity of the phase.

SW propagation within the waveguide was further investigated for the structures with $L_D = 2L_A$ and $L_D = L_A$. Since the scalar potential $\Phi(x)$ was defined in Eq.3.37, the profile of $\Phi(x)$ at arbitrary position x_0 can be calculated by using matrix approach method as shown in Fig.3.11. SWs were injected from the left side. A value of $\Phi(x)$ was usually given as a complex number, thus only a real part was displayed. When $L_A = L_D$, $\Phi(x)$ was immediately attenuated. On the other hand, $\Phi(x)$ was enhanced in the vicinity of the defect layer when $L_A = 2L_D$. Therefore the SW was localized in the defect layer, hereby such extended mode is called localized mode. Finite oscillation was still observable at the waveguide end. In former case, the waveguide becomes a Bragg mirror, and there is no doubt the SW cannot enter to the structure. The later case is a magnonic microcavity, in which the SW was trapped at the defect layer as expected. The accompanying magnetic field can be calculated by $h_x = -\nabla_x \Phi(x)$. It is clearly seen that the slope of $\Phi(x)$ was remarkably enhanced at the defect layer. Hence one of the key features of microcavity was confirmed. At the defect layer, a physical phenomena accompanied by h_x would be enhanced.

Transmission spectra were also investigated in the experiment. The result for $L_D = L_A$ (Bragg mirror) is shown in Fig.3.12a and b, and for $L_D = 2L_A$ (magnonic microcavity) is shown in Fig.3.12 c and d. Since SWs were sensitive to H_0, all measurements and calculations were done for various H_0 values. In both results, experimentally obtained spectra showed weaker transmission intensity by a factor of ~ 10 dB due to the

Table 3.1 Parameters used in the experiment and calculation

Parameter	Value	Description
L_A	213 μm	Gap width between Cu stripes
L_M	193 μm	Width of Cu stripe
L_D	—	Gap width of the defect layer
L	5 mm	Propagation distance
N	10	Number of Cu stripes
d	90 μm	YIG thickness
H_0	400 Oe	Bias magnetic field

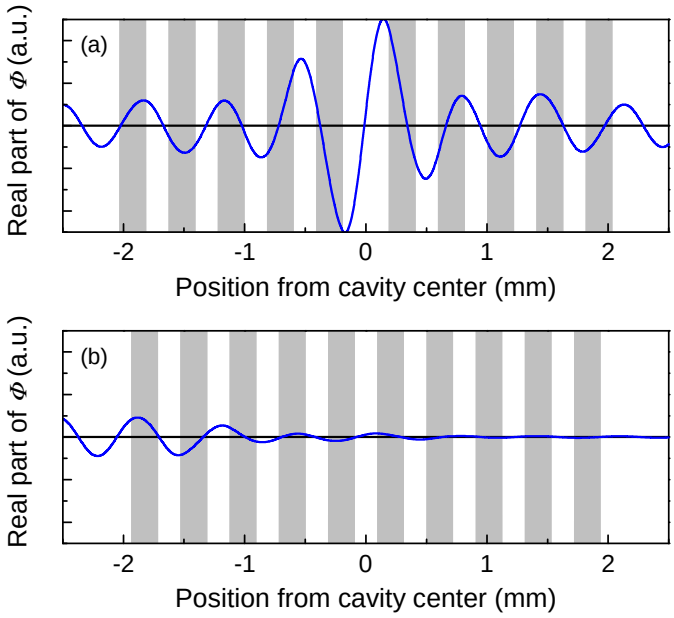

Figure 3.11 Distribution of the scalar potential $\Phi(x)$ in the waveguides with (a) $L_D = 2L_A$ and (b) $L_D = L_A$. Shaded area represents MS slab. Excitation frequency is assumed to 3.4379 GHz.

insertion loss of transducers. However, observed H_0 dependence of DE-SWs seemed to exhibit reasonable agreement with the calculations.

In Fig.3.12a, a stop band appeared in the up-side of the propagation band. This can be seen as a darker line in the graph (noted by a green arrow). Position of the stop band is also H_0 dependent, and appeared in the entire H_0 range. This was also confirmed by the experiment. In Fig.3.12c, localized mode appeared instead of stop bands. This can be seen as a narrow bright track inside the stop band. Similar localized mode was also confirmed in the experiment. From these experiments, AMLs composed of metallic stripes can form Bragg mirrors and microcavities as well, and demonstrated spectra depended on the H_0 values.

To investigate the detail, transmission spectra in the vicinity of the Bragg frequency at $H_0 = 400$ Oe were extracted from Fig.3.12. This is graphed in Fig.3.13. In this view, experimental results showed obvious discrepancies on the peak position and frequency linewidth. For example, Q-factors, which was defined as a ratio of the peak frequency and frequency linewidth of the primary peaks, were calculated to compare the result of transfer matrix approach Q_{calc} and that of experiment Q_{exp}. Peak frequencies are pointed by triangles in Fig.3.13. When $L_D = L_A$, $Q_{\mathrm{calc}} = 107$ and $Q_{\mathrm{exp}} = 162$ were obtained. When $L_D = 2L_A$, $Q_{\mathrm{calc}} = 1298$ and $Q_{\mathrm{exp}} = 89$ were obtained. In the case of $L_D = L_A$, Q-factors showed relatively good accordance, but the depth of the stop band was completely different. Q-factors exhibited non-negligible mismatch in the case

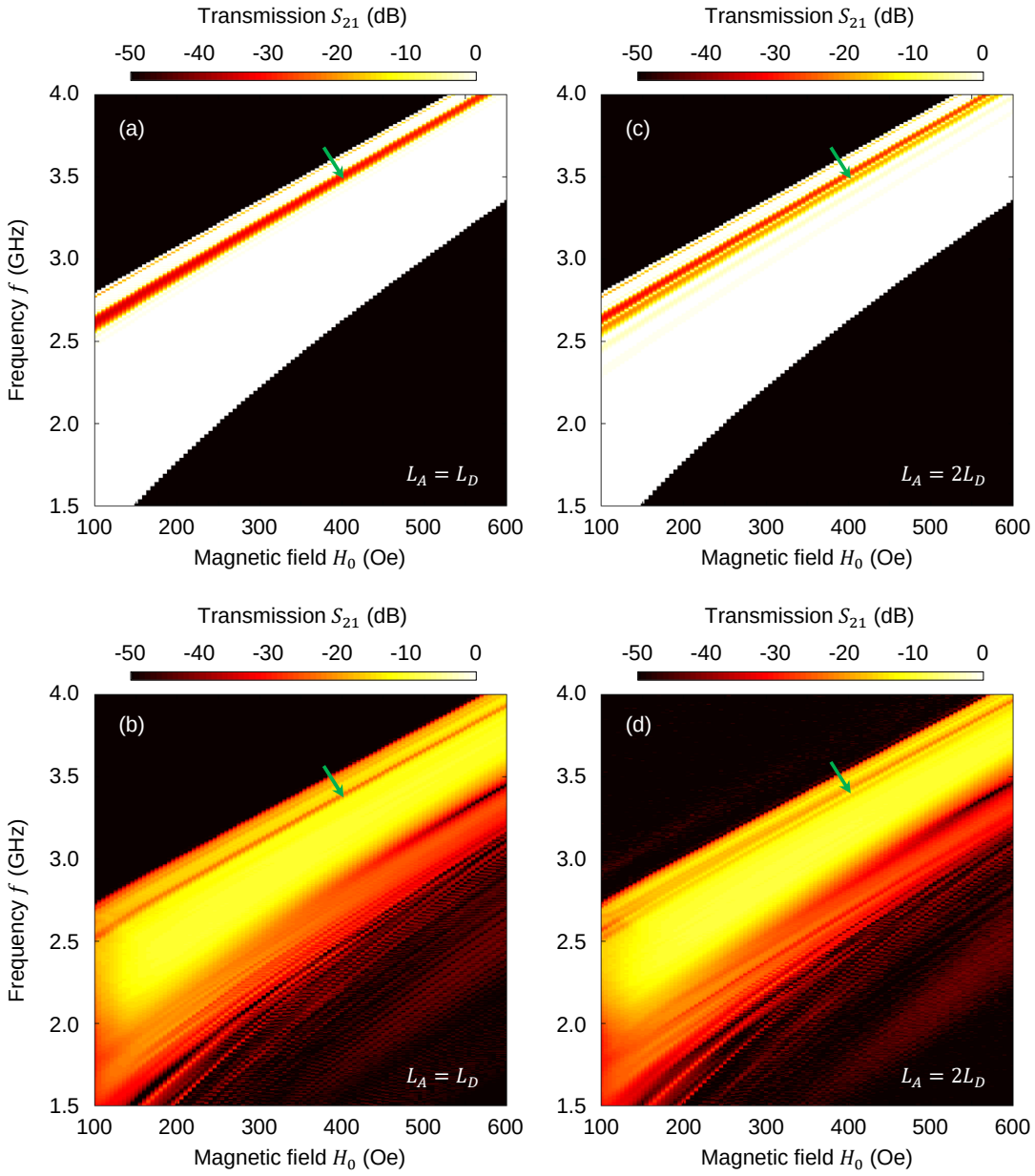

Figure 3.12 Transmission spectra of magnonic microcavities. Transmission spectra with $L_A = L_D$ obtained by (a) transfer matrix approach and (b) experiment. Transmission spectra with $L_A = 2L_D$ obtained by (c) transfer matrix approach and (d) experiment. Color represents transmission intensity. Bright area indicates strong SW propagation. Bragg frequencies at $H_0 = 400$ Oe are pointed by green arrows.

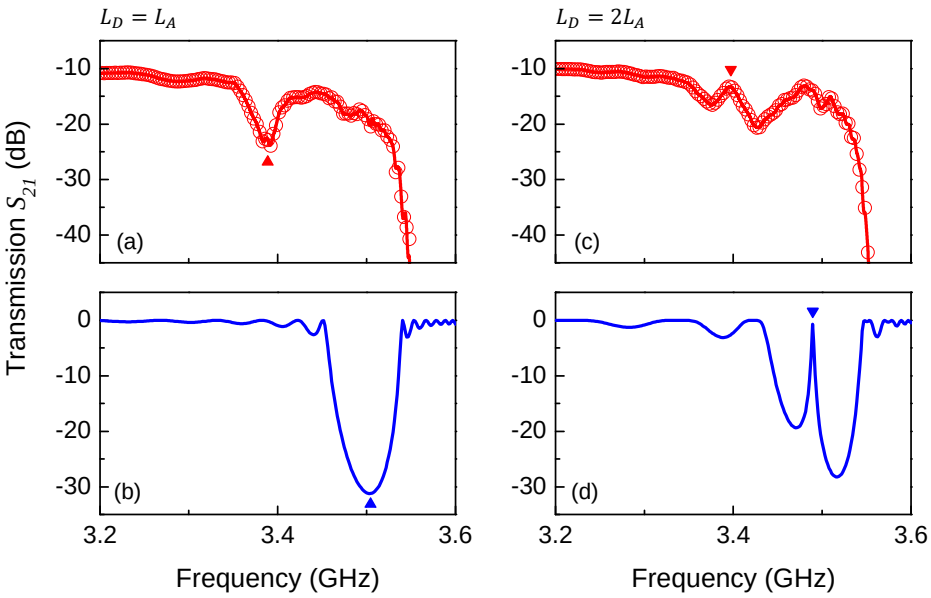

Figure 3.13 Transmission spectra at $H_0 = 400$ Oe. Transmission spectra in the vicinity of the Bragg frequency are displayed. (a) Experimental result and (b) calculated result for $L_D = L_A$. (c) Experimental result and (d) calculated result for $L_D = 2L_A$. Triangles point positions of the primary peaks.

of $L_D = 2L_A$. In both experimental result, quality of fabricated AMLs were remarkably degraded, and the provided model in the previous part was not sufficient. Nevertheless, in the optical counterpart, transmission spectra obtained by the transfer matrix approach usually show good accordance with experimental results.[101] And the model used in the calculation was based on the optical counterpart. Thus there would be different matter in magnonic counterpart. To design AMLs correctly, such factor should be specified, and considered in the calculation.

3.2.4 Consideration of the Demagnetizing Field

As shown in Fig.3.12, the localization by AMLs exhibited strong dependence on H_0. This was an unique property of SWs, thus the further investigation of magnetic field distribution was expected to give a hint for preventing the degradation of property. Since the shape of YIG waveguide was too complicated to calculate the demagnetization coefficient analytically, the H_0 distribution inside the waveguide was simulated by the magnetostatic analysis in finite element method (COMSOL Multiphysics). In the magnetostatic problems where no electric current s are present, the scalar potential V_m can be defined, and the system solves problem of $\boldsymbol{\nabla} \cdot B = 0$. The magnetic flux $\boldsymbol{B} = (B_x, B_y, B_z)^T$ inside the

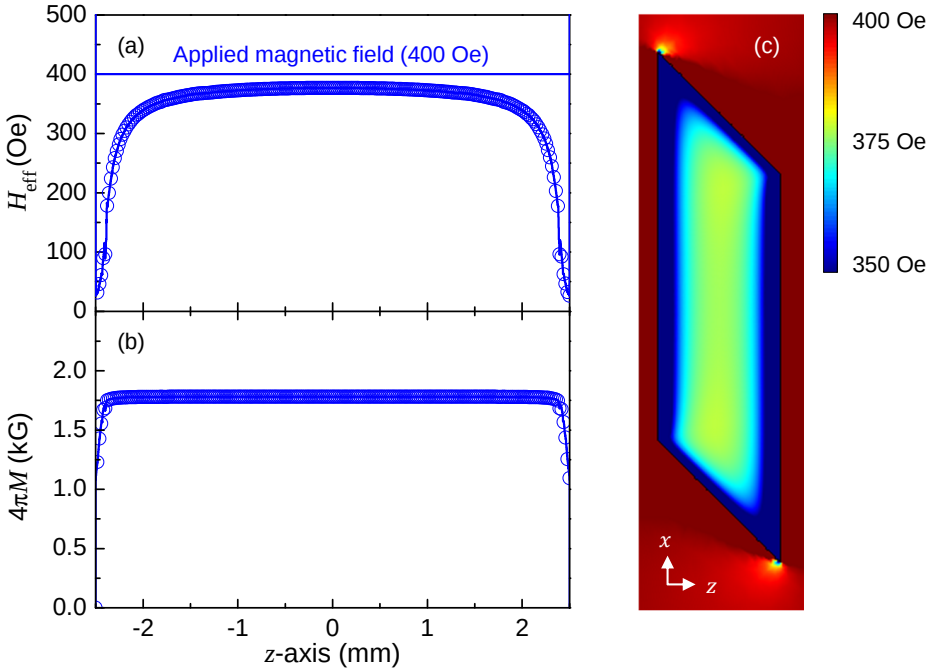

Figure 3.14 Simulated H_0 distribution inside the YIG waveguide. (a) H_0 distribution and (b) $4\pi M$ distribution along the cross section. (c) In-plane H_0 distribution. Color represents intensity of H_0. Blue colored region is strongly attenuated.

YIG was described by

$$\begin{pmatrix} B_x \\ B_y \\ B_z \end{pmatrix} = - \begin{bmatrix} \mu_{xx} & 0 & 0 \\ 0 & \mu_{yy} & 0 \\ 0 & 0 & \mu_{zz} \end{bmatrix} \nabla V_m, \tag{3.49}$$

where μ_{xx}, μ_{yy} and μ_{zz} are diagonal permeabilities. If the crystallographic anisotropy can be ignored, this is given by $\mu_{xx} = \mu_{yy} = \mu_{zz} = \mu_{\text{int}}$. The value of μ_{int} represent the intrinsic permeability of YIG. To roughly estimate μ_{int}, the magnetic hysteresis curve of YIG specimen cut into 5 mm square was measured by using the vibrating sample magnetometer (Tamagawa, TM-VSM261483-HGC). To minimize the contribution of the shape magnetic anisotropy, in-plane hysteresis loop was measured.

Since the YIG waveguide was exposed by the strong H_0 to saturate magnetization, a value of μ_{int} was no longer constant to the magnetic field H. Therefore it was require to reflect the behavior of near saturation region of the magnetic hysteresis on $\mu_{\text{int}}(H)$. However, the formalism of the magnetic hysteresis property was not easy. I focused on the functions, which can express saturation behaviors, and figured out the sigmoid

function can trace the magnetic hysteresis in the most of cases. The sigmoid function was optimized to reflect the magnetic hysteresis, and the modulated function was named as *sigmoid-hysteresis* (SH) function. According to the function, a value of $4\pi M$ at specific H can be derived by

$$\mathrm{SH}(H) = 2M_S \left\{ 1 - \exp\left(- \left(\frac{H}{H_{cj}} + 1 \right) \ln \frac{1+\mathrm{SR}}{1-\mathrm{SR}} \right) \right\}^{-1}, \tag{3.50}$$

where $4\pi M_S$ is the saturation magnetization, H_{cj} is the coercivity, and SR is the squareness ratio. All parameters can be obtained by a single magnetic hysteresis measurement. It is noteworthy that Eq.3.50 is capable of fitting the demagnetizing curve. By using SH function, $\mu_{\mathrm{int}}(H)$ was given by

$$\mu_{\mathrm{int}}(H) = \frac{H + \mathrm{SH}(H)}{H}. \tag{3.51}$$

Eq.3.51 was substituted to Eq.3.49, and H_0 distribution inside the waveguide was simulated. The result is shown in Fig.3.14. Not only H_0 distribution, but $4\pi M$ distribution was also given thanks to the SH function. Basic principle of magnetostatic analysis is $\boldsymbol{\nabla} \cdot \boldsymbol{B} = 0$, so that magnetic poles were formed at the waveguide fringe. Excited magnetic poles attenuated H_0 at the fringe, and $4\pi M$ transited to the unsaturated region of magnetic hysteresis. The demagnetized $4\pi M$ weakened magnetic poles again, and the exquisite balance of the magnetic dipole yielded the gradient H_0 distribution along the fringe of the waveguide. This inhomogeneity was not considered in the previous analysis. Here the strong dependence of SWs on H_0 is reminded, and the reason of discrepancy in Fig.3.13 is clearly given from this result.

To prove this idea, the wavelengths of propagating DE-SWs were calculated reflecting the H_0 distribution shown in Fig.3.14a. Wavelength was calculated for different frequencies at 2.5 GHz and 3.4 GHz. When homogeneous $H_0 = 400$ Oe was assumed as previous calculations, the wavelength exhibited no spatial distribution. In addition, the frequency at 2.5 GHz was out of the propagation band so that SW propagation was prohibited. However, as shown in Fig.3.15, when the effect of the demagnetizing field is considered, H_0 was attenuated in the fringe of the waveguide, and the waveguide fringe is capable of exciting finite wavenumber. This indicated SWs can propagate along the waveguide fringe at lower frequency, yielding in the propagation of edge mode. On the other hand, in the case of frequency at 3.4 GHz, SWs propagating in the vicinity of the waveguide center satisfied the Bragg condition. And these waves clearly showed the stop band or localized mode. Nevertheless, SWs propagating in the fringe cannot satisfy the Bragg condition. This yields of the spectral broadening of the peaks. Namely, this is the incoherence of SWs due to the demagnetizing field.

To feedback the behavior incoherent SWs on the transfer matrix approach, a simple method was introduced. Transmission property was calculated by using the conventional transfer matrix approach for the each track $z = z_0$ of the waveguide. The internal field

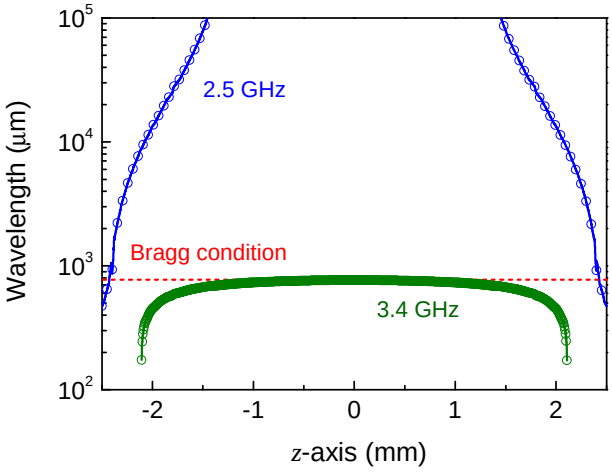

Figure 3.15 Wavelength distributions inside the waveguide with inhomogeneous H_0 distribution. Blue squares represent wavelengths at 2.5 GHz (edge mode), and green squares represent wavelengths at 3.4 GHz. Bragg condition is calculated for the structure with $L_A = 193$ μm and $L_M = 213$ μm.

$H_0(z)$ of each track was available in Fig.3.14a. Thus transmission spectra $S_{21}(z)$ was position dependent. Magnetic interactions between tracks were ignored for simplification. Calculated transmission spectra were averaged. Thus transmission spectra S_{21} was derived in the following manner:

$$S_{21} = \int_{-W/2}^{W/2} S_{21}(H_0(z))\ dz, \tag{3.52}$$

where $W = 5$ mm is the width of the waveguide. The resulting transmission spectrum reflects inhomogeneous distribution of H_0 along z-axis. The updated results are shown in Fig.3.16. By considering the demagnetization effect in YIG slab, calculated transmission spectra can represent well the experimental result.

Slight mismatch between the experiments and calculations were still remained in Fig.3.16, because of the rough estimation in Eq.3.52. As shown in Fig.3.14c, magnetic field inhomogeneity was appeared not only in z-axis, but also in x-axis. Non-negligible interaction among SWs propagating different z coordinate should be taken care, but the transfer matrix approach cannot be efficiently expanded in the 2-D plane. After all, the finite element method is rather favorable to realize perfect accordance with the experimental result. However, the magnetostaic-electromagnetic coupled analysis with sufficient meshing would require a large-scale computing. Such requirement is not efficient in the viewpoint of trend analysis. The provided method showed sufficient accuracy and easiness at the same time. Hence improved transfer matrix approach would be convenient to examine some preferable AML structures from hundreds of possibilities, e.g. as the preprocessing of the finite element method.

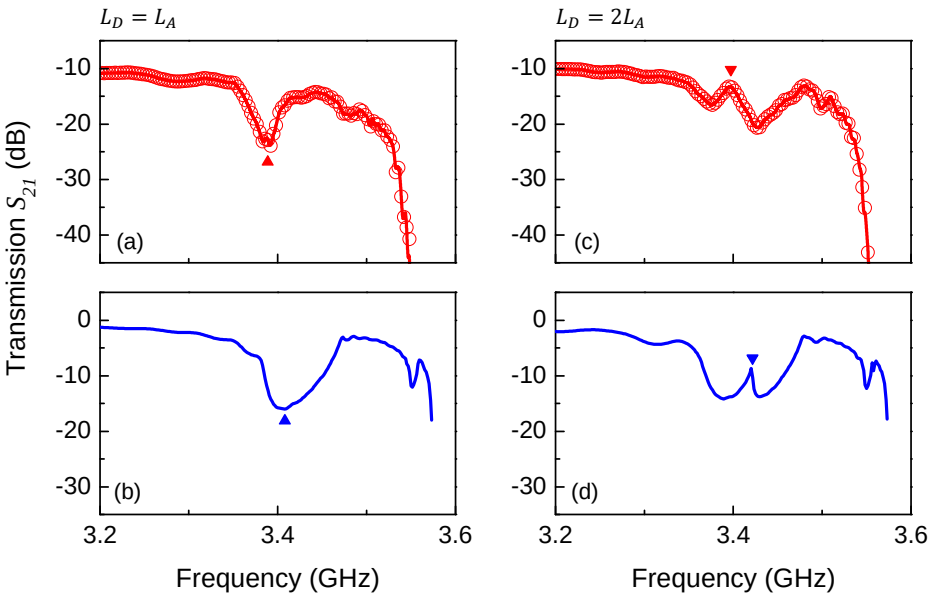

Figure 3.16 Transmission spectra at $H_0 = 400$ Oe with consideration of the demagnetization effect in YIG slab. Frequencies in the vicinity of the Bragg frequency are displayed. (a) Experimental result and (b) calculated result for $L_D = L_A$. (c) Experimental result and (d) calculated result for $L_D = 2L_A$.

AMLs for SWs require the design of demagnetizing field as well as the periodic structure. Homogeneous H_0 may be achieved by the optimization of the waveguide thickness. For example, when $W = 5$ mm, waveguide thickness of 10 μm is enough to reduce the contribution of demagnetizing field. Apart from this, J. Adam *et al.* used the YIG waveguide surrounded by polycrystalline dummy waveguides covered by aluminum.[128] In this structure, SWs were not excited in the dummy waveguides thanks to the skin effect of aluminum, while magnetic dipole of the waveguide fringe was canceled out by dummy waveguides. Such waveguide design could be effective to improve performance of AMLs. In contrast, F. Ciubotaru *et al.* rather positively used the demagnetizing field to form AMLs with edge grooved waveguides.[129] This would be another direction.

3.3 Summary

In this chapter, AMLs to control SW flow were intensively investigated. Surface metalization of the waveguide modulated the SW dispersion. Therefore periodic metalization was capable of realizing AMLs. The Bragg mirror and microcavity were demonstrated as magnonic AMLs, and the importance of the demagnetization effect on the design was discussed.

In §3.1, SW dispersion curve was solved for the arbitrary bias magnetic field config-

uration. Two types of ferromagnetic slab, namely BS slab and MS slab, were analyzed, and SW dispersion curves in the film plane were calculated for situations of in-plane and out of plane magnetization. Out of plane magnetization exhibited the isotropic dispersion curve regardless of metalization, i.e. SWs can propagate any direction. On the other hand, in-plane magnetization exhibited the splitting of dispersion branches, and some propagation directions were forbidden. Metalization gave a nonreciprocal effect on this configuration, i.e. forward propagation and backward propagation along certain symmetric axis can be isolated. In all cases, metalization modulated dispersion curves, and remarkable shift of dispersion curves was obtained in DE-SW configuration.

In §3.2, transmission spectra of AMLs composed of periodically connected BS and MS slabs in series were investigated. Transfer matrix approach was introduced to analyze periodic structures. When the defect layer was inserted at the center of the periodic structure, SWs were trapped and exhibited localization peak at the Bragg frequency. When this defect layer was removed, the structure behaved as a Bragg mirror. However, the transmission spectra obtained by the calculation and experiment showed remarkable frequency deviation and distortion of peak profiles. To explain the reason, demagnetizing field was considered in the calculation. Such demagnetizing field yielded of the inhomogeneity of effective magnetic field in the waveguide and resulted propagating wavelengths. Such incoherence resulted in the broadening of peaks, and this idea explained the experimental result well. In this section, new technique to calculate transmission spectra of AMLs were provided based on transfer matrix approach.

Chapter 4

Magnetic Field Sensors

In this chapter, the performances of SWs as magnetic field sensors are investigated. Since SWs are quite sensitive to a magnetic field, it is worth to evaluate the prospect as a magnetic field sensor. In §4.1, magnonic microcavities are used as magnetic field sensors, in which a steep slope of the localized peak is expected to give sensitive response to the magnetic field change. Homemade evaluation system is prepared and the threshold sensitivity is estimated. In addition, a fundamental drawback of temperature drift is also discussed. In §4.2, a differential circuit of SW is introduced to overcome the issue of temperature drift. In this circuit, each waveguide is oppositely magnetized so that magnetic field dependence is given as a normal mode signal, thus temperature drift of the signal can be canceled. This concept is also tested in the experiment.

4.1 Magnonic Microcavity for Sensors

4.1.1 Motivation

Magnetic field sensors have been widely used in industries, and there are a variety of sensors for each magnetic field range as shown in Fig.4.1. Magnetic field measurement is contactless and noninvasive investigation, meaning the measurement can be done without destroying a target. Such advantage makes the magnetic field measurement a suitable techniques for observation of biomedical signals. Compared to the measurement of bioelectric potentials, biomagnetic fields exhibit minor artifacts because most of biotissues are made of nonmagnetic material. However, biomagnetic fields are generally tiny amount, and a high resolution magnetic field sensors are required to measure biological activities. Such tiny magnetic field can be measured using superconducting quantum interference device (SQUID), and the outstanding resolution of SQUID sensors can cover the investigation of magnetic fields produced by human brain activities.[131,132] Magnetic fields from a human heart are stronger than that of the human brain, and there are several options of magnetic field sensors in this range. Recently, optical pumping sensors demonstrated a capability of magnetocardiogram (sensing of a heartbeat).[133–135] However, the mainstream of this measurement is the electrocardiogram, because of the complication

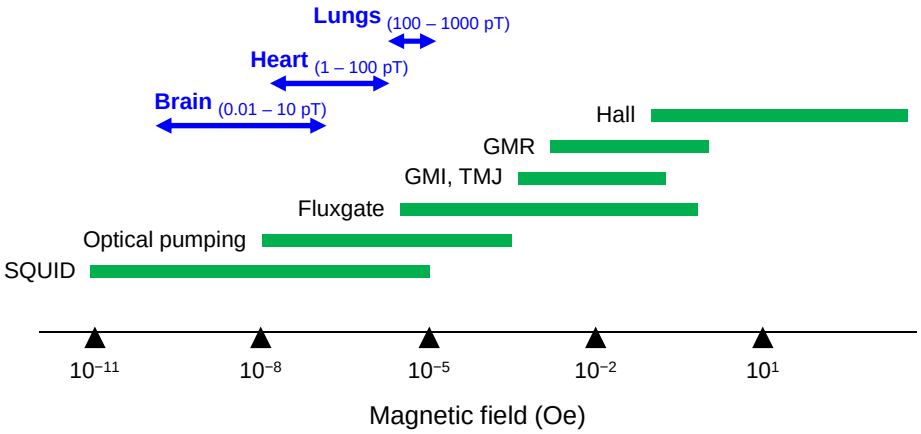

Figure 4.1 Range of application of magnetic field sensors. Original data is given by S. Tumanski (2011).[130]

of those magnetic field sensors. SQUID sensors require very low temperature for manifestation of superconductivity, and optical pumping sensors are composed of the laser setup. Even though portable sensors with capability of cardiograph are expected in the viewpoint of the prevention of heart disease.

Magnetic field dependence of SWs is expected to apply high sensitive magnetic sensors, and usage of shorter wavelength yields of miniaturization of SWDs at the same time. M. Inoue *et al.* showed the availability of AMLs as a magnetic field sensor.[28] In the vicinity of stop band, SWs drastically changes the transmission gain, and the Bragg frequency can be shifted several MHz by the testing magnetic field H_T of 1 Oe. Thus change of H_T is appeared in the transmission gain of SWs. Reported sensitivity of AML-based sensor outperformed that of GMI sensors. Furthermore, conceivable advantages of SWs are listed as follows.

- Wide dynamic range
- Flat waveguide structure
- Small power consumption

Wide dynamic range is fundamental property of SWs. For example, flux gate sensors reflect a change of permeability due to H_T, therefore the installed magnetic material should stay in the unsaturated region of magnetic hysteresis curve. Feedback coils are usually installed in such sensors to prevent magnetic saturation.[136] In contrast, SWs propagate in the saturated region, thus AML-based sensors would be functional in wider range of H_T. AMLs are usually planar structure, and proximity contact to the source object is possible. This is a good point because a magnetic field is monotonically decreased with respect to the distance. Potential of small power consumption is preferable for portability. Nevertheless, the minimum resolution of AML-based sensor was not reported, thus

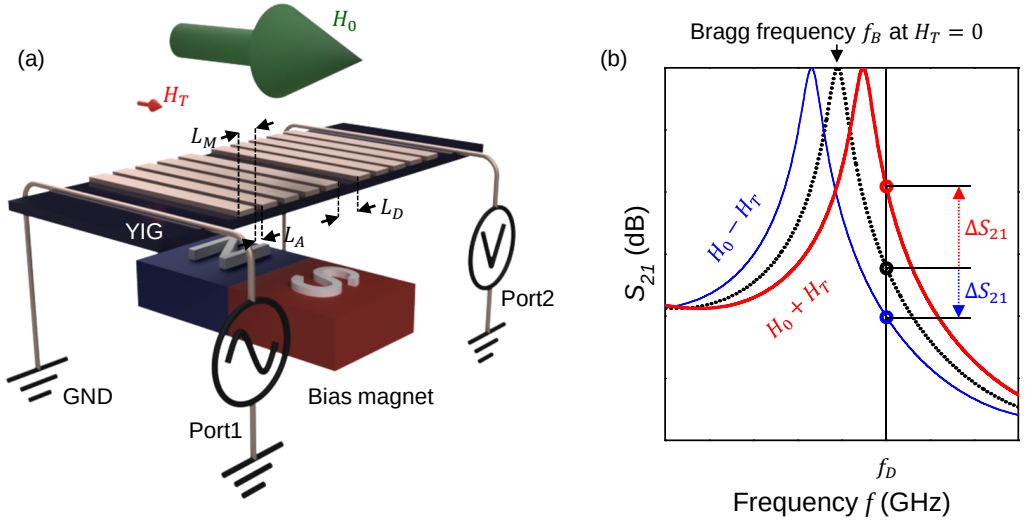

Figure 4.2 Principle of magnetic field measurement by using SWs. (a) Schematic illustration of the setup. Bias magnetic field H_0 is given by the bias magnet. H_T is the testing magnetic field. Transmission properties of DE-SWs from port 1 to port 2 are measured. Magnonic microcavity is composed of the structure with metalization width L_M, gap width L_A, and the defect gap width L_D. (b) Typical transmission spectra in the vicinity of the Bragg frequency. Frequency shift due to H_T is overlaid.

the performance of magnetic field sensors especially minimum resolution was investigated in this chapter.

4.1.2 Principle

Even though propagation frequencies of SWs are sensitive to H_T, transmission spectra of SWs are lacking in intensity change. A sensitivity of transmission signal S_{21} to H_T can be written by

$$\frac{\partial S_{21}}{\partial H_T} = \frac{\partial S_{21}}{\partial f}\frac{\partial f}{\partial H_T}, \tag{4.1}$$

where f is propagation frequency. Based on the nature of SWs, a value of $\partial f/\partial H_T$ is almost constant and ranging in the order of several MHz/Oe. Thus remained possibility to enhance sensitivity is the control of $\partial S_{21}/\partial f$ by AMLs. The value of $\partial S_{21}/\partial f$ corresponds to the slope of transmission band, and it is necessary to have steep S_{21} change on frequency. It is noteworthy that a localized peak gives a large value of $\partial S_{21}/\partial f$, and the slope can be further designed by the structure of microcavity. In contrast to the previous report using Bragg mirrors, higher transmission gain is expected by using such localized peaks. This yields of the increase of signal to noise ratio. The schematic

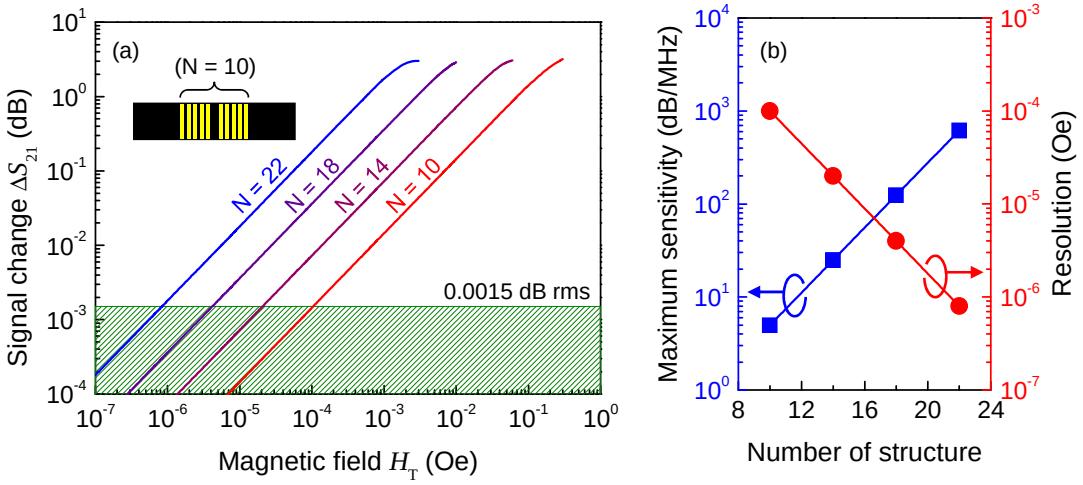

Figure 4.3 (a) Given signal change ΔS_{21} for various values of H_T of magnonic microcavities with $L_M = 213$ µm, $L_A = 193$ µm and $L_D = 386$ µm. A bias magnetic field $H_0 = 200$ Oe is assumed together with the 110 µm-thick YIG. Inset is a schematic drawing of microcavity with $N = 10$. A yellow stripes represent metalized layer. (b) Extracted sensitivity $\partial S_{21}/\partial f$ and the minimum resolution with different N.

drawings are illustrated in Fig.4.2. A testing magnetic field $+H_T$ $(-H_T)$ gives up-shift (down-shift) of the Bragg frequency f_B. By measuring a change of signal ΔS_{21} at specific driving frequency f_D, H_T can be estimated. To obtain the maximum sensitivity, a value of $\partial S_{21}/\partial f$ should be maximized at f_D.

The dependence of ΔS_{21} on the number of periodic structure was calculated to review an aspect of AML-based magnetic field sensors. For simplicity, Gilbert damping, coupling efficiency to the excitation antennas, and contribution of Gaussian noise were ignored in the calculation. Basic design of periodic structure was consistent with one used in §3.2 ($L_M = 213$ µm, $L_A = 193$ µm and $L_D = 386$ µm). Calculated ΔS_{21} for different N from 10 to 22 is shown in Fig.4.3a. Evaluating frequencies are adjusted for each N to maximize $\partial S_{21}/\partial f$. For example, a value of $\partial S_{21}/\partial f = -4.97$ dB/MHz at 2.9084 GHz for $N = 10$. This became -614.98 dB/MHz at 2.9078 GHz for $N = 22$. A change of evaluating frequency is caused by the narrowing of the localized peaks. As a result, larger N gave a higher sensitivity as expected. In addition, given ΔS_{21} was monotonically decreased with reduction of H_T.

A value of S_{21} is generally measured by using a vector network analyzer (VNA) to diminish noise spectral density in GHz region. The use of VNA yields following requirements for H_T measurement.

- A signal level of S_{21} overcomes the noise floor (typically $\sim$ -70 dB)
- A signal change ΔS_{21} exceeds the trace noise

The first requirement was absolutely satisfied thanks to the higher transmission intensity of localized peak, e.g. a calculated $S_{21} = -3.19$ dB at $H_T = 0$ Oe for $N = 10$. Therefore the latter requirement determines the minimum resolution of H_T. A high grade VNA, e.g. KEYSIGHT, E5080A, gives a small trace noise of 0.0015 dB rms, the limit of discriminable ΔS_{21} was determined based on this value. This limit was overlaid on Fig.4.3a as a greed shaded area. Therefore Signal change ΔS_{21} in the shaded area cannot be distinguished.

In the microcavity with large N number, ΔS_{21} was kept discriminable even in smaller H_T region. As a result, increase of N increased the resolution of H_T, and the minimum resolution is expected to reach the range of 10^{-7} Oe at $N = 22$. This resolution is sufficient for the application of magnetocardiogram. The trend of the sensitivity and minimum resolution for different N are summarized in Fig.4.3b. This suggests that further increase of N will give enhancement of the minimum resolution overtaking SQUID sensors. This is the basic strategy to obtain smaller resolution by AML-based magnetic field sensors.

4.1.3 Experimental Setup

A prospect of AMLs as a magnetic field sensor was experimentally investigated. For this investigation, homemade evaluation setup was constructed. Testing field H_T was provided by a handmaid Helmholtz coil. The winding diameter of each coil was 180 mm, and number of winding was 20. Each coil was coaxially aligned with 90 mm separation. This geometry ensured a homogeneous H_T distribution within an error of 0.01 % inside 10 mm square at the center of the Helmholtz coil. The block diagram of the setup is shown in Fig.4.4a. A magnonic microcavity under testing was placed at the center of the Helmholtz coil. To apply bias magnetic field H_0, a ferrite magnet was placed beneath the YIG waveguide. The waveguide was placed on the MSL substrate, and a position of the ferrite magnet was carefully adjusted to show a good localized mode. In the experiment, the magnonic microcavity with $N = 10$ was prepared because larger N made the structure larger, yielding in the H_T inhomogeneity. With $N = 10$, the length of periodic structure became about 4.2 mm, and this was enough smaller than the area of homogeneous H_T given by the Helmholtz coil. Microcavities with larger N can be miniaturized by using thinner YIG films. Thus the microcavity with $N = 10$ was the proof-of-principle-type form, and the minimum resolution of 10^{-4} Oe was expected.

Transmission properties of the microcavity was measured by VNA (KEYSIGHT, 8753ES). A value of H_T was controlled by the current source (Agilent, E3640A), and the applied current was monitored by the ammeter (KEITHLEY, 2000). The minimum amount of the controllable current by the equipment was 1 mA, thus an external current divider with the dividing ratio of 1:1000 was introduced to control H_T in fine region. With the current divider, the minimum amount of the controllable current became 1 μA.

The I-H curve of the Helmholtz coil was calibrated by the fluxgate sensor (Bartington Instruments, Mag-01H). The result is shown in Fig.4.5. Applied current blow 1 mA was achieved by using the current divider. The target H_T of 10^{-6} Oe was compara-

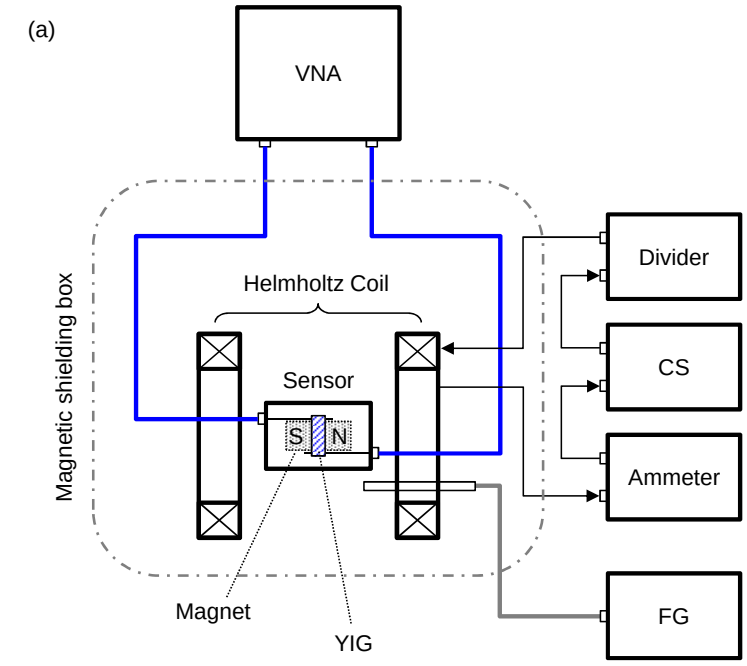

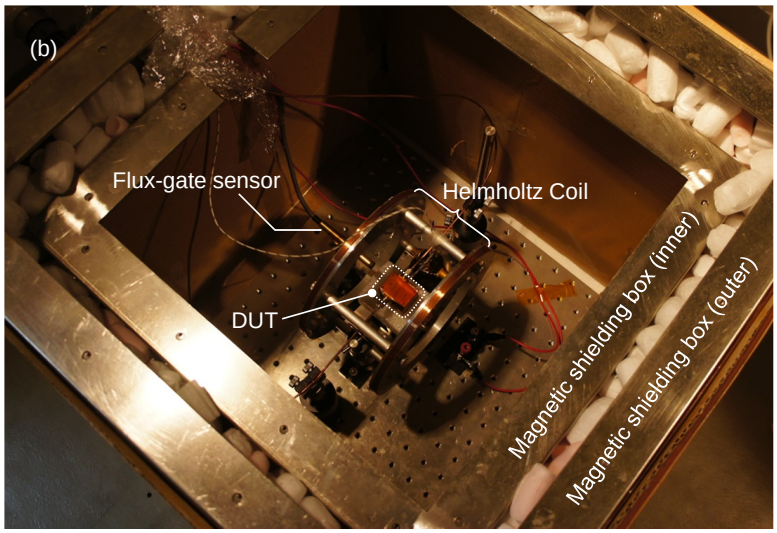

Figure 4.4 Setup for evaluation of magnetic field sensors. (a) Block diagram. Abbreviations are: VNA (vector network analyzer), CS (current source) and FG (fluxgate sensor). I-H curve of Helmholtz coil was calibrated by the fluxgate sensor. (b) The photograph of the measurement setup constructed in the magnetic shielding box.

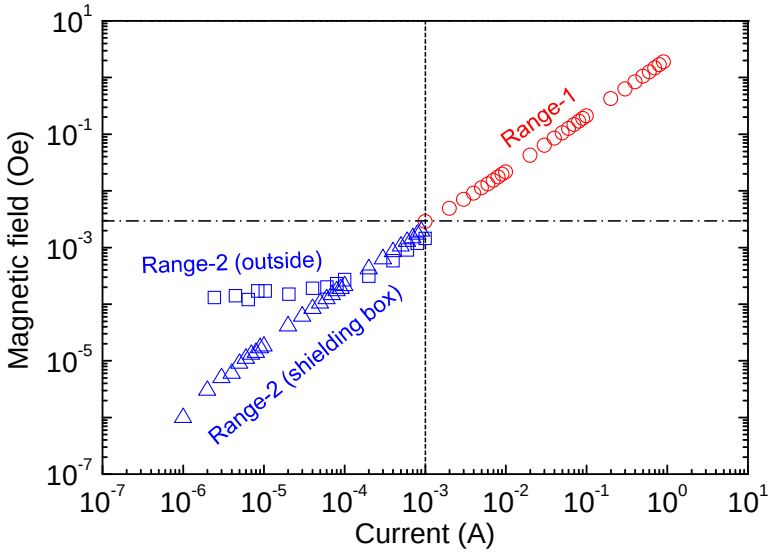

Figure 4.5 Measured I-H curve of the Helmholtz coil. Red circles represent result without divider, and blue triangles and squares represent results with divider. Squares are measured outside the shielding box and triangles are inside the shielding box.

ble to the biomagnetic field, and smaller than the urban magnetic noise. The measured magnetic field was bottomed out at 2×10^{-4} Oe, outside the magnetic shielding box (see blue squares). In contrast, a linear I-H curve with the slope of 2.10 Oe/A was obtained in the range from 10^{-6} Oe to 1 Oe, inside the magnetic shielding box (see blue triangles). Below 10^{-6} Oe, the fluxgate sensor was out of range, and thus no data point is shown. From the result, the evaluation system was functional at fine H_T region, and the magnetic shielding was required to test smaller H_T than 10^{-4} Oe. As shown in Fig.4.4b, magnetic shielding box were composed of double layers of high permeability material to shut the magnetic flux from the cable introduction part. A gap of layers was filled with pieces of styrene foam to prevent heat convection, and the shielding box was covered by the corrugated carton to stabilize temperature fluctuation. To reduce the contribution of environmental electromagnetic noise as much as possible, The shielding box shown in Fig.4.4b was further enclosed by the magnetic shielding room (NEC TOKIN Corporation). A residual static magnetic field was less than 100 nT inside the room. Before the measurement, the magnetic shielding room had been closed over a day to suppress thermal convection inside.

Then, values of $S_{21}(f_D)$ were measured with and without the current divider to evaluate H_T dependence from 10^{-6} Oe to 1 Oe, and the resulted signal change ΔS_{21} was calculated as a difference from the reference measurement at $H_T = 0$ Oe. This measurement sequence was repeated 10 times and the result was obtained as the average value of these measurements.

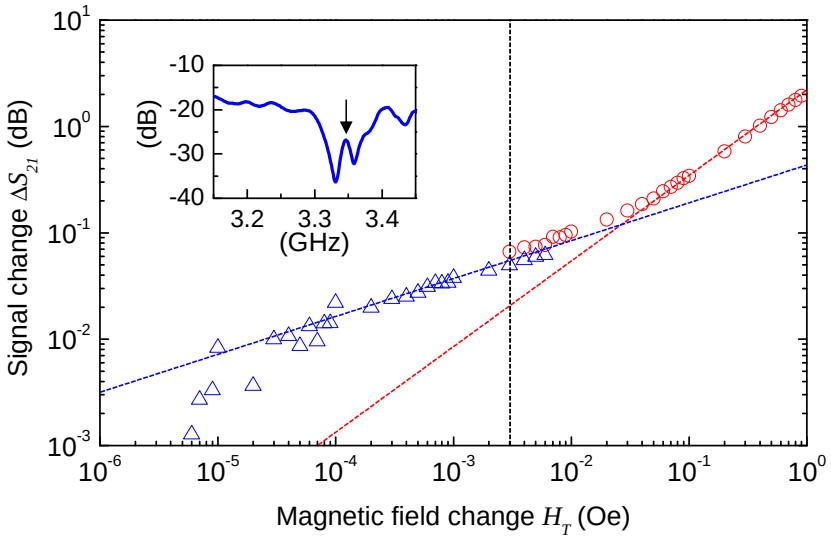

Figure 4.6 Measured response of the magnonic microcavity to H_T. Red circles represent the result obtained without the current divider, and blue triangles represent the result obtained with the current divider. Each point is the average of 10 repeated measurement. Inset graph shows the S_{21} spectrum in the vicinity of localized peak. Black arrow points at the Bragg frequency.

4.1.4 Result

Transmission spectrum around the Bragg frequency was measured after temperature stabilization process, and the obtained S_{21} spectrum exhibited a clear localized spectrum with Q-factor of 256 as shown in the inset graph of Fig.4.6. According to this result, the evaluating frequency was set to $f_D = 3.35$ GHz. At this frequency, H_T dependence of ΔS_{21} was evaluated. The result is displayed in Fig.4.6. Obtained output ΔS_{21} seemed to have a linear dependence on H_T. Below $H_T = 10^{-4}$ Oe, a fluctuation of ΔS_{21} was drastically increased. However, the output slope seemed to be still proportional to H_T. Thus the magnonic microcavity might exhibit observable sensitivity to the magnetic field less than 10^{-4} Oe. This result agreed very well with the theoretical prediction shown in Fig.4.3. Nevertheless, the slope of ΔS_{21} is perfectly constant in the entire range of H_T in the calculation. In contrast, a change of the slope was confirmed at $H_T = 10^{-2}$ Oe, or $\Delta S_{21} \sim 10^{-1}$ dB in the experiment. Thus the behavior was slightly different from the expectation. This anomalous behavior was reproduced by the calculation considering a Gaussian noise.

The calculation was still based on the transfer matrix approach. In the realistic measurement, a certain level of noise was superimposed to the measured spectrum, and this noise gave unpredictable deviation on the S_{21}. The effect of the noise was considered as a linear sum, and no frequency dependence was assumed. Accordingly, the calculated

transmission property was renewed with the Gaussian noise as follows:

$$A'_{21}(f) = 10^{-S_{21}(f)/20} + N(\mu, \sigma_N), \tag{4.2}$$

where $N(\mu, \sigma_N)$ represents the Gaussian noise with mean value μ and deviation σ_N. From experiences so far, a typical level of noise floor was around -70 dB. Values of $\mu = 0$ and $\sigma_N = 3.16 \times 10^{-4}$ well reproduced such noise floor. A resulting $S'_{21}(f)$ is then calculated by $20 \log_{10} |A'_{21}(f)|$. Magnetic field sensitivities were calculated with the same situation as Fig.4.3, with the Gaussian noise. In addition to the effect of Gaussian noise, three different calculation conditions for the Gilbert damping α and the coupling efficiency to the antennas η were employed.

Condition L1 : Considering $\alpha = 10^{-4}$ and $\eta = 0.2$.

Condition L2 : Considering $\alpha = 0$ and $\eta = 0.2$.

Condition L3 : Considering $\alpha = 0$ and $\eta = 1$.

Among these conditions, the condition L3 represents the almost perfect condition except for the Gaussian noise. From the condition L3 to condition L1, the performance of the AML is deteriorated. Results of calculation are shown in Fig.4.7. In all graphs, the reference calculation based on the condition L3 without the Gaussian noise was overlaid as black lines. As shown in Fig.4.7a-c, the calculated transmission spectra became ambiguous due to the effect of the Gaussian noise, but this effect was very limiting in the high gain region. The condition L3 seemed to be almost unchanged from the reference curve due to the effect of the Gaussian noise. Considering the effect of coupling efficiency, the calculated result of $S_{21}(f_D)$ for $\eta = 0.2$ was attenuated from -3.21 dB to -18.2 dB (L3 $\rightarrow$ L2). In addition, the introduction of Gilbert damping close to the actual value of $\alpha = 10^{-4}$ further reduced $S_{21}(f_D)$ from -18.2 dB to -23.1 dB (L2 $\rightarrow$ L1). Therefore levels of $S_{21}(f_D)$ were overestimated in L3 and L2. Such overestimation was also included in the calculation of Fig.4.3. Next, the effect of intensity of $S_{21}(f_D)$ on the magnetic field sensitivity ΔS_{21} is calculated.

Magnetic field sensitivity ΔS_{21} with the condition L3 is shown in Fig.4.7d. Although remarkable difference was not confirmed in the transmission spectrum, deviation of ΔS_{21} from the reference line was clearly seen in $\Delta S_{21} < 10^{-2}$ dB. However, a certain measure of linearity was kept to the extent of $H_T = 10^{-4}$ Oe. Below this point, ΔS_{21} was no longer significant due to the effect of Gaussian noise. In Fig.4.7e, the same calculation for the condition L2 is displayed. Comparing to the condition L3, deviation of ΔS_{21} was remarkably increased due to the reduction of the level of $S_{21}(f_D)$. As a result, calculated ΔS_{21} was no longer significant in $H_T < 10^{-3}$ Oe. Consideration of the Gilbert damping further reduced $S_{21}(f_D)$. The resulting sensitivity of the condition L1 is shown in Fig.4.7f. Calculated ΔS_{21} was no longer significant in $H_T < 10^{-2}$ Oe. In addition, values of ΔS_{21} were slightly down-shifted from the reference line. This result indicated the broadening of the localized peak due to the damping effect reduced the

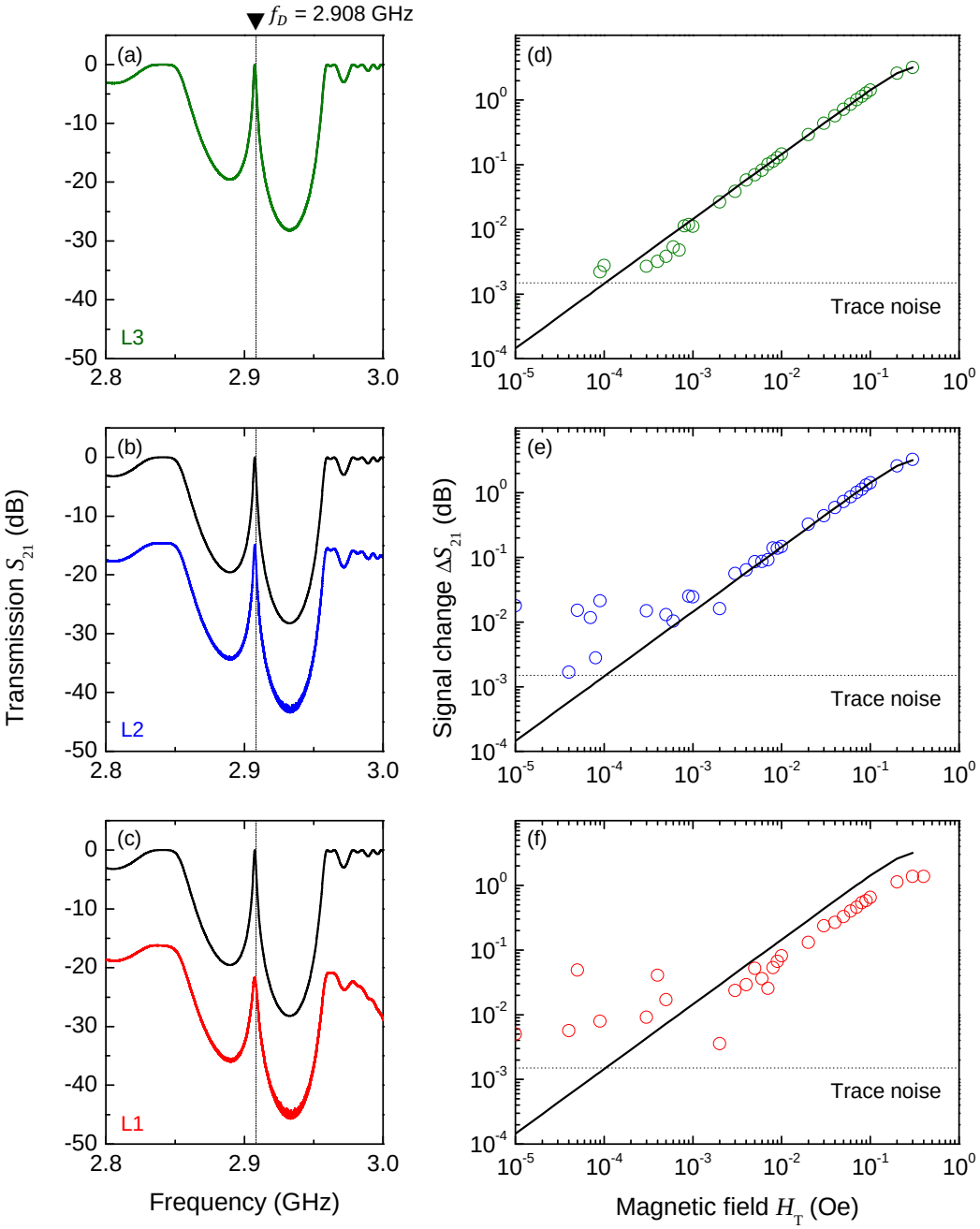

Figure 4.7 Limits of the magnetic field resolution with different conditions. Transmission spectrum of AMLs in the vicinity of f_D calculated with the (a) condition L1, (b) condition L2, and (c) condition L3. Magnetic field sensitivity ΔS_{21} at f_D against to various H_T values calculated with the (d) condition L1, (e) condition L2, and (f) condition L3. All black curves represent the reference calculations based on the condition L3 without the Gaussian noise. Driving frequency of $f_D = 2.908$ GHz is used.

slope of intensity $\partial S_{21}/\partial f$.

It is noteworthy that the experimental result shown in Fig.4.7 was the average of 10 repeated measurements, and this averaging slightly suppressed the deviation. The effect of such small number of averaging appeared as the change of the slope at $H_T = 10^{-2}$ Oe. Therefore under this point, a signal to noise ratio was assumed to be drastically decreased, and the resulted values were no longer reliable. In this graph, error bars cannot be directly shown due to the logarithmic vertical axis. By considering such Gaussian noise effect, a reliable magnetic field resolution obtained in the experiment was limited to 10^{-2} Oe at the most.

According to the weak law of large numbers, the Gaussian noise term in Eq.4.2 would be converged to $N(\mu, \sigma_N) \to \mu$ with sufficient number of averaging, in which the mean value is $\mu = 0$. Therefore, in principle, a deviation of ΔS_{21} due to the Gaussian noise can be removed and the true slope of ΔS_{21} against H_T would be given. Although the effect of Gaussian noise may become negligible by enough large number of sampling, there is another effect of temperature drift; this effect cannot become negligible under such huge number of measurements. This effect is discussed on the following part.

From above calculations, it can be understood that a higher level of $S_{21}(f_D)$ yielded in the small deviation of ΔS_{21}. This is reasonable because the ΔS_{21} is a relative value so that the ratio of the Gaussian noise to ΔS_{21} depends on the level of $S_{21}(f_D)$. Some specific examples were calculated for an input signal of 1 mW. In the case of the condition L3, a transmitting power at f_D was 0.69 mW, while it became 0.07 mW in the condition L1. A noise floor with the intensity of -70 dB corresponded to the averaged noise power of 0.32 μW. If the change of H_T gave ΔS_{21} of 0.1 dB, the resulting change of the transmitting powers were 8.0 μW and 0.81 μW for the condition L3 and condition L1, respectively. Therefore the given signal to noise ratios were 25 and 2.5 for the condition L3 and condition L1, respectively. Thus the increase of the signal level $S_{21}(f_D)$ is also needed as well as the increase in the transmission slope $\partial S_{21}/\partial f$.

4.1.5 Design of Magnetic Field Sensors

Based on the previous discussion, important factors to design S_{21} spectra were obtained. A slope of transmission spectra $\partial S_{21}/\partial f$ has a dominant effect on the dynamic range. An output signal change ΔS_{21} was distinguishable only when the difference exceeded the trace noise of an equipment. Therefore $\partial S_{21}/\partial f$ should take a large value. It is convenient to use Q-factors for this evaluation, because the Q-factor represent a sharpness of localized peak. Another issue was the signal level of $S_{21}(f_D)$, which is a dominant factor for the signal to noise ratio. Reduction of the effect of Gaussian noise by sufficient number of averaging would be possible, but this sacrifices time resolution of the measurement. Moreover the integration of the device usually increases the noise floor. Therefore it is more preferable to have a sufficiently high level of $S_{21}(f_D)$. It is convenient to measure the peak intensity, which is appeared at the Bragg frequency f_B, namely $S_{21}(f_B)$. Use of the signal intensity at the driving frequency $S_{21}(f_D)$ might be more direct, but it is complicate due to the dependence of f_D on the periodic number N. Accordingly, a

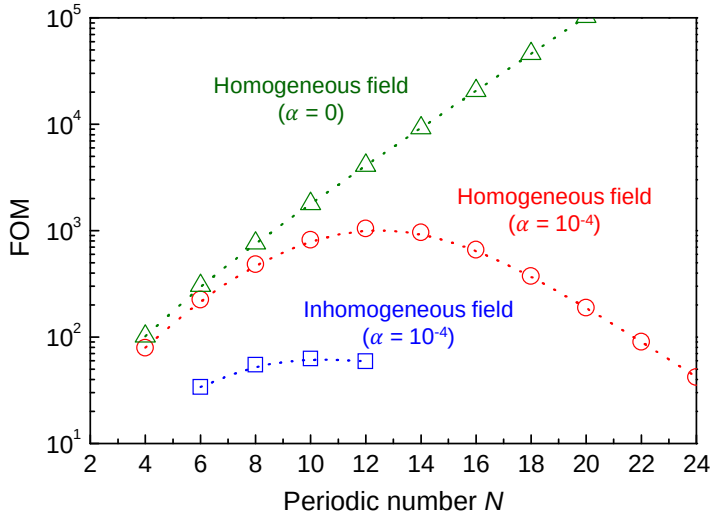

Figure 4.8 Figure of merit for various magnonic microcavities. Blue squares represent FOM calculated with demagnetizing field and finite magnetic damping. Red circles represent FOM without demagnetizing field and with finite magnetic damping. Green triangles represent FOM without demagnetizing field and magnetic damping.

figure of merit (FOM) for the AML-based magnetic field sensors was introduced as in the following manner.

$$\mathrm{FOM} = 10^{S_{21}(f_B)/20} \times (Q\text{−factor}) = 10^{S_{21}(f_B)/20} \frac{f_B}{\Delta f}, \tag{4.3}$$

where Δf is the full width at half maximum (FWHM) of the local peak frequency. Evaluated FOMs for various magnonic microcavities are shown in Fig.4.8. Green triangles are the ideal calculation, which corresponds to the data shown in Fig.4.3. In this case, FOM monotonically increased as increase of periodic number N. Therefore in the basic principle, increase of N gave increase of the sensitivity and the signal to noise ratio at the same time. However, FOM value showed maximum at $N = 12$ in the red circles calculated with a finite Gilbert damping of $\alpha = 10^{-4}$. This is due to the confinement of SWs in the defect layer, in which Fabri-Perot resonance enhances the damping effect inside the microcavity. This reduced $S_{21}(f_B)$ yielded of the degradation of the signal to noise ratio. Blue squares reflected the most realistic situation, in which the demagnetization effect was also considered as discussed in §3.2. Thus broadening of the peak increased Δf, yielding in the degradation of Q-factor. Therefore FOM exhibited drastically small values in an order of magnitude.

To improve the FOM of AML-based magnetic field sensors, it is necessary to have a homogeneous H_0 distribution, because the demagnetizing effect is the dominant reason of the degradation of FOM through the reduction of signal intensity S_{21} and the increase of linewidth Δf. According to the calculation in Fig.4.3, appropriate N to have the

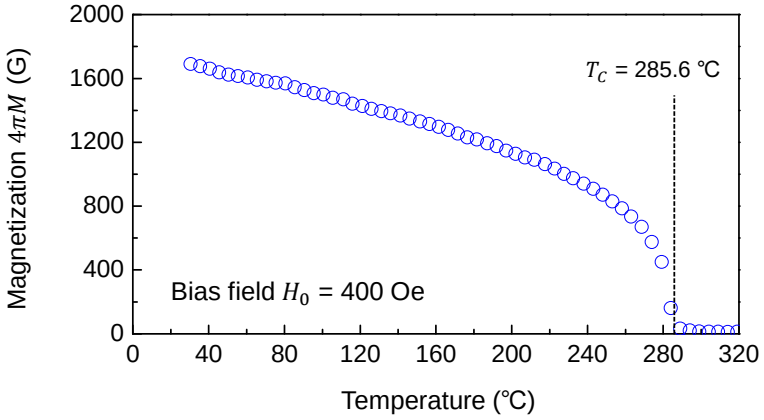

Figure 4.9 Temperature dependence of in-plane magnetization $4\pi M$ of YIG. Magnetic field $H_0 = 400$ Oe was applied.

maximum FOM varies by the condition of AML. For example, the elimination of the demagnetizing effect improves the value of the maximum FOM from 66 at $N = 10$ to 1,086 at $N = 12$. Furthermore, if the value of α at the defect layer was diminished, the maximum value of FOM can be easily extended by using the structure with large N. YIG films with smaller α in the order of 10^{-5} are available at the laboratory level.[70–72] At this damping value, the maximum FOM of 11,780 can be obtained at $N = 18$. Nevertheless, improvement of the film quality to this level is still challenging issue.

On the other hand, amplification of SWs was experimentally demonstrated by using the spin transfer torque,[137] or by using a parallel pumping technique.[138,139] Such techniques would compensate the enhancement of the damping effect at the defect layer. If the damping effect at the defect layer is completely compensated, FOM would be monotonically increased with N. These suggestions are outside the scope of this chapter, and would be a road map for the further researches.

4.1.6 Temperature Compensation

While YIG is one of the best materials for SWDs, temperature sensitivity might be a serious issue. This bothers the estimation of magnetic field resolution and reduced reliability of the measured H_T. Temperature dependence of $4\pi M$ of 110 μm-thick YIG is shown in Fig.4.9. This curve was measured by using the vibrating sample magnetometer (Tamagawa, TM-VSM261483-HGC), while applying an in-plane magnetic field $H_0 = 400$ Oe. The Curie temperature of the film was $T_C = 285.6$°C, and the value agreed well with the literature.[49] A temperature dependence of $4\pi M$ around R.T. was estimated as $a_{\mathrm{YIG}} = -2270$ ppm/°C. This yields the magnetization change about 4 G for 1°C of the temperature drift. In addition, remnant field of the bias magnet is also drifted. This H_0 also had a temperature dependence α_{MAG}. These contributions due to the temperature

drift ΔT are appeared as changes of Lamor frequencies.

$$\omega_H = \gamma(1 + a_{\mathrm{MAG}}\Delta T)H_0. \tag{4.4}$$

$$\omega_M = \gamma(1 + a_{\mathrm{YIG}}\Delta T)4\pi M_S. \tag{4.5}$$

Since the contribution of ΔT is written as a linear sum, this model is valid for the small ΔT because $4\pi M$ had nonlinear dependence on T as shown in Fig.4.9. Consequently, this assumption seemed to be valid around R.T. A dispersion curve of SWs obtained in §3.1 was too complicated to formulate as a function of ΔT. However, deviation of the frequency f can be written as following to the perturbation theory as long as ΔT is sufficiently small.

$$f\left(k(T + \Delta T)\right) = f\left(k(T)\right) + f'\left(k(\Delta T)\right), \tag{4.6}$$

where f, f' are frequencies and $k(T)$ is the wavenumber as a function of T.

To confirm this idea in experiment, a Bragg frequency f_B was tracked against ΔT as an index of dispersion shift. The position of f_B was estimated by using an AML composed of the structure with L_M = 213 μm, L_A = 193 μm, and L_D = 193 μm together with 110 μm-thick YIG. Thus the AML was the Bragg mirror, in which a sharp notch-shaped stop band was observed. The measurement setup was constructed in the thermostat chamber (ESPEC, SH661) to control the ambient temperature T. To monitor T, a T-type thermocouple was placed by the YIG waveguide. The temperature was measured by the scanner system with a fixed temperature point (KEITHLEY, 2001-TCSCAN). The position of ferrite magnet was carefully adjusted to have a clear stop band in the measured frequency range, and the transition property was measured in the temperature range from 25°C to 35°C with interval of 0.5°C.

Obtained result is shown in Fig.4.10a. The position of f_B was down shifted as T increased. This was caused by the heat demagnetization both of the YIG waveguide and the ferrite magnet. A change of the depths of stop bands was also observed. This might be caused by the change of demagnetizing effect inside the YIG waveguide. Important point was the linearity of f_B shift on T. The relation between f_B and T is shown in Fig.4.10b, and the linearity between them can be clearly seen with a constant slope of $C_B = -6.2$ MHz/°C.

This result motivated the compensation of the effect of temperature drift using temperature feedback circuit. A value of T monitored by the thermocouple determined the compensation magnetic field H_{cp}, and H_{cp} was applied by the Helmholtz coil. The evaluated H_T dependence of f_B was comparable to the gyromagnetic ratio γ = 2.8 MHz/Oe. Eq.4.6 was written with the contribution of H_{cp} while taking into account the

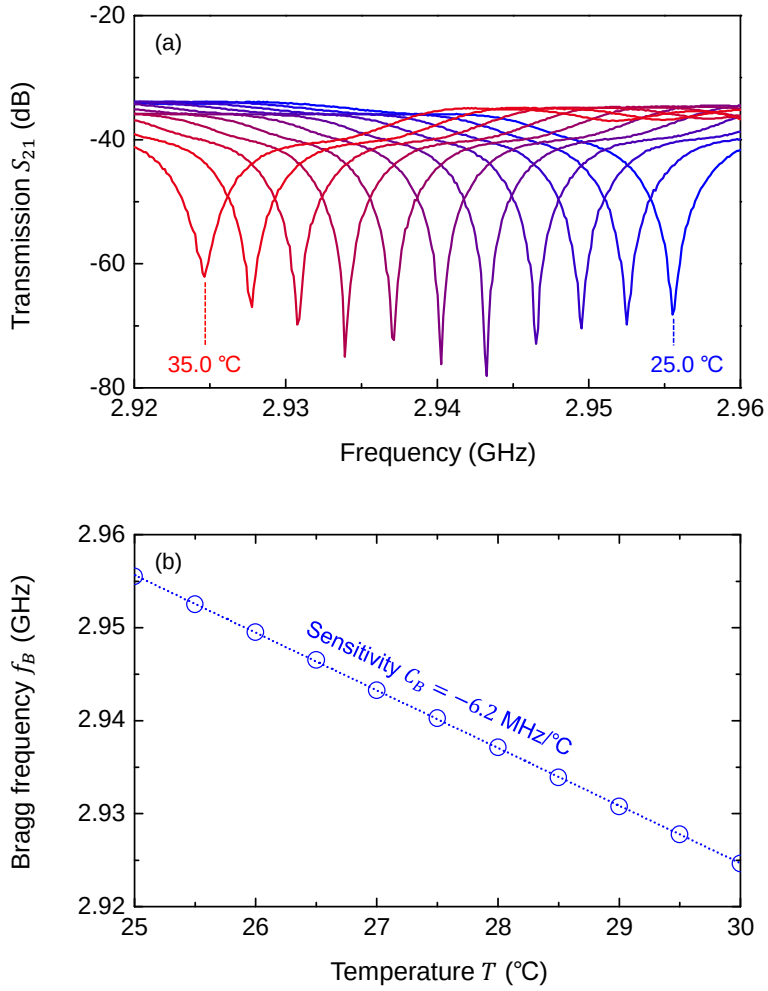

Figure 4.10 Temperature drift of the Bragg frequency f_B. (a) Transmission spectra S_{21} in the vicinity of f_B with various temperatures T from 25.0°C to 35.0°C with 0.5°C increments. The temperature increases from blue colored lines to red colored lines. (b) Extracted dependence of f_B on T.

linearity of the temperature dependence.

$$f_B\Big(k(T+\Delta T)\Big) = f_B\Big(k(T)\Big) + C_B\Delta T + \gamma H_{\rm cp}. \tag{4.7}$$

To compensate the temperature drift $C_B\Delta T$ in Eq.4.7, $H_{\rm cp}$ was given as

$$H_{\rm cp} = -\frac{C_B\Delta T}{\gamma}. \tag{4.8}$$

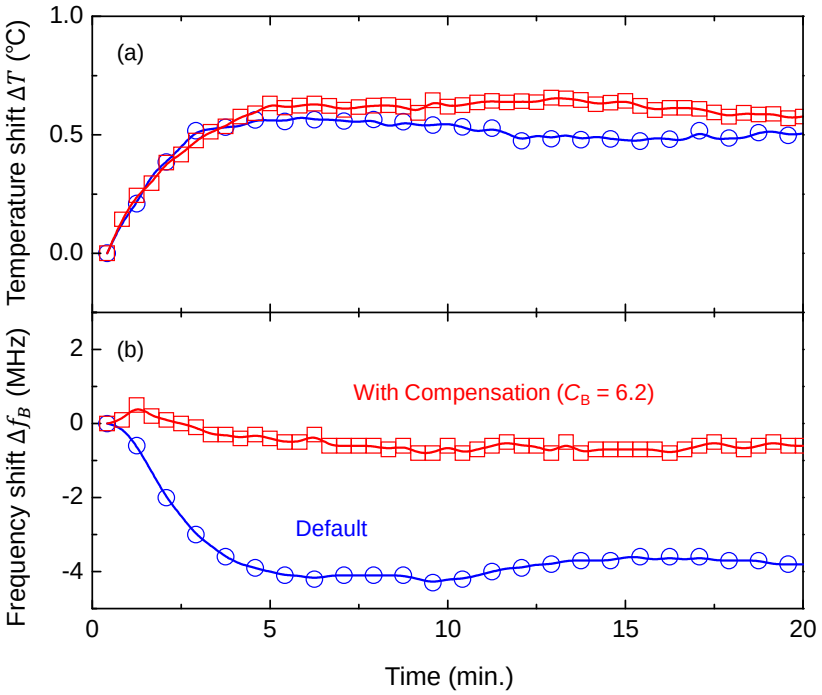

Figure 4.11 Implementation of temperature feedback circuit. (a) Time shift of controlled ambient temperature. (b) Time shift of f_B. Red squares (blue circles) represent the result with (without) the feedback circuit. $C_B = -6.2$ MHz/°C is used as the compensation parameter.

During the measurement, Eq.4.8 was calculated by the computer, and real-time feedback was given to the measuring system. A well controlled ΔT ramping 0.5°C was given by the thermostat chamber, and frequency shift of f_B were tracked on short time intervals. The results are shown in Fig.4.11. Bragg frequency f_B was monotonically decreased with T increasing without the feedback circuit. On the other hand, f_B was recovered to the original position within the error of 2.87 ppm when the feedback circuit was activated. Therefore the temperature compensation with Eq.4.8 was possible in principle.

The temperature feedback circuit seemed to work well in the experiment with the environment precisely prepared. A change of T was stabilized after ramping, and this was quite rare case in the practical situation. In the experiment, there was a small overshoot in f_B even with the temperature feedback circuit. The system took about 5 minutes to recover f_B at the original position. This time lag would be caused by the mismatch of heat capacities of the YIG waveguide and thermocouple. Monolithic integration of these circuit might improve the situation, but real-time compensation is challenging.

Finally, the effect of temperature profiles on the possibility of compensation was investigated. According to Eq.4.8, the compensation magnetic field $H_{\rm cp}$ to control the position of f_B was determined from observed ΔT with the control constant C_B. There-

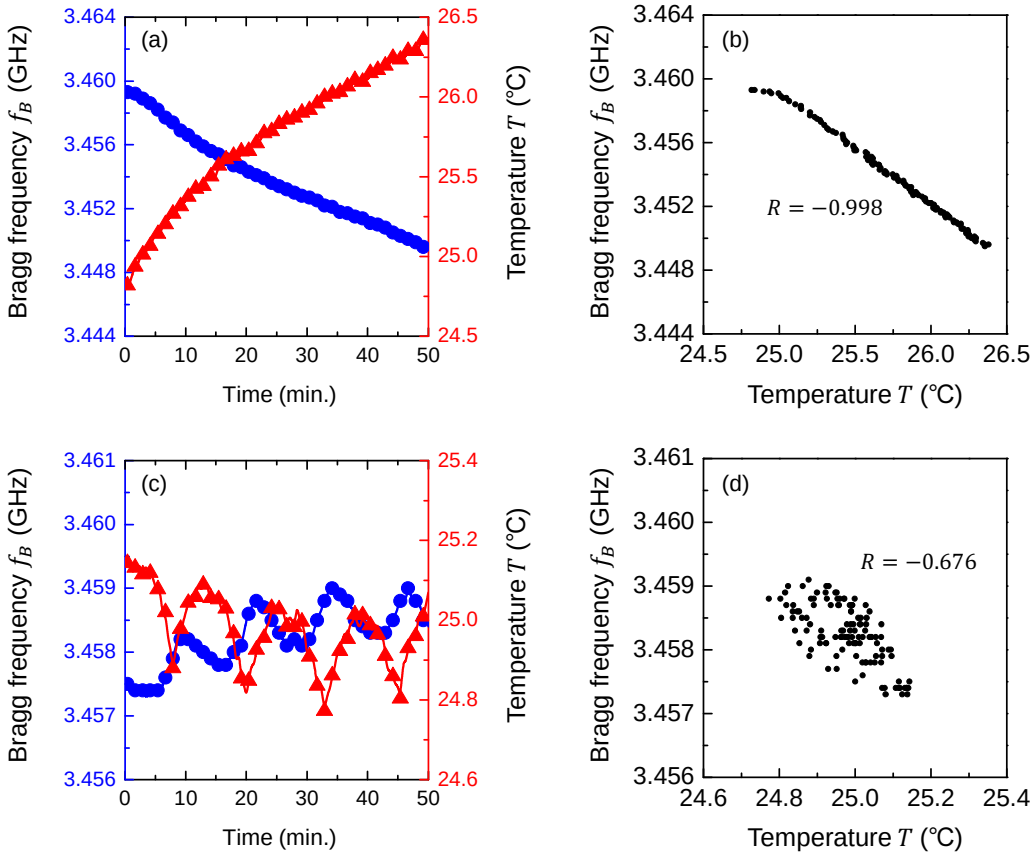

Figure 4.12 Deviation of f_B to the different types of temperature drift artificially controlled by the thermostat chamber. Ramping type: (a) time dependence of f_B and T and (b) relationship of these parameters. Oscillating type: (c) time dependence of f_B and T and (d) relationship of these parameters. Feedback compensation is not used.

fore T should be uniquely corresponding to the resulting shift of f_B. This is the basic requirement for the feedback compensation. In the experiment, following temperature profiles were artificially provided for 50 minutes by the thermostat chamber: ramping temperature and oscillating temperature. Former profile is often seen in the situation with slow temperature drift, e.g. outdoor temperature. On the other hand, latter profile is often seen in the controlled situation, e.g. air conditioning system. During the measurement, feedback control was switched off and pure responses of f_B were evaluated.

In Fig.4.12, measured profiles of f_B for two different types of temperature drift are graphed. In Fig.4.12a, the result of ramping temperature is shown, in which the value of T increased monotonically, and f_B decreased monotonically. The relationship of f_B and T is summarized in Fig.4.12b. In this situation, the correlation coefficient of these parameters was evaluated as -0.998. Thus T and f_B were almost uniquely corresponding, and

the profile of ramping temperature satisfied the requirement for feedback compensation. In Fig.4.12c, another result of the profile of oscillating temperature is shown, in which values of T and f_B were oscillating with about 10 minutes cycle. In the same manner, the relationship of f_B and T is summarized in Fig.4.12d. In this situation, the correlation coefficient was reduced to -0.676. This result indicated T and f_B were not uniquely corresponding due to the mismatch of temperature sensitivities of the YIG waveguide and thermocouple, and accuracy of the feedback compensation would be remarkably decreased. Unfortunately, temperature drift of the practical situation is usually similar to the profile of oscillating temperature. Currently, the temperature feedback circuit can be used at the laboratory level environment, and another fundamental solution is needed to solve this issue.

4.2 Differential Spin Wave Circuit for Sensors

4.2.1 Principle

One of the most commonly used techniques to suppress an environmental noise is the differential circuit, in which the contribution of noise from environment and the radiation of noise originated in a source are suppressed by the subtraction of received signals. This technique has been seen in the telephone wires ans so on. I introduced the magnonic counterpart of differential circuit to suppress temperature drift of the system, namely differential spin wave circuit (DSWC). This idea was first introduced in this field.

In general differential circuits, input signals are given in the normal mode (phase-inverted signals) and a noise is given in the common mode. Therefore the contribution of the noise can be suppressed. In the case of magnetic field sensors, the contribution of H_T to the bias magnetic field H_0 modifies the transmission property $S_{21}(f_D)$. And the heat demagnetization ΔM also modulates $S_{21}(f_D)$. Therefore both of H_T and ΔM dependent shift are appeared as common mode in SWDs, and usual subtraction process excludes information of H_T as well as ΔM. In this work, a simple trick was introduced to solve this problem. This concept was schematically shown in Fig.4.13 The system was composed of two YIG waveguides, namely circuit A and B, magnetized in anti-parallel by the opposite H_0. Accordingly, the contribution of H_T and ΔM to the magnetic flux $B = H_0 + M$ inside the waveguide is written by

$$\begin{aligned} B_A &= +H_0 + H_T + (M + \Delta M) \\ B_B &= +H_0 - H_T + (M + \Delta M) \end{aligned} . \tag{4.9}$$

It is noteworthy that the coordinate system is defined by the direction of H_0 in each circuit. This model is valid because these circuits can be considered separately due to no interaction between them. In this scheme, only H_T dependent shift is appeared as the normal mode, thanks to the different polarization with H_0. Thus the subtraction of received signals from each circuit selectively eliminates ΔM dependent shift. Since

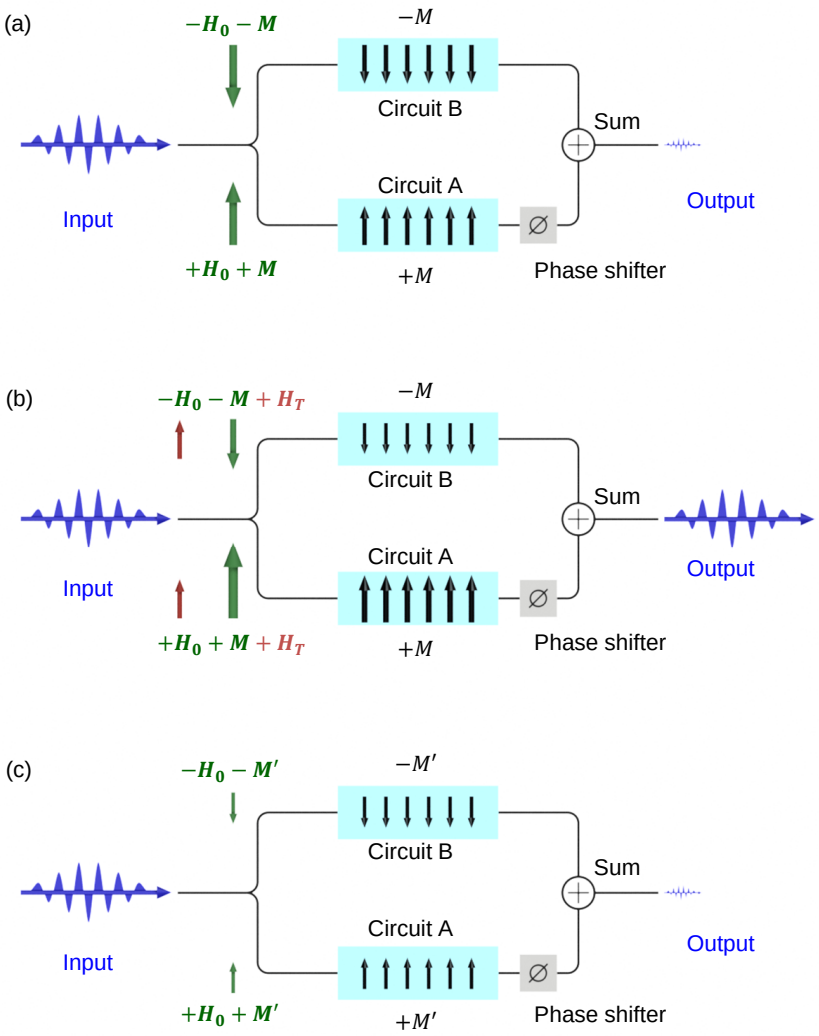

Figure 4.13 Concept of DSWC. (a) Initial state. Green arrows represent an intensity and direction of magnetic flux inside waveguides. (b) When H_T is applied (shown as red arrows). (c) When ΔM is given by temperature drift. The size of blue arrows represent amplitudes of input/output signals.

propagating SWs are presumed to be plane wave, the phase rotation within the circuit is given by $2\pi f_D t - kL$ with the wavenumber k and the waveguide length L. In these parameters, only k shows H_T and ΔM dependence, thus deviation of k is again expanded by the perturbation theory. By assuming the sinusoidal form for the received signals from each circuit, given signals are given by

$$\begin{aligned} S_A &= A_0 \sin\left(2\pi f_D t + \Big(k(H_0, M) + k_1(H_T) + k_2(\Delta M)\Big) L + \theta_{\text{ofs}}\right) \\ S_B &= A_0 \sin\left(2\pi f_D t + \Big(k(H_0, M) - k_1(H_T) + k_2(\Delta M)\Big) L\right) \end{aligned}, \tag{4.10}$$

where A_0 is signal amplitude, and k_1 and k_2 are perturbation term to the original k due to T_H and ΔM, respectively. Only in the circuit A, the received microwave signal is further phase shifted by θ_{ofs} by using an external phase shifter. When common mode and normal mode terms are separately written, Eq.4.10 became

$$\begin{aligned} S_A &= A_0 \sin\left(\Big(2\pi f_D t + k_C L\Big) + \Delta k_1 H_T L + \theta_{\text{ofs}}\right) \\ S_B &= A_0 \sin\left(\Big(2\pi f_D t + k_C L\Big) - \Delta k_1 H_T L\right) \end{aligned}, \tag{4.11}$$

where $k_C = k + k_2$ is the common mode wavenumber, and $\Delta k_1 H_T$ represents the term appeared in the Maclaurin expansion

$$k_1(H_T) = k_1(0) + \frac{\partial k_1(0)}{\partial H_T}\frac{1}{1!}H_T + \frac{\partial^2 k_1(0)}{\partial H_T^2}\frac{1}{2!}H_T^2 ... \sim \Delta k_1 H_T. \tag{4.12}$$

An linear sum of $S_A + S_B$ yields of an output amplitude A_{out} given by

$$A_{\text{out}}^2 = 2A_0^2\left(1 + \cos(2\Delta k_1 H_T L + \theta_{\text{ofs}})\right). \tag{4.13}$$

When $\theta_{\text{ofs}} = 0$, Eq.4.13 became

$$A_{\text{out}}^2 = 2A_0^2\left(1 + \cos(2\Delta k_1 H_T L)\right). \tag{4.14}$$

When $\theta_{\text{ofs}} = \pi$, Eq.4.13 became

$$A_{\text{out}}^2 = 2A_0^2\left(1 - \cos(2\Delta k_1 H_T L)\right). \tag{4.15}$$

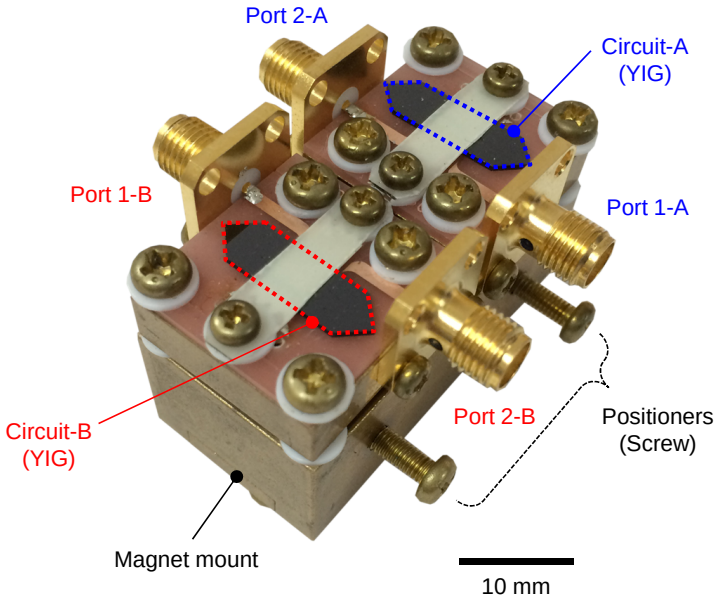

Figure 4.14 Photograph of DSWC. Combination of two SW transducers. Two neodymium iron boron magnets are installed inside a base made of copper-zinc alloy to apply opposite H_0 for each circuit.

Eq.4.14 and Eq.4.15 shows H_T dependence in the cosine function with the different signs. The sign is quite important in the S-parameter measurement, because S-parameter is usually given in the logarithmic scale. To see the resolution for the magnetic field sensor, target H_T is ranging in very small order less than 10^{-3} Oe. In the limit of $H_T \to 0$, Eq.4.15 approaches to 0 so the value of $\log A_{\mathrm{out}}$ takes a huge negative number in this limit, and the sensitivity ΔS_{21} is drastically increased. When the total input signal $A_{\mathrm{in}} = 2A_0$ is assumed, given S-parameter S_{OI} become

$$S_{\mathrm{OI}} = 20 \log_{10} \frac{A_{\mathrm{out}}}{A_{\mathrm{in}}} = 10 \log_{10} \frac{1 - \cos(2\Delta k_1 H_T L)}{2}. \tag{4.16}$$

It is noteworthy that the common mode wavenumber k_C is vanished in Fig.4.16, and the system has no temperature sensitivity. This is the trick of DSWC and the temperature feedback circuit is no longer required.

4.2.2 Robustness to Temperature Drift

Temperature stability of the DSWC was experimentally demonstrated. Transmission properties of two circuits are measured by the 4 port VNA (KEYSIGHT, E5071C). A testing field H_T was applied by using the Helmholtz coil. The setup was constructed in the thermostat chamber to control the ambient temperature. The DSWC was fabricated

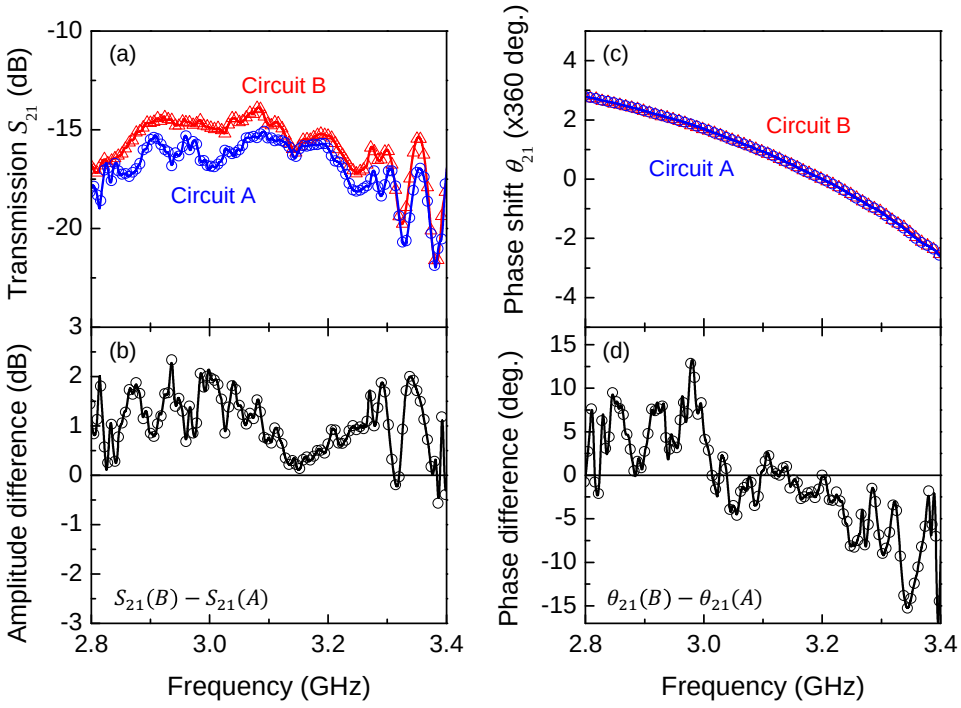

Figure 4.15 Transmission properties of DSWC. (a) Transmission S_{21} spectra of independent circuits. (b) Deviation of S_{21}. (c) Phase θ_{21} spectra of independent circuits. (d) Deviation of θ_{21}. Blue circles (red triangles) represent properties of circuit A (B). Black circles represent a deviation of transmission properties.

by combining two transducers composed of MSL antennas separated by $L = 5$ mm. A 110 μm-thick YIG film was used for the waveguide of each circuit. The phonograph of the prototype device is shown in Fig.4.14. To achieve anti-parallel H_0 configuration, two neodymium iron boron magnets were installed inside the base made of copper-zinc alloy. In this setup, the consistent intensity of H_0 is required as well as anti-parallel direction. Therefore positions of these magnets were precisely aligned by screw positioners. In the photograph, port 1 denotes an input port, and port 2 denotes an output port. A location of these ports was reversed between the circuit A and B, because coupling efficiency of DE-SWs depend on the direction of H_0, i.e. nonreciprocal property.

First, transmission properties of the circuit A and B at $H_T = 0$ were measured. The results are shown in Fig.4.15. Since measured signals should be totally common mode in this case, it was expected to have the consistent transmission properties for the circuit A and B. However, some deviations from the ideal condition such as imperfection of magnetic field alignment and slight mismatch of YIG qualities caused discrepancy in these spectra. The deviation was defined both for the amplitude $S_{21}(B) - S_{21}(A)$ (Fig.4.15b) and phase $\theta_{21}(B) - \theta_{21}(A)$ (Fig.4.15d). The deviation of amplitude was within ±3 dB, and the error of phase was within ±15 deg. According to Eq.4.11, deviation of phase

can be compensated by extra phase modulation θ_{ofs}, and that of amplitude could be compensated by microwave attenuators. However, deviations of these parameters were completely frequency dependent and the balance of these signal would be easily broken by the dispersion shift due to either H_T or ΔM. Therefore the evaluation of device performance by the superposed amplitude of output signals from the circuit A and B was difficult with the fabricated device. Instead of using the superposed amplitude, phase rotation of each circuit was independently measured by the vector network analyzer to confirm the principle of DSWC. In this approach, a testing field H_T was appeared as the phase shift of $2\Delta k_1 H_T L$.

Temperature dependence was measured in the temperature range from 30°C to 45°C under $H_T = 0$ Oe, and magnetic field dependence was measured at $T = 36.0$°C. These results are shown in Fig.4.16. When the temperature was varied, the phases of the circuit A and B were equally drifted, because the ΔM dependent shift was appeared as common mode. On the other hand, the phases of the circuit A and B were oppositely drifted when H_T was applied, because H_T dependent shift was appeared as normal mode. Therefore the basic principle of DSWC was successfully demonstrated.

The performance of DSWC was further investigated in detail. Temperature and magnetic field dependences were again measured with the resolution of 1°C and 0.2 Oe, respectively. The results were evaluated as the phase difference (DSWC) and the averaged phase of each circuit. The result is shown in Fig.4.17. As shown in Fig.4.17a, the phase difference of the circuit A and B was quite stable against to the temperature drift. This sensitivity was estimated as -9.5×10^{-3} deg./°C, while a single circuit exhibited the sensitivity of -20 deg./°C. The result yielded the differential operation can suppress the effect of temperature drift by a factor of 2,100 compared to the single circuit operation. The remaining finite temperature sensitivity would be due to the imperfection of the fabrication. Temperature imbalance between waveguides were another possibility, since two waveguides were physically separated and had no contact to the heat bath. Under the temperature imbalance, k_2 in Eq.4.11 was no longer appeared as common mode, and the common mode rejection ratio (CMRR) of the circuit was degraded. Because the target H_T comparable to the biomagnetic field was quite tiny amount, the CMRR should be increased as high as possible.

On the other hand, in Fig.4.17b, the output phase dependence on magnetic field is also graphed. While temperature dependence was clearly suppressed, the phase difference was linearly increased for H_T. Therefore DSWC can selectively observe the magnetic field dependent signal. In addition, magnetic field dependence was doubled to that of the single circuit, yielded the sensitivity of 20.6 deg./Oe. This result supported the prediction of the response given by $2\Delta k_1 H_T L$. From the observed sensitivity, the parameter of normal mode wavenumber shift $\Delta k_1 = 35.9$ rad.$(\mathrm{m{\cdot}Oe})^{-1}$ was obtained.

According to the original concept of DSWC, the final output is given by the amplitude of superposed wave. Thus performance of the DSWC without spectral deviation was virtually estimated with the obtained Δk_1. For comparison with magnonic microcavities,

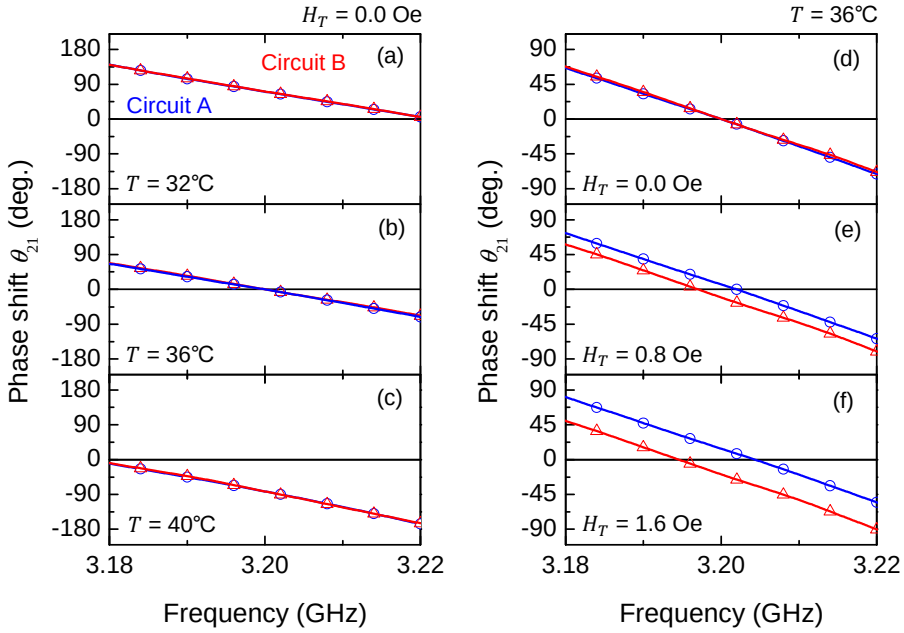

Figure 4.16 Demonstration of DSWC. Temperature dependence of phase properties (a) at $T = 32.0$°C, (b) at $T = 36$°C, and (c) at $T = 40$°C. Magnetic field dependence of phase properties (d) at $H_T = 0$ Oe, (e) at $H_T = 0.8$ Oe, and (f) $H_T = 1.6$ Oe. Blue circles (red triangles) represent the phase of the circuit A (B).

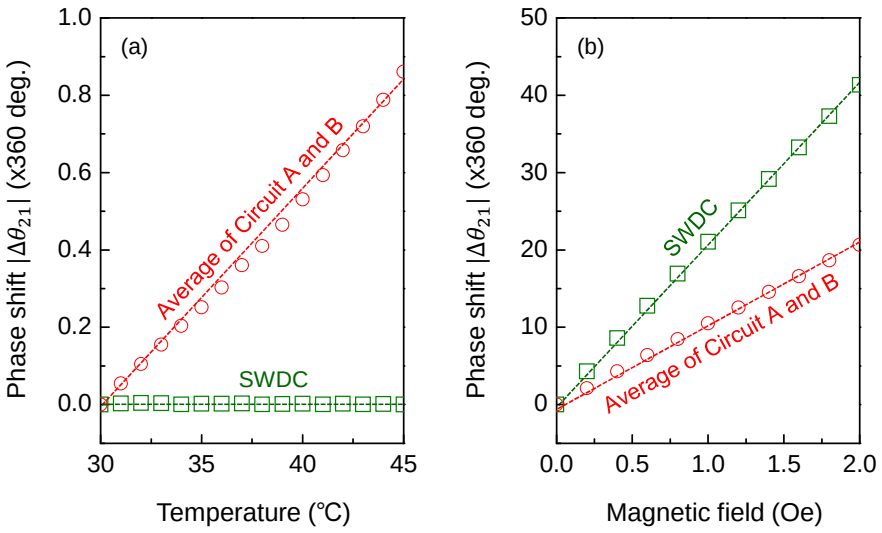

Figure 4.17 Performance of DSWC. (a) Temperature T dependence of the output phases. (b) Testing field H_T dependence of the output phases. Green squares represent a phase difference of the circuit A and B, namely DSWC. Red circles represent an averaged phase of the circuit A and B. Resulting phase is evaluated in absolute values because the circuit A and B exhibit output in reversed polarity to H_T.

Eq.4.16 was rewritten as the sensitivity ΔS_{OI}.

$$\frac{\partial S_{OI}}{\partial H_T} = 8.68\Delta k_1 L \frac{\sin(2\Delta k_1 L H_T)}{1-\cos(2\Delta k_1 L H_T)}. \tag{4.17}$$

In the case of magnonic microcavities, a sensitivity $\partial S_{21}/\partial H_T$ was constant for the specific N. Therefore ΔS_{21} was drastically reduced at fine H_T region. On the other hand, Eq.4.17 exhibited the sensitivity depending on H_T. When $H_T = 10^{-6}$ Oe is given, Eq.4.17 shows a value of 8.68×10^6 dB/Oe. This performance is several order of magnitude larger than the magnonic microcavity with $N = 22$. For small variation of H_T around 10^{-6} Oe, the value of ΔS_{OI} can be approximated as

$$\Delta S_{\mathrm{OI}} = 8.68 \times 10^6 H_T = 8.68 \quad [\mathrm{dB}]. \tag{4.18}$$

The value of ΔS_{21} of the magnonic microcavity with $N = 22$ was 1.80×10^{-3} dB at the same calculation condition. Therefore the DSWC is capable of remaining a gigantic signal change even in the finer H_T region. However, the demonstrated device included a finite amplitude mismatch within ± 3 dB as shown in Fig.4.15b, such ideal performance cannot be directly extracted, and finite temperature sensitivity was still confirmed due to the reduced CMRR.

In the future, microfabrication and integration of the structure will help to suppress the temperature imbalance and inhomogeneity of the film quality, yielding in the increase of CMRR. In the integrated device, the anti-parallel H_0 configuration of importance would be hardly achieved due to the difficulty of integration of magnetic closed circuit. Instead of using magnetic closed circuit, use of natural magnetic domain structures such as closure domains,[140,141] or magnetic vortex cores[142,143] might be useful for the integration. In the viewpoint of the sensitivity, enhancement of Δk_1 is important. Since Δk_1 is directly connected to the band structure of SWs, AMLs can contribute in this manner.

4.3 Summary

In this chapter, magnetic field sensors using the magnetic field dependence of SWs were intensively investigated. The main mission of this chapter is to review the prospect of AMLs as a magnetic field sensor, by investigating the magnetic field dependence and temperature dependence. The minimum resolution of 10^{-6} Oe is considered as the boundary of high sensitive sensor which is capable of the biomagnetic field measurement.

In §4.1, AML-based magnetic field sensor was presented. Since steep S_{21} change in the vicinity of the localized peak gave a large ΔS_{21}, high sensitivity was expected. In the calculation by the matrix approach method, the minimum resolution of AML-based magnetic field sensor was proportional to the periodic number N. In the experiment, the microcavity with $L_M = 213$ μm, $L_A = 193$ μm, and $L_M = 386$ μm composed of

110-μm thick YIG was tested. The resulting resolution was 10^{-4} Oe with the best effort, and reliable zone was limited over 10^{-2} Oe. The deviation from the calculation was caused by the contribution of Gaussian noise, since the intensity of the localized peak was attenuated by the poor coupling with MSL antennas and the spin relaxation within the defect layer. Demagnetizing effect also degraded the sensitivity. These factors limited the resolution of AML-based magnetic field sensors. Obtained sensitivity was just comparable to typical Hall sensors, which was still far from the sensitive sensor. In addition, the large temperature drift was the fundamental drawback of the AML-based sensor. Temperature feedback as the compensation magnetic field was rather effective, but only functional in the limited environment. Therefore outstanding performance was not confirmed compared to other magnetic field sensors.

In §4.2, differential operation was introduced by SWDs, namely DSWC, to overcome the drawback of temperature drift. In DSWC, two YIG waveguides are oppositely magnetized to have H_T dependent signal shift as normal mode. Such attempt was new in this field, thus the basic principle was mathematically proofed and the effect of temperature drift was not appeared in the given output. The prototype device was fabricated by the combination of two transducers, and the validity of idea was also experimentally confirmed. The prototype device exhibited a mismatch of the transmission intensities between two waveguides within ±3 dB. In the experiment, two waveguides were separately measured and performance was calculated at the post process. Obtained phase shift for H_T was 20.6 deg./Oe, while temperature drift was suppressed in -9.5×10^{-3} deg./°C. Therefore the differential operation was experimentally demonstrated. Furthermore, if two waveguides exhibited totally consistent properties, DSWC could exhibit gigantic signal change of 8.68×10^6 dB/Oe at $H_T = 10^{-6}$ Oe. Thus DSWCs showed prospect as a sensitive magnetic field sensor, but the magnetic field resolution was not directly investigated due to the difficulty of the device fabrication with the perfect matching of transmission properties of two waveguides.

Unfortunately, predominance of SWDs as a magnetic field sensor could not be shown. However, obtained aspects of magnetic field and temperature sensitivity of SWs, and related measurement techniques are rather utilized in the following investigation of wave-oriented logic elements.

Chapter 5

Spin Wave Interferometer

In this chapter, SW interferometers using FV-SW are presented. Such interferometers become a key component of wave-oriented logic element, since SWs encode information in their phase, and process information via interference. In §5.1, 2 wave interferometry with a liner waveguide is investigated. Effect of the FV-SW backscattering at the waveguide ends is further discussed. Based on earlier reports, two different approaches were tested to suppress this backscattering. In §5.2, SW termination by roughened surfaces is studied, in which such roughness is expected to induce additional scattering effect. In §5.3, SW termination by metalized surfaces with thin gold is studied. The mechanism of termination is investigated in detail. Finally, SW terminators composed of thin gold is combined to the linear waveguide, and robust 2 wave interferometry against a change of bias magnetic field is demonstrated in §5.4.

5.1 Spin Wave Interference

5.1.1 Motivation

Wave-oriented logic elements work on the basis of superposition of waves in interferometers, in which the tunability of magnonic band structures becomes the powerful advantage. In principle, majority function with multiple fan-in and fan-out can be efficiently implemented by using interferometers.[144] Nevertheless, there is a few experimental reports of such interferometers in the field of magnonics. Previously, 2 wave interferometry of SWs were investigated by several groups with in-plane magnetized configuration.[35,39,145] Such configuration is preferable in the viewpoint of bias magnetic field H_0, because the perpendicular magnetized configuration requires stronger H_0 due to the shape magnetic anisotropy, especially in the ferromagnetic metals like CoFeB and Ni-Fe. However, as discussed in §3.1, in-plane magnetized configuration exhibits strong anisotropy on the dispersion curve, and the phase information is propagation angle dependent. Thus in the viewpoint of phase information, utilization of the perpendicular magnetized configuration is rather preferable than that of in-plane magnetization. It is worth to note that the YIG waveguides can be easily magnetized perpendicularly thanks

to its small saturation magnetization of $5\mu_B \sim 1760$ G, and FV-SWs have an isotropic dispersion curve.

Based on above discussion, SW interferometers with the perpendicular magnetized configuration are worth to be studied. In this configuration, FV-SWs are excited in the waveguide. Even though FV-SWs have an advantage of the isotropic dispersion curve, SWDs utilizing the mode are rather minor. Thus in this chapter, 2 wave interferometry of FV-SWs is experimentally demonstrated, and the aspect of FV-SWs in the SWDs is also investigated.

5.1.2 Interference Experiment

In the experiment, 2 wave interferometry of FV-SWs is investigated with different injection phases. The entire setup is shown in Fig.5.1a. Injection amplitudes and phases were controlled in the external microwave circuit. Microwave signal of the excitation frequency at 4 GHz was generated from the signal generator (Keithley, E8257C). This signal was divided into two microwave signals and the injection phase of signal S_1 was modulated by the mechanical phase shifter (P1608DRE, Advanced Technical Materials). An extra insertion loss due to the phase shifter was compensated by microwave attenuators #1 and #2. Input signals were monochromatic and adjusted to have the same amplitude A_0. Therefore input waveforms S_1 and S_2 can be written as

$$\begin{aligned} S_1 &= A_0 \sin(\omega t + \xi' + \theta_1) \\ S_2 &= A_0 \sin(\omega t + \theta_2) \end{aligned} , \tag{5.1}$$

where ξ' is the controllable phase shift by the phase shifter, and θ_1 and θ_2 are the phase offset given by input microwave circuits. Generally, $\theta_1 \neq \theta_2$ is appeared unless special equipment, e.g. phase matched cable, is employed. In the experimental setup, arbitrary deskewing was possible by adjusting ξ'. When $\xi' = \theta_2 - \theta_1 + \xi$ was given, Eq.5.1 can be rewritten by

$$\begin{aligned} S_1 &= A_0 \sin(\omega t + \xi + \theta_2) \\ S_2 &= A_0 \sin(\omega t + \theta_2) \end{aligned} . \tag{5.2}$$

These signals were injected in the YIG waveguide via MSL antennas, as shown in Fig.5.1b. Resulting wave was detected beneath the central antenna and the output signal S_0 was given. The output peak-peak amplitude V_{pp} was observed by the oscilloscope (Tektronix, TDS8000B). Superposition of Eq.5.2 yields of the resulting V_{pp} as the function of ξ. This is given by

$$V_{\mathrm{pp}} = 2\sqrt{2}A_0 \Big(1 + \cos(\xi)\Big)^{1/2}. \tag{5.3}$$

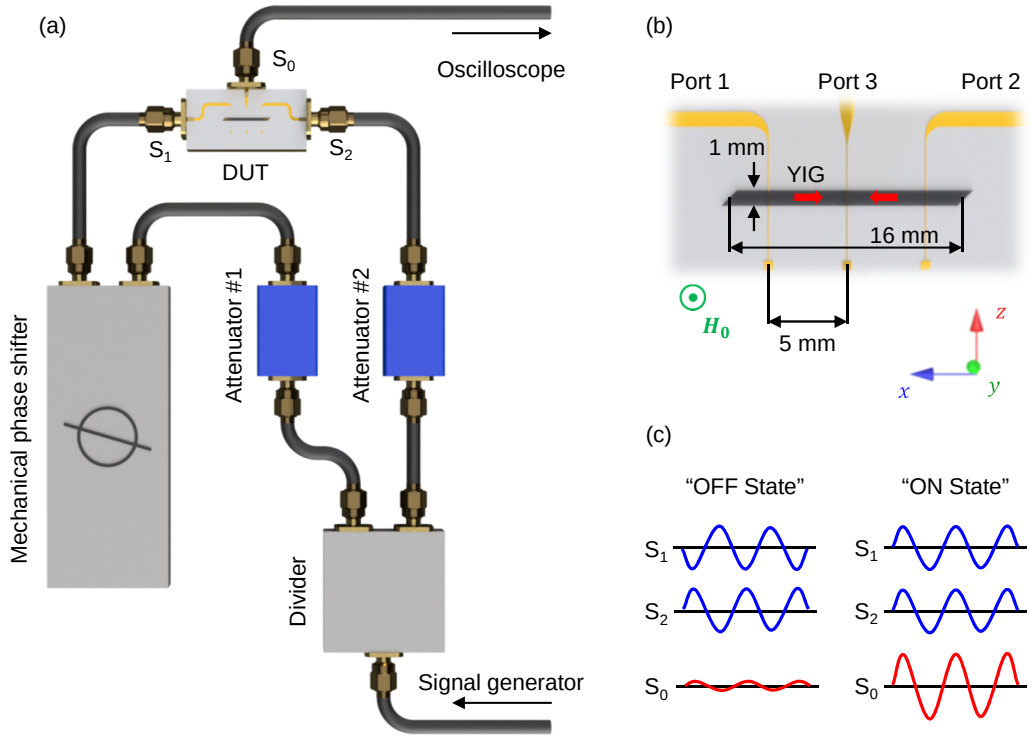

Figure 5.1 Schematic drawing of 2 wave interference of FV-SWs. (a) Experimental setup. Device under test (DUT) represents the interferometer, and injected microwave signals S_1 and S_2 are shaped by external microwave circuit. Output signal S_0 is observed by the oscilloscope. (b) Detail of the DUT. A linear waveguide composed of 18.4 μm-thick YIG is located on the MSL antennas. (c) Principle of operation. Destructive and constructive interferences are represented as OFF and ON state, respectively.

This calculation can be justified unless nonlinear phenomena are induced with a large input power. In the experiment, the input power to DUT was less than 1 mW, which was enough smaller than the nonlinear excitation region.[146] Therefore when $\xi = 0$ (in-phase), V_{pp} takes the maximum value of $4A_0$. When $\xi = \pi$ (anti-phase), V_{pp} takes the minimum value of 0. These special ξ condition are defined as "ON" state and "OFF" state, respectively (Fig.5.1c).

In the experiment, 18.4 μm-thick YIG was used as a waveguide. YIG was cut into 1 mm-wide and 16 mm-long parallelogram shape with an edge angle of 45° to form the waveguide. This waveguide was perpendicularly magnetized by the electromagnet with a bias magnetic field $H_0 = 3050$ Oe, and the accompanying demagnetizing field $H_d = 1682$ Oe was assumed. During the measurements, temperature of the DUT was controlled to be 40°C and the input signals with peak-peak voltage of 200 mV were given. Output voltage was measured by changing ξ with a step of 10°. Experimental result is shown in Fig.5.2a. As expected, V_{pp} was maximized at in-phase condition and minimized at

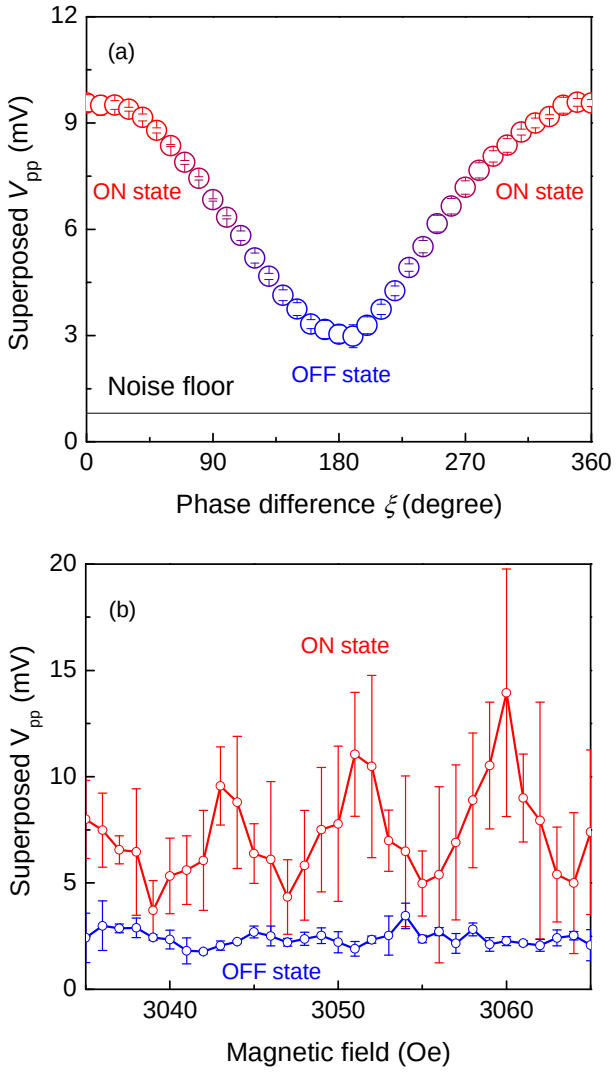

Figure 5.2 Amplitude of the superposed output wave $V_{\rm pp}$ detected at port 3 versus (a) the phase difference ξ between two injected waves, and (b) bias magnetic field H_0. Error bars correspond to the standard deviation of five repeated measurements.

anti-phase condition. Output voltages were $V_{\rm ON} = 9.56 \pm 0.24$ mV and $V_{\rm OFF}$ 3.04 ± 0.25 mV at ON state and OFF state, respectively. Consequently the isolation ratio, defined as the ratio of these amplitudes, was 9.95 dB.

As in the previous chapter, SWs are sensitive to H_0 as applicable to magnetic field sensors. However, H_0 dependence causes the instability of operation in logic elements. Therefore it is important to evaluate stability of ON and OFF states against H_0 deviation. The intensity of H_0 was swept from 3035 Oe to 3065 Oe by 1 ± 0.1 Oe steps. Output voltage was measured at ON state and OFF state. The result is shown in Fig.5.2b.

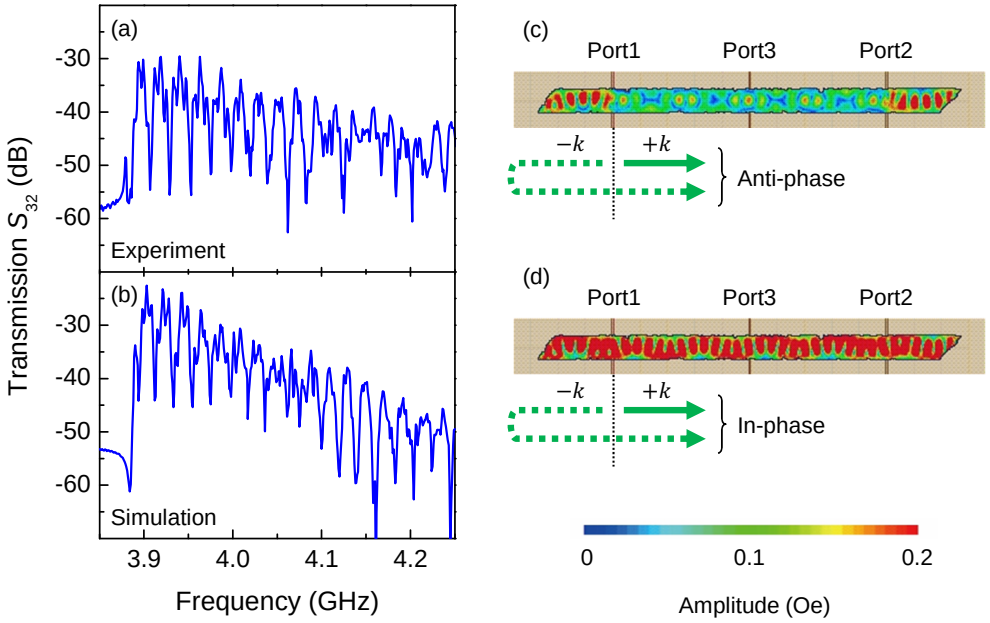

Figure 5.3 (a) Transmission properties from port2 to port3 in experiment under $H_0 = 3050$ Oe. (b) Result of electromagnetic simulated with an effective field of $H_0 - H_d = 1368$ Oe. Field distributions inside the waveguide are obtained from the result of electromagnetic simulation (c) at 3.998 GHz (ripple bottom) and (d) at 4.001 GHz (ripple top). Color represents the intensity of FV-SW.

Signal level of V_{ON} and V_{OFF} exhibited strong dependence on H_0. At certain H_0, ON and OFF states were no longer distinguishable. This instability limited the use of the SW interferometer at the laboratory environment and thus the suppression of this deviation was the primary issue.

5.1.3 Reflected Spin Waves and Transmission Ripple

To investigate the reason of H_0 instability, transmission spectrum from the input port2 to the output port3 of the waveguide was measured by the vector network analyzer (Anritsu, 37347C). In addition, the transmission spectrum was also calculated by the electromagnetic simulation (ANSYS HFSS ver.15.0). As shown in Fig.5.3a, the ripples similar to that of simulation result shown in Fig.5.3b was observed. Since the simulation showed good accordance with the experimental result, FV-SW distributions inside the waveguide were further investigated by the simulation at different frequencies. The field distributions inside the waveguide, where SWs were excited from the input port 1 and port 2, are shown for the bottom of ripple (3.998 GHz) and the top of ripple (4.001 GHz) in Fig.5.3c and d, respectively. Although the injected SWs were in-phase at both frequencies, remarkable difference of the distribution can be seen. At the bottom of ripple,

the intensity of injected FV-SWs was drastically decreased between the port 1 and port 2, and the strong standing modes were confirmed between input ports and waveguide ends. On the other hand, at the top of ripple, such standing mode was formed within the entire waveguide. The difference of the distribution was caused by the change of wavelength depending on H_0. The excitation at an input port generates two SW flows inward ($+k$) and outward ($-k$) in a direction to the output port 3. This $-k$ emission was backscattered at the waveguide end, and regenerated in the flow of $+k$ emission. Phase difference of the original $+k$ emission and the backscattered $-k$ emission was depending on the waveguide length and wavelength. In Fig.5.3c, the backscattered $-k$ emission seemed to become anti-phase, and resulting injection to the port 3 was canceled out. In contrast to this, in Fig.5.3d, the backscattered $-k$ emission seemed to become in-phase, and resulting injection to the port 3 was enhanced. Because of the extra interference of $-k$ and $+k$ emissions, the net power flow from an input port to the detection port 3 became frequency dependent. Since a wavenumber is depending on the magnetic field H_0 as well as excitation frequency, such change of the net power flow would be caused against to H_0. These discussions were in the case of in-phase condition, namely ON state. In the case of OFF state, input waves became destructive regardless of the backscattered wave. Therefore a large deviation of signal level was observed only in the ON state.

Based on this explanation, transmission ripples observed in the experiment can be eliminated by terminating SW at waveguide ends. In the case of in-plane magnetized configuration, such termination can be easily achieved by the tapered waveguide end. However, this approach was no longer valid in the perpendicular magnetized configuration, because two-magnon scattering was hardly appeared due to the isotropic dispersion of FV-SWs. Fortunately, there are earlier works on the purpose of FV-SW termination, e.g. J. H. Collins *et al.* reported the FV-SW termination by using a roughened waveguide surface,[147] and J. Adam reported the FV-SW termination realized by placing 500 Å thick aluminum close to the surface of YIG.[148] These methods were investigated separately, and the applicability to the FV-SW interferometer is discussed in the following sections.

5.2 Spin Wave Termination by Surface Roughness

5.2.1 Waveguide Termination

In the experiment, 110 μm-thick YIG was cut into a 20 mm-long and 1.3 mm-wide rectangular shape as waveguides. Following the paper from J. H. Collins *et al.*,[147] surfaces of both ends of waveguide were roughened by the sandpaper with #600-grid. This mechanical scratching induced the surface roughness R_a. The value of R_a was measured by using the stylus profilemeter (Ryokosha Corp., ET4000). The R_a of bare surface of the waveguide was about 0.1 nm, while termination part was about 118 nm. This waveguide was placed on the transducer as shown in Fig.5.4a. Transmission spectra S_{21} of waveguides were measured by the vector network analyzer (Anritsu, 37347C), with applying $H_0 = 2100$ Oe perpendicular to the surface for the excitation of FV-SWs.

Measured S_{21} are shown in Fig.5.4b and c for without and with the roughening,

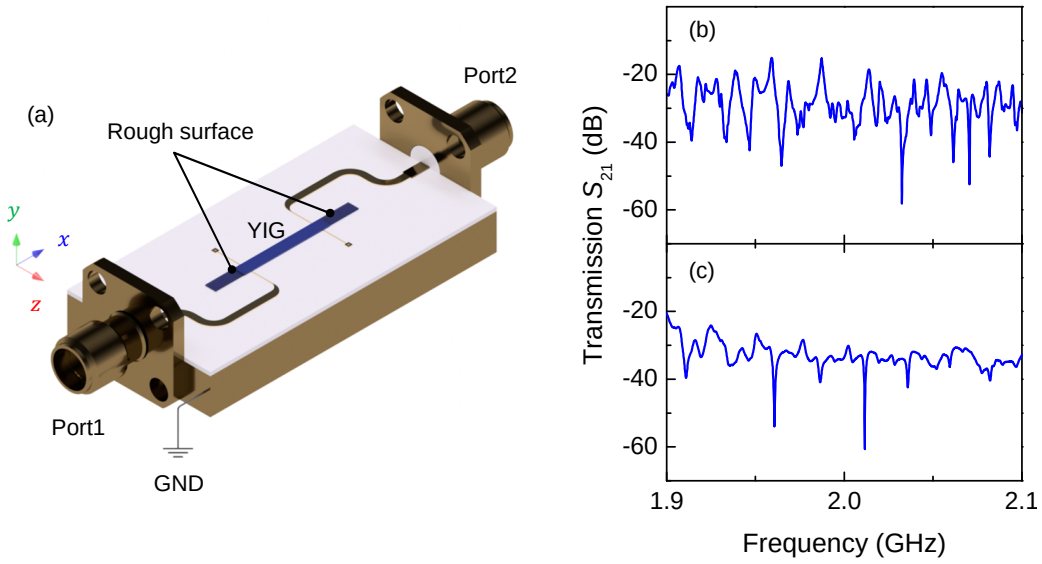

Figure 5.4 Suppression of transmission ripple by roughening of waveguide ends. (a) Schematic drawing of 2 port transducer. 110 μm-thick YIG was located on the dielectric substrate. Observed transmission spectra S_{21} of the waveguide with (b) bare surface waveguide end and (c) roughened surface waveguide end. Magnetic field $H_0 = 2100$ Oe is applied.

respectively. Transmission ripples was slightly suppressed with the roughening. To evaluate the degree of rippling, a standard deviation σS_{21} was evaluated for the data points from 1.9 GHz to 2.1 GHz. Without roughening the standard deviation of the ripple was $\sigma S_{21} = 5.79$ dB, while with roughening that was $\sigma S_{21} = 3.66$ dB. The termination effect was clearly visible, but further reduction of σS_{21} was required. Following Eq.5.3, the resulting output $V_{\rm pp}$ becomes 0 when $\xi = \pi$ (OFF state). On the other hand, that of $\xi = 0$ (ON state) becomes $V_{\rm pp} = 4A_0$, where $2A_0$ is an input voltage in peak to peak. According to the previous discussion for Fig.5.3, the net power flow towards the output port 3 was frequency or magnetic field dependent, and yielded σS_{21} in the transmission spectra. Therefore the amplitude of A_0 determining the level of ON state was also deviated proportional to σS_{21}. When the threshold value of $V_{\rm pp}$ for the ON and OFF states is given as a 50% of the ON state level, the transmission ripples should be $\sigma S_{21} < 3$ dB to ensure the ON level output overcoming the threshold.

The origin of termination effect was considered as the scattering of SWs at the surface defects, and this scattering was expected to result in the extra momentum relaxation.[149,150] In earlier studies, such relaxation mechanisms have been investigated both experimentally and theoretically.[65,151,152] Following these reports, the degree of relaxation was quantitatively evaluated in next part to obtain the aspect of termination.

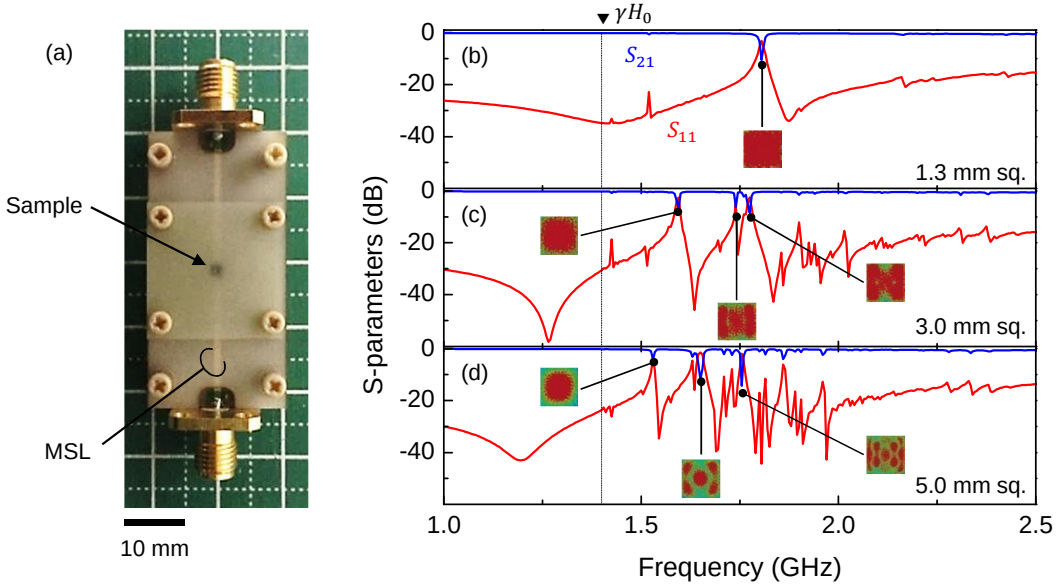

Figure 5.5 Construction of homemade VNA-FMR setup. (a) photograph of DUT. Ferromagnetic sample is located on the 50 Ω-matched MSL. Position of the sample is precisely aligned by the dielectric guides made of FR-4. Calculated S-parameters of samples with different lengths of sides of (b) 1.3 mm, (c) 3.0 mm and (d) 5.0 mm. Insets represent the amplitude of magnetization precession within the sample at notable absorption peaks of S_{21}. Red color indicates stronger excitation. All calculation is under $H_0 = 500$ Oe. Typical physical parameters of YIG are set in the measured sample.

5.2.2 Construction of Ferromagnetic Resonance Setup

The evaluation of momentum relaxation is just to measure the FMR linewidth ΔH or Gilbert damping α, and the FMR measurement is the powerful tool to investigate these properties. In this part, a homemade FMR measurement setup was constructed, and the effect of the roughening to FMR spectra was investigated.

There are two major techniques to measure FMR spectra. So called cavity FMR technique uses a microwave cavity for the measurement.[153] Microwave cavities are usually designed for a specific frequency, thus the bias magnetic field H_0 is swept during the measurement. Obtained signal is enhanced by the Q-factor of the microwave cavity, thus fine spectra can be observed. However, this technique requires a large electromagnet to apply homogeneous H_0 to the microwave cavity. Another technique is often called VNA-FMR, where planar antennas are used for the measurement.[79] Such planar antennas are capable of the broadband excitation, thus frequency is swept rather than H_0. Since these antennas can be formed on a small dielectric substrate, the setup can be easily implemented with inexpensive equipment. Therefore the VNA-FMR setup was employed in this study.

There are two major techniques to measure FMR spectra. So called cavity FMR technique uses a microwave cavity for the measurement.[153] Microwave cavities are usually designed for a specific frequency, thus H_0 is swept during the measurement. Obtained signal is enhanced by the Q-factor of the microwave cavity, thus fine spectra can be observed. However, this technique requires a large electromagnet to apply homogeneous H_0 to the microwave cavity. Another technique is often called VNA-FMR, where planar antennas are used for the measurement.[79] Such planar antennas are capable of the broadband excitation, thus frequency is swept under the constant H_0. Since these antennas can be formed on a small dielectric substrate, the setup can be easily implemented with inexpensive equipment. Therefore the VNA-FMR setup was employed in this study.

In Fig.5.5a, a photograph of the DUT for VNA-FMR setup is shown. Ferromagnetic sample is placed at the center of the 50 Ω-matched through line. The position of the sample was aligned by the dielectric guides made of FR-4, and fixed by screws. As explained in §2.2, planar antennas give the inhomogeneous excitation, in which $k = 0$ is not included. The primary excitation of the MSL was $k \sim 1.76 \times 10^3$ m^{-1}. Thus FV-SWs are excited in the sample, and numbers of accompanying standing modes contribute to the spectrum. To obtain clear spectra, the lateral length of the sample should be precisely chosen: the length of the sample is sufficiently long to overcome the attenuation length of FV-SWs, or sufficiently short to suppress multiple resonance. Therefore, the dependence of the spectra on the sample geometry was evaluated by the electromagnetic simulation (ANSYS HFSS ver.15.0).

The results are shown in Fig.5.5b-d for square samples with a side length of 1.3 mm, 3.0 mm, and 5.0 mm. In these graphs, transmission spectra S_{21} and reflection spectra S_{11} were displayed as blue and red curves, respectively. In S_{11} spectra, numbers of remarkable peaks can be seen. Since a reflection of the electromagnetic waves was caused at the discontinuous point of characteristic impedance, where the dielectric constant or permeability constant was changed, S_{11} spectra included the information of dielectric constant as well as the permeability constant of interest. On the other hand, small dips in S_{21} spectra represent the absorption of propagating electromagnetic waves by the magnetization dynamics. Of course S_{11} spectra were also important for the precise analysis, but small dips in S_{21} spectra were rather focused because the spectra directly represents the magnetization dynamics. Distributions of the precession amplitude within the sample were also calculated at the frequency where notable dips were appeared in S_{21} spectra. These results are also overlaid as inset pictures.

Since YIG is the material with quite small damping, its attenuation length is also drastically extended. The 5.0 mm sq. sample still exhibited many resonance peaks, further extension of the sample size was difficult due to the setup. The theoretical FMR frequency can be derived by γH_0, corresponding to 1.4 GHz in this calculation. The frequency position was noted by the dotted line. In all sample geometries, pure FMR signal was not obtained due to $k > 0$ excitation of the MSL antenna. Therefore all resonance peaks were caused by the FV-SW excitation. The strong peaks were appeared around 1.7 GHz. At this frequency, estimated k of the FV-SW was 2.69×10^3 m^{-1}. This was quite reasonable from the primary excitation of the MSL. In Fig.5.5c and d, notable peaks were

also appeared in the lower frequencies, because of the geometrical resonances of FV-SW. On the other hand, clear single peak was obtained with the 1.3 mm sq. sample. At this peak, the entire sample was homogeneously excited. Even though SWs were excited, the dip in S_{21} spectra reflected an absorption of microwave energy by the ferromagnetic system. Hereby a sample with 1.3 mm sq. was employed as a standard geometry of this setup. Of course the absorption spectrum was broadened by SW excitation. Such broadening effect belongs to the extrinsic contribution ΔH_0 as derived in Eq.2.46. Thus frequency linewidths of these peaks cannot directly represent the momentum relaxation of the ferromagnetic system.

More precisely, the measured spectra represent the behavior of electromagnetic wave propagating along the MSL. Its propagation constant under the bias magnetic field H_0, namely $\beta(H_0)$, at frequency f can be derived by

$$\beta(H_0) = \frac{2\pi f}{c_0}\sqrt{\tilde{\varepsilon_r}\tilde{\mu_r}(H_0)}, \tag{5.4}$$

where c_0 is speed of light in vacuum, $\tilde{\varepsilon_r}$ is relative permittivity, and $\tilde{\mu_r}(H_0)$ is relative permeability at magnetic field H_0. A value of $\tilde{\varepsilon_r}$ is almost constant at the measured frequencies. Therefore $\tilde{\mu_r}(H_0)$ of interest is given by

$$\tilde{\mu_r}(H_0) \propto \left(\frac{c_0}{2\pi f}\beta(H_0)\right)^2. \tag{5.5}$$

It is noteworthy that $\tilde{\mu_r}(H_0)$ spectra include the contribution of dielectric materials such as the gadolinium gallium garnet substrate and FR-4 substrate, since the YIG sample just partly occupies the space in the vicinity of the MSL. Therefore it is more reliable to use a complex magnetic susceptibility $\chi(H_0)$ instead. This can be given by

$$\chi(H_0) = \mu_r(H_0) - 1 \propto \tilde{\mu_r}(H_0) - \tilde{\mu_r}(H_{\mathrm{ref}}), \tag{5.6}$$

where $\mu_r(H_0)$ is the intrinsic permeability of the YIG sample. A magnetic field H_{ref} denote a reference field, in which the SW contribution is appeared at the outside of measured frequencies. At H_{ref}, observed spectra represent extra contribution due to dielectric materials independent of H_0. By subtracting $\tilde{\mu_r}(H_{\mathrm{ref}})$, pure contribution of the YIG sample can be extracted.

In addition, β measured by the VNA includes the extra contribution of the MSL, because the sample occupies just 1.3 mm of the entire MSL length. C. Bilzer *et al.* provided a method to exclude the extra contribution based on the transfer matrix approach. In this method, the S-parameter of the MSL without sample is used as a reference.[154] To perform this analysis, a full 2 port data set composed of S_{11}, S_{21}, S_{12}, and S_{22} was required. This approach was implemented in the system, and thus the obtained $\mu_r(H_0)$ spectra represent almost pure response of the ferromagnetic samples.

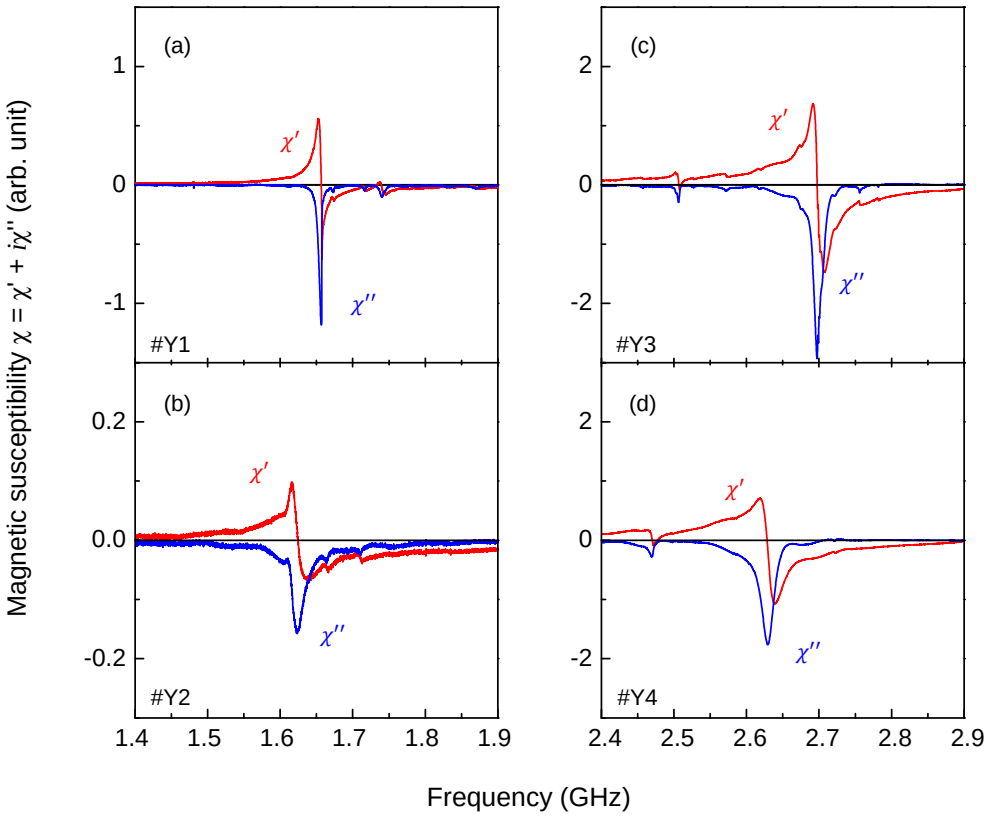

Figure 5.6 Measured χ spectra. (a) Sample #Y1, (b) Sample #Y2, (c) Sample #Y3 and (d) Sample #Y4. Red bold lines are real part and blue bold lines are imaginary part.

In the earlier report from J. H. Collins *et al.*,[147] the effect of surface roughness was investigated for the YIG film with a single thickness of 25μm. The termination effect might be caused by the scattering induced by the surface roughness, in which excited mode with wavenumber k might be scattered into other mode with wavenumber k'. Since k is thickness dependent in the dipolar interaction region, the difference of momentum relaxation in thickness is worth to be investigated. In Table5.1, prepared YIG samples for the FMR measurement are presented. To investigate the effect of film thickness, 10 μm-thick and 110 μm-thick YIG films were used. All samples were cut into 1.3 mm by

Table 5.1 Prepared YIG samples for FMR measurement

Sample	Thickness (μm)	R_a (nm)
#Y1	10	0.2
#Y2	10	94
#Y3	110	0.1
#Y4	110	118

1.3 mm square, and #Y2 and #Y4 were roughened by the sandpaper with #600-grid. As a result, comparable R_a was induced in roughened samples. FMR spectra were measured for these samples with $H_{\rm ref} = 3300$ Oe. Complex magnetic susceptibility spectra $\chi = \chi' + i\chi''$ at $H_0 = 2300$ Oe are shown in Fig.5.6. Measured spectra showed broadening of a peak in χ'' of #Y2 and #Y4, indicating the increase of FMR linewidth by roughening process. The value of χ'' at effective magnetic field $H_{\rm eff}$ can be expressed by[79]

$$\chi'' = \gamma^2 \frac{4\pi M_S \left(4\pi M_S + H_{\rm eff}\right)}{f_r^2 - f(f - i\Delta f)}, \tag{5.7}$$

where $f_r = \gamma H_{\rm eff}$ is the FMR frequency, and Δf is the frequency-swept linewidth. It should be emphasized that a magnetic field-swept linewidth ΔH is commonly used as a measure of momentum relaxation rather than Δf. Therefore the relationship of $\Delta H = \Delta f/\gamma$ were introduced for the conversion. According to Eq.5.7, the spectra χ'' were fit using Lorentzian function to extract values of Δf. Converted values of ΔH were given as 2.4 Oe (#Y1), 7.1 Oe (#Y2), 4.6 Oe (#Y3), and 6.7 Oe (#Y4), respectively. As expected, broadening of the resonance peaks due to the roughening process seemed to be slightly enhanced in 10 μm-thick samples. The f_r was down-shifted slightly by the roughening process, indicating the change of the demagnetization field, which is sensitive to the changes in film thickness.

5.2.3 Estimation of Damping Parameters

Observed damping ΔH is usually composed of the intrinsic term and extrinsic term as derived in Eq.2.46. The intrinsic term is given by the Gilbert damping α, and describing the momentum relaxation of uniform mode $k = 0$ into the lattice system, e.g. spin-orbit interaction. On the other hand, uniform mode is often scattered into other modes with finite k, and these modes are rapidly damped. In this manner, observed ΔH is broadened from the original resonance peak of the intrinsic process. This is a general picture of the extrinsic process, which is represented by ΔH_0. Therefore the parameter of ΔH_0 would represent the effect of roughness induced scattering. However, in this experiment, SWs with finite k was directly excited by the MSL antenna, thus extra contribution to ΔH_0 was superposed by the imperfection of experimental setup. To investigate relaxation process in more detail, the intrinsic process should be separated, and the extra ΔH_0 due to the SW excitation should be removed. Since ΔH is frequency dependent and the value of ΔH_0 is given as a dc-component, VNA-FMR was done with various H_0 to shift f_r. By comparing obtained ΔH_0 of the samples #Y1 and #Y2 (#Y3 and #Y4), the contributions of roughened surfaces can be extracted as the difference of ΔH_0.

In the experiment, H_0 was swept from 1200 Oe to 2500 Oe in 20 Oe increments. The results are shown in Fig.5.7. Obtained plots were linearly fit using Eq.2.46 and overlaid on the data points as the dotted lines. Large variation of data was observed in the lower-frequency region by the inhomogeneity of crystallographic field, giving small perturbation in $H_{\rm eff}$,[155,156] thus this region was ignored, and fit curves were determined

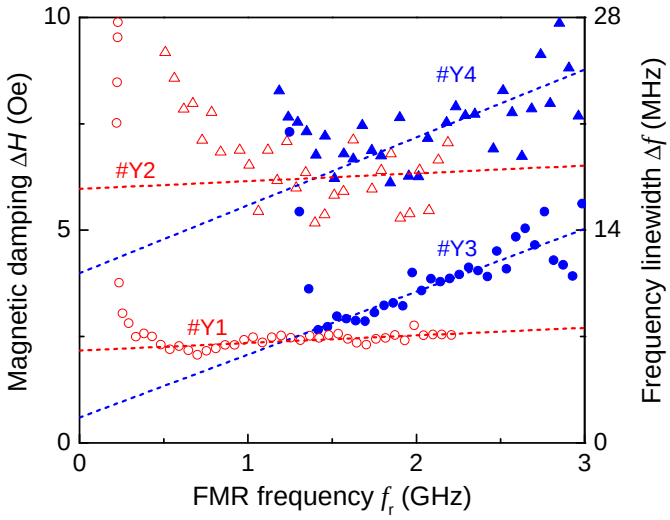

Figure 5.7 FMR frequency f_r dependence of ΔH. Triangles and circles correspond to polished and unpolished samples, respectively. Open and closed symbols represent 10- and 110 μm-thick samples, respectively. Dashed lines are linear fits determined using FMR frequency region f_r >1.5 GHz.

using f_r >1.5 GHz.

The slopes of the curves remain almost unchanged by the roughening process for both the 10- and 110 μm-thick samples. The resulting α and ΔH_0 values are listed in Table5.2. The large difference in α might be due to the difference between the qualities of the two crystals. The extrinsic process ΔH_0 was increased by the roughening process from 2.17 Oe to 5.97 Oe (+3.8 Oe) and from 0.59 Oe to 3.99 Oe (+3.4 Oe) for the 10- and 110 μm-thick samples, respectively. As expected, roughness induced scattering belongs to the extrinsic process. The scattering potential may be explained by the fluctuation in the effective magnetic field that is caused by the demagnetization effect, which was introduced by the surface defects in this case. Hence, ΔH_0 enhancements in the 10 μm-thick samples were larger than those in 110 μm-thick samples, because the modulation of demagnetization field introduced by the surface roughness would have more significantly affected the thinner films.

Table 5.2 Estimated damping parameters of 10- and 110 μm-thick YIG samples.

Sample	α	ΔH_0 (Oe)
#Y1	2.50×10^{-4}	2.17
#Y2	2.51×10^{-4}	5.97
#Y3	2.07×10^{-3}	0.59
#Y4	2.23×10^{-3}	3.99

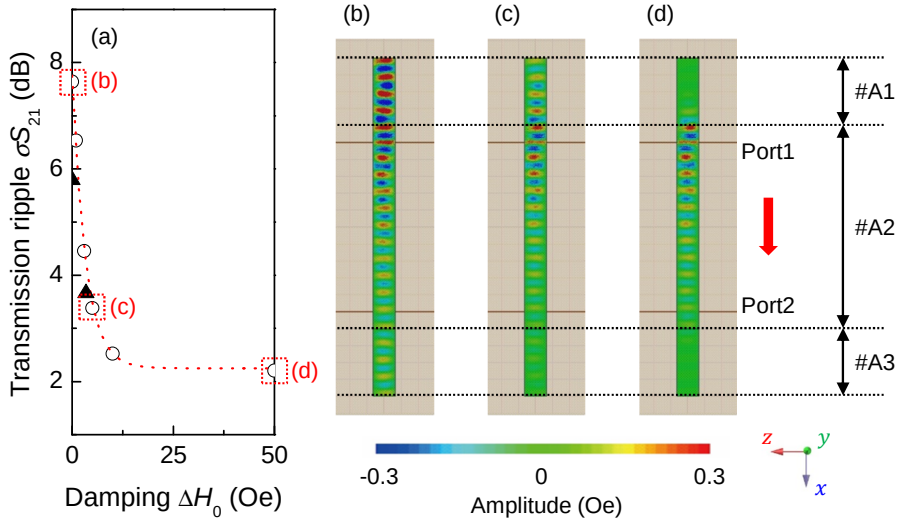

Figure 5.8 Simulation of transmission ripples with various ΔH_0. (a) ΔH_0 dependence of σS_{21} at frequencies ranging from 1.9 GHz to 2.1 GHz. Open circles represent simulated results, and closed triangles indicate experimental results. Dashed line is exponential fit. FV-SW distribution within the waveguide at 2 GHz with ΔH_0 values of (b) 1 Oe, (c) 5 Oe, and (d) 50 Oe. Finite ΔH_0 values were defined in regions #A1 and #A3. Color represents amplitude of FV-SW.

5.2.4 Estimation of Required Damping Value

The effect of the surface roughening with $R_a \sim 100$ nm was quantitatively estimated by VNA-FMR experiment. The reduction of ripples in Fig.5.4c can be explained by the increase in ΔH_0 of 3.4 Oe at waveguide ends. For further suppression of transmission ripples, the enhancement of ΔH_0 would be required. So the ΔH_0 dependence of the termination effect was estimated by using electromagnetic simulation (ANSYS HFSS ver.15.0).

The simulation model was the same as the experimental setup shown in Fig.5.4a except for SMA-type connectors. In this simulation, the waveguide had the typical electromagnetic properties of monocrystalline YIG with the thickness of 110 μm: $4\pi M_S =$ 1760 G, relative dielectric constant $\varepsilon_r = 15.3$, and $\gamma = 2.8$ MHz/Oe. From Table5.2, $\alpha = 2.07 \times 10^{-3}$ was employed. $H_{\text{eff}} = 500$ Oe was perpendicularly applied within the waveguide, so that FV-SWs propagated. In Fig.5.8b-d, both waveguide ends (#A1 and #A3) were set to have finite ΔH_0, while ΔH_0 was set to 0 in region #A2. Hence #A1 and #A3 represent the waveguide with the roughened surface. FV-SW was injected from the MSL on the #A1 side.

From the calculated spectra, the standard deviations of transmission ripples σS_{21} were calculated at frequencies ranging from 1.9 GHz to 2.1 GHz in the same manner. The result is shown in Fig.5.8a, as a function of ΔH_0. Experimentally obtained σS_{21}

for Fig.5.4b and c were overlaid in the plot as triangles. Experimental results exhibited similar termination effect with the calculation. In the plot, termination effect was saturated at higher ΔH_0 region, but there was still room to increase ΔH_0 to enhance the termination effect. In Fig.5.8b-d, the distributions of FV-SWs within the waveguide at 2 GHz were displayed. As ΔH_0 increased, the intensity of the backscattering in the region #A1 remarkably decreased. In Fig.5.8c, which is close to the experimental condition, the backscattered wave still exists in the region #A1.

To achieve $\sigma S_{21} < 3$ dB, $\Delta H_0 = 6.6$ Oe is required from the result of calculation. The value of $\Delta H_0 = 3.8$ Oe in 10 μm-thick samples with $R_a \sim 100$ nm, and the effect of the thickness was not drastic in this case. The value of R_a would affect the termination effect, but precise control of R_a by sandpapers is challenging. Chemical etching might be useful,[157] but termination by the roughened surface is not preferable in the viewpoint of device integration.

5.3 Spin Wave Termination by Thin-Metal Over Layer

5.3.1 Waveguide Termination

In the experiment, transmission spectra of FV-SWs propagating in 18.4 μm-thick YIG waveguides were measured. The waveguide used in the experiment was consistent with one used in §5.1. The surface of the waveguide was polished with $R_a = 0.4$ nm so that effects of resonant coupling with a perpendicular standing SWs or the roughness-induced scattering can be separated. Both waveguide ends were covered by a 30 nm-thick continuous gold layer with the same R_a, instead of using aluminum layer reported by J. D. Adam to prevent oxidation.[148] This gold layer was deposited by magnetron sputtering. A value of $\alpha = 2.35 \times 10^{-4}$ of this film was evaluated in advance, by using the VNA-FMR setup introduced in §5.2.

Transmission spectra were measured by using the 2 port transducer shown in Fig.5.9a. A bias magnetic field $H_0 = 3100$ Oe was applied along y-axis so that FV-SWs propagated along x-axis. In Fig.5.9b and c, the effect of the gold layer was obviously seen. Evaluated σS_{21} were 6.37 dB for the bare surface, and this value was reduced to 2.13 dB by the gold layer. The termination effect was much better than that of the roughened surface, and this process also has advantage in the ease of fabrication, and affinity with the device integration.

Comparable geometry was also reported in the field of spintronics.[70,158,159] So called spin pumping effect manifests at the interface between noble metals and the ferromagnetic system, yields of the extra damping α_{sp}. Since the effect directly deal with the torque of precession, given α_{sp} directly contributes to the intrinsic damping as $\alpha + \alpha_{\mathrm{sp}}$. A value of α_{sp} can be given by[160]

$$\alpha_{\mathrm{sp}} = \frac{g\mu_B}{4\pi M_S} g_{\uparrow\downarrow} \frac{1}{d}, \tag{5.8}$$

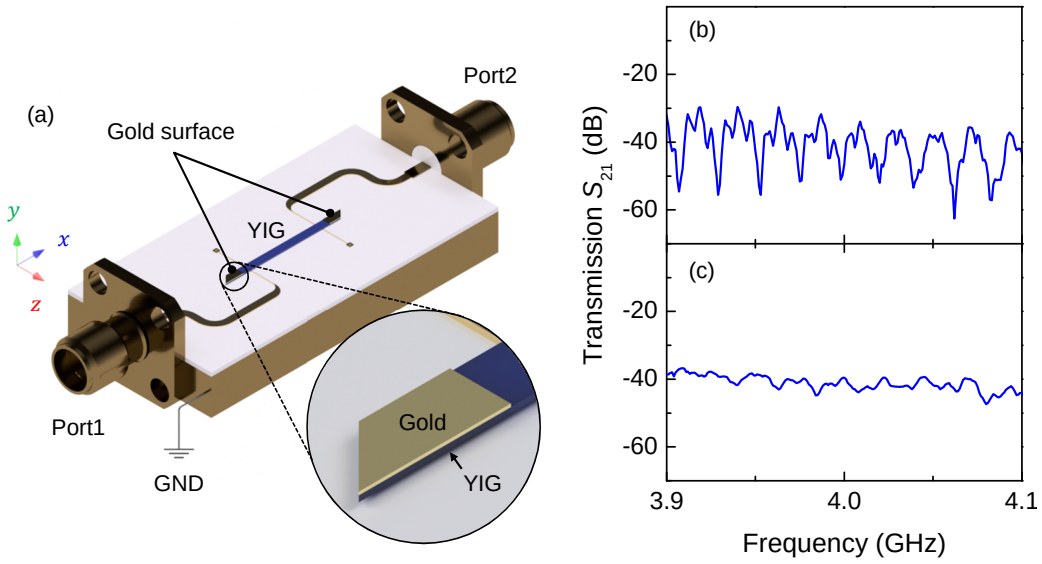

Figure 5.9 Suppression of transmission ripple by gold deposition on waveguide ends. (a) Schematic drawing of 2 port transducer. 18.4 μm-thick YIG was located on the dielectric substrate. Inset is the detail of the waveguide end. Observed transmission spectra S_{21} of the waveguide with (b) bare surface waveguide end and (c) gold surface waveguide end. Magnetic field $H_0 = 3050$ Oe is applied.

where g = 2 is the Landé g-factor, $\mu_B = 9.274 \times 10^{-21}$ erg/G is the Bohr magneton, $4\pi M_S = 1760$ G is the saturation magnetization of YIG, $g_{\uparrow\downarrow} = 1.2 \times 10^{14}$ cm^{-2} is the spin mixing conductance at the Au/YIG boundary,[161] and $d = 18.4$ μm is the waveguide thickness. Substitution of these values into Eq.5.8 gave $\alpha_{sp} = 6.87 \times 10^{-7}$. This value was much smaller than $\alpha = 2.35 \times 10^{-4}$ of the YIG film. Hence the spin pumping effect was less dominant in the experiment, because of the large d value. Such interfacial effects will be dominant in the nanometer thick films, and spin pumping cannot explain the termination effect. The origin can be considered more macroscopic, and FV-SW propagation in the Au/YIG slab is electromagnetically analyzed in later parts.

5.3.2 FV-SW Dispersion Curve in YIG with TMOL

In Fig.5.10, the model of analysis is displayed. YIG layer was covered by the thin-metal without dielectric gap. Unlike to the metalized slab shown in Fig.3.4, the thickness t_{Au} and conductivity σ of the thin-metal layer take finite values. Since AMLs were demonstrated with thick copper layers with finite σ in §3.2, a value of t_{Au} might be effective for the termination effect. Hereby the termination effect given by such thin-metal over layers is specially defined as TMOL.

According to the finite t_{Au} and σ, magnetostatic approximation is no longer avail-

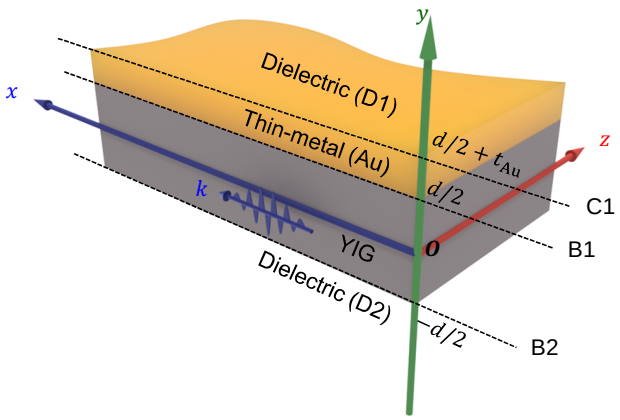

Figure 5.10 Model of YIG slab with thin-metal over layer. From the top, there are dielectric (D1) layer, thin-metal (Au) layer, YIG layer, and dielectric (D2) layer. SW propagates along x-axis. Boundary B1 is at $y = d/2$, B2 is at $y = -d/2$, and C1 is at $y = d/2 + t_{\mathrm{Au}}$, where d is the thickness of the slab and t_{Au} is the thickness of thin-metal.

able in the Au layer. Thus Maxwell equation with quasi-steady approximation becomes dominant equation in the layer, and effective boundary condition model was employed to bridge equations with the YIG layer and other dielectric layers where magnetostatic approximation was applied.[162] In the Au layer,

$$\boldsymbol{\nabla} \times \boldsymbol{H} = \frac{4\pi\sigma}{c_0}\boldsymbol{E}, \tag{5.9}$$

$$\boldsymbol{\nabla} \times \boldsymbol{E} = -\frac{i\omega}{c_0}\boldsymbol{h}, \tag{5.10}$$

$$\boldsymbol{\nabla} \cdot \boldsymbol{h} = 0. \tag{5.11}$$

Vectors of $\boldsymbol{H} = \boldsymbol{H_0} + \boldsymbol{h}$ and $\boldsymbol{E} = \boldsymbol{E_0} + \boldsymbol{e}$ represent magnetic field and electric field, respectively. Lower case represents perturbation term showing the time dependence of $e^{i\omega t}$. In addition, magnetic flux can be given by $\boldsymbol{B} = \boldsymbol{H}$ (G) because the layer is non-magnetic and calculation is in CGS Gausian unit system. Furthermore, $\partial/\partial z = 0$ was

assured in all cases. Eq.5.11 yields in

$$\frac{\partial h_x}{\partial x} = -\frac{\partial h_y}{\partial y}. \tag{5.12}$$

From Eq.5.9 and Eq.5.10, following equations are obtained.

$$\frac{\partial h_y}{\partial x} - \frac{\partial h_x}{\partial y} = \frac{4\pi\sigma}{c_0} E_z, \tag{5.13}$$

$$\frac{\partial E_z}{\partial y} = -\frac{i\omega}{c_0} h_x. \tag{5.14}$$

Solving Eq.5.13 for E_z and substitution into Eq.5.14 gives

$$\frac{\partial}{\partial y}\left(\frac{\partial h_y}{\partial x} - \frac{\partial h_x}{\partial y}\right) = -i\frac{4\pi\omega\sigma}{c_0^2} h_x. \tag{5.15}$$

A partial differential equation of h_x is derived by substitution of Eq.5.12 into Eq.5.15.

$$\left(-\frac{\partial^2}{\partial x^2} - \frac{\partial^2}{\partial y^2} + i\frac{4\pi\omega\sigma}{c_0^2}\right) h_x = 0. \tag{5.16}$$

Accordingly, a general solution of h_x can be defined as

$$h_x = \left(a_1 e^{k_m y} + a_2 e^{-k_m y}\right) e^{i(\omega t - kx)}. \tag{5.17}$$

Substitution of Eq.5.17 into Eq.5.16 gives an equation for unknown k_m as

$$\left(k^2 - k_m^2 + i\frac{4\pi\omega\sigma}{c_0^2}\right) h_x = 0. \tag{5.18}$$

Non-trivial solution for h_x gives k_m as follows

$$k_m^2 = k^2 + i\frac{4\pi\omega\sigma}{c_0^2} = k^2 + i\frac{2}{\delta^2}, \tag{5.19}$$

where

$$\delta = \sqrt{\frac{c_0^2}{2\pi\omega\sigma}}. \tag{5.20}$$

The introduced δ is often called as the skin depth, which represents a penetration depth of electromagnetic field in the conductive layer. Finally, substitution of Eq.5.17 into Eq.5.12 gives

$$h_y = i\frac{k}{k_m}\left(a_1 e^{k_m y} + a_2 e^{-k_m y}\right) e^{i(\omega t - kx)} = b_y \text{ (G)}. \tag{5.21}$$

Since other layers are insulating, application of the magnetostatic approximation yields of scalar potentials ϕ and ψ in the YIG and dielectric layers, respectively. As the same procedure shown in §3.1, h_x and b_y can be derived in these layers. In the YIG layer:

$$h_x = ik\left(\phi_{01} e^{\tilde{\zeta}_+ ky} + \phi_{02} e^{\tilde{\zeta}_- ky}\right) e^{i(\omega t - kx)}, \tag{5.22}$$

$$b_y = -k\left(\tilde{\mu}_+ \phi_{01} e^{\tilde{\zeta}_+ ky} + \tilde{\mu}_- \phi_{02} e^{\tilde{\zeta}_- ky}\right) e^{i(\omega t - kx)}, \tag{5.23}$$

where $\tilde{\mu}_\pm = \tilde{\zeta}_\pm \mu_{22} - i\mu_{21}$. In the dielectric layer D1 and D2:

$$h_x = ik\left(\psi_{01}^{(N)} e^{ky} + \psi_{02}^{(N)} e^{-ky}\right) e^{i(\omega t - kx)}, \tag{5.24}$$

$$b_y = -k\left(\psi_{01}^{(N)} e^{ky} - \psi_{02}^{(N)} e^{-ky}\right) e^{i(\omega t - kx)}, \tag{5.25}$$

where N represents the label of dielectric layers $N \in (1, 2)$. Coefficients become $\psi_{01}^{(1)} = 0$ and $\psi_{02}^{(2)} = 0$ to ensure $\psi \to 0$ at infinite point. Now the state vector (h_x, b_y) is given for all boundaries. At each boundary, the continuity of the state vector is ensured. Therefore following set of equations is derived.

$$\psi_{01}^{(2)} e^{-kd/2} = \phi_{01} e^{-\tilde{\zeta}_+ kd/2} + \phi_{02} e^{-\tilde{\zeta}_- kd/2}, \tag{5.26}$$

$$\psi_{01}^{(2)} e^{-kd/2} = \tilde{\mu}_+ \phi_{01} e^{-\tilde{\zeta}_+ kd/2} + \tilde{\mu}_- \phi_{02} e^{-\tilde{\zeta}_- kd/2}, \tag{5.27}$$

$$ik\left(\phi_{01} e^{\tilde{\zeta}_+ kd/2} + \phi_{02} e^{\tilde{\zeta}_- kd/2}\right) = a_1 e^{k_m d/2} + a_2 e^{-k_m d/2}, \tag{5.28}$$

$$\tilde{\mu}_+ \phi_{01} e^{\tilde{\zeta}_+ kd/2} + \tilde{\mu}_- \phi_{02} e^{\tilde{\zeta}_- kd/2} = -\frac{i}{k_m}\left(a_1 e^{k_m d/2} - a_2 e^{-k_m d/2}\right), \tag{5.29}$$

$$a_1 e^{k_m (d/2 + t_{\mathrm{Au}})} + a_2 e^{-k_m (d/2 + t_{\mathrm{Au}})} = ik\psi_{02}^{(1)} e^{-k(d/2 + t_{\mathrm{Au}})}, \tag{5.30}$$

$$\frac{i}{k_m}\left(a_1 e^{k_m (d/2 + t_{\mathrm{Au}})} - a_2 e^{-k_m (d/2 + t_{\mathrm{Au}})}\right) = \psi_{02}^{(1)} e^{-k(d/2 + t_{\mathrm{Au}})}. \tag{5.31}$$

Solving Eq.5.26-Eq.5.31 for the eigenvector $(\phi_{01}, \phi_{02})^T$ of the FV-SW in the YIG layer gives the characteristic equation by

$$\begin{bmatrix} \left(\tilde{\mu}_+ - \frac{k}{k_m}\frac{\Gamma-1}{\Gamma+1}\right) e^{\tilde{\zeta}_+ kd/2} & \left(\tilde{\mu}_- - \frac{k}{k_m}\frac{\Gamma-1}{\Gamma+1}\right) e^{\tilde{\zeta}_- kd/2} \\ (\tilde{\mu}_+ - 1)\, e^{-\tilde{\zeta}_+ kd/2} & (\tilde{\mu}_- - 1)\, e^{-\tilde{\zeta}_- kd/2} \end{bmatrix} \begin{pmatrix} \phi_{01} \\ \phi_{02} \end{pmatrix} = 0, \tag{5.32}$$

where

$$\Gamma = \frac{k - k_m}{k + k_m} e^{-2k_m t_{\mathrm{Au}}}. \tag{5.33}$$

Non-trivial solution for the eigenvector determines the dispersion curve.

$$e^{(\tilde{\zeta}_+ - \tilde{\zeta}_-)kd} = \frac{\tilde{\mu}_+ - 1}{\tilde{\mu}_- - 1} \frac{\tilde{\mu}_- k_m(\Gamma+1) - k(\Gamma-1)}{\tilde{\mu}_+ k_m(\Gamma+1) - k(\Gamma-1)}. \tag{5.34}$$

Eq.5.34 cannot be directory solved for k as a function of ω, therefore the solution was numerically solved by using Levenberg-Marquardt method for specific frequency $\omega = 2\pi f$. In the Levenberg-Marquardt method, a residual error function F was defined as:

$$F(k, \omega) = k - \frac{A + B - C - D}{(\tilde{\zeta}_+ - \tilde{\zeta}_-)d} \to 0, \tag{5.35}$$

where

$$A = \mathrm{Log}\left[\tilde{\mu}_+ - 1\right] + i\mathrm{arg}\left[\tilde{\mu}_+ - 1\right], \tag{5.36}$$

$$B = \mathrm{Log}\left[\tilde{\mu}_- k_m(\Gamma+1) - k(\Gamma-1)\right] + i\mathrm{arg}\left[\tilde{\mu}_- k_m(\Gamma+1) - k(\Gamma-1)\right], \tag{5.37}$$

$$C = \mathrm{Log}\left[\tilde{\mu}_- - 1\right] + i\mathrm{arg}\left[\tilde{\mu}_- - 1\right], \tag{5.38}$$

$$D = \mathrm{Log}\left[\tilde{\mu}_+ k_m(\Gamma+1) - k(\Gamma-1)\right] + i\mathrm{arg}\left[\tilde{\mu}_+ k_m(\Gamma+1) - k(\Gamma-1)\right]. \tag{5.39}$$

Eq.5.34 was converted by taking natural logarithm. This operation prevented oscillation of F, because the solution k was generally complex number, in which exponential function include uncertainty of 2π.

According to Eq.5.35, F was calculated with following parameters: $H_0 = 1368$ Oe,

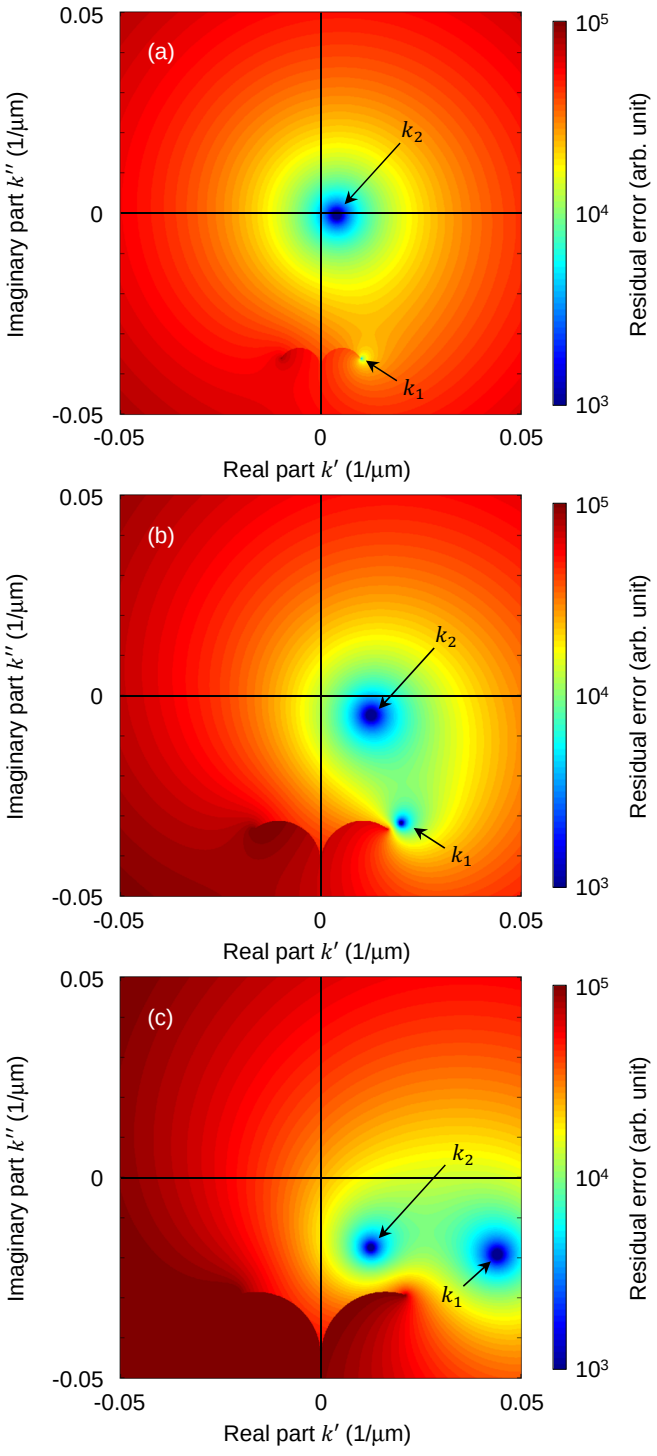

Figure 5.11 Residual error function F in Gaussian plane. Wavenumber of the YIG slab with TMOL is calculated with $H_0 = 1368$ Oe, $4\pi M_S = 1760$ G, YIG thickness $d = 18.4$ μm, Au thickness $t_{\mathrm{Au}} = 30$ nm, conductivity $\sigma = 4.1 \times 10^7$ S/m, $\alpha = 2.35 \times 10^{-4}$. Excitation frequency of (a) 4.0 GHz, (b) 4.3 GHz and (c) 4.6 GHz. Color represents the amount of residual error in logarithmic manner.

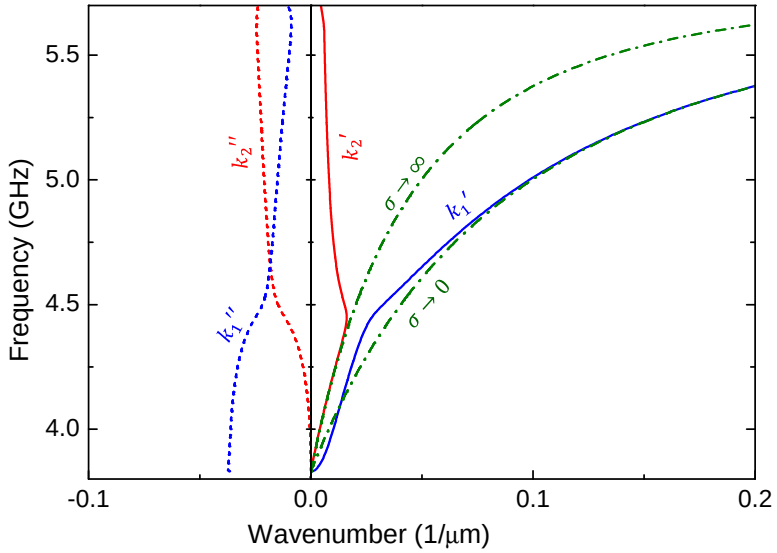

Figure 5.12 Dispersion curves of the YIG slab with TMOL. Blue and red lines represent mode k_1 and k_2, respectively. Bold lines correspond to the real part and dotted lines correspond to the imaginary part. Green lines are dispersion curves calculated with $\sigma \to 0$ and $\sigma \to \infty$.

$4\pi M_S = 1760$ G, YIG thickness $d = 18.4$ μm, Au thickness $t_{\mathrm{Au}} = 30$ nm, conductivity $\sigma = 4.1 \times 10^7$ S/m, $\alpha = 2.35 \times 10^{-4}$. It was also assumed the solution $k = k' + ik''$ lies in the Gaussian plane (k', k'') defined by $-0.05 \leq k', k'' \leq 0.05$.

Calculated results are shown in Fig.5.11 with different excitation frequencies. In Fig.5.11, blue colored areas represent a small residual error, and these areas are possible to have solutions. Relatively large F value was due to the rough resolution of the Gaussian plane. At each frequency, a pair of solutions $k_1 = k_1' + ik_1'', k_2 = k_2' + ik_2''$ can be confirmed. Both k_1, k_2 were frequency dependent. Interestingly, k_1 seemed to be an irregular solution at 4.0 GHz, but strongly presented at 4.6 GHz. Superiority of these mode might have frequency dependence. From the Gaussian plane, the YIG slab with TMOL seemed to manifest two independent propagation modes.

Next, dispersion curve was then calculated to minimize $F \to 0$ to have the specific k_1, k_2 values. Initial values were precisely chosen not to mix these modes. Apart from $\sigma = 4.1 \times 10^7$ S/m, $\sigma \to 0$ (Air), ∞ (PEC) were also calculated. Obtained dispersion curves are shown in Fig.5.12. As a result, the mode k_1 became consistent with k of $\sigma \to 0$ at higher frequencies. In contrast, the mode k_2 become consistent with k of $\sigma \to \infty$ at lower frequencies. Imaginary part of these modes were remarkably reduced where k_1' (k_2') is closer to the slabs with $\sigma \to 0$ (∞). Reflecting this nature, k_1 and k_2 were defined as quasi-Air (q-Air) mode and quasi-PEC (q-PEC) mode, respectively.

In this calculation, q-Air mode and q-PEC mode were separately calculated. Discrepancy in the wavenumber gives different contributions on the dipole interaction, and

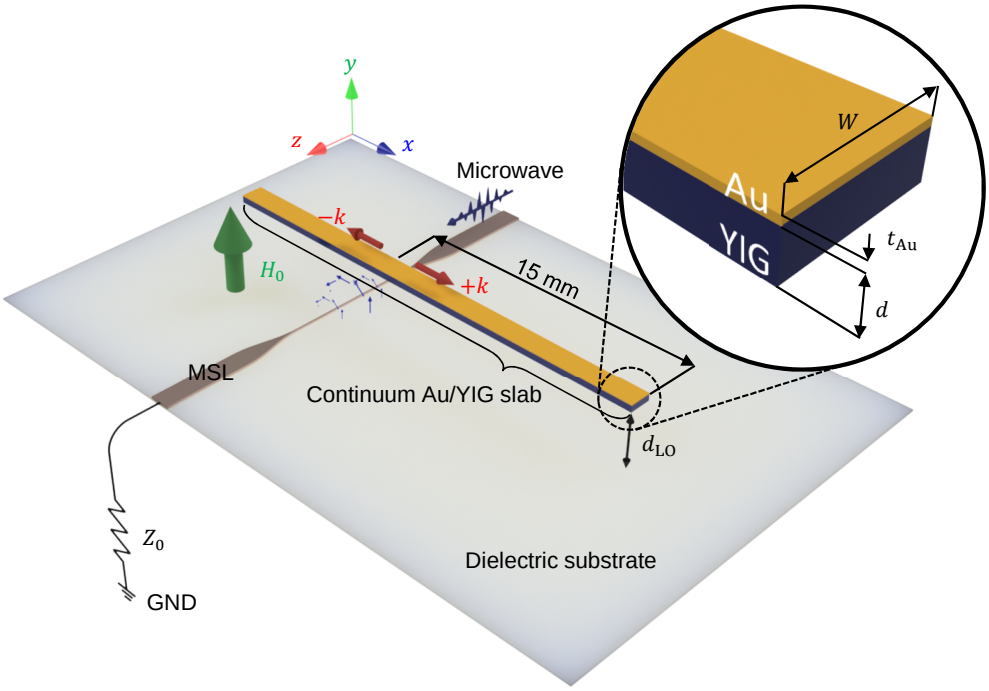

Figure 5.13 Simulation model for the YIG slab with TMOL. FV-SW is excited by the MSL. The slab with width $W = 1$ mm is located on the MSL with liftoff gap $L_{\mathrm{LO}} = 70$ μm. Precession of magnetization m_x is calculated along $+x$ direction from the center of the MSL. At both waveguide ends, extra damping $\Delta H = 10$ Oe is applied to suppress the backscattering. Excitation frequency is at 4 GHz and $H_0 = 1368$ Oe is perpendicularly applied to the slab.

these waves might be interacted. In this approach, further investigation about the actual behavior of waves inside the waveguide is difficult. Therefore electromagnetic simulation was again introduced to investigate the behavior of FV-SWs in the YIG slab with TMOLs.

5.3.3 Estimation of Decay Length and Wavelength of FV-SWs

In the simulation, a continuum Au/YIG slab was modeled as shown in Fig.5.13. The parameter set of the slab was the same as one used in Fig.5.12. Waveguide width $W = 1$ mm was further included, which was consistent with the waveguide used in the experiment shown in Fig.5.9. Because of the limited computing resources, the slab with infinite propagation length cannot be calculated as previous part. Therefore the backscattering from the waveguide ends was suppressed by applying the extra damping $\Delta H = 10$ Oe in the region within 5 mm from the edge. By using this trick, the region within 10 mm from the MSL can be regarded as a Au/YIG slab without waveguide end. Within this region,

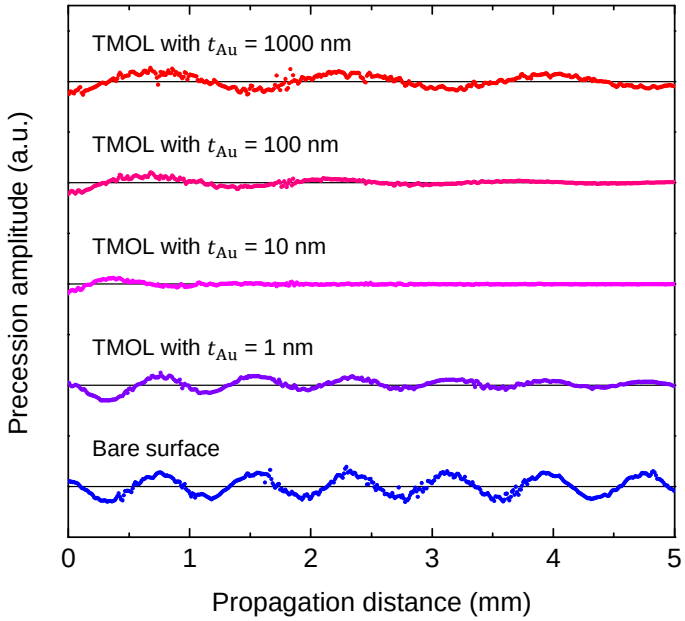

Figure 5.14 Calculated precession profile of m_x with different t_{Au} at 4 GHz.

magnetization precession m_x was calculated along $+k$ direction. In addition, a liftoff gap d_{LO} was included between the MSL and slab. When the slab was directly contacted to the MSL, both surfaces of the slab were sandwiched by conductive layers. The dispersion curve of such slab is given by Eq.3.33, in which no SW excitation is allowed. Moreover, stronger excitation field from the MSL distorted m_x profile in the vicinity of excitation region, and appropriate d_{LO} was also useful to extract pure decay profile of m_x. From these reasons, $d_{\mathrm{LO}} = 70$ μm was optimized for the slab condition.

Obtained profiles of m_x are shown in Fig.5.14. In the bare surface slab, oscillation of m_x with spatial period of 0.80 mm was confirmed. The wavelength of FV-SW with corresponding parameters was given as 0.78 mm, thus the calculated m_x well represented the profile of FV-SW. In addition, the attenuation of oscillation amplitude was very little. The spatial period of the oscillation was monotonically extended as t_{Au} increased. However, strong attenuation was obviously seen at $t_{\mathrm{Au}} = 10$ nm. Thus the termination effect was strongly depending on t_{Au}, and enhanced at specific thicknesses. These oscillation profile was fit by

$$m_x(x) = m_{x0} e^{-x/L_{\mathrm{att}}} e^{-i2\pi x/\lambda}, \tag{5.40}$$

where L_{att} is attenuation length, and λ is wavelength. A value of m_{x0} is the oscillation amplitude at $x = 0$, or the center of the MSL. In Eq.5.40, values of λ and L_{att} give important information about the real and imaginary part of the wavenumber $k = k' + ik''$, respectively. The relationship can be given by $k' = 2\pi/\lambda$ and $k'' = -1/L_{\mathrm{att}}$.[60]

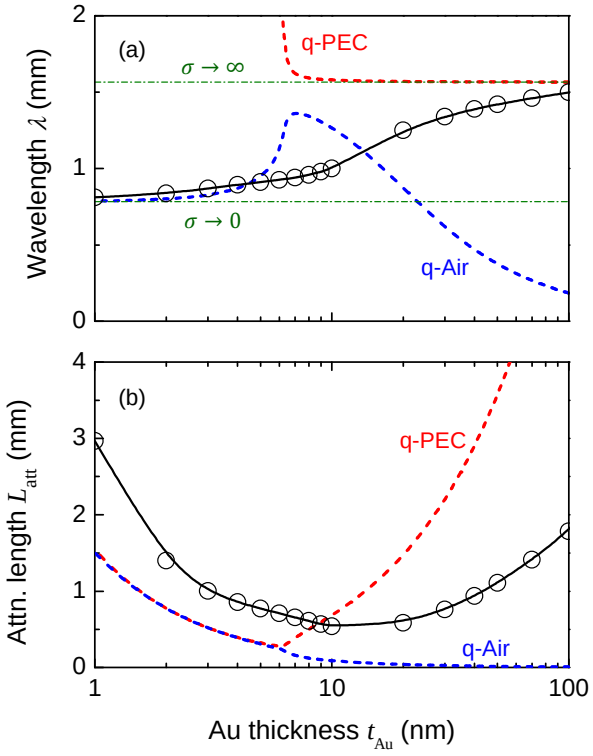

Figure 5.15 (a) Au thickness dependence of λ. Red and blue lines represent to the wavelengths of q-PEC and q-Air modes. Open circles show the extracted λ from the electromagnetic simulation. Green lines show that of air-surface ($\sigma \to 0$) and PEC-surface ($\sigma \to \infty$). (b) Au thickness dependence of $L_{\rm att}$. Red and blue lines represent the attenuation lengths of q-PEC and q-Air modes. Open circles show the extracted $L_{\rm att}$. In all calculations, the excitation frequency is at 4 GHz, and $H_0 = 1368$ Oe.

Accordingly, the fitting of m_x profile bridges the dispersion relation shown in Fig.5.12 and the behavior of the FV-SW propagating in the YIG slab with TMOLs. Values of λ and $L_{\rm att}$ were further calculated around $t_{\rm Au} = 10$ nm. This result is graphed in Fig.5.15.

In Fig.5.15a, values of λ are presented. When $\sigma \to 0$ (∞), calculated λ of the FV-SW was 0.78 mm (1.57 mm). Wavelengths of q-Air and q-PEC were $t_{\rm Au}$ dependent. In the thick $t_{\rm Au}$ region, q-PEC was almost comparable to the slab with $\sigma \to \infty$. On the other hand, in the thin $t_{\rm Au}$ region, q-Air was almost comparable to the slab with $\sigma \to 0$. In the middle thicknesses, e.g. 3 nm $\sim$ 7 nm, both modes exhibited a mismatch from $\sigma \to 0$ and ∞. The results of the electromagnetic simulation were overlaid as black circles. As shown in Fig.5.14, oscillations of q-PEC and q-Air cannot exist at the same time, since the profile was able to be fit by a single λ value. Interestingly, a value of λ exhibited good accordance with q-PEC at $t_{\rm Au}$ over 100 nm, and with q-Air at $t_{\rm Au}$ less than 5 nm. Between these thicknesses, a value of λ was gradually transit from the q-

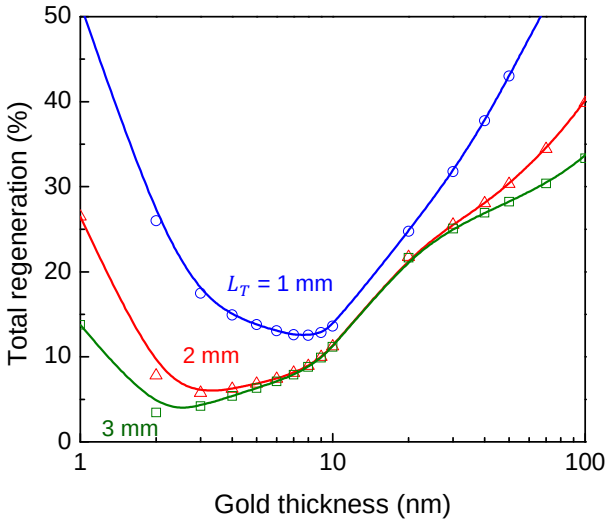

Figure 5.16 Total regeneration due to the backscattering with TMOLs. Curves with different L_T are calculated. The parameters are given by Fig.5.15.

PEC to q-Air modes. In this transition region, a contribution of q-PEC and q-Air might be mixed, yielding in the hybridization. In the experiment, t_{Au} exhibited the sufficient termination effect, where the mode might be hybridized.

In Fig.5.15b, values of L_{att} are presented. The q-PEC mode exhibited a cup-shaped dependence, while the q-Air mode exhibited monotonically decrease with increase of t_{Au}. When $t_{\mathrm{Au}} < 6$ nm, L_{att} of these modes were degenerated. Similar cup-shaped dependence was also confirmed in the result of electromagnetic simulation. In is noteworthy that the bottom of the cup was located within the transition region of λ. This implies the termination effect was enhanced in the hybridization region. At $t_{\mathrm{Au}} = 10$ nm, $L_{\mathrm{att}} = 0.54$ mm was given. At $t_{\mathrm{Au}} = 30$ nm used in the experiment, $L_{\mathrm{att}} = 0.76$ mm was given. This value was slightly larger than the optimized value, but even smaller than the $L_T = 2$ mm which is the length of the waveguide covered by the TMOL. According to Eq.5.40, the amplitude of the backscattered wave is given by

$$|A_B| = \frac{m_x(2L_T)}{m_{x0}} = e^{-2L_T/L_{\mathrm{att}}}, \tag{5.41}$$

where the oscillation term was ignored. When $t_{\mathrm{Au}} = 30$ nm, $|A_B|$ becomes 0.51%. Thus TMOLs show a great potential to terminate backscattered waves.

Nevertheless, the obtained $\sigma S_{21} = 2.13$ dB in the experiment was rather large compared to the expected value from the $|A_B|$. To estimate the total regeneration from the TMOLs, it is also necessary to take into account of the effect of reflection at the boundary. In the bare surface waveguide, wavenumber was estimated as $k_0 = 7.82 \times 10^3$ m^{-1}. As shown in Fig.5.15a, the wavenumber $k = 2\pi/\lambda$ with TMOLs is t_{Au} dependent

and slightly smaller than k_0. Since the wave is injected from the bare surface side, finite difference between k and k_0 gives rise in the reflection. This reflection was calculated by the boundary conditions of the scalar potential ϕ and normal magnetic flux $b_x = -i\mu k\phi$. In the case of vertical incidence, reflectivity R at the boundary can be written as

$$R = \frac{k_0 - k}{k_0 + k}. \tag{5.42}$$

Considering Eq.5.41 and Eq.5.42 at the same time, the total regeneration is derived by

$$R_0 = |R| + 4\frac{k_0 k}{(k_0 + k)^2}|A_B|. \tag{5.43}$$

The first term represents the direct reflection from the boundary, and second term represents the backscattering with the finite transmittance at the boundary. When $t_{\mathrm{Au}} = 30$ nm, R_0 becomes 25%, namely the non-negligible mismatch between k and k_0 increased R term. The trends of R_0 with different L_T are shown in Fig.5.16. In Fig.5.15, thinner t_{Au} reduces the mismatch of k and k_0, but L_{att} is increased at the same time. When there is a room to include enough L_T, thinner t_{Au} can greatly reduce the total regeneration.

5.4 Demonstration of Robust XNOR Operation

5.4.1 Suppression of Transmission Ripple by TMOL

The waveguide with TMOL fabricated in §5.3 was used for the interference experiment in this part. In advance, transmission spectrum S_{32} was measured with the same condition as Fig.5.3. The result is shown in Fig.5.17. Transmission spectra of the waveguide with bare surface were overlaid from Fig.5.3. Clearly the transmission ripples, which are due to the backscattering at the waveguide end, were suppressed by the terminator, in reasonable agreement with the calculated results shown in Fig.5.17b. Transmission ripples observed at frequencies higher than 4.1 GHz were caused by the higher order modes in the width direction, and this cannot be suppressed by TMOLs.[163,164] These ripples were formed at frequencies enough higher than that of the operation at 4.0 GHz, thus these resonances had no effect to the experiment. Small differences between the experimental results and simulations in this frequency range may be attributed to the inhomogeneity of the demagnetization field.

Distributions of FV-SWs inside waveguides were also compared in Fig.5.17c and d. FV-SWs were injected from both port 1 and 2 in the in-phase condition. Thanks to the TMOL with $t_{\mathrm{Au}} = 30$ nm, the amplitude of backscattered waves was terminated at the waveguide ends, and the propagation pattern became almost the same regardless of excitation frequencies. This stability of transmission spectra also gives rise in the stable interference of FV-SW within the waveguide.

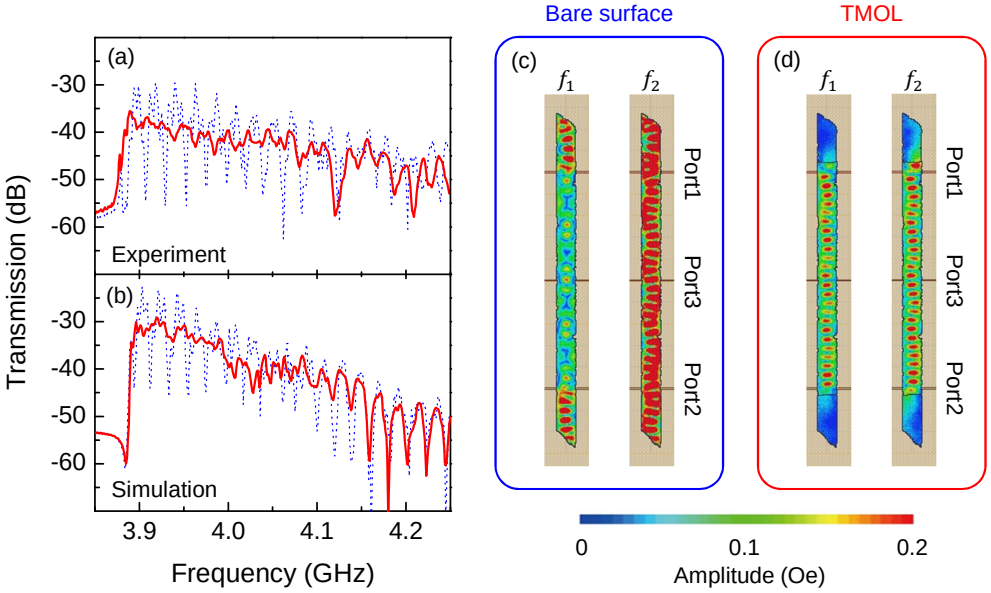

Figure 5.17 (a) Transmission properties from port2 to port3 in experiment under $H_0 = 3050$ Oe. (b) Simulated under an effective field of $H_0 - H_d = 1368$ Oe. Blue dashed lines and red bold lines show transmission behavior inside the waveguide with bare surface and with TMOL, respectively. (c) Distribution of FV-SW inside the waveguide (c) with bare surface and (d) with TMOL. Frequency $f_1 = 3.998$ GHz and $f_2 = 4.001$ GHz.

5.4.2 FV-SW Interference with TMOL

Interference experiments were done with the same procedure with §5.1. The measured stability of ON and OFF state with the bare surface waveguide was given from Fig.5.2b. In Fig.5.18c, amplitudes of the output wave versus phase difference ξ is shown. By the application of TMOL with $t_{\mathrm{Au}} = 30$ nm, the amplitude of V_{ON} was reduced to 6.31 ± 0.12 mV, and also V_{OFF} was reduced to 1.30 ± 0.11 mV, because the TMOL terminated outward flow of FV-SWs at port 3 and only inward flow contributed to the interference. Hence the insertion loss of the interferometer was increased 3 dB in maximum. However, the removal of outward flow further reduced the offset of the OFF state, and the resulting isolation of ON state and OFF state was rather increased from 9.95 dB to 13.7 dB. The measured stability of these state is shown in Fig.5.18b. Deviation of ON state was clearly suppressed by the application of the TMOL. Standard deviations of the level of ON and OFF states within the H_0 ranging from 3035 Oe to 3065 Oe were evaluated as σ_{ON} and σ_{OFF}. And the noise margin was also defined as the discrimination between ON and OFF levels including errors in 1σ, which can be understood as a gap height between red and blue bands. All evaluated parameters are listed in Table5.3. Especially the noise margin is important index as a measure of robustness, and this was increased from 0.85 mV to 4.14 mV, thanks to the termination effect. According to this factor, the stability

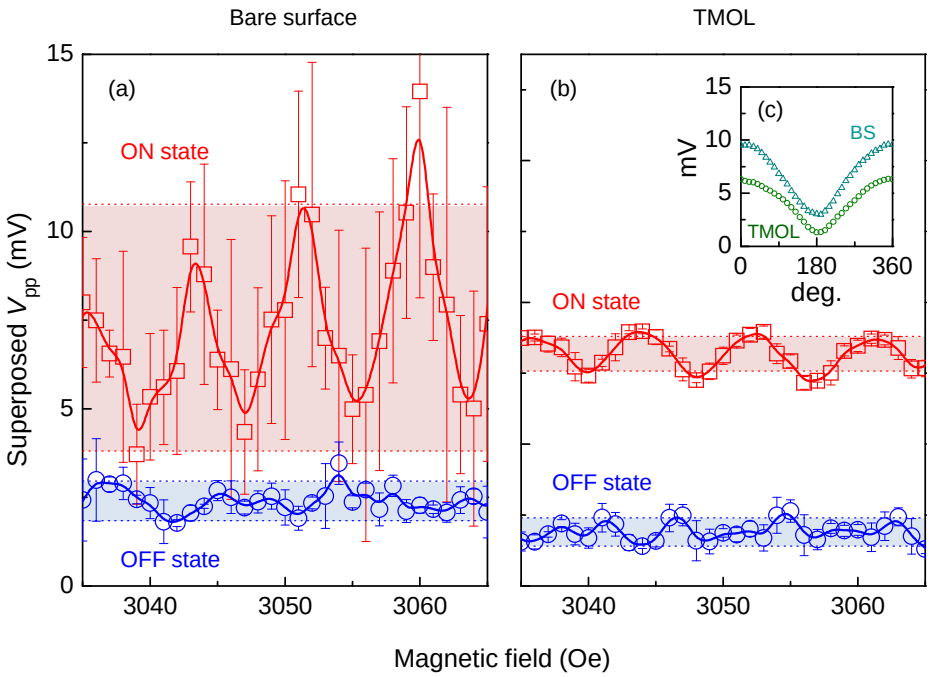

Figure 5.18 Robustness of operation against magnetic field disturbance. Red squares show V_{ON} and blue circles show V_{OFF}, for the device (a) with bare surface and (b) with TMOL. The width of the colored band represents the standard deviation. Error bars corresponds to the standard deviation of five repeated measurement at one field. (c) Output amplitudes of V_{pp} detected at port 3 versus ξ between two injected waves, for the YIG waveguide with bare surface (BS) and with TMOL. All signals are at 4 GHz.

of the interferometer was improved by a factor of ~ 5.

In the practical situation, the bias magnetic field of the commercial microwave devices is usually given by permanent magnets. A value of H_0 is rather temperature dependent, since the remnant magnetic field of the magnet is quite sensitive to the temperature as studied in §4.1. J. D. Adam also reported a temperature dependence of the FV-SW propagating in the YIG waveguide.[165] In this report, the waveguide was magnetized by using a samarium cobalt magnet. The resulting temperature dependence was evaluated as an equivalent magnetic field dependence, yielded in the value of 3.2

Table 5.3 Spec of FV-SW interferometers with different waveguide ends

	V_{ON} (mV)	V_{OFF} (mV)	Isolation (dB)	σ_{ON} (mV)	σ_{OFF} (mV)	Noise margin (mV)
Bare surface	9.56 ± 0.24	3.04 ± 0.25	9.95	3.48	0.56	0.85
TMOL	6.31 ± 0.12	1.30 ± 0.11	13.7	0.50	0.40	4.14

Oe/°C. In Fig.5.18, robustness of the interferometers was evaluated for H_0 drift over 30 Oe, which is comparable to the temperature drift of ~ 10°C. This result indicates the FV-SW interferometer with TMOL can be used not only in the laboratory, but also in the general environments with temperature drift.

5.5 Summary

In this chapter, 2 wave interferometry of FV-SWs were first experimentally demonstrated by using the interferometer composed of the linear waveguide. FV-SWs have an advantage on the device integration due to its isotropic dispersion curve. Nevertheless, the termination of the backscattering at the waveguide ends becomes a serious issue for studies. Thus the concrete device structure was never shown.

In §5.1, the 2 wave interferometry of FV-SWs was investigated on a trial. The constructive (ON state) and destructive (OFF state) interference of injected waves was confirmed with the isolation of 9.95 dB. However, this isolation was obviously deviated by the bias magnetic field. The mechanism of deviation was discussed by using the electromagnetic simulation, and the backscattering of FV-SWs at the waveguide end gave rise in the instability. Therefore to suppress the backscattering, two different termination structure were studied in §5.2 and §5.3.

In §5.2, SW termination by roughness-induced scattering was investigated. The surface of the waveguide ends were roughened by the #600-grid sandpaper. The resulting R_a of about 100 nm suppressed transmission ripples to $\sigma S_{21} = 3.66$ dB. The VNA-FMR setup was constructed to observe the effect of momentum relaxation caused by the roughening process. The roughened surface of 110 μm-thick YIG yielded of the increase in the extrinsic damping ΔH_0 of 3.4 Oe, while the intrinsic damping α was almost unchanged. In 10 μm-thick YIG films, ΔH_0 was further enhanced to 3.8 Oe. However, the reduction of σS_{21} to the permissible range (< 3 dB) required the enhancement of $\Delta H_0 \sim 6.64$ Oe. This would be achieved by optimizing R_a, but the precise control of R_a by the sandpaper was technically difficult. And such roughening process is not preferable in the viewpoint of the device integration. Even though the finite termination effect was confirmed by the roughening process, further optimization was not done in this study.

In §5.3, SW termination by the TMOL composed of a 30 nm-thick gold layer was investigated. The application of TMOL at waveguide ends yielded of the sufficient reduction of the backscattering with $\sigma S_{21} = 2.32$ dB. Thus the given termination effect was more efficient than that of the roughening process. Mechanism of the termination effect by TMOL was investigated by using electromagnetic analysis. When the gold thickness t_{Au} was enough thin, two independent modes, namely q-Air and q-PEC, were confirmed on the dispersion curve of the slab. According to the result of electromagnetic simulation, these modes showed the hybridization at such t_{Au} of several 10 nanometers, and the propagation loss was drastically increased. The amplitude of the backscattering was suppressed less than 1% with $t_{\mathrm{Au}} = 30$ nm. By considering the reflection at the boundary of the termination area, the total regeneration became less than 25%. Thus

further optimization is possible by t_{Au} and the length of terminator.

In §5.4, TMOL with $t_{\mathrm{Au}} = 30$ nm was applied into the waveguide ends of FV-SW interferometer. Canceling of the outward flow at the central port by TMOLs gave a well controlled flow of SWs in the interferometer. As a result, the isolation of ON and OFF states was increased from 9.95 dB to 13.7 dB. Deviation of the output signal by the instability of magnetic field was remarkably suppressed. The noise margin of these states was improved from 0.85 mV to 4.14 mV by the termination of the SWs at the waveguide ends. This result is an important milestone for further developments of the network of SWDs with FV-SWs.

Chapter 6

Reconfigurable Logic Device

In the previous chapter, fundamental properties of the FV-SW interferometry were investigated in the linear waveguide. The essence and nature of FV-SWs are the isotropic dispersion within the device plane, and thus more complex waveguide topology can be realized. The purpose of this chapter is to demonstrate the interferometer with 3 fan-in, comprising of the Ψ-shaped waveguide. In §6.1, the basic aspect of majority logic is reviewed, and the concept of reconfigurable functionality using a three-input majority gate is presented. In §6.2, the Ψ-shaped waveguide geometry is designed on the electromagnetic simulation, and fabricated by different techniques. In §6.3, the reconfigurable functionality is experimentally demonstrated, and the stability of operation is discussed. Finally, in §6.4, the flow of FV-SWs in the junction area is investigated.

6.1 Spin Wave Majority Function

6.1.1 Fundamental Property

The Boolean algebra is generally expanded with the combinations of AND ($x \cdot y$), OR ($x + y$), and NOT ($\bar{x}$) operations, in which x and y take Boolean values of 0 or 1. Each logic function $F(x, y)$ has at least one Boolean expression, and can be expanded by the Shannon's expansion as follows

$$F(x, y) = \bar{x} \cdot (\bar{y} \cdot F(0, 0) + y \cdot F(0, 1)) + x \cdot (\bar{y} \cdot F(1, 0) + y \cdot F(1, 1)). \tag{6.1}$$

This expansion is given by the combination of AND, OR, and NOT operations. Generally, arbitrary logic function with N logical variables can be also expanded in the same manner. This property is called completeness. Moreover, OR operation can be replaced by $\overline{\bar{x} \cdot \bar{y}}$, hence AND and NOT operation are enough to realize completeness. In addition, by using the NAND ($\overline{x \cdot y}$) operation, NOT operation can be further replaced by NAND(x, x). Realization of the NAND operation is sufficient to show the completeness of logic functions. In the electronic circuit, a NAND gate can be implemented with 4

Table 6.1 Truth table of 3 wave interferometry

#L	θ_1	θ_2	θ_3	θ_0	A_0
1	0	0	0	0	$3A_{\text{in}}$
2	0	π	0	0	A_{in}
3	π	0	0	0	A_{in}
4	π	π	0	π	A_{in}
5	0	0	π	0	A_{in}
6	0	π	π	π	A_{in}
7	π	0	π	π	A_{in}
8	π	π	π	π	$3A_{\text{in}}$

transistors. Therefore Boolean algebra becomes an element forming the basis of todays electronic circuit.

In contrast to transistors, interference of waves cannot show completeness in the same manner. By considering the phase 0 and π as Boolean values, wave propagation of $\lambda/2$ yields of NOT operation, where λ is the wavelength. As shown in the chapter 5, 2 wave interferometry exhibits the constructive and destructive output. In this case, the resulting amplitude becomes 0 (1) when 2 input waves are anti-phase (in-phase). This behavior corresponds to the XNOR ($\overline{x \oplus y}$) operation. Combination of XNOR and NOT operations yields of XOR operation, and Eq.6.1 can be replaced by XOR operations. Thus it is also possible to express arbitrary logic function. This is called the Reed-Muller expansion.[166] Nevertheless, the logical output of 2 wave interferometry is given in the amplitude, thus no further cascading is possible, or the amplitude-phase converter is required for cascading.

In 3 wave interferometry, which is presented in this chapter, the behavior of the interferometer is rather the majority logic (MAJ(x, y, z)) than the XNOR operation. In general, wave interference with N input waves can be represented by

$$\theta_0 = \tan^{-1}\left\{\sum_{i=1}^{N} A_i \sin\theta_i \Big/ \sum_{i=1}^{N} A_i \cos\theta_i\right\}, \tag{6.2}$$

$$A_0 = \sum_{i=1}^{N}\left\{A_i^2 + \sum_{i\neq j} A_i A_j \cos(\theta_i - \theta_j)\right\}, \tag{6.3}$$

where θ_0 and A_0 are the phase and amplitude of the resulting wave, and θ_i and A_i are those of the input waves. According to Eq.6.3 and Eq.6.2, A_0 and θ_0 of the resulting wave are calculated and summarized in Table6.1 for the case of 3 wave interferometry with all $A_i = A_{\text{in}}$. In Table6.1, the resulting θ_0 becomes π (0), when π (0) in the input θ_i is majority. Thus θ_0 represent the majority logic MAJ($\theta_1, \theta_2, \theta_3$). Since the number

of π (0) determines θ_0, order of θ_i is interchangeable (symmetric function). By using the majority logic, compatible gates of AND and OR operation can be realized.

$$\mathrm{MAJ}(\theta_1, \theta_2, 0) = \theta_1 \cdot \theta_2. \tag{6.4}$$

$$\mathrm{MAJ}(\theta_1, \theta_2, \pi) = \theta_1 + \theta_2. \tag{6.5}$$

The behavior of Eq.6.4 is appeared in #L1-#L4 of Table6.1, and the behavior of Eq.6.5 is appeared in #L5-#L8 of Table6.1. Of course the NOT operation can be realized by the phase inversion. Since all of these operations are expressed only by phases, the 3 wave interferometry yields of the possibility of cascading, in contrast to the 2 wave interferometry. These equations give the important aspect of this chapter.

6.1.2 General Applications of Majority Gates

In 1954, E. Goto invented *parametron* based on this scheme, which is the computer based on the parametric oscillation of ferrites.[167] Even though parametrons had advantages of rigidity and cost, a slow clocking speed of a few megahertz allowed transistors to become involved in the computing later on. In contrast, SWDs can work in the frequencies even at tens of gigahertz, and the potential of such high speed clocking may allow the reutilization of the fundamental architectures of parametrons such as full adder circuit.

Apart from parametrons, majority gates are also important in the digital communication technology. Transfered data is often affected by noise, thus it is important to protect the data from errors. Thus data is coded in advance, and decoded by the receiver in the certain manner. Repetition code is the simplest case, in which each bit of the transfered data is repeated n times. When a number of error bit is less than $n/2$, the received bit can be corrected by majority function with n fan-in. This is called *majority decoder*, and also studied for several codes.[168]

Further possibility is given in the form of threshold function. Threshold function is generalized majority function, and the form given by

$$F(x, y, z) = \begin{cases} 1 & ; w_1 x + w_2 y + w_3 z \geq T \\ 0 & ; \text{other} \end{cases}, \tag{6.6}$$

where w_i denote weight of real number and T is threshold value. When all $w_i = 1$ and $T = 2$, Eq.6.6 gives the same result as $\mathrm{MAJ}(x, y, z)$. W. McCulloch and W. Pitts presented the concept known as *formal neuron*. In this model, value of w_i represents connectivity of each neurons, and its sign represents polarity of connection, i.e. positive (negative) w_i denotes excitatory (inhibitory) synapse.[169] This modes is the primitive form of *perceptron*, which is one of the basic principles of machine learning. In the wave

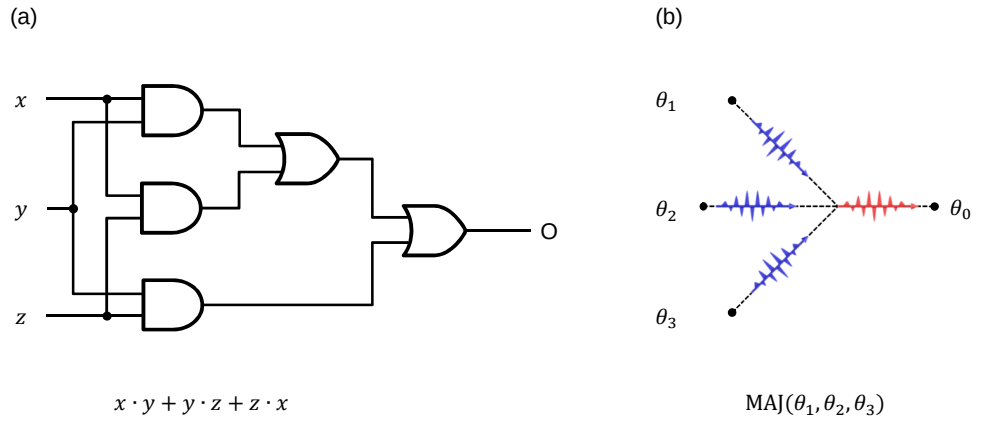

Figure 6.1 Expression of majority function. (a) Constructed by the conventional combinational logic circuit, in which x, y, and z are Boolean variables. (b) Constructed by 3 wave interferometry.

interferometry, the threshold function may be written as

$$F(\theta_1, \theta_2, \theta_3) = w_1 \sin(\omega t + \theta_1) + w_2 \sin(\omega t + \theta_2) + w_3 \sin(\omega t + \theta_3) + T \sin(\omega t + 0), \tag{6.7}$$

where ω is frequency. It is noteworthy that the weight w_i is given as an amplitude of input waves. According to the expression, the resulting phase become π at $t = 0$ when the superposed amplitude of input waves with $\theta_i = \pi$ exceeds the amplitude T. The resulting phase takes either 0 or π as long as input phases are given by either 0 or π. By using medium values, analog computing would be possible. In addition, the transmission gain of the input waveguide, i.e. weight, can be controlled by AMLs.

6.1.3 Scope of Study

From the primitive level to abstractive scheme, the prospect of applications is presented. Such powerful majority logic can be implemented not only by the wave interferometry, but also by the conventional CMOS transistors. In the combinational logic circuit, $\mathrm{MAJ}(x, y, z) = x \cdot y + y \cdot z + z \cdot x$. Difference of these implementations is shown in Fig.6.1. To implement the majority gate by transistors, five 2-input gates are required, while 3 wave interferometry can implement the majority logic based on its wave nature. Such hardware inefficiency argues the transistor based implementation of the majority gate to be an issue of conventional combinational logic circuit.

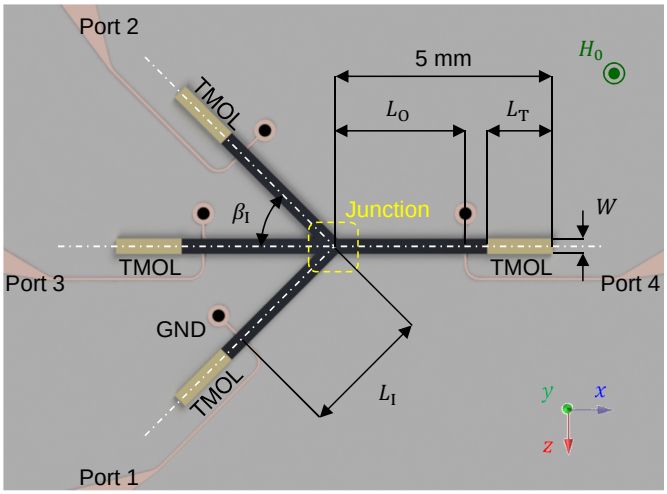

Figure 6.2 Structure of the Ψ-shaped FV-SW interferometer placed on MSL antennas. TMOLs are located at each waveguide ends for termination.

In this chapter, the majority logic is implemented by 3 wave interferometry of FV-SWs. The goal of this chapter is to demonstrate one of the basic principles of majority gate, which is derived by Eq.6.4 and Eq.6.5. Since AND operation and OR operation can be switched by the phase of θ_3, this behavior was defined as *reconfigurable functionality*, and θ_3 is called control input in this scheme.

As shown in Table6.1, this function is not still perfect due to the amplitude mismatch in #L1 and #L8. This might be avoided by the stronger excitation nearly nonlinear region, in which extra intensity of $3A_{\text{in}}$ is saturated by the parametric excitation of exchange spin wave with drastically short attenuation lengths. Such frequency selective attenuation is originally used in the signal to noise enhancers.[170] In addition, by considering a cascaded connection, synchronization of interferometers is strictly required. Other issues are also exist in the system level, and these issues are outside the scope of this work. Nevertheless, a single majority gate also overcomes the hardware inefficiency of the transistor logic as discussed, especially in large fan-in region. Such majority gate is enough useful for some applications, e.g. parity check circuit. Therefore instead of considering the system level application, a flow of SWs inside the Ψ-shaped interferometer is further investigated, and a guideline of designing such interferometers is reviewed in the later part.

6.2 Ψ-shaped FV-SW Interferometer

6.2.1 Control of Wave Flow

This topology belongs to the type-II (see §1.3), and different approaches are required for waveguide design, comparing to the simple linear waveguide shown in the

Table 6.2 Geometrical parameters of the Ψ-shaped FV-SW interferometer.

Parameter	Value	Description
d	10 μm	Thickness of YIG.
t_{Au}	10 nm	Thickness of gold comprising TMOLs.
W	350 μm	Width of waveguide.
L_{I}	3 mm	Length of input waveguides.
L_{O}	3 mm	Length of output waveguide.
L_{T}	1.5 mm	Length of terminators.
β_{I}	45°	Angle of incidence.

former chapter. In this study, a 10 μm-thick YIG film on gadolinium gallium garnet substrate was used to form the waveguide. Due to the limitation of the substrate size, the length of each waveguide was 5 mm in maximum. In addition, TMOLs with length L_T were applied in the waveguide end to suppress backscattering. All designing factors are listed in Table6.2. To prevent the direct electromagnetic coupling of MSL antennas, $\beta_{\mathrm{I}} = 45°$ and $L_{\mathrm{I}} = L_{\mathrm{O}} = 3$ mm were employed. Thanks to these requirements, the intensity of direct coupling among input antennas was less than -40 dB, and that between input and output antennas was about -60 dB in average. Remaining parameters to be designed are waveguide width W, gold thickness t_{Au}, and length of TMOLs L_{T}. These parameters were precisely chosen to guide input and output waves in better condition. To find reasonable values for these parameters, the electromagnetic simulation (ANSYS HFSS ver.16.1) was used.

The Ψ-shaped FV-SW interferometer should be designed to realize reconfigurable functionality described in the previous part. As the 3 wave interferometry was modeled by simple superposition of waves, monochromatic input waves without backscattering contribution should be guided to the junction area shown in Fig.6.2. Input waves from the port 1 and 2 are defined as S_1 and S_2, and that from the port 3 is defined as S_3. These definitions for the ith port are corresponding to Table6.1. The resulting wave was detected by the port 4. The operating frequency was set to 4 GHz.

A value of W is known to affect the shape of wavefront.[42,171] Wider W allows generation of standing modes in the lateral direction, since the fringe of ridge waveguide is considered as a pinning site for magnetization. In the former analysis, e.g. BS slab shown in Fig.3.2, lateral dependence of scalar potential was ignored. This situation corresponds to the case of $W \to \infty$, and this is not realistic for the ridge waveguides. The wave confinement in the lateral direction can be given by

$$k_m = \frac{m\pi}{W}. \qquad ; m = 1, 2, 3... \tag{6.8}$$

Reflecting this confinement, the wavenumber k of FV-SWs in the ridge waveguide takes an effective value of $k_W = \sqrt{k^2 + k_m^2}$. Accordingly, the dispersion curve of the ridge

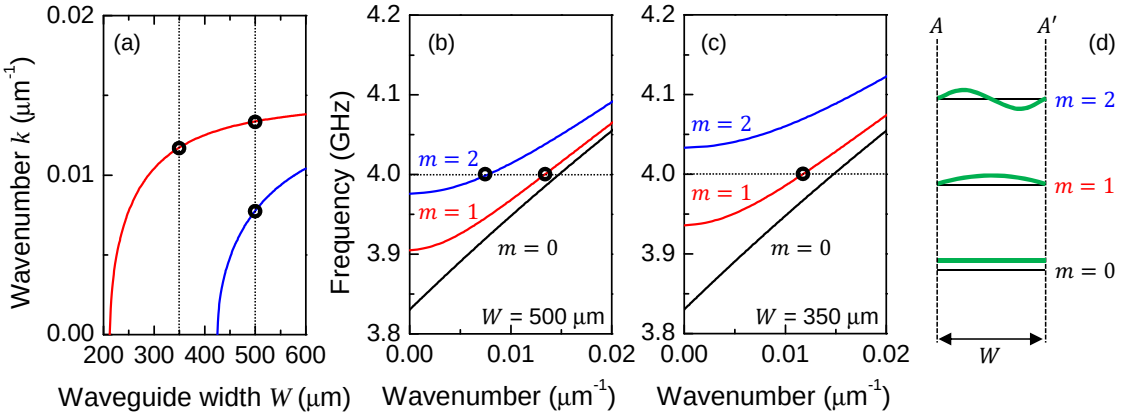

Figure 6.3 Dispersion curves of FV-SWs in the waveguide with a finite width W. (a) Wavenumber k dependence on W at excitation frequency of 4.0 GHz. (b) Dispersion curve of the ridge waveguide with W = 500 μm and (c) W = 350 μm. (d) Schematic illustration of wave amplitude within the cross section of the waveguide. Line A and A' denote edges of the waveguide. Curves with different mode number m = 0, 1 and 2 are shown. Black circles marks capable excitation. In all calculations, H_0 = 1368 Oe is used.

waveguide was formulated as[163]

$$\left\{i\zeta\left(1-Te^{2i\zeta k_W d}\right)\coth(k_W t_{\mathrm{G}})-\left(1+Te^{2i\zeta k_W d}\right)\right\}e^{-2i\zeta k_W d}\to 0, \tag{6.9}$$

$$T=\frac{\zeta^2-1}{\zeta^2+1}-i\frac{2\zeta}{\zeta^2+1}. \tag{6.10}$$

where $\zeta=\sqrt{-\mu}$. The parameter μ represent diagonal component of the permeability tensor. A parameter t_{G} represents a distance between the surface of waveguide to the GND. In the experimental setup, GND was formed on the backside of the dielectric substrate with the thickness of t_{G} = 500 μm. This yields of $\coth(k_W t_{\mathrm{G}})\sim 1$ at typical value of $k\sim 10^4$ m^{-1}. In the limit of $k_W t_{\mathrm{G}}\to\infty$, Eq.6.9 can be simplified.

$$k=\left\{\left(\frac{1}{2i\zeta d}\ln\frac{i\zeta-1}{i\zeta+1}\,\frac{1}{T}\right)^2-\left(\frac{m\pi}{W}\right)^2\right\}^{1/2}. \qquad ;m=1,2,3... \tag{6.11}$$

The dispersion curves were calculated with various W and for the mode number m = 0, 1 and 2. The result for W dependence is shown in Fig.6.3a. When W was ranging from 212 to 425 μm, a waveguide was capable of excitation with only m = 1. Such waveguide is often called as single mode. Outside this range, a waveguide was further excited the mode with m = 2, and such waveguides are called as multi mode. At W = 350

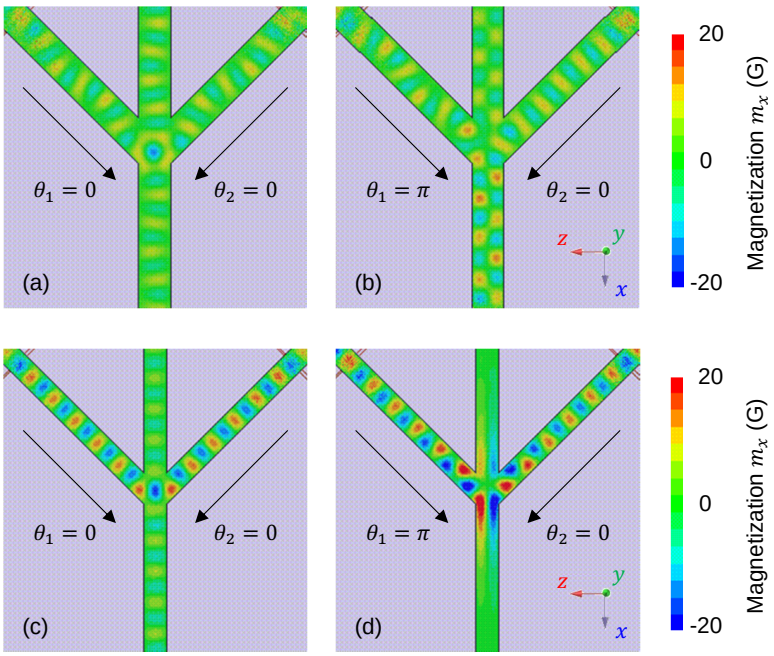

Figure 6.4 Distribution of FV-SWs given by 2 wave interferometry in the junction area. (a) In-phase interference and (b) anti-phase interference with the waveguide with $W = 500$ μm. (c) In-phase interference and (d) anti-phase interference with the waveguide with $W = 350$ μm. FV-SWs are injected from the port 1 and port 2, while port 3 is terminated. FV-SWs are excited at 4 GHz with $H_0 = 1368$ Oe in all calculations.

μm, the waveguide was capable of the excitation of $k_1 = 1.17 \times 10^4$ m^{-1}. However, at $W = 500$ μm, the waveguide was capable of the excitation both of $k_1 = 1.34 \times 10^4$ m^{-1} and $k_2 = 0.78 \times 10^4$ m^{-1}. The mode $m = 0$ cannot be overlaid because this mode is excited only in $W \to \infty$, or the BS slab without pinning at the edge. As shown in Fig.6.4d, the amplitude of waves of modes $m = 1$ and 2 becomes zero at the edge due to the pinning of magnetization. Such lateral confinement within the ridge waveguide was not strictly considered previously, since the excitation field of MSL antennas was usually homogeneous. For example, a typical wavelength of electromagnetic waves at 4 GHz was about 46 mm, which was sufficiently longer than that of the waveguide width, e.g. $W = 1$ mm. The maximum phase difference of excitation field induced in the lateral direction was only about 7.8°. To excite the FV-SW with $m = 2$, the phase difference of $k_m W = 2\pi$ is required. In the linear waveguides, such even modes are not appeared unless k_m is drastically changed by scatterings. In Fig.6.3b and c, dispersion curves with $W = 500$ μm and 350 μm are graphed, respectively. At the operating frequency of 4 GHz, the waveguide with $W = 500$ μm was multi mode. However, this waveguide showed single mode propagation below 3.97 GHz. In the same manner, the waveguide with $W = 350$ μm was also capable of exciting $m = 2$ over 4.03 GHz. Therefore the

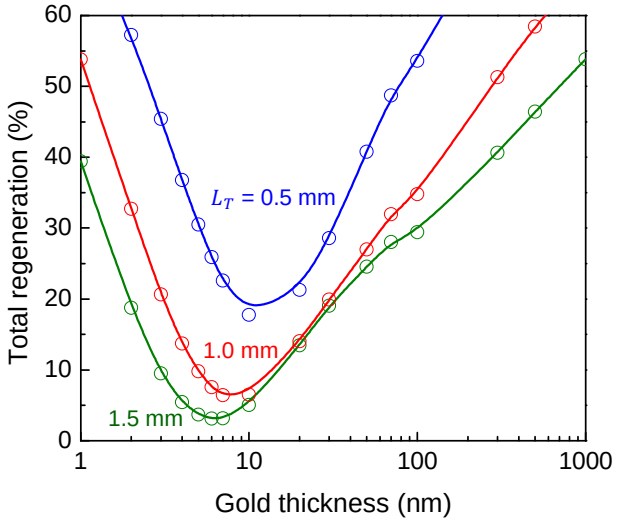

Figure 6.5 Design of TMOL for the Ψ-shaped FV-SW interferometer. Total regeneration from the termination area with various L_{T} are shown. FV-SWs are excited at 4 GHz with $H_0 = 1368$ Oe in all calculations.

propagation mode was also frequency dependent. It is noteworthy that the frequency tolerance of $m = 1$ and 2 is slightly higher in the case of $W = 350$ μm.

In Fig.6.4, the effect of propagation mode on the 2 wave interferometry is displayed. Contrary to the previous experiment with the linear waveguide, 2 waves were obliquely injected to the junction are with $\beta_{\mathrm{I}} = 45°$. In the output waveguide, a change of the propagation direction drastically affected the result of the interference. In Fig.6.4a and c, the results of constructive interferences are displayed. Regardless of W, a finite intensity of the resulting wave can be confirmed. On the other hand, the results of destructive interferences were totally different as shown in Fig.6.4b and d. In the multi mode waveguide with $W = 500$ μm, prohibited propagation of the resulting wave was confirmed as the propagation of mode $m = 2$. Therefore the design of W is quite important to prevent such errors in the Ψ-shaped interferometer. By considering the process margin, a value of $W = 350$ μm was employed in this study.

Finally, values of t_{Au} and L_{T} were determined to suppress backscattering from the waveguide ends. The approach to design TMOLs was already summarized in §5.3. Therefore the same calculation was done for the geometrical parameters shown in Table6.2 with various t_{Au} and L_{T}. The result is shown in Fig.6.5. Due to the geometrical limitation, $L_{\mathrm{T}} < 2$ mm was assumed. To suppress backscattering as much as possible, larger L_{T} was preferable. However, the interferometer was mounted on the MSL antennas by flip-chip with manual alignment. Therefore $L_{\mathrm{T}} = 1.5$ mm was chosen to include a separation of 500 μm to the neighboring MSL antenna. With $L_{\mathrm{T}} = 1.5$ mm, the bottom of regeneration was appeared around $t_{\mathrm{Au}} \sim 6$ nm. The designed TMOLs were deposited by magnetron sputtering later on, and the resulting t_{Au} was about 10 nm. This mismatch

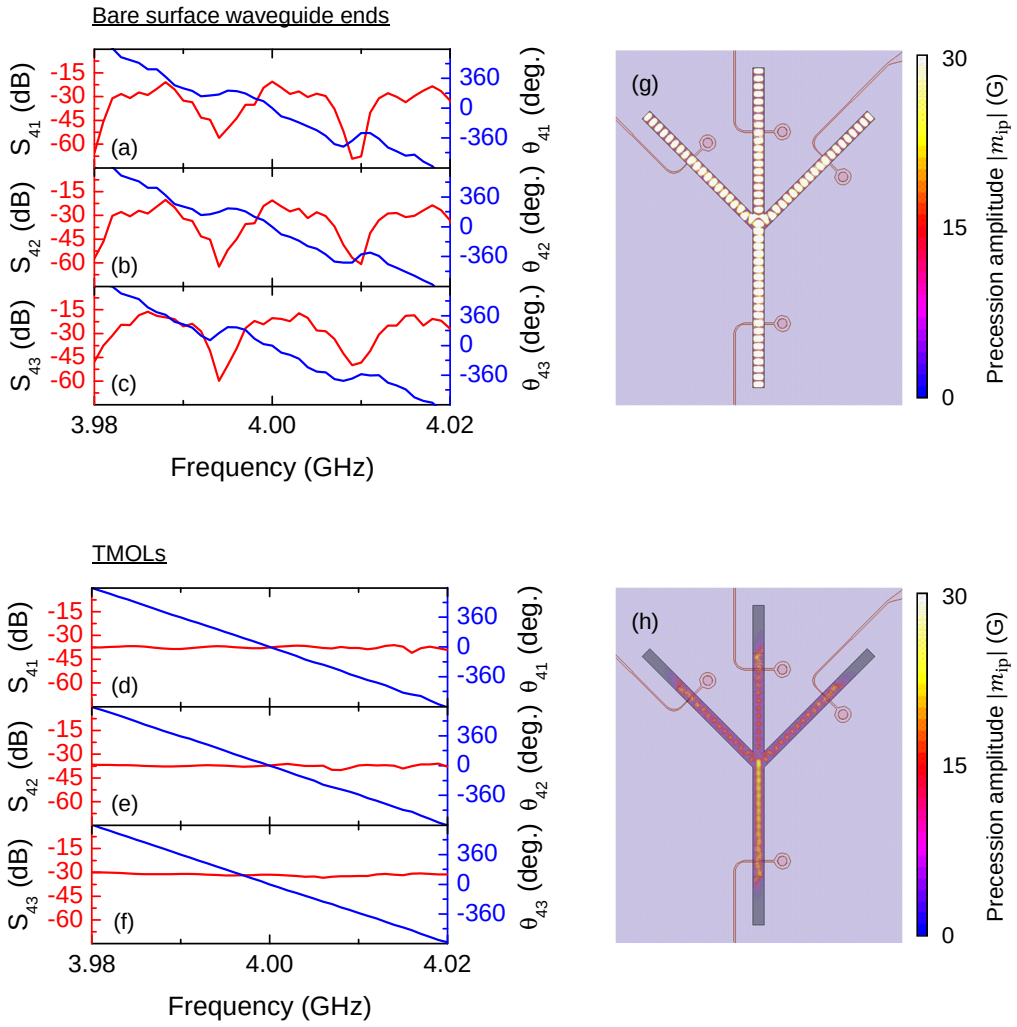

Figure 6.6 Transmission properties of the designed Ψ-shaped FV-SW interferometers. Transmission spectra of the waveguide (a)-(c) with bare surface waveguide end, and (d)-(f) with TMOLs. Red and blue lines represent transmission intensity and phase, respectively. S_{ij} denote transmission from the port j to port i. Distribution of the wave amplitudes at 4 GHz (g) with bare surface waveguide end, and (h) with TMOLs. $H_0 = 1368$ is applied in all calculations. All input ports are excited by the injected power of 1 mW.

was still within the allowable range, in which the total regeneration yields of only 5% of coming waves.

Now all parameters were determined. Transmission properties of the designed interferometer were also calculated. The results are shown in Fig.6.6. Without TMOLs, transmission spectra of the waveguides exhibited ripples due to the standing modes.

Table 6.3 Process flow of phosphoric acid etching.

#	Process	Notes
1	Cleaning	Persulfuric acid, 70°C, 5 min.
		Acetone, 10 min., Ultrasonic cleaning
		Isopropanol (IPA), 10 min., Ultrasonic cleaning
	Baking	170°C, 2 min.
2	Resist spin coat	LOR20B
		500 rpm., 5 sec.
		3000 rpm., 45 sec.
	Soft bake	170°C, 300 sec.
4	Resist spin coat	AZ5214
		500 rpm., 5 sec.
		3000 rpm., 45 sec.
		6000 rpm., 1 sec.
	Soft bake	100°C, 60 sec.
5	Exposure	16 sec.
6	Develop	AZ400:H_2O = 1:5, 200 sec.
7	Hard bake	150°C, 120 sec.
8	SiO_2 deposition	Ion beam sputtering, $\sim$ 2.8 nm/min. ($>$ 1 μm)
9	Liftoff	AZ700 remover, Acetone, IPA
10	YIG etching	Phosphoric acid, 140°C, $\sim$ 77.2 nm/min.
11	Rinse	Pure H_2O
12	SiO_2 removal	BHF (9%), $\sim$ 140 nm/min.

Phase spectra were also rippling, in which complicated wave flow was generated inside the waveguide. In Fig.6.6g, the behavior of the standing mode at 4 GHz is clearly seen. On the other hand, transmission spectra were completely smoothed by the application of TMOLs. In Fig.6.6h, amplitude of backscattering from the waveguide end is clearly suppressed. By using the designed geometrical parameters, the Ψ-shaped interferometer was capable of guiding all injected waves into the junction area in the sufficient condition.

6.2.2 Fabrication of Waveguide

To fabricate the Ψ-shaped FV-SW interferometer, etching of the ridge waveguide was essential process. Since YIG has excellent chemical stability and Mohs hardness of 7.0,[172] micro-fabrication of waveguide is generally difficult. In this study, the designed ridge waveguide was formed by two different approaches, and the resulting transmission properties were compared.

Phosphoric acid etching is widely used approach for the patterning of YIG substrate. In this process, the surface of YIG was patterned by SiO_2 mask, and then the substrate was etched by phosphoric acid heated around 150°C.[157,173–175] Detailed condition was based on the earlier work in [173]. In this work, two different etchant temperatures of

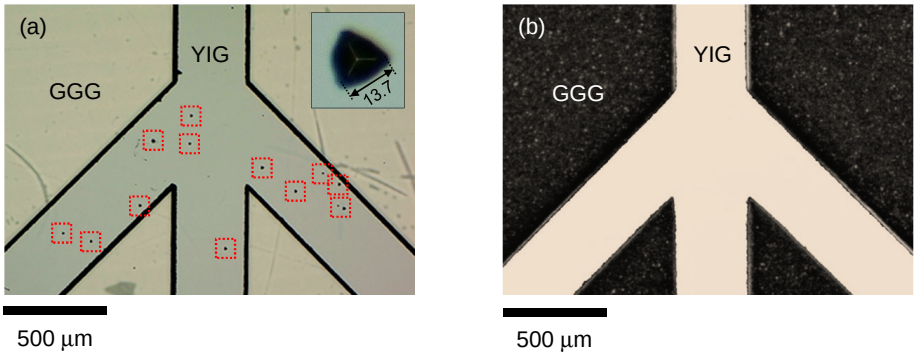

Figure 6.7 Microscope images of waveguides in the vicinity of the junction area. (a) Waveguide fabricated by phosphoric acid etching. Red squares mark positions of etch pits. Inset shows the typical enlarged image of etch-pit. (b) Waveguide fabricated by sandblast technique. Difference of textures on the surface of GGG substrate is due to the roughness induced by sandblast.

140°C and 160°C was tested, and lower temperature exhibited less damage to the etched YIG substrate. Process flow was shown in Table6.3. The SiO_2 layer with a thickness over 1 µm was deposited by iron beam sputtering (#8). Because of a long time duration of etching process ($\sim$ 2 hours), such thicker SiO_2 mask was prepared. Liftoff process was used for the patterning of SiO_2 (#9) to minimize the undercut of mask layer. During the etching process (#10), temperature of etchant was controlled by the oiling bath (AZ ONE, OBS-200M), and the etched substrate was fixed on the Teflon basket. During the etching, almost constant etching rate was confirmed.

After the etching process, several etch-pits were found on the surface of YIG substrate as shown in Fig.6.7a. Typical size of each etch-pit was in order of 10 µm, and the shape of inverted pyramid probably reflected the crystalline plane of (111). These etch-pits were not confirmed before the etching process (#11), and obvious defect was not visible beneath the SiO_2 mask in microscopy (#9). Therefore cracks or voids might be induced during the etching process (#10), possibly due to poor adhesion of SiO_2. After the etching process, SiO_2 was removed by buffered hydrofluoric acid (BHF).

The second approach to form the ridge waveguide was micro-sandblast etching. This technique is used for fabrications of micro electro-mechanical system (MEMS), in which the impact of a high velocity powder beam elaborates microstructures.[176] There are also few reports about application of this technique to the YIG waveguide.[177] In this study, the interferometer was fabricated by using commercial process at Elfo-tec Co., Ltd. Fabricated waveguide is displayed in Fig.6.7b. Etch-pit was not confirmed in the result of this process.

Height profile of the waveguide fringe was also measured by using a stylus profilemeter (Ryokosha Corp., ET4000). Since the thickness of YIG layer was 10 µm, an etched depth over 10 µm was required. Measured properties of fabricated waveguides

Table 6.4 Comparison of waveguides fabricated by different techniques.

	Micro-sandblast etching	Phosphoric acid etching
Waveguide width	342.8 μm	333.5 μm
Etched depth	35 μm	11 μm
Tapering angle	52.1°	25.2°
Etch-pit density	—	∼ 20 defects/5 mm sq.
Chipping	∼ 5 μm	∼ 5 μm

are shown in Table6.4. The etched depth of micro-sandblast etching was deeper than expected, but the effect on SW was supposed to be insignificantly. Apart from etch-pit, tapering angle of the waveguide fringe was remarkably process dependent. Tapering angle of 90° is preferable, since the dispersion of the ridge waveguide is width dependent. According to the simulation, lower tapering angle in the vicinity of 10° could drastically change the transmission property of guided waves. In the viewpoint of tapering, micro-sandblast etching was better for the waveguide fabrication. In the result of both processes, the circumferential part of waveguide was chipped about 5 μm in maximum.

After the ridge waveguide was fabricated, TMOLs were deposited on the waveguide ends by magnetron sputtering and photolithography processes. Due to the deep etched depths of the ridge waveguides, conventional spin coating technique was not preferable to apply the photo resist, because of the resist pool formed at the circumferential part. Therefore spray coating and projection exposure techniques were employed to form the mask pattern of TMOLs. After deposition, the surfaces of waveguide ends were completely covered by TMOLs with $t_{\mathrm{Au}} = 10$ nm.

6.2.3 Transmission Properties

In Fig.6.8, photographs of the device under test (DUT) are displayed. MSL antennas were connected to the equipment thorough SMA-type connectors. Dielectric substrate (FR-4) was fixed on the base mount made of copper-zinc alloy. Thermistor was embedded inside the base mount to monitor the temperature of DUT, and the temperature was controlled by the Peltier element connected to the base mount via a 150 mm-long copper plate to separate the control current of the Peltier element. Thermoelectric controller (Cell System Co,.LTD, TDC-1020A) was used to stabilize temperature deviation during the measurement. Fabricated substrate was mounted on the DUT by flip-chip, and fixed by the holder made of acrylic resin. Position of the substrate was manually aligned within the error of 1 mm. A bias magnetic field $H_0 = 3095$ Oe was perpendicularly applied to the substrate so that FV-SWs were excited. The two-port vector network analyzer (Anritsu, 37347C) was used to measure the transmission property.

Measured transmission spectra of fabricated waveguides are displayed in Fig.6.9. Since the DUT had 4 ports, the combination of input and output ports yielded of 16 different spectra. In the interference experiment, the output signal was detected from the port 4. Therefore important spectra must be S_{41}, S_{42}, and S_{43}, representing the wave

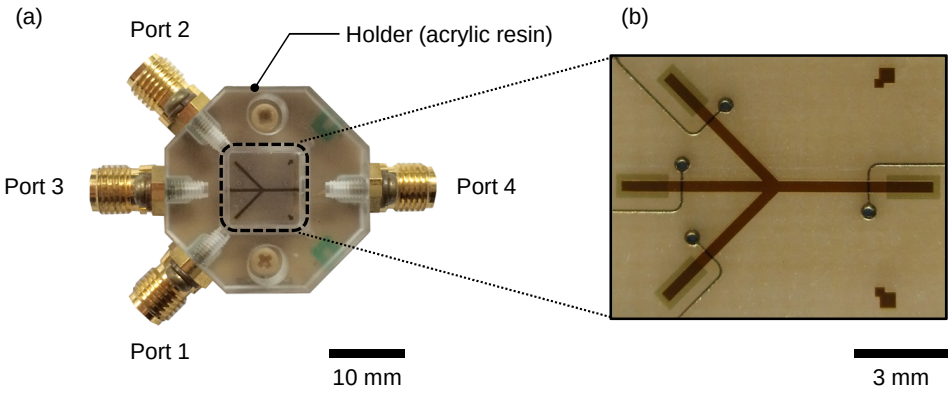

Figure 6.8 Photographs of the device under test with Ψ-shaped FV-SW interferometer. (a) SW transducer. (b) Enlarged image of fabricated interferometer.

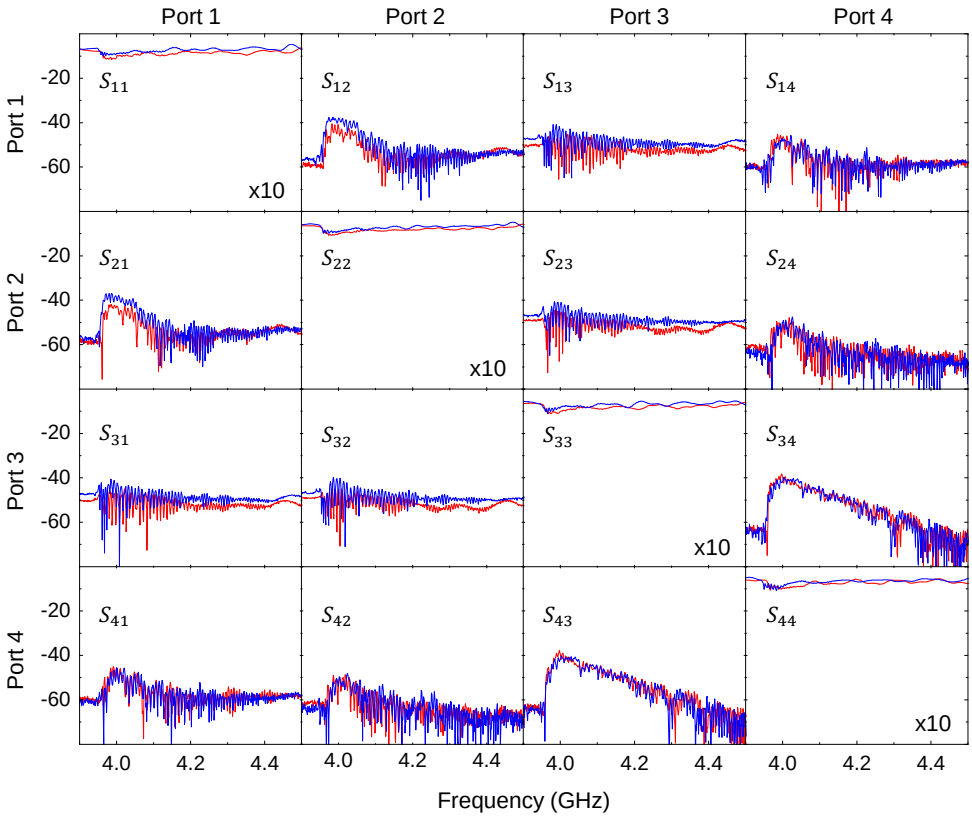

Figure 6.9 Transmission spectra of the Ψ-shaped FV-SW interferometers. Red and blue curves represent the waveguide fabricated by phosphoric acid etching and micro-sandblast etching, respectively. $H_0 = 3095$ Oe is applied and the temperature of substrate is remained at 27.0°C. Spectra of S_{11}, S_{22}, S_{33}, and S_{44} are enlarged by a factor of 10.

flow from the port 1, port 2 and port 3, respectively. Spectra of S_{41} and S_{42} exhibited similar transmission gain, but that of S_{43} was remarkably different. This difference was originated in the geometry of Ψ-shape. Even though measured substrates were fabricated by different processes with resulting geometries shown in Table6.4, observed spectra were almost the same. Thus the fabrication processes and resulted geometrical difference were minor effect on the SW propagation. Detail of transmission spectra is further analyzed in the end of this chapter.

6.3 Demonstration of Reconfigurable Functionality

6.3.1 Experimental Setup

In Fig.6.10, the block diagram of the constructed experimental setup is shown. A monochromatic radio frequency signal at the frequency of 4.0 GHz was provided by the signal generator (PSG-1: Keysight, E8757C). The signal was divided by the divider (D1) into 4 paths, and one path was terminated. Remaining signals were modulated by the phase shifters and attenuators to obtain the target phase θ_i and equivalent input amplitude A_{in} to demonstrate the reconfigurable functionality. During the experiment, the control phase θ_3 was switched only one time to change gate function as derived in Eq.6.4 and Eq.6.5. On the other hand, θ_1 and θ_2 were swept from 0° to 360° with 10° increments to investigate the behavior of the interferometer. The total combination of θ_1 and θ_2 yielded of 1,369 measurements. According to this large number of measurements, the programmable delay line (PDL: Colby, PDL-200A-625PS) was introduced. This equipment automatically controlled θ_1 and θ_2 independently with the accuracy of 0.043°. Then modulated signals were divided by dividers (D2) to monitor the condition of input signals. Divided signals S_1, S_2, and S_3 were connected to the oscilloscope (OSC: Tektronix, DSA70804). Other paths were connected to the radio frequency switches (RFS: Keysight, 44476A with switching module 3499B). As shown in Fig.6.9, S_{41}, S_{42} and S_{43} exhibited different transmission intensities due to the waveguide structure. Amplitudes of input signals were independently adjusted by attenuators, so that each output amplitude from different input ports was normalized to about 10 mV. This adjustment required each input port to be excited selectively, while other input ports were terminated. This switching was done by the RFS. Since the RFS ensured the good reproducibility for reconnection of the signal paths, phase error due to the adjustment was completely diminished. Finally, all input signals were injected into the DUT which was placed in the electromagnet. Applied magnetic field H_0 was adjusted by the current source (CS: Keysight, N5750A) with the feedback signal from the Gauss meter (GM: F.W. Bell, 7030). Resulting output signal from the DUT was amplified by a factor of 30 dB, by using the microwave amplifier (AMP: Amplifier research, 1S1G4A). This amplified signal S_0 was observed by the OSC, then the output amplitude A_0 and phase θ_0 were evaluated.

Trigger signal at frequency of 2.0 GHz was supplied by the extra signal generator (PSG-2: Keysight, 83732A). All input ports of the OSC were occupied by S_1, S_2, S_3, and S_0. During the measurement, these signals cannot provide a constant timebase because

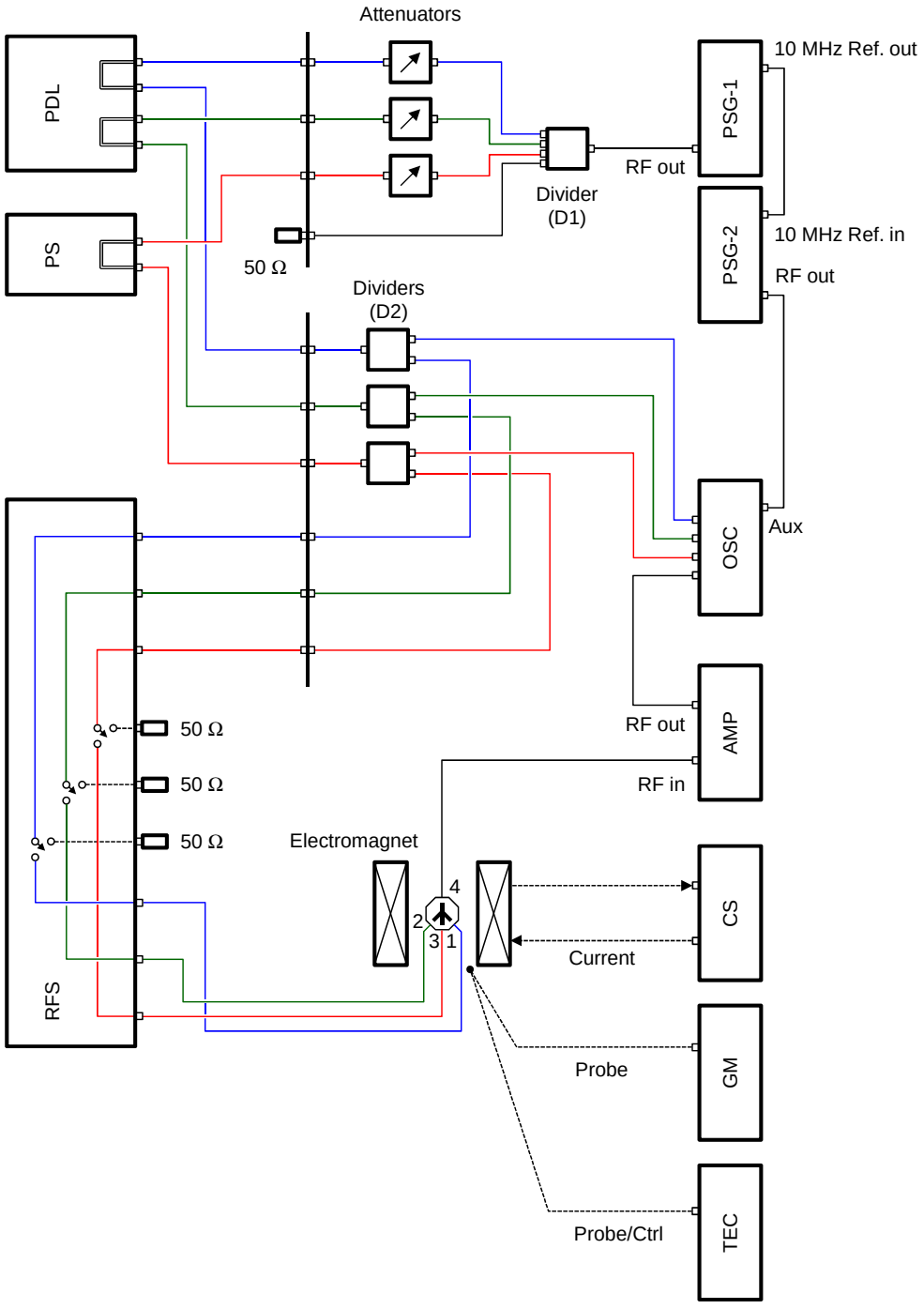

Figure 6.10 Setup for the 3 wave interferometry. Blue, green and red lines represent signal paths for port 1, port 2, and port 3, respectively. Abbreviations are as follows: PSG (pulsed signal generator), OSC (oscilloscope), AMP (amplifier), CS (current source), GM (Gauss meter), TEC (thermoelectric controller), PDL (programmable delay line), PS (mechanical phase shifter), and RFS (radio frequency switch).

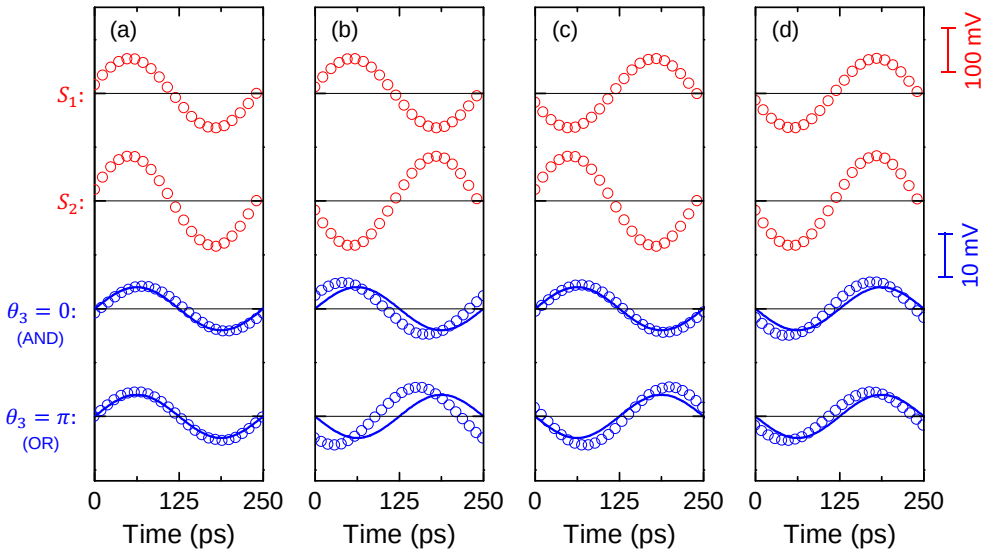

Figure 6.11 Experimental results of 3 wave interferometry of FV-SWs with different input phases: (a) $\theta_1 = 0$, $\theta_2 = 0$, (b) $\theta_1 = 0$, $\theta_2 = \pi$, (c) $\theta_1 = \pi$, $\theta_2 = 0$, and (d) $\theta_1 = \pi$, $\theta_2 = \pi$ with $H_0 = 3050$ Oe. Red circles represent input waveforms of S_1 and S_2. Blue circles represent the resulting waveform with $\theta_3 = 0$ and π. Blue bold lines show calculated waveforms with $A_i = 10$ mV in peak to peak, by using Eq.6.2 and Eq.6.3. Input and output waveforms are shown in different scales. Output waveforms with $\theta_1 = 0$, $\theta_2 = 0$, and $\theta_3 = 0$, and with $\theta_1 = \pi$, $\theta_2 = \pi$, and $\theta_3 = \pi$ are normalized by factor 1/3.

of the phase modulation. Thus auxiliary input was used to receive the timebase provided by PSG-2. Since PSG-2 was independent of the measurement system, constant timebase was generated. Due to the limited bandwidth of the auxiliary input, the trigger signal was given at 2.0 GHz. To diminish timing gritter, PSG-1 and PSG-2 were synchronized by the 10 MHz reference signal. By using this technique, absolute phase values can be determined based on the constant timebase.

6.3.2 Effect of Wavenumber Deviation

In Fig.6.11, experimental results of the 3 wave interferometry are displayed. In this experiment, the interferometer fabricated by the micro-sandblast etching was employed. Blue bold lines show calculated waveforms against various input phases θ_1, θ_2, and θ_3. Since θ_3 belongs to the control input, output waveforms are separately shown in the case of $\theta_3 = 0$ and π. When $\theta_3 = 0$, calculated waveform was reversed only in Fig.6.11d. On the other hand, those of $\theta_3 = \pi$ were reversed except for Fig.6.11a. The former condition yields of the AND operation, and the later condition yields of the OR operation. This behavior is shown in Table6.1 and underlies the function of majority gate. Nevertheless, in

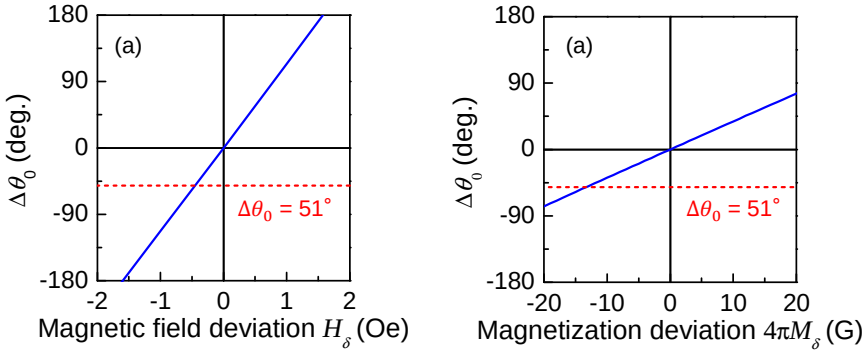

Figure 6.12 Phase deviation $\Delta\theta_0$ on (a) magnetic field deviation H_δ and (b) magnetization deviation $4\pi M_\delta$ with following parameter set: $H_0 = 1368$ Oe, $4\pi M_S = 1760$ G, $f = 4$ GHz, $W = 350$ μm, $L_\mathrm{I} = L_\mathrm{O} = 3$ mm, and $d = 10$ μm. Phases of fundamental mode ($m = 1$) are calculated. Red lines represent a reference of $\Delta\theta_0 = 51°$.

the experiment, measured waveforms exhibited horizontal shift resulted in the deviation output phase θ_0. The maximum deviation of $\Delta\theta_0 = 51°$ was confirmed in Fig.6.11b.

Since an input phase θ_i was carried to the junction area and the resulting phase θ_0 was further carried to the port 4 by propagating wave with wavenumber k, Eq.6.2 can be strictly expressed by replacing $\theta_i \to \theta_i - kL_\mathrm{I}$, and by replacing $\theta_0 = \theta_0 - kL_\mathrm{O}$, respectively. Actual measured phase θ_0 was thus given by

$$\theta_0 = \tan^{-1}\left\{\sum_{i=1}^{N} A_i \sin(\theta_i - kL_\mathrm{I}) \Big/ \sum_{i=1}^{N} A_i \cos(\theta_i - kL_\mathrm{I})\right\} - kL_\mathrm{O}. \tag{6.12}$$

Even though kL_I and kL_O were tuned to an integer multiples of 2π, k was sensitive to environmental change such as temperature drift and magnetic field deviation. The extra phase shift $\Delta\theta_0$ of Eq.6.12 by deviation of k was derived by conducting differential of k. The result became

$$\Delta\theta_0 = -(L_\mathrm{I} + L_\mathrm{O})\Delta k. \tag{6.13}$$

According to Eq.6.11, a value of k is a function of the waveguide thickness d. Eq.6.13 is further approximated for obtaining the aspect of deviation.

$$\Delta\theta_0 \sim -\frac{L_\mathrm{I} + L_\mathrm{O}}{d} k_d(H_\delta, 4\pi M_\delta), \tag{6.14}$$

where k_d is wavenumber normalized by d, which is a function of magnetic field deviation H_δ and that of magnetization $4\pi M_\delta$. This result indicates the instability of θ_0 is

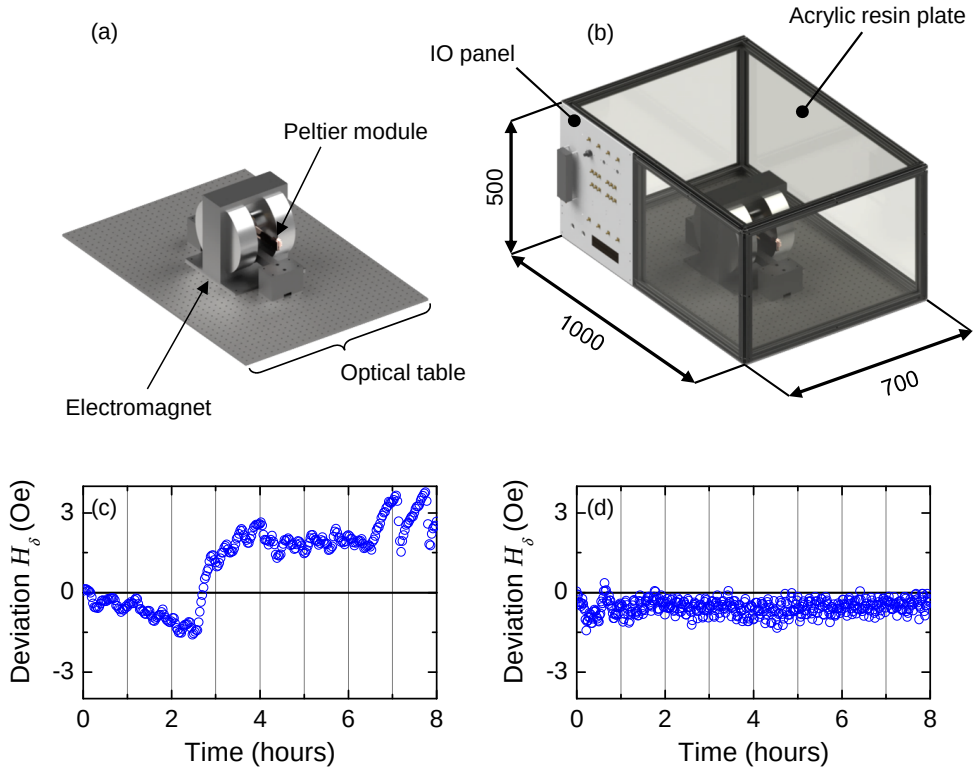

Figure 6.13 Improvement of measurement system. (a) Schematization of original setup. Temperature is controlled by the Peltier module. (b) Schematization of setup enclosed by 5 mm-thick acrylic resin plate. IO panel provides interface with DUT and provides frame ground for microwave components. (c) Temperature drift of H_δ in the original setup with $H_0 = 2700$ Oe, and (d) that in the setup with acrylic resin cabinet with $H_0 = 3000$ Oe.

enhanced by geometrical factors, and thicker and shorter waveguide is preferable in the viewpoint of robustness. However, thicker waveguides usually extend wavelength, and shorter waveguides suppress characteristics of wave, e.g. application of AMLs. Preferably, dispersion curve of k_d is rather modulated in order to have less sensitivities for H_δ and $4\pi M_\delta$. For example, application of SWDC with parallel H_0 configuration might be one of the solutions (§4.2).

In Fig.6.12, calculated dependences of $\Delta\theta_0$ on H_δ and $4\pi M_\delta$ are shown. Red reference line of $\Delta\theta_0 = 51°$ was the maximum value observed in the experiment shown in Fig.6.11. A value of $\Delta\theta_0$ exhibited large sensitivity on H_δ as shown in Fig.6.12a, in which H_δ of only 0.45 Oe caused phase deviation of 51°. Generally, such small deviation can be easily caused. In contrast, $\Delta\theta_0$ was relatively robust for $4\pi M_\delta$. Taking a value of -2270 ppm/°C into account, temperature drift of about 3.4°C would be required to give rise in $\Delta\theta_0 = 51°$. As shown in Fig.6.13a, temperature of the DUT was precisely controlled by the Peltier module with a standard deviation less than 0.1°C. Accompa-

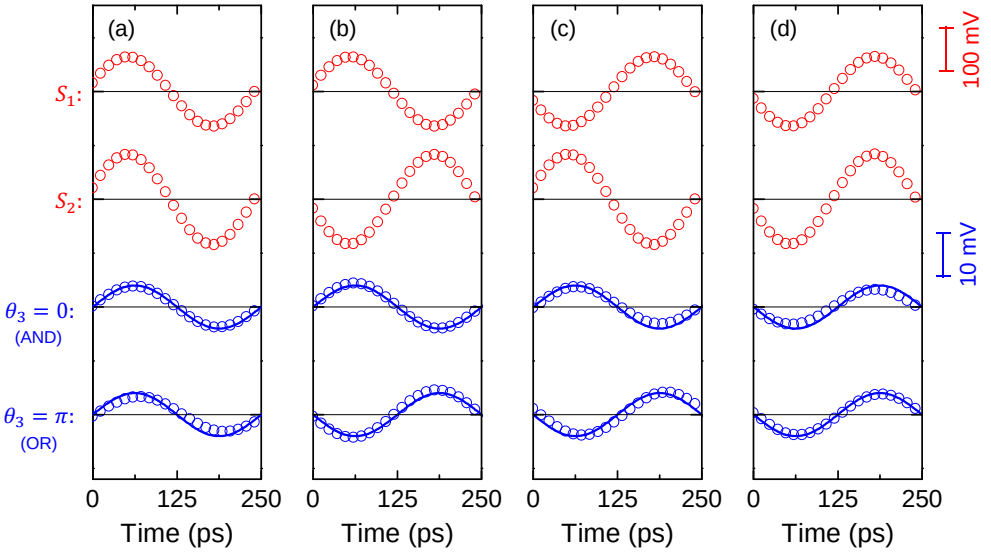

Figure 6.14 Experimental results of 3 wave interferometry with acrylic resin cabinet and chiller. (a) $\theta_1 = 0$, $\theta_2 = 0$, (b) $\theta_1 = 0$, $\theta_2 = \pi$, (c) $\theta_1 = \pi$, $\theta_2 = 0$, and (d) $\theta_1 = \pi$, $\theta_2 = \pi$ with $H_0 = 3095$ Oe. All waveforms are shown in the same manner as Fig.6.11.

nied magnetization drift was negligible. Thus the dominant reason of phase deviation was supposed to be H_δ.

A value of H_δ of the electromagnet was monitored for 8 hours with constant current. The result is shown in Fig.6.13c. Fluctuation of magnetic field exceeded 1.6 Oe in standard deviation, and oscillation with certain periodicity was confirmed. Since the iron core of electromagnet was slightly sensitive to temperature, change of its permeability brought small H_0 deviation. Accordingly, temperature of the iron core was also stabilized as follows:

- **Heat convection**
  Heat convection due to air conditioning system influenced the housing of the electromagnet with longer period. Air convection was suppressed by enclosing the entire setup with acrylic resin cabinet. Schematic image of constructed cabinet is displayed in Fig.6.13b.

- **Cooling water**
  Temperature of cooling water drastically influenced the iron core with shorter period. Inverter controlled chiller (Orion, RKE750A1-V) was introduced to supply cooling water with the constant temperature. Cooling temperature was set to 15°C to keep the chiller in loaded condition for precision of 0.1°C.

After these improvements, standard deviation of H_δ was significantly reduced to 0.2 Oe, which was close to the resolution of the Gauss meter in this measurement range.

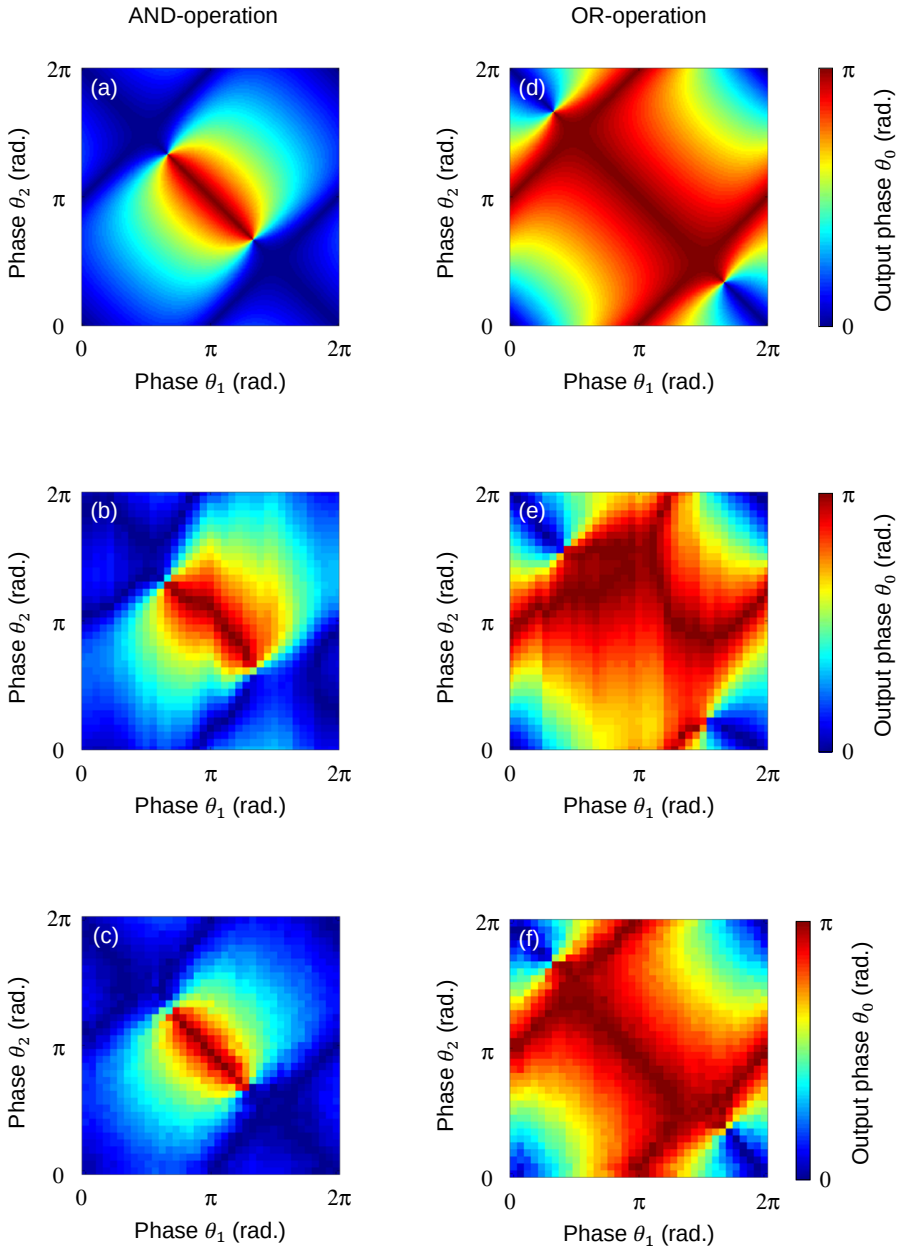

Figure 6.15 Output phase θ_0 for various combinations of θ_1 and θ_2. The results of AND operation obtained by (a) calculation, (b) experiment in Fig.6.13a, and (c) experiment in Fig.6.13b. The results of OR operation obtained by (d) calculation, (e) experiment in Fig.6.13a, and (f) experiment in Fig.6.13b. Color represent output phase shift θ_0.

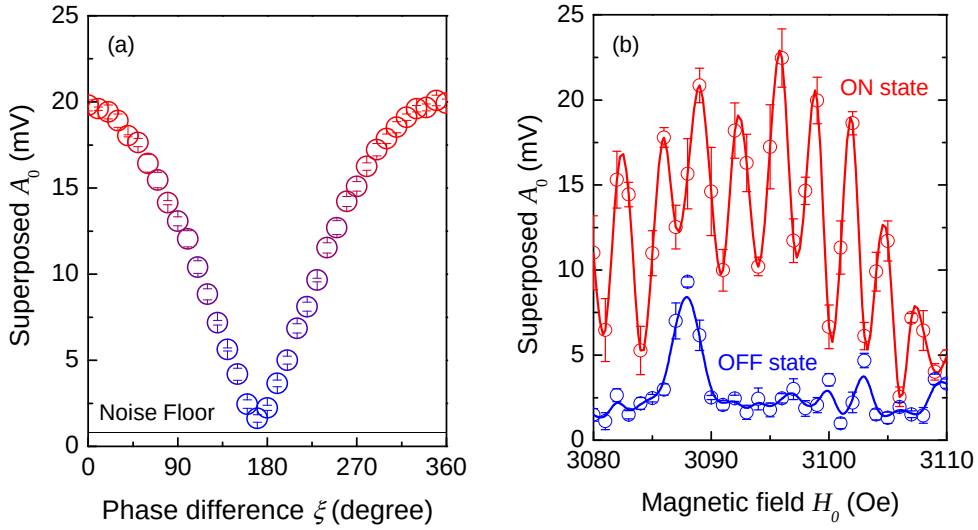

Figure 6.16 XNOR operation with the Ψ-shaped FV-SW interferometer. Port 3 is terminated. (a) Dependence of output amplitude A_0 in peak to peak on input phase difference ξ with $H_0 = 3095$ Oe. (b) Robustness of ON state and OFF state against H_0. Error bars represent standard deviation of five duplicated measurements.

This is graphed in Fig.6.13d. Almost constant H_0 was obtained. By using acrylic resin cabinet and chiller, 3 wave interferometry was again carried out. The experiment was started after 3 hours of stabilization process with $H_0 = 3000$ Oe for warming up of the electromagnet. Results are shown in Fig.6.14. No remarkable $\Delta\theta_0$ was confirmed, and reliability of operation was significantly improved. In this setup, majority function was experimentally demonstrated with the Ψ-shaped FV-SW interferometer.

Finally, output phase θ_0 was investigated for intermediate input values in quire detail. Phases of θ_1 and θ_2 were independently swept from 0° to 360° with 10° increments, while θ_3 was fixed to provide either AND or OR operation. Results are displayed in Fig.6.15. Without acrylic resin cabinet and chiller, remarkable distortion of θ_0 from the calculated results was confirmed both in the case of AND and OR operation (Fig.6.15b and e), due to temperature deviation of the iron core of electromagnet. However, such distortion was clearly suppressed in the improved setup (Fig.6.15c and f). Thus reliability of the 3 wave interferometry was proved for every intermediate values of θ_1 and θ_2. This results indicated the capability of analog computing, in which intermediate phase values can be used for data input and output.

6.3.3 XNOR Operation by 2 Wave Interferometry

In the previous part, spin wave majority function was successfully demonstrated by the Ψ-shaped FV-SW interferometer. In addition, XNOR operation given by 2 wave

Table 6.5 Truth table of phase-amplitude converter.

#L	θ_0	θ_r	A_0
1	0	π	OFF
2	π	π	ON

interferometry (§5.4) can be also available in the Ψ-shaped interferometer by terminating one port. In principle, amplitude signal A_0 is robust for wavenumber drift Δk. By replacing $\theta_i \to \theta_i - kL_I$ in Eq.6.3, the output amplitude A_0' becomes

$$A_0' = \sum_{i=1}^{N} \left\{ A_i^2 + \sum_{i \neq j} A_i A_j \cos\Big((\theta_i - kL_I) - (\theta_j - kL_I)\Big) \right\} = A_0. \tag{6.15}$$

From this consideration, we immediately understand A_0 is independent of k. By taking XNOR function with the reference phase $\theta_r = \pi$, one can convert output phase θ_0 to amplitude A_0 as shown in Table6.5. Such phase-amplitude converter might be useful to output the resulting logic value to external circuit. It is noteworthy the result of conversion is robust for disturbances, since the contribution of kL_I is canceled between θ_0 and θ_r.

Result of the 2 wave interferometry is shown in Fig.6.16a. Resulting A_0 exhibited the maximum value at in-phase condition, while that exhibited the minimum value at anti-phase condition. This behavior was comparable to that of the 2 wave interferometry in the linear waveguide, and satisfied functionality of Table6.5. To use this output as a phase-amplitude converter, in the realistic case, it is required to balance the amplitudes of two input waves, and to match the total input waveguide length L_I. Specific design is outside the scope of this chapter.

Next, H_0 stability was also tested. Stability was measured for the states #L1 (ON) and #L2 (OFF). Corresponding result is displayed in Fig.6.16b. According to Eq.6.15, A_0 should be stable against to change of k. Nevertheless, experimental result exhibited remarkable deviation. This reason was clearly appeared in the spectra of S_{41} and S_{42} shown in Fig.6.9. Even though optimized TMOLs were applied to the waveguide ends to terminate backscattering, non-negligible ripples were confirmed. In addition, behavior of the OFF state was completely different compared to that of the linear waveguide shown in Fig.5.2b. In the case of the linear waveguide without TMOLs, such deviation was confirmed only on the ON state. On the other hand, in the Ψ-shaped interferometer, irregular A_0 was confirmed at $H_0 = 3088$ Oe. It should be noted that error bar was small, indicating the result was not appeared accidentally.

Considering this result, behavior of SWs in the junction area of Ψ-shaped interferometer might be different from that in the linear waveguide. To understand the flow of SWs in the device plane, this behavior was further analyzed by using electromagnetic simulation.

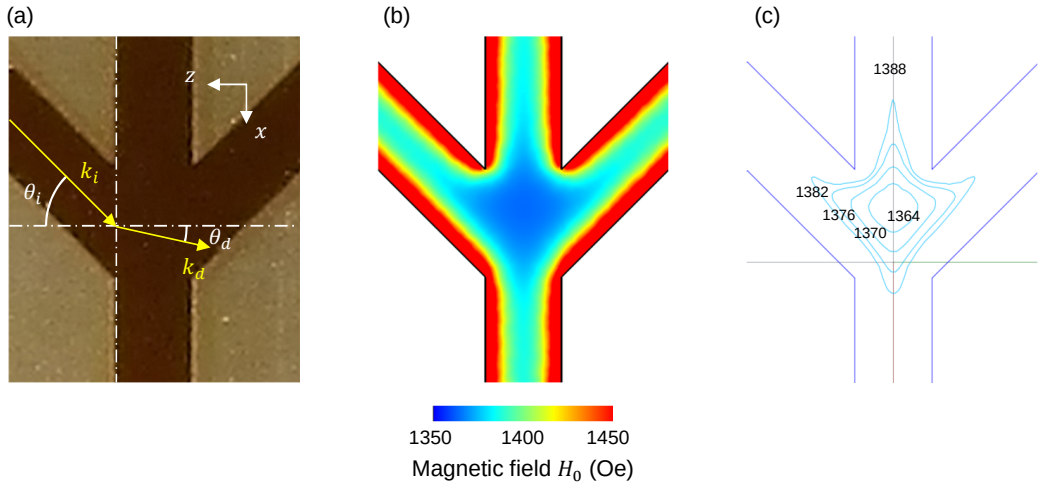

Figure 6.17 Model of the junction area. (a) SW diffraction based on Snell's law. Given k_i and k_d denote incident and diffracted wavenumber. (b) Calculated effective magnetic field distribution under $H_0 = 3095$ Oe and $4\pi M_S = 1749$ G. (c) Contour plot of $H_0 - H_d$ used in HFSS simulation. Numbers represent value of $H_0 - H_d$ for each domain boundary.

6.4 Flow of SWs in the Junction Area

6.4.1 Spin Wave Diffraction

As shown in Fig.6.9, transmission spectra of S_{41} and S_{42} exhibited remarkably lower efficiency than that of S_{43}, and thus the resulted spectra became sensitive to slight ripples due to change of wavelength. Since S_{41} and S_{42} represent the flow of oblique incident to the junction area, the effect of oblique incidence is worth to be discussed. In Fig.6.17a, model of wave flow in the junction area is illustrated. Since SWs are kind of wave, its propagation through a boundary can be expressed by Snell's law[178]

$$\theta_d = \sin^{-1} \frac{k_i}{k_d} \sin \theta_i, \tag{6.16}$$

where k_i is incident wavenumber, and k_d is diffracted wavenumber. It is clear that a lower θ_d increases the spin wave flow toward port 2, and a higher θ_d increases the spin wave flow toward the output port 4. Since the flow toward port 2 represents backflow of information to another input port, this flow should be prohibited especially from the viewpoint of the concatenation of denser. Since θ_d is monotonically increases with θ_i, choice of lower incident angle is quite reasonable. However, the limitation of incident angle yields of the restriction on topology of network, and other options not restricted to the geometrical parameters are rather preferable. On the other hand, the factor k_i/k_d is also able to control $theta_d$. In the junction area of Ψ-shaped interferometer, difference

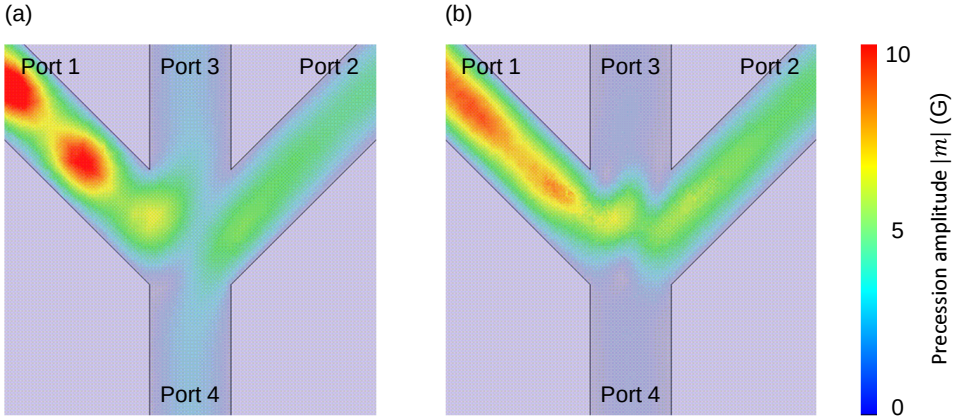

Figure 6.18 Effect of demagnetizing field on the wave flow in the junction area. (a) Homogeneous $H_0 = 1388$ Oe. (b) Inhomogeneous $H_0 - H_d$ with the distribution shown in Fig.6.17c. Only port 1 is excited at 4 GHz with 1 mW. Color represents intensity of precession.

of k_i and k_d was given by following factors:

1. Lateral confinement of propagating waves in the ridge waveguide,
2. Inhomogeneity of the shape magnetic anisotropy.

As shown in Fig.6.3c, enhancement of k_d in the junction area can be explained by the contribution of lateral confinement of waves within the ridge waveguide. Since an incident wave came from waveguides with $W = 350$ μm, the value of $k_i = 3.7 \times 10^3$ m^{-1} was given at internal magnetic field $H_0 - H_d = 1388$ Oe. In the junction area, the waveguide was extended in x-axis, and the broadening of apparent width suppressed the lateral confinement of waves. Thus the propagation mode became almost the same as that of $m = 0$. Accordingly, wavenumber was extended to $k_d = 9.7 \times 10^3$ m^{-1} within the junction area. The extension of diffracted wavenumber limited the diffraction angle θ_d to 15.7°. The calculated spin wave propagation is shown in Fig.6.18a. It is clearly visible that the intensity of propagating wave was larger toward port 2, rather than that toward port 4. However, spin wave propagation toward port 4 was still significant.

As discussed in §3.2, a change of waveguide geometry further induced an inhomogeneity of the shape magnetic anisotropy, yielding in the inhomogeneous demagnetization field H_d. Internal magnetic field $H_0 - H_d$ inside the waveguide was analyzed by the finite element method (COMSOL Multiphysics). The result is displayed in Fig.6.17b. From the result, remarkable inhomogeneity of $H_0 - H_d$ was confirmed especially in the junction area. In this area, intensity of magnetic field was reduced over 20 Oe due to the shape magnetic anisotropy. Such inhomogeneity was not appeared in the linear waveguide. This is one of important differences between type-I topology and type-II topology (Fig.1.4), which is originated in the magnetic waveguide. In general, smaller magnetic

field increases k at specific frequency, and thus the decrease in k_i/k_d yielded of more smaller θ_d angle. On the other hand, in the case of vertical incidence $\theta_i = 0$, resulted θ_d becomes always zero. Thus wave flow from the port 3 to port 4 was not affected, but those from the port 1 and port 2 were strongly affected. Inhomogeneous distribution of $H_0 - H_d$ was taken account of electromagnetic simulation. Since a stand-alone license of ANSYS HFSS ver 16.1 cannot include $H_0 - H_d$ distribution directly, Fig.6.17b was divided into sub-domains according with the contour plot shown in Fig.6.17c. Resulted wave flows are shown in Fig.6.18b. When inhomogeneous demagnetizing effect was considered, the wave flow toward the port 4 was almost suppressed. By using the minimum value of $H_0 - H_d = 1364$ Oe at the junction area, the diffracted wavenumber was further extended to $k_d = 1.59 \times 10^4$ m^{-1}. This values led $\theta_d = 9.6°$. Such small θ_d was no longer capable of the wave flow toward the port 4. In addition, such demagnetizing effect could explain the irregular OFF state in Fig.6.16b, since a distribution of H_d was H_0 dependent.

Transmission spectra of the Ψ-shaped interferometer were calculated using the electromagnetic simulation to include this inhomogeneous shape magnetic anisotropy. Results are shown in Fig.6.19, together with the transmission spectra of the Ψ-shaped interferometer fabricated by the micro-sandblast etching. Calculated results agreed well with the experimental results. In the calculation, the internal magnetic field distribution shown in Fig.6.18c was applied. In addition, the extrinsic damping $\Delta H_0 = 1.9$ Oe was introduced to fit transmission intensities. Without considering this, transmission intensities overcame -40 dB in the calculation, and ripples were almost suppressed thanks to TMOLs. Such results were already shown for S_{41}, S_{42}, and S_{43} in Fig.6.6. Thus the extra propagation loss due to the ΔH_0 drastically reduced the signal level to below -40 dB. Such parameter was not used in the calculation of the linear waveguide, but the result showed good agreement with the experimental result as shown in §5.4. The linear waveguide was fabricated by mechanical dicing (DAD321, Disco), thus tapering angle of the waveguide fringe was $\sim 90°$. On the other hand, that of the waveguide fabricated by micro-sandblast etching was 52.1°. The electromagnetic simulation with such tapering effect yielded in the slight change of transmission spectra, but strong attenuation cannot be explained. Damage on sidewalls of the ridge waveguide during the etching process might explain the results, but quantitative evaluation of damage, e.g. roughness, on sidewalls was difficult. Accordingly, ΔH_0 is just an empirical parameter at present, and further investigation of the mechanism will give hint to improve performance of majority gate.

6.4.2 Core-Clad Waveguide

Reduction of θ_d due to the lateral confinement of waves and the inhomogeneity of shape magnetic anisotropy is not avoidable as long as the ridge waveguide is used, and thus conventional ridge waveguides are no longer proper for the junction of spin wave device networks. To avoid a deviation of shape magnetic anisotropy, waveguides should be formed within a solid film without changing magnetization. In the optical fiber, optical

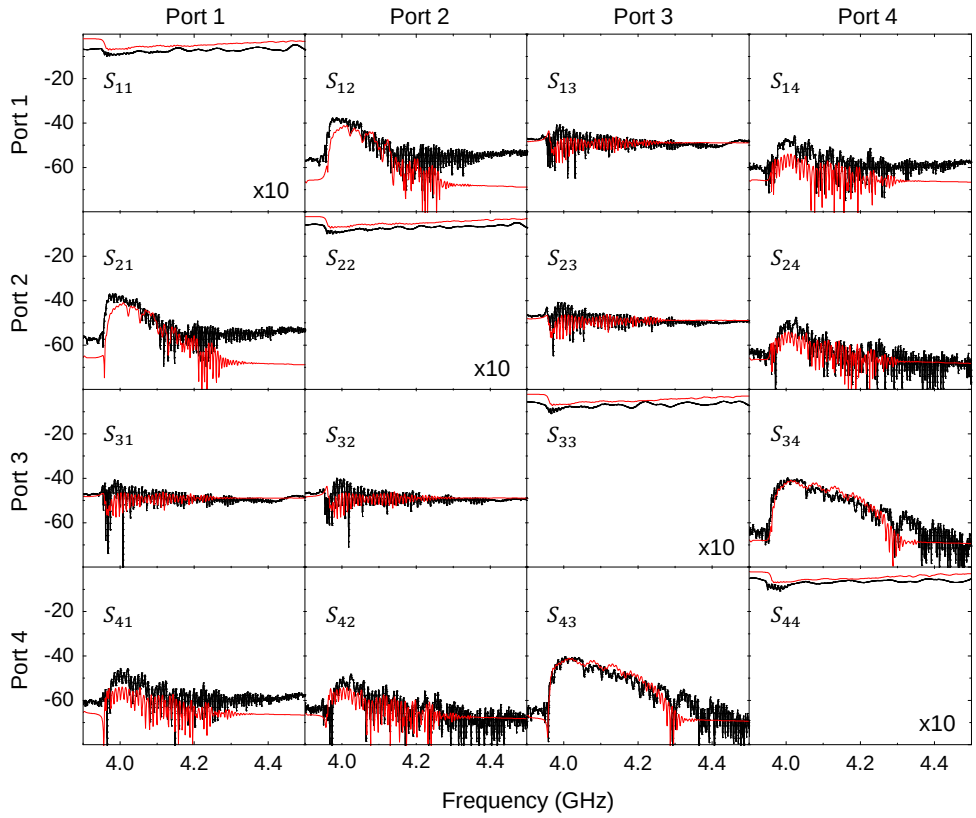

Figure 6.19 Transmission spectra of the Ψ-shaped FV-SW interferometers. Black and red curves represent transmission spectra of the waveguide fabricated by micro-sandblast etching with $H_0 = 3095$ Oe and calculated by electromagnetic simulation with demagnetizing effect and extrinsic damping $\Delta H_0 = 1.9$ Oe. Spectra of S_{11}, S_{22}, S_{33}, and S_{44} are enlarged by a factor of 10.

waves are transmitted in the core region, where the refractive index is greater than surroundings called clad. Since a higher refractive index yields of a higher wavenumber, the relation of core-clad structure is just like a BS-MS slabs where the wavenumber of BS slabs is about double of MS slabs. It is noteworthy that metalization of surface does not change the magnetization property of the waveguide. Thus such core-clad structures can form the junction area without lowering of θ_d due to the change of shape magnetic anisotropy. In addition, magnetization pinning is not occurred at the interface of BS slab to MS slab, and thus the effect of lateral confinement could be suppressed.

The proposed model of core-clad structure is shown in Fig.6.20a. In this structure, a YIG disk partially covered by 100 nm-thick gold was placed at the center of the Ψ-shaped interferometer. As shown in Fig.5.15a, the wavelength of MS slab approaches to that of BS slab when gold thickness is below 10 nm, the gold thickness of clad layer should be over 100 nm to have enough change in the wavenumber. Since the demagnetizing field

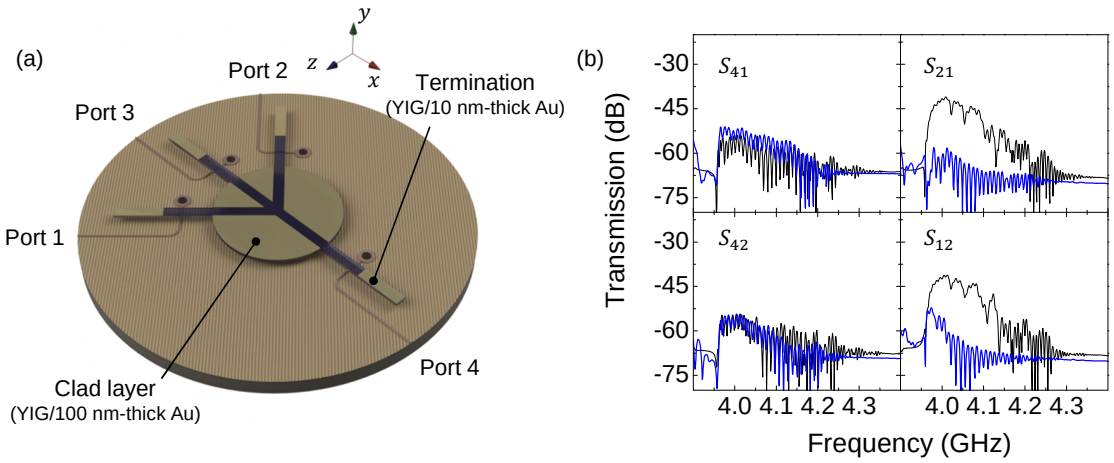

Figure 6.20 Core-Clad waveguide composed of BS-MS slabs. (a) Schematic illustration of proposed model. In the center of the Ψ-shaped interferometer, a YIG disk partially covered by 100 nm-thick gold is placed instead of the ridge waveguide. Radius of the disk is 2 mm. (b) Calculated transmission properties of the oblique incident paths. Blue and black curves represent transmission properties of the core-clad waveguide and the ridge waveguide, respectively.

is attenuated along the fringe of magnetic waveguide, the internal field $H_0 - H_d$ in the junction area becomes homogeneous in this structure. Calculated transmission spectra for the oblique incident paths of interest are shown in Fig.6.20b. Black curves represent that of the ridge waveguide calculated in Fig.6.19. In the ridge waveguide, transmission efficiency was higher in S_{21} and S_{12} than those in S_{41} and S_{42} due to the lowering of θ_d. Therefore large amount of the input signal was returned to another input port. On the other hand, transmission intensities of S_{21} and S_{12} were drastically reduced in the core-clad waveguide, and transmission intensities of S_{41} and S_{42} overcame those of S_{21} and S_{12}.

Nevertheless, increase of intensities of S_{41} and S_{42} were rather low for the drastic decrease in intensities of S_{21} and S_{12}. Thus reflectivity of FV-SWs at the interface of BS slab to MS slab was analyzed in detail. The model of analysis is shown in Fig.6.21a. Incident wave, reflected wave, and transmitted wave at the interface are represented by scalar potentials Ψ. At the interface $x = x_0$, continuity of tangential component of magnetic field h_z and normal component of magnetic flux b_x were considered as boundary conditions. Since $\Psi \propto e^{i(\omega t - \boldsymbol{k}\cdot\boldsymbol{r})}$, the magnetic field $\boldsymbol{h}$ is given by

$$\boldsymbol{h} = -\boldsymbol{\nabla}\Psi = i\boldsymbol{k}\cdot\boldsymbol{r}\Psi = \begin{pmatrix} h\cos\theta \\ 0 \\ h\sin\theta \end{pmatrix}. \tag{6.17}$$

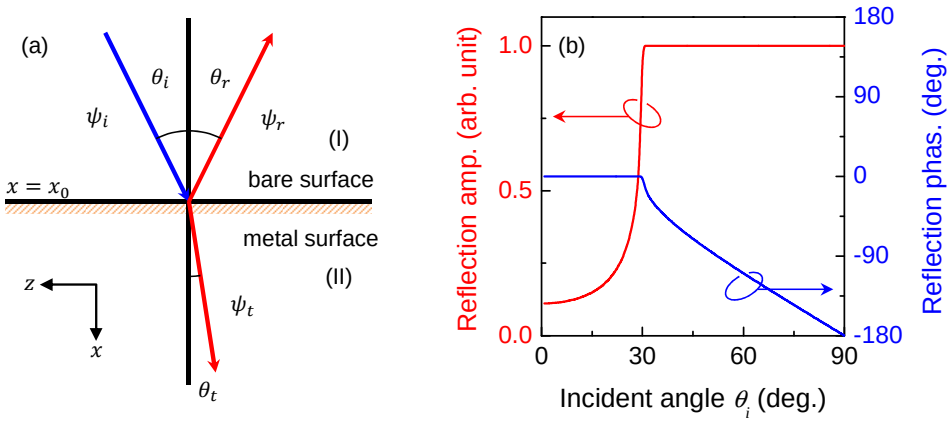

Figure 6.21 Reflectivity of spin waves at the boundary of BS slab to MS slab. (a) Schematic illustration of boundary. Labels Ψ_i, Ψ_r, and Ψ_t show the scalar potential of incident wave, reflected wave, and transmitted wave, respectively. (b) Reflectivity spectra against incident angle θ_i. Red and blue curves represent reflected amplitude and phase of Ψ_r, respectively.

Since the slab is magnetized along y-axis, the magnetic flux $\boldsymbol{b}$ is given by

$$\boldsymbol{b} = \bar{\mu}_G \boldsymbol{h} = \begin{bmatrix} \mu & 0 & -i\kappa \\ 0 & 1 & 0 \\ i\kappa & 0 & \mu \end{bmatrix} \begin{pmatrix} h_x \\ 0 \\ h_z \end{pmatrix} = \begin{pmatrix} \mu h_x - i\kappa h_z \\ 0 \\ i\kappa h_x + \mu h_z \end{pmatrix}. \tag{6.18}$$

Carefully considering the direction of the wave vectors shown in Fig.6.21a, following set of equations were obtained from Eq.6.17 and Eq.6.18.

$$h_i \sin\theta_i + h_r \sin\theta_r = h_t \sin\theta_t, \tag{6.19}$$

$$(\mu\cos\theta_i + i\kappa\sin\theta_i)\, h_i - (\mu\cos\theta_r - i\kappa\sin\theta_r)\, h_r = (\mu\cos\theta_t + i\kappa\sin\theta_t)\, h_t, \tag{6.20}$$

where h_i, h_r, and h_t are the amplitudes of accompanied magnetic field by incident wave, reflected wave, and transmitted wave, respectively. Therefore reflectivity r at the interface of BS slab to MS slab is derived by

$$r = \frac{h_r}{h_i} = -\frac{\sin\theta_i\,(\mu\cos\theta_t + i\kappa\sin\theta_t) - \sin\theta_t\,(\mu\cos\theta_i + i\kappa\sin\theta_i)}{\sin\theta_r\,(\mu\cos\theta_t + i\kappa\sin\theta_t) + \sin\theta_t\,(\mu\cos\theta_r - i\kappa\sin\theta_r)}. \tag{6.21}$$

It is noteworthy that $\theta_r = \theta_i$ according to the Huygens' principle, and θ_t can be represented by θ_d in Eq.6.16. Thus reflectivity r is uniquely determined from the incident

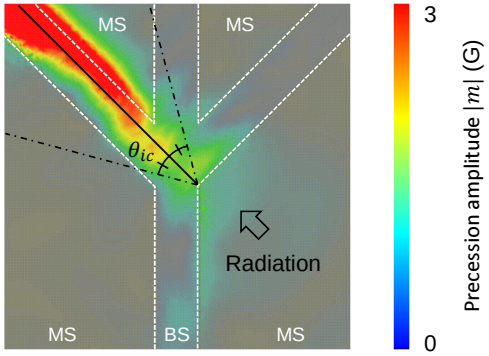

Figure 6.22 Wave flow in the vicinity of the junction area of core-clad waveguide. Wave is injected from the port 1. BS and MS denote BS slab and MS slab with gold thickness of 100 nm. White dot line shows boundary of BS-MS slab, and black broken lines determined by the critical angle θ_{ic} represent incident area resulted in the radiation. Color represents intensity of magnetization precession.

angle θ_i. Calculated result of r is shown in Fig.6.21b. In this calculation, reflection the amplitude was given by $|r|^2$, and phase was given by $\tan^{-1}\mathrm{Imag}(r)/\mathrm{Real}(r)$. As a result, total reflection range was appeared over $\theta_i > \theta_{ic} = 30°$, where θ_{ic} is the critical angle. This is reasonable because $\theta_d = 90°$ was given from Eq.6.16 at $\theta_i = 30°$ when $k_i/k_d = 2$, which means no transmitted wave is appeared beyond the boundary. Thus the core-clad waveguide can steer the FV-SWs in $\theta_i > 30°$.

Simulated wave flow in the vicinity of the junction area is shown in Fig.6.22. Comparing to the wave flow in ridge waveguide shown in Fig.6.18b, the strong diffraction toward port 2 seemed to be suppressed. As expected, lowering of θ_d due to the lateral confinement and inhomogeneous shape magnetic anisotropy was eliminated. Nevertheless, non-negligible radiation from the core-clad waveguide can be confirmed in the junction area. As shown in Fig.6.22, incident angle θ_i of the wave was lower than the critical angle θ_{ic}. Radiated wave outside the BS slab was immediately attenuated due to the significant attenuation length of MS slab with gold thickness of 100 nm. This caused a large insertion loss in S_{41} and S_{42}.

To form ideal junction area against any injection angle for flexibility of network topology, the total reflection range should be obtained regardless of θ_i. Such condition is achieved only when $k_d = 0$ in Eq.6.16, which means magnetization should be pinned at the boundary, i.e. the ridge waveguide. Thus to eliminate the radiation in the junction area, core-clad waveguides should be carefully designed to satisfy $\theta_i < \theta_{ic} = 30°$, accompanying the limitation of network topology. Therefore core-clad waveguides may be better than the ridge waveguides, but still not be the best candidate for the SWD network. On the other hand, use of AMLs instead of the clad structure could help to suppress the radiation, thanks to the formalism of complete band gap in the device plane.[179] Since spin wave propagation is prohibited regardless of θ_i within the complete band gap,

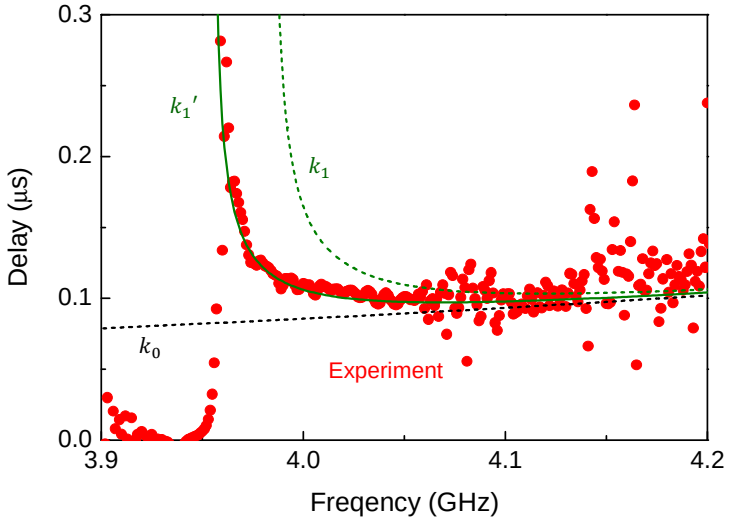

Figure 6.23 Group delay of Ψ-shaped interferometer. Red points represent the experimental result. Points show the average of S_{41}, S_{42} and S_{43} of the interferometer fabricated by micro-sandblast etching under $H_0 = 3095$ Oe. Black and green lines are the results of dispersion analysis with typical parameters $H_0 - H_d = 1388$ Oe and $4\pi M_S = 1749$ G. The label k_0 denotes the wavenumber of the BS slab with infinite width, and k_1 and k_1' denote that of the ridge waveguide with different effective widths.

a sequence of defect can steer the wave flow without the leakage, i.e. line-defect waveguides.[180,181] Unfortunately, presented works were based on arrays of holes, and thus the effect of the shape magnetic anisotropy may be unavoidable. Replacement of the hole array by surface metalization could suppress the change of shape magnetic anisotropy in the junction area. Moreover, diffraction angle θ_d in the junction area could be enhanced by AMLs. In the optical counterpart, a large θ_d of 70° was experimentally demonstrated using AMLs embedded in the junction area.[182] Such phenomenon is known as the superprism effect. In the future, such concomitant use of AMLs would increase propagation efficiencies of the SWD networks.

6.4.3 Transmission Speed

Transmission speed of waves is of equal importance to the efficiency of transmission for information processing. In the end of this chapter, the transmission speed is discussed to evaluate the potential of spin wave majority function. The carrier wave should be modulated to transmit meaningful information, and thus group velocity v_g is important rather than phase velocity v_p. Accordingly, the time required for the single majority operation by the Ψ-shaped interferometer can be estimated as a group delay τ_g of the

signal paths S_{41}, S_{42}, and S_{43}.

$$\tau_g = \frac{L_I + L_O}{v_g} = (L_I + L_O)\left(\frac{d\omega}{dk}\right)^{-1}, \tag{6.22}$$

where $L_I + L_O$ is the total waveguide length, k is the wavenumber, and ω is the angular frequency. According with Eq.3.35, Eq.6.22 can be also given by

$$\tau_g \sim \frac{d}{d\omega} k\,(L_I + L_O) = -\frac{d\theta}{d\omega}, \tag{6.23}$$

where θ is the phase shift within the waveguide. Since the waveguide length was $L_I + L_O =$ 6 mm for S_{41}, S_{42}, and S_{43}, the values of τ_g were basically the same for these paths. Measured group delay τ_g of the Ψ-shaped interferometer is shown in Fig.6.23. A values of τ_g were evaluated by using Eq.6.23 from the measured phase spectra $\theta(\omega)$. For S_{41}, S_{42}, and S_{43}, obtained values of τ_g at 4 GHz were 0.110 μs, 0.113 μs, 0.109 μs, respectively. Thus the averaged $\tau_g = 0.111$ μs was plotted in Fig.6.23. Beyond about 4.05 GHz, strong deviation on τ_g was confirmed because of the contribution of higher lateral modes. Based on this result, the available clock speed of majority operation with the carrier frequency at 4 GHz was estimated as $f_c = 1/\tau_g = 9.01$ MHz. In the commercial parametron units, the maximum clock speed was only $f_c = 140$ kHz due to the limitation of frequency at which a ferrite core was excited.[167] Thus comparing to the parametron technology, available f_c of the majority logic was drastically boosted. Nevertheless, comparing to the today's CMOS elements, the speed of logic operation was quite slow. This is due to the slow group velocity v_g of SWs, which has been rather used as delay lines in the conventional microwave circuit.[11] By using Eq.6.22, $v_g = 5.41 \times 10^4$ m/s was estimated from the experimental data. On the other hand, that of the electromagnetic wave in silicon ($\varepsilon_r = 12$) can be roughly estimated as $v_g = c_0/\sqrt{\varepsilon_r} = 8.66 \times 10^7$ m/s without dispersion, and thus the v_g of SWs was three orders of magnitude slower than that of electromagnetic waves.

Similar dependence was also obtained by the numerical calculation using Eq.6.22, which indicates τ_g can be evaluated from the slope of dispersion curves. The result of calculated τ_g based on Eq.3.29 was overlaid in Fig.6.23 as the black dot line with the label k_0, in which typical BS slab without the lateral confinement was assumed with $H_0 - H_d = 1388$ Oe, $4\pi M_S = 1749$ G, and waveguide thickness $d = 10$ μm. This result agreed with the experimental result at frequencies over 4.1 GHz, but remarkable discrepancy was confirmed around 4.0 GHz. This was due to the contribution of lateral confinement, where the lower band edge was distorted so that flat band was formed as shown in Fig.6.3c, yielding in the reduction of v_g and increase of τ_g. Thus, dispersion curve was recalculated with Eq.6.11 to include the contribution of lateral confinement with the waveguide width $W = 350$ μm, which was used in the experiment. The result was overlaid as the green dot line with the label k_1. In this calculation, increase of τ_g at lower band edge was confirmed, but the calculated delay spectrum of k_1 still showed the

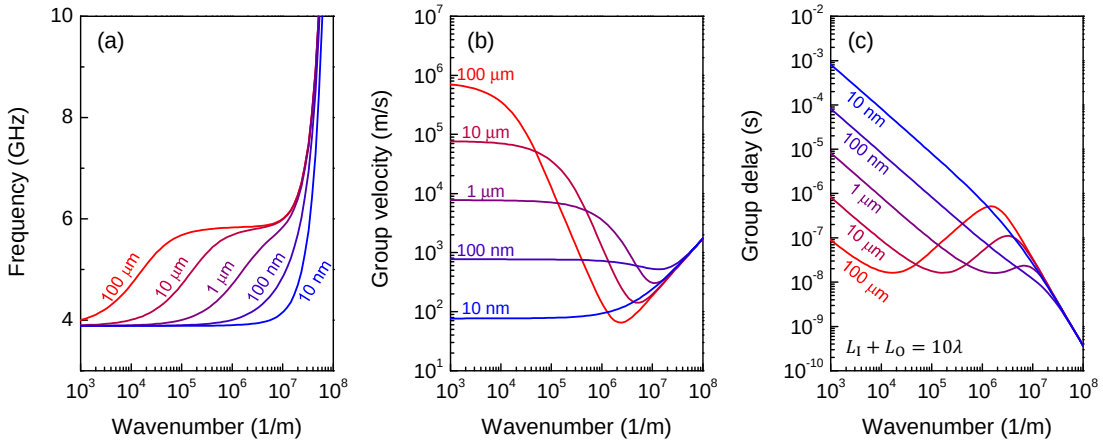

Figure 6.24 Thickness dependence of transmission speed. (a) Dispersion curve. (b) Group velocity. (c) Group delay in the waveguide with the length of 10 λ, where $\lambda = 2\pi/k$ is the wavelength. In all calculations, $H_0 - H_d = 1388$ Oe and $4\pi M_S = 1749$ G are assumed.

mismatch from the experimental result. The effective waveguide width $W' = W + \Delta W$ was introduced to fit the spectrum, where ΔW may denote the increase of effective waveguide width by the Goos-Hänchen effect.[183] As a result, the value of $\Delta W = 250$ μm exhibited perfect fit to the experimental result, which was overlaid as green bold line of k_1'.

Finally, the effect of miniaturization is discussed. Because τ_g is proportional to the waveguide length $L_I + L_O$, reduction of τ_g can be expected by the miniaturization of circuit. However, such miniaturization including the thickness of the waveguide d gives rise in the strong exchange interaction rather than the dipolar interaction. Thus dispersion curves were calculated by Eq.2.39, Eq.2.41, and Eq.2.43 with the typical $\lambda_{\mathrm{ex}} = 3 \times 10^{-16}$ m^2 of YIG. The results are graphed in Fig.6.24a. In this calculation, the effect of lateral confinement and Goos-Hänchen effect were ignored for simplification. In the range of wavenumber over 10^7 m^{-1}, quadratic behavior caused by the propagation of exchange spin waves was confirmed, and the dipole-exchange spin waves appeared within the thicknesses d below 100 nm. By using these curves, group velocity $v_g = d\omega/dk$ was calculated. The results are shown in Fig.6.24b. In the dipolar interaction region, v_g was proportional to the film thickness d, and thus the miniaturization seems to be inefficient because v_g is reduced. On the other hand, such thickness dependence was suppressed within the exchange interaction region. Then, τ_g was estimated according with Eq.6.22. In this calculation, the waveguide length $L_I + L_O$ was supposed to be 10 times longer than the wavelength λ so that the wave behavior is clearly appeared, e.g. control of waves by AMLs requires sufficient waveguide length to include periodic structures in a wavelength scale. The results are shown in Fig.6.24c. As a result, local minima of $\tau_g \sim 10^{-8}$ s was appeared in the dipolar interaction region, regardless of thickness d. When the thickness d was below 100 nm, τ_g was monotonically decreased

with the increase of wavenumber. In the case of CMOS-based implementation, τ_g of such majority gates is around from 10^{-11} to 10^{-10} s.[184,185] Comparing to this, transmission speed was three orders of magnitude slower in the spin wave majority function based on YIG. However, in the exchange interaction region, τ_g can be reduced by several orders of magnitude. Thus, use of exchange spin waves is one of the directions to realize smaller τ_g comparable to the CMOS-based majority gate. According to the calculation, values of τ_g in the order of 10^{-10} s was obtained below $k \sim 6 \times 10^7$ m^{-1} ($\lambda \sim 100$ nm).

It is noteworthy that capable wavenumber k depends on the structure of excitation antenna. According with Fig.2.5c, the primary excitation of 50 μm-wide MSL antenna is ranging in $k \sim 10^4$ m^{-1}, and the waveguide thickness $d = 100$ μm shows the smallest τ_g around this wavenumber. In the case of submicrometer-wide coplanar waveguides, $k \sim 10^6$ m^{-1} was usually reported,[60] and the thickness d ranging from 100 nm to 1 μm seems to exhibit good performance. However, to reduce τ_g in the order of 10^{-10} s, finer antennas reaching to $k \sim 10^8$ m^{-1} are required. Development of such antennas is still challenging opportunity, but may be realized by grating couplers incorporating AMLs into antennas.[23,186]

6.5 Summary

In this chapter, spin wave majority function was demonstrated by using the Ψ-shaped FV-SW interferometer. Among various possibilities of majority gate, the most fundamental functionality of AND/OR operation was experimentally proved. Since these operation is interchangeable by the phase reversal of the control signal, thus the interferometer provided the reconfigurable functionality.

In §6.1, principle of majority logic was presented together with several applications. Majority circuit is capable of being put to full adder circuit, coding network, and neural network. In the past, majority gate-based computer was developed, which was called parametron, but such computers were completely replaced by transistors because of the low frequency and huge power consumption of parametric excitation of ferrite cores. In this work, replacement of the signal carrier by spin waves was aimed at, with expecting the high frequency operation and lower power consumption.

In §6.2, concrete design of the Ψ-shaped FV-SW interferometer was investigated based on the electromagnetic simulation. Waveguide width W, terminator length L_{T}, and thickness of TMOL t_{Au} were precisely chosen to obtain good interferometer. Since wider W was capable of multi mode excitation, this value was limited to 350 μm so that the waveguide became single mode at the excitation frequency of 4 GHz. Precise design of $L_{\mathrm{T}} = 1.5$ mm and $t_{\mathrm{Au}} = 10$ nm yielded the total regeneration from the terminator of less than 5%. Designed ridge waveguide structure was fabricated by two different approaches: phosphoric acid etching and micro-sandblast etching. Significant difference between these fabrication processes on transmission spectra was not confirmed.

In §6.3, the 3 wave interferometry was experimentally investigated by using fabricated Ψ-shaped FV-SW interferometer. In the first trial, non-negligible deviation of

the output phase θ_0 was confirmed. Since each input information was carried by the propagating FV-SWs, deviation of its wavenumber k degraded stability of θ_0. Under the original experimental setup, wavenumber k exhibited strong sensitivity on the magnetic field. Thus, the whole setup was covered by the acrylic resin cabinet and the cooling water supply was replaced by a precise inverter chiller. This improvement yielded the stability of applied magnetic field with the standard deviation of only 0.2 Oe, and stable k resulted in the stable θ_0. In the improved setup, the spin wave majority function was successfully demonstrated. In addition, the 2 wave interferometry was also investigated by using the same device to show a prototype of phase-amplitude converter, but instability to the magnetic field deviation was rather high.

In §6.4, wave flow in the junction area was analyzed in detail by using the electromagnetic simulation. As a result, extrinsic damping $\Delta H_0 = 1.9$ Oe was confirmed in the fabricated interferometer. In addition, SW diffraction in the junction area was modeled by the Snell's law. Lowering of the diffraction angle θ_d was caused by the lateral confinement of waves within the ridge waveguide and strong demagnetizing effect in the junction area. The decreased θ_d increased the backpropagating flow of SWs toward another input port rather than output port. Such effects of the lateral confinement and demagnetizing field were fundamental drawbacks of the conventional ridge waveguides. Thus I proposed core-clad type waveguide, where the MS slab covered by 100 nm-thick gold functions as a cladding layer, and the BS slab functions as a core layer. The result of electromagnetic simulation exhibited remarkable decrease of backpropagation. Furthermore, transmission speed of SWs within the demonstrated majority gate was investigated. Evaluated delay of the device was about 100 ns, which was quite slower than that of CMOS-based implementation. According with the theoretical calculation, use of exchange spin waves may reduce the delay to the order of 100 ps.

In this study, spin wave majority gate was experimentally demonstrated and the flow of waves was analyzed. Use of AMLs can realize a line-defect waveguide, which may overcome the drawbacks of conventional ridge waveguides. In addition, use of exchange spin waves may reduce the waveguide delay. To expand functionalities, development of peripheral circuits, amplification, phase shifting, and phase synchronization and related technologies are further required.

Chapter 7

Conclusion and Outlook

Conclusion

SWs propagate even in magnetic insulators such as yttrium iron garnet (YIG), because they transmit spin momentum rather than electron. This potential meets the requirement of the reduction of Joule heat, which is crucial in the recent silicon electronics. In this thesis, several waveguide structures composed of YIG were studied in order to control flow of SWs, and to provide functionalities. In the following, summary of results is given.

In chapter 1, overview of this work was given. Because of the capability of broad excitation in the wavelength from tens of nanometers to millimeters, magnonic band can be easily modulated by arbitrary waveguide structure. Thus importance of positive utilization of wave nature from the viewpoint of application was emphasized. As examples of application, magnetic field sensors and full adder circuits were introduced from previous studies. In the first half of this thesis, flow of SWs in artificial magnetic lattices (AMLs) was investigated, and a performance of SWs as a magnetic field sensor was tested. In the later half, flow of SWs, especially FV-SWs, in the ridge waveguide was investigated, and several interferometers were demonstrated.

In chapter 2, general background of magnetism and spin waves was presented. The LLG equation and permeability tensor were introduced to as besic equations to describe magnetization dynamics. Propagation modes of SWs with dipolar interaction were explained together with the basis of SW excitation. In this work, SWs were excited by using all electrical spin wave spectroscopy (AESWS) technique with 50 μm-wide microstrip line (MSL) antenna. Typical magnetic properties of YIG was also explained, and applicability for spin wave devices (SWDs) was reviewed. In the viewpoint of miniaturization and low power consumption, YIG was the best material so far.

In chapter 3, SW propagation in the periodic structure was discussed. Dispersion curves of SWs with dipolar interaction region was numerically solved for the bare surface (BS) slab and metalized surface (MS) slab. Then, SW propagation within the device plane was calculated for in-plane and perpendicular magnetized configurations. Perpen-

dicular magnetized configuration exhibited isotropic propagation of FV-SWs, while in-plane magnetized configuration exhibited anisotropic propagation composed of DE-SWs and BV-SWs. Surface metalization reduced the wavenumber k at certain frequency, thus alternating connection of BS and MS slabs form periodic structure. Effect of metalization was also observed in the experiment. In the later half of this chapter, transfer matrix approach was introduced to design periodic structure with metalization width L_M and gap width L_A. Transmission properties of AMLs with different defect layer with extra gap width L_D were calculated. The AML with $L_D = L_A$ formed a Bragg mirror, and band gap was confirmed at the Bragg frequency. The AML with $L_D = 2L_A$ exhibited localization of SWs in the defect layer, and a localized transmission peak was confirmed at the Bragg frequency. However, these results exhibited remarkable discrepancy with the experimental results. The reason was explained by the demagnetizing effect. Inhomogeneous of demagnetizing field within the waveguide yielded in the incoherence of SWs, since wavelength of SWs was magnetic field dependent. By considering the demagnetizing effect, broadening of transmission peaks in the vicinity of the Bragg frequency was reasonably explained. Thus improved transfer matrix approach was introduced to calculate transmission property of AMLs.

In chapter 4, a performance of DE-SWs in the AML with $L_D = 2L_A$ was evaluated to realize magnetic field sensors. A large slop of transmission intensity in the vicinity of the localized peak was used to form magnetic field sensors together with the sharp dependence of magnonic band on applied magnetic field. Since the slope of localized peak can be enhanced by the number of periodic structure N, sensitivity can be controllable and a tiny magnetic field such as biomagnetic fields is detectable in principle. In the experiment, structure with $N = 10$ was employed. Resulted resolution was in order of 10^{-4} Oe in the best effort, which was comparable to that of Hole sensors. Limitation was given by the temperature drift and enhancement of spin relaxation by Fabri-Perot resonance at the defect layer. Later issue was fundamental drawback of AMLs as a sensor, in which reduction of signal intensity resulted in the smaller signal to noise ratio. By considering a finite waveguide damping, Q-factor was saturated at certain N and the slope of transmission intensity was no longer possible to be enhanced. Material breakthrough might be required in the factor of Gilbert damping, but materials overcoming YIG in this factor was never reported. On the other hand, temperature drift was successfully compensated by differential spin wave circuit (DSWC). DSWC was composed of two YIG waveguides magnetized in anti-parallel direction. This anti-parallel magnetization gave magnetization sensitivity of phases in opposite sign, thus the difference of phases of each waveguide selectively sense the magnetic field and temperature drift. As a result, temperature sensitivity of phase of DSWC was suppressed from -20 deg./°C to -9.5×10^{-3} deg./°C, while magnetic field sensitivity was doubled. From this result, performance of SWDs as a magnetic field sensor was rather low, and outstanding feature compared to the conventional technologies, e.g. SQUID and flux gate sensors, cannot be confirmed. However, obtained background of magnetic field ans temperature sensitivity was rather utilized in the design of interferometers.

In chapter 5, spin wave interferometer using FV-SWs was experimentally demon-

strated. Since FV-SWs exhibit an isotropic dispersion within the device plane, a potential of device integration can be expected. In this chapter, the fundamental 2 wave interferometry with a linear waveguide was investigated. Constructive and destructive interference of input waves in in-phase and anti-phase injection were experimentally confirmed. By assigning constructive and destructive interference as ON and OFF state, respectively, XNOR operation was realized with the isolation ratio of 9.95 dB. However, these states were instable against to the change of bias magnetic field H_0 due to the contribution of the backscattering from waveguide ends. Thus terminator for the backscattering was investigated from two approaches. First approach was the use of roughened surface, in which such roughness R_a induced extra scattering effects. Waveguide ends were roughened by the sandpaper with $R_a \sim 100$ nm. This roughness yielded in the increase of extrinsic damping of $\Delta H_0 = 3.4$ Oe for 110 μm-thick YIG film. This was slightly increased in 10 μm-thick film with the value of $\Delta H_0 = 3.8$ Oe. Nevertheless such ΔH_0 values were not sufficient to suppress the backscattering. Next, termination effect with thin-metal over layer (TMOL) composed of gold film with thickness t_{Au} was investigated. This structure exhibited sufficient termination effect. The mechanism of termination was further investigated by the electromagnetic analysis. When t_{Au} became thinner, two independent dispersion branches with different wavenumber, namely q-Air and q-PEC modes, were appeared. In the region of t_{Au} with tens of nanometers, these modes were hybridized and strong attenuation was confirmed. Finally, a liner waveguide with terminator composed of TMOLs with $t_{\mathrm{Au}} = 30$ nm was fabricated. By using this waveguide, instability against to H_0 was drastically suppressed and isolation ratio was also increased to 13.7 dB. Robustness to H_0 deviation was evaluated as a noise margin between ON and OFF state, which was increased from 0.85 mV to 4.14 mV in the magnetic field deviation over 30 dB. This is the first experimental report of the interferometer using FV-SWs.

In chapter 6, spin wave majority function was experimentally demonstrated by using the Ψ-shaped FV-SW interferometer. Waveguide geometry was precisely designed based on the electromagnetic simulation. Designed waveguide was single mode at the operation frequency of 4 GHz, and the backscattering from the waveguide ends was suppressed to less than 5% by using TMOLs. Switching of AND/OR operation based on majority function was experimentally confirmed, in which one input signal was assigned to control, and phase reversal of the control input alternated AND and OR operation. Therefore the interferometer exhibited a kind of reconfigurable functionality. To demonstrate the reconfigurable functionality, applied magnetic field was precisely controlled in order to suppress deviation within 0.2 Oe. Notable difference with the linear waveguide was seen in the SW propagation including oblique incident paths. Such propagation was drastically attenuated, and exhibited transmission ripples regardless of TMOLs. Therefore the wave flow in the junction area was further investigated by the electromagnetic simulation. Base on the simulation, increase of the extrinsic damping ΔH_0 of 1.9 Oe was confirmed. This ΔH_0 was supposed to be induced by the fabrication process of the ridge waveguide, but specific reason was not declared. Furthermore, demagnetizing effect and lateral confinement of the ridge waveguide resulted in the lowering of diffraction angle in the junction area. Such effects diffracted SWs toward another input port rather than the

output port. This backpropagation was the fundamental drawback of the ridge waveguide, and thus the concept of core-clad waveguide was introduced to suppress lowering of the diffraction angle. Core-clad waveguide exhibited decrease of the backpropagation, but leakage from the waveguide was confirmed. Furthermore, transmission delay of the demonstrated majority gate was measured. Mean value of the group delay was 111 ns, which yielded in the clock cycle of about 9 MHz. This is the first experimental report and the analysis of SW flow within the spin wave majority gate based on Ψ-shaped FV-SW interferometer.

Outlook

Next, an outlook for spin waveguide and its application is given. According to the results, performance of AML-based magnetic field sensors was not predominant. Since a damping of the magnetic waveguides is several orders of magnitude larger than that of the optical waveguides,[187] a localization effect with gigantic Q-factor comparable to optical AMLs cannot be expected. Therefore in realistic cases, magnonic AMLs with the defect layer seem essentially unfit for applications requiring large Q-factor, e.g. resonator, memory, sensor and so on. Such AMLs are rather useful for controlling propagating waves, where the gigantic Q-factor was not always necessary. For example, two dimensional array of AMLs with a sequence of defect can steer propagating waves, which is called line-defect waveguide. By using metalization-based AMLs, waveguides can be formed even inside the solid magnetic films, and thus a troublesome contribution of demagnetizing effect would be canceled. On the other hand, use of nonlinear effect may upgrade the functionality of AMLs. For example, A. V. Chumak *et al.* used an AML to enhance a probability of four-magnon scattering process, and the scattering process can control transmission efficiency of propagating waves. Usually such nonlinear effects have previously required a quite strong excitation power. However, concentration of SWs inside the AML reduced injection power to cause nonlinear effect. Accordingly, such AMLs functions as a gate of transistor, where the injection of SWs inside the AML can switch propagation of another SW passing through the AML.[188] Such nonlinear effects have been often observed in the SW-system, and thus nonlinear phenomena like chaos have been studied for a long time.[26,189,190] Recently, in the field of optics, application of chaos phenomenon is focused on the secure communication.[191] In the same manner, application of SW chaos to communication system may advance current silicon electronics in the viewpoint of More than Moore strategy. Use of AMLs may reduce the required injection power to handle chaotic dynamics.

Such outlook is also given for spin wave majority gates. Demonstrated gate was rather large due to the use of micrometer-thick YIG film. However, the gate size can be miniaturized thanks to the scalability based on the waveguide thickness d. Recently, H. Yu *et al.* reported the spectroscopy of SWs in the YIG film with $d = 20$ nm and the resulting attenuation length of about 600 μm. Because the ratio of d used in this work and the reported work was 500 to 1, the simple scaling by d indicates the capability

of the Ψ-shaped interferometer implemented in a 20 μm square. However, the delay of data transmission may be in the order from 10 ns to 100 ns, because the group velocity v_g is proportionally decreased with d in the dipolar interaction region. Thus the delay is almost unchanged by the miniaturization, and that value is about 10^3 times larger than that of CMOS-based majority gates. Accordingly, the throughputs of the spin wave majority gate becomes drastically smaller. Further integration of spin wave majority gates and use of orthogonal frequency-division multiplexing[25] may increase the throughputs, but overcoming the throughputs of CMOS-based majority gate seems to be still challenging. Therefore, in principle, spin wave majority gates have an advantage on processing less amount of data with lower power consumption, which may be suitable for small devices without constant power supply. To overcoming CMOS devices also in the arithmetic capacity, increase of v_g is necessary. In the exchange interaction region, v_g is independent of d, and thus the miniaturization of device may efficiently decrease the delay. Subnanosecond data transmission may be possible in this limit, where the throughputs becomes comparable to that of CMOS devices. In this limit, the wavenumber of SWs exceeds $k = 10^7$ m^{-1} and further miniaturization of excitation antenna is also indispensable. In the latest report, excitation of SWs with the wavelength of 88 nm ($\sim 7 \times 10^7$ m^{-1}) was experimentally observed by using grating coupler.[23] In this range, wavenumber of excitation structure is crucial rather than the film thickness. Strictly, the input phases were controlled by the external microwave phase shifters in this work, direct estimation of the total processing speed cannot be given. In the general field of magnonics, the phase control of SWs is one of the important challenges, and some structures have been studied by several groups. For example, a propagating SW can be modulated by magnetostriction, and thus multiferroic heterostructures composed of piezoelectric and ferromagnetic layers, e.g. ME cells, have been studied.[192] Because the structure is voltage controlled and free of the charge current, most of benchmark is given in this scheme.[4,5] Nevertheless, high frequency control of the piezoelectricity is typically limited in the order of kilohertz.[193]

From these consideration, a large gap of performances can be seen between the spin wave majority function and CMOS devices at present. However, number of input data N can be easily increased by extending waveguides. Implementation of large input majority gates is one of the difficult tasks of CMOS devices, and thus the spin wave majority gates may be useful for the another arithmetic system requiring large input majority gate. In addition, even small v_g of SWs becomes an advantage in some computing schemes. For example, very slow global clock of 1 kHz was used in the TrueNorth, which is the well-known *neuromorphic* computer demonstrated by the research group in IBM. Regardless of such a slow clocking, this computing scheme exhibited sufficient performance in the image recognition tasks.[194] In conclusion, the spin wave majority gate cannot overcome the performance of CMOS devices at present, but several positive prospects were brought thanks to the underling unique physics. One of the important results of this work is the experimental demonstration of AND operation and OR operation[195] based on the majority gate. The result pave the way for future development of SW logic devices based on majority function.

Acknowledgment

First, I would like to express my deepest gratitude to Prof. Mitsuteru Inoue for giving me a chance to work at Spin Electronics Group, for many fruitful discussions about all aspects of my work and for giving me great opportunities to evolve into a good scientist.

I am equally grateful to Prof. Yuichi Nakamura for supervision of the PhD examination. Apart from the scientific guidance, I am also particularly thankful for the personal advices to everything.

Special thanks also goes to Dr. Taichi Goto for passionate guidance and discussion on experiments and publications.

I also wish to extend my warmest thanks to the following people who contributed in some manner to the successful conclusion of this thesis:

- Prof. Hironaga Uchida, Prof. Hiroyuki Takagi, Prof. Lim Pang Boey for scientific guidance at Spin Electronic Group.
- Prof. Alexander B. Granovsky for scientific discussion on theoretical matter and giving me opportunity to know many outstanding researches from Russia.
- Prof. Caroline A. Ross for scientific discussion on magnetic garnet and supervision of my English writing.
- Dr. Koji Sekiguchi for supervision of spin wave interference experiment and warm encouragement for my PhD.
- Takashi Hasegawa, Takaya Wada and Shingo Okajima from Murata Manufacturing for scientific collaboration on the development of magnetic field sensors, and technical guidance for radio frequency equipment and electromagnetic simulation.
- Prof Dirk Grundler for giving me an opportunity to join the laboratory and supervision of AESWS and the research topic of investigation for magnetization dynamics in CoFeB at Technische Universitat Munchen.
- Ioannis Stasinopoulos for experimental collaboration and support my exchange study at Technische Universitat Munchen.

- Prof. Alexander Grishin for giving me an opportunity to join the laboratory and study fundamental of spin waves at Royal Institute of Technology.
- Dr. Hideki Goto, Dr. Yoji Kunihashi, and Dr. Takehiko Tawara for supervision of my internship and technical guidances of optical experiment and low temperature measurement at NTT Basic Research Laboratory.
- Prof. Hiromu Ishii for enthusiastic support of my carrier path.
- All staffs in *Program for Leading Graduate Schools* for many supports of activities in the program.
- All staffs in *Tailor Made Baton Zone Educational Program* for many supports of activities in the program.
- Yumiko Yamamoto for organizational support.
- All coworkers at Spin Electronics Group for collaboration and great atmosphere.
- Prof. Mitsuo Fukuda, Prof. Akihiro Wakahara, and Prof. Takashi Ohira for accepting to participate in my thesis defense.

The financial support provided through the Grants-in-Aid for JSPS Fellows under contract No. 15J07286 is gratefully acknowledged.

Finally, I want to express my deepest thanks to my parents, my brother and my wider family for being unwavering in their support.

Bibliography

[1] C.-H. Jan, U. Bhattacharya, R. Brain, S.-J. Choi, G. Curello, G. Gupta, W. Hafez, M. Jang, M. Kang, K. Komeyli, *et al.*, "A 22nm soc platform technology featuring 3-d tri-gate and high-k/metal gate, optimized for ultra low power, high performance and high density soc applications," in *Electron Devices Meeting (IEDM), 2012 IEEE International*, pp. 3–1, IEEE, 2012.

[2] E. Vogel, "Technology and metrology of new electronic materials and devices," *Nature nanotechnology*, vol. 2, no. 1, pp. 25–32, 2007.

[3] A. B. Kahng, "Scaling: More than moore's law.," *IEEE Design & Test of Computers*, vol. 27, no. 3, pp. 86–87, 2010.

[4] K. Bernstein, R. K. Cavin, W. Porod, A. Seabaugh, and J. Welser, "Device and architecture outlook for beyond cmos switches," *Proceedings of the IEEE*, vol. 98, no. 12, pp. 2169–2184, 2010.

[5] D. E. Nikonov and I. A. Young, "Overview of beyond-cmos devices and a uniform methodology for their benchmarking," *Proceedings of the IEEE*, vol. 101, no. 12, pp. 2498–2533, 2013.

[6] S. J. Tans, A. R. Verschueren, and C. Dekker, "Room-temperature transistor based on a single carbon nanotube," *Nature*, vol. 393, no. 6680, pp. 49–52, 1998.

[7] D. Wei, L. Xie, K. K. Lee, Z. Hu, S. Tan, W. Chen, C. H. Sow, K. Chen, Y. Liu, and A. T. S. Wee, "Controllable unzipping for intramolecular junctions of graphene nanoribbons and single-walled carbon nanotubes," *Nature communications*, vol. 4, p. 1374, 2013.

[8] D. D. Stancil and A. Prabhakar, *Spin waves*. Springer, 2009.

[9] A. Gurevich and G. Melkov, "Magnetization oscillations and waves crc," *New York*, vol. 245, 1996.

[10] W. Ishak and K. Chang, "Magnetostatic-wave devices for microwave signal-processing," *Hewlett-Packard Journal*, vol. 36, no. 2, pp. 10–20, 1985.

[11] J. Adam, "Analog signal processing with microwave magnetics," *Proceedings of the IEEE*, vol. 76, no. 2, pp. 159–170, 1988.

[12] H. Tanbakuchi, D. Nicholson, B. Kunz, and W. Ishak, "Magnetically tunable oscillators and filters," *IEEE Transactions on Magnetics*, vol. 25, no. 5, pp. 3248–3253, 1989.

[13] V. Kruglyak, S. Demokritov, and D. Grundler, "Magnonics," *Journal of Physics D: Applied Physics*, vol. 43, no. 26, p. 264001, 2010.

[14] S. O. Demokritov and A. N. Slavin, *Magnonics: From fundamentals to applications*, vol. 125. Springer Science & Business Media, 2012.

[15] A. Chumak, V. Vasyuchka, A. Serga, and B. Hillebrands, "Magnon spintronics," *Nature Physics*, vol. 11, no. 6, pp. 453–461, 2015.

[16] A. Serga, A. Chumak, and B. Hillebrands, "Yig magnonics," *Journal of Physics D: Applied Physics*, vol. 43, no. 26, p. 264002, 2010.

[17] R. Linares, "Epitaxial growth of narrow linewidth yttrium iron garnet films," *Journal of Crystal Growth*, vol. 3, pp. 443–446, 1968.

[18] S. Blank and J. Nielsen, "The growth of magnetic garnets by liquid phase epitaxy," *Journal of Crystal Growth*, vol. 17, pp. 302–311, 1972.

[19] H. Glass and M. Elliott, "Accommodation of pb in yttrium iron garnet films grown by liquid phase epitaxy," *Journal of Crystal Growth*, vol. 27, pp. 253–260, 1974.

[20] S. A. Manuilov, S. Khartsev, and A. M. Grishin, "Pulsed laser deposited y3fe5o12 films: Nature of magnetic anisotropy i," *Journal of applied physics*, vol. 106, no. 12, p. 123917, 2009.

[21] M. Onbasli, A. Kehlberger, D. Kim, G. Jakob, M. Kläui, A. Chumak, B. Hillebrands, and C. Ross, "Pulsed laser deposition of epitaxial yttrium iron garnet films with low gilbert damping and bulk-like magnetization," *APL Materials*, vol. 2, no. 10, p. 106102, 2014.

[22] O. d. Kelly, A. Anane, R. Bernard, J. B. Youssef, C. Hahn, A. H. Molpeceres, C. Carrétéro, E. Jacquet, C. Deranlot, P. Bortolotti, *et al.*, "Inverse spin hall effect in nanometer-thick yttrium iron garnet/pt system," *Applied Physics Letters*, vol. 103, no. 8, p. 082408, 2013.

[23] H. Yu, O. d. Kelly, V. Cros, R. Bernard, P. Bortolotti, A. Anane, F. Brandl, F. Heimbach, and D. Grundler, "Approaching soft x-ray wavelengths in nanomagnet-based microwave technology," *Nature communications*, vol. 7, 2016.

[24] P. Shabadi, S. N. Rajapandian, S. Khasanvis, and C. A. Moritz, "Design of spin wave functions-based logic circuits," in *SPIN*, vol. 2, p. 1240006, World Scientific, 2012.

[25] A. Khitun, "Multi-frequency magnonic logic circuits for parallel data processing," *Journal of Applied Physics*, vol. 111, no. 5, p. 054307, 2012.

[26] S. M. Rezende and F. De Aguiar, "Spin-wave instabilities, auto-oscillations, and chaos in yttrium-iron-garnet," *Proceedings of the IEEE*, vol. 78, no. 6, pp. 893–908, 1990.

[27] I. Shariv and A. Friesem, "All-optical neural network with inhibitory neurons," *Optics letters*, vol. 14, no. 10, pp. 485–487, 1989.

[28] M. Inoue, A. Baryshev, H. Takagi, P. B. Lim, K. Hatafuku, J. Noda, and K. Togo, "Investigating the use of magnonic crystals as extremely sensitive magnetic field sensors at room temperature," *Applied Physics Letters*, vol. 98, no. 13, p. 132511, 2011.

[29] J. D. Joannopoulos, S. G. Johnson, J. N. Winn, and R. D. Meade, *Photonic crystals: molding the flow of light*. Princeton university press, 2011.

[30] A. B. Ustinov, A. V. Drozdovskii, and B. A. Kalinikos, "Multifunctional nonlinear magnonic devices for microwave signal processing," *Applied physics letters*, vol. 96, no. 14, p. 142513, 2010.

[31] A. Karenowska, A. Chumak, A. Serga, J. Gregg, and B. Hillebrands, "Magnonic crystal based forced dominant wavenumber selection in a spin-wave active ring," *Applied Physics Letters*, vol. 96, no. 8, p. 082505, 2010.

[32] A. Chumak, V. Vasyuchka, A. Serga, M. Kostylev, V. Tiberkevich, and B. Hillebrands, "Storage-recovery phenomenon in magnonic crystal," *Physical review letters*, vol. 108, no. 25, p. 257207, 2012.

[33] K. Rao, F. Humphrey, and J. Costa-Krämer, "Very large magneto-impedance in amorphous soft ferromagnetic wires," *Journal of Applied Physics*, vol. 76, no. 10, pp. 6204–6208, 1994.

[34] T. Schneider, A. Serga, B. Leven, B. Hillebrands, R. Stamps, and M. Kostylev, "Realization of spin-wave logic gates," *Applied Physics Letters*, vol. 92, no. 2, p. 022505, 2008.

[35] N. Sato, K. Sekiguchi, and Y. Nozaki, "Electrical demonstration of spin-wave logic operation," *Applied Physics Express*, vol. 6, no. 6, p. 063001, 2013.

[36] M. Kostylev, A. Serga, T. Schneider, B. Leven, and B. Hillebrands, "Spin-wave logical gates," *Applied Physics Letters*, vol. 87, no. 15, p. 153501, 2005.

[37] A. M. Shams, T. K. Darwish, and M. A. Bayoumi, "Performance analysis of low-power 1-bit cmos full adder cells," *IEEE Transactions on Very Large Scale Integration (VLSI) Systems*, vol. 10, no. 1, pp. 20–29, 2002.

[38] H. Akima, Y. Katayama, M. Sakuraba, K. Nakajima, J. Madrenas, and S. Shigeo, "Cmos majority circuit with large fan-in," *IEICE Transactions on Electronics*, vol. 99, no. 9, pp. 1056–1064, 2016.

[39] M. Jamali, J. H. Kwon, S.-M. Seo, K.-J. Lee, and H. Yang, "Spin wave nonreciprocity for logic device applications," *Scientific reports*, vol. 3, 2013.

[40] Y. Nakashima, K. Nagai, T. Tanaka, and K. Matsuyama, "Optimum design consideration for interferometric spin wave logic operations," *Journal of Applied Physics*, vol. 109, no. 7, p. 07D318, 2011.

[41] S. Klingler, P. Pirro, T. Brächer, B. Leven, B. Hillebrands, and A. V. Chumak, "Spin-wave logic devices based on isotropic forward volume magnetostatic waves," *Applied Physics Letters*, vol. 106, no. 21, p. 212406, 2015.

[42] S. Klingler, P. Pirro, T. Brächer, B. Leven, B. Hillebrands, and A. V. Chumak, "Design of a spin-wave majority gate employing mode selection," *Applied Physics Letters*, vol. 105, no. 15, p. 152410, 2014.

[43] K.-S. Lee and S.-K. Kim, "Conceptual design of spin wave logic gates based on a mach–zehnder-type spin wave interferometer for universal logic functions," *Journal of Applied Physics*, vol. 104, no. 5, p. 053909, 2008.

[44] A. Khitun, M. Bao, and K. L. Wang, "Magnetic cellular nonlinear network with spin wave bus for image processing," *Superlattices and Microstructures*, vol. 47, no. 3, pp. 464–483, 2010.

[45] S. Nakamura and H. Morise, "Signal processing device using magnetic film and signal processing method," Aug. 5 2014. US Patent 8,797,060.

[46] H. Morise, S. Nakamura, D. Saida, and T. Kondo, "Adder," June 3 2014. US Patent 8,745,120.

[47] Y. Katayama, T. Yamane, D. Nakano, R. Nakane, and G. Tanaka, "Wave-based neuromorphic computing framework for brain-like energy efficiency and integration," *IEEE Transactions on Nanotechnology*, vol. 15, no. 5, pp. 762–769, 2015.

[48] M. S. Sodha and N. Srivastava, *Microwave propagation in ferrimagnetics*, vol. 266. Springer, 1981.

[49] D. D. Stancil, *Theory of magnetostatic waves*. Springer Science & Business Media, 2012.

[50] A. Chumak, A. Serga, S. Wolff, B. Hillebrands, and M. Kostylev, "Scattering of surface and volume spin waves in a magnonic crystal," *Applied Physics Letters*, vol. 94, no. 17, p. 172511, 2009.

[51] D. D. Stancil, B. E. Henty, A. G. Cepni, and J. Van ' t Hof, "Observation of an inverse doppler shift from left-handed dipolar spin waves," *Physical Review B*, vol. 74, no. 6, p. 060404, 2006.

[52] A. Chumak, P. Dhagat, A. Jander, A. Serga, and B. Hillebrands, "Reverse doppler effect of magnons with negative group velocity scattered from a moving bragg grating," *Physical Review B*, vol. 81, no. 14, p. 140404, 2010.

[53] S. Demokritov, V. Demidov, O. Dzyapko, G. Melkov, A. Serga, B. Hillebrands, and A. Slavin, "Bose–einstein condensation of quasi-equilibrium magnons at room temperature under pumping," *Nature*, vol. 443, no. 7110, pp. 430–433, 2006.

[54] J. Parekh, "Magnetostatic surface waves on a partially metallized yig plate," *Proceedings of the IEEE*, vol. 61, no. 9, pp. 1371–1373, 1973.

[55] B. Kalinikos and A. Slavin, "Theory of dipole-exchange spin wave spectrum for ferromagnetic films with mixed exchange boundary conditions," *Journal of Physics C: Solid State Physics*, vol. 19, no. 35, p. 7013, 1986.

[56] B. Kalinikos, M. Kostylev, N. Kozhus, and A. Slavin, "The dipole-exchange spin wave spectrum for anisotropic ferromagnetic films with mixed exchange boundary conditions," *Journal of Physics: Condensed Matter*, vol. 2, no. 49, p. 9861, 1990.

[57] M. R. Freeman and Z. Diao, "Spintronics: All-optical spin-wave control," *Nature Photonics*, vol. 6, no. 10, pp. 643–645, 2012.

[58] J. Alzate, P. Upadhyaya, M. Lewis, J. Nath, Y. Lin, K. Wong, S. Cherepov, P. K. Amiri, K. Wang, J. Hockel, *et al.*, "Spin wave nanofabric update," in *2012 IEEE/ACM International Symposium on Nanoscale Architectures (NANOARCH)*, pp. 196–202, IEEE, 2012.

[59] V. E. Demidov, S. Urazhdin, and S. O. Demokritov, "Direct observation and mapping of spin waves emitted by spin-torque nano-oscillators," *Nature materials*, vol. 9, no. 12, pp. 984–988, 2010.

[60] V. Vlaminck and M. Bailleul, "Spin-wave transduction at the submicrometer scale: Experiment and modeling," *Physical Review B*, vol. 81, no. 1, p. 014425, 2010.

[61] K. Kennewell, M. Kostylev, and R. Stamps, "Calculation of spin wave mode response induced by a coplanar microwave line," *Journal of applied physics*, vol. 101, no. 9, p. 09D107, 2007.

[62] J. Parekh and H. Tuan, "Meander line excitation of magnetostatic surface waves," *Proceedings of the IEEE*, vol. 67, no. 1, pp. 182–183, 1979.

[63] J. Adam, R. Patterson, and T. O ' Keeffe, "Magnetostatic wave interdigital transducers," *Journal of Applied Physics*, vol. 49, no. 3, pp. 1797–1799, 1978.

[64] F. B. F. Forrat, "Structure of ferrimagnetic rare-earth ferrites," *Compt. Rend., Paris*, vol. 242, pp. 382–384, 1956.

[65] R. LeCraw, E. Spencer, and C. Porter, "Ferromagnetic resonance line width in yttrium iron garnet single crystals," *Physical Review*, vol. 110, no. 6, p. 1311, 1958.

[66] S. Serrano-Guisan, H.-C. Wu, C. Boothman, M. Abid, B. Chun, I. Shvets, and H. Schumacher, "Thickness dependence of the effective damping in epitaxial fe3o4/mgo thin films," *Journal of Applied Physics*, vol. 109, no. 1, p. 013907, 2011.

[67] M. Nagata, K. Tanabe, T. Moriyama, D. Chiba, J.-I. Ohe, M. Myoka, T. Niizeki, H. Yanagihara, E. Kita, and T. Ono, "Ferromagnetic resonance in magnetite thin films," *IEEE Transactions on Magnetics*, vol. 50, no. 1, pp. 1–3, 2014.

[68] V. Castel, N. Vlietstra, B. Van Wees, and J. B. Youssef, "Frequency and power dependence of spin-current emission by spin pumping in a thin-film yig/pt system," *Physical Review B*, vol. 86, no. 13, p. 134419, 2012.

[69] P. Pirro, T. Brächer, A. Chumak, B. Lägel, C. Dubs, O. Surzhenko, P. Görnert, B. Leven, and B. Hillebrands, "Spin-wave excitation and propagation in microstructured waveguides of yttrium iron garnet/pt bilayers," *Applied Physics Letters*, vol. 104, no. 1, p. 012402, 2014.

[70] Y. Kajiwara, K. Harii, S. Takahashi, J. Ohe, K. Uchida, M. Mizuguchi, H. Umezawa, H. Kawai, K. Ando, K. Takanashi, *et al.*, "Transmission of electrical signals by spin-wave interconversion in a magnetic insulator," *Nature*, vol. 464, no. 7286, pp. 262–266, 2010.

[71] C. Hauser, T. Richter, N. Homonnay, C. Eisenschmidt, M. Qaid, H. Deniz, D. Hesse, M. Sawicki, S. G. Ebbinghaus, and G. Schmidt, "Yttrium iron garnet thin films with very low damping obtained by recrystallization of amorphous material," *Scientific reports*, vol. 6, 2016.

[72] H. Chang, P. Li, W. Zhang, T. Liu, A. Hoffmann, L. Deng, and M. Wu, "Nanometer-thick yttrium iron garnet films with extremely low damping," *IEEE Magnetics Letters*, vol. 5, pp. 1–4, 2014.

[73] T. Liu, H. Chang, V. Vlaminck, Y. Sun, M. Kabatek, A. Hoffmann, L. Deng, and M. Wu, "Ferromagnetic resonance of sputtered yttrium iron garnet nanometer films," *Journal of Applied Physics*, vol. 115, no. 17, p. 17A501, 2014.

[74] R. Iguchi, K. Ando, R. Takahashi, T. An, E. Saitoh, and T. Sato, "Spin pumping without three-magnon splitting in polycrystalline bi1y2fe5o12/pt bilayer structure," *Japanese Journal of Applied Physics*, vol. 51, no. 10R, p. 103004, 2012.

[75] A. Kehlberger, K. Richter, M. C. Onbasli, G. Jakob, D. H. Kim, T. Goto, C. A. Ross, G. Götz, G. Reiss, T. Kuschel, *et al.*, "Enhanced magneto-optic kerr effect and magnetic properties of cey 2 fe 5 o 12 epitaxial thin films," *Physical Review Applied*, vol. 4, no. 1, p. 014008, 2015.

[76] S. Shiomi, E. Ohno, S. Iwata, and S. Uchiyama, "Dynamic properties of bubbles and stripes in tilted [111] garnet films," *IEEE Transactions on Magnetics*, vol. 17, no. 6, pp. 2772–2774, 1981.

[77] T. Kubota, S. Tsunegi, M. Oogane, S. Mizukami, T. Miyazaki, H. Naganuma, and Y. Ando, "Half-metallicity and gilbert damping constant in co fe mn si heusler alloys depending on the film composition," *Appl. Phys. Lett*, vol. 94, p. 122504, 2009.

[78] K. Kobayashi, N. Inaba, N. Fujita, Y. Sudo, T. Tanaka, M. Ohtake, M. Futamoto, and F. Kirino, "Damping constants for permalloy single-crystal thin films," *IEEE Transactions on Magnetics*, vol. 45, no. 6, pp. 2541–2544, 2009.

[79] S. S. Kalarickal, P. Krivosik, M. Wu, C. E. Patton, M. L. Schneider, P. Kabos, T. Silva, and J. P. Nibarger, "Ferromagnetic resonance linewidth in metallic thin films: Comparison of measurement methods," *Journal of Applied Physics*, vol. 99, no. 9, p. 093909, 2006.

[80] C. Bilzer, T. Devolder, J.-V. Kim, G. Counil, C. Chappert, S. Cardoso, and P. Freitas, "Study of the dynamic magnetic properties of soft cofeb films," *Journal of applied physics*, vol. 100, no. 5, pp. 53903–53903, 2006.

[81] T. Kasuya and R. LeCraw, "Relaxation mechanisms in ferromagnetic resonance," *Physical Review Letters*, vol. 6, no. 5, p. 223, 1961.

[82] H. Glass and M. Elliot, "Attainment of the intrinsic fmr linewidth in yttrium iron garnet films grown by liquid phase epitaxy," *Journal of Crystal Growth*, vol. 34, no. 2, pp. 285–288, 1976.

[83] H. Yu, O. d. Kelly, V. Cros, R. Bernard, P. Bortolotti, A. Anane, F. Brandl, R. Huber, I. Stasinopoulos, and D. Grundler, "Magnetic thin-film insulator with ultra-low spin wave damping for coherent nanomagnonics," *Scientific reports*, vol. 4, 2014.

[84] M. Hurben and C. Patton, "Theory of two magnon scattering microwave relaxation and ferromagnetic resonance linewidth in magnetic thin films," *Journal of applied physics*, vol. 83, no. 8, pp. 4344–4365, 1998.

[85] K. Sun, "Mssw and msvw in a multilayered ferrimagnetic structure with an arbitrary orientation between two static magnetizations," *IEEE transactions on microwave theory and techniques*, vol. 41, no. 6, pp. 1143–1148, 1993.

[86] L. Brundle and N. Freedman, "Magnetostatic surface waves on a yig slab," *Electronics Letters*, vol. 7, no. 4, pp. 132–134, 1968.

[87] H. Yu, R. Huber, T. Schwarze, F. Brandl, T. Rapp, P. Berberich, G. Duerr, and D. Grundler, "High propagating velocity of spin waves and temperature dependent damping in a cofeb thin film," *Applied Physics Letters*, vol. 100, no. 26, p. 262412, 2012.

[88] S. Neusser, G. Duerr, H. Bauer, S. Tacchi, M. Madami, G. Woltersdorf, G. Gubbiotti, C. Back, and D. Grundler, "Anisotropic propagation and damping of spin waves in a nanopatterned antidot lattice," *Physical review letters*, vol. 105, no. 6, p. 067208, 2010.

[89] J. P. Walter and M. L. Cohen, "Calculation of the reflectivity, modulated reflectivity, and band structure of gaas, gap, znse, and zns," *Physical Review*, vol. 183, no. 3, p. 763, 1969.

[90] M. V. Fischetti and S. E. Laux, "Band structure, deformation potentials, and carrier mobility in strained si, ge, and sige alloys," *Journal of Applied Physics*, vol. 80, no. 4, pp. 2234–2252, 1996.

[91] R. De Groot, F. Mueller, P. Van Engen, and K. Buschow, "New class of materials: half-metallic ferromagnets," *Physical Review Letters*, vol. 50, no. 25, p. 2024, 1983.

[92] J. D. Joannopoulos, P. R. Villeneuve, S. Fan, *et al.*, "Photonic crystals: putting a new twist on light," *Nature*, vol. 386, no. 6621, pp. 143–149, 1997.

[93] T.-T. Wu, L.-C. Wu, and Z.-G. Huang, "Frequency band-gap measurement of two-dimensional air/silicon phononic crystals using layered slanted finger interdigital transducers," *Journal of Applied Physics*, vol. 97, no. 9, p. 094916, 2005.

[94] M. Kauranen and A. V. Zayats, "Nonlinear plasmonics," *Nature Photonics*, vol. 6, no. 11, pp. 737–748, 2012.

[95] S. Neusser and D. Grundler, "Magnonics: spin waves on the nanoscale," *Advanced Materials*, vol. 21, no. 28, pp. 2927–2932, 2009.

[96] E. Yablonovitch, "Inhibited spontaneous emission in solid-state physics and electronics," *Physical review letters*, vol. 58, no. 20, p. 2059, 1987.

[97] E. Yablonovitch, T. Gmitter, and K. Leung, "Photonic band structure: The face-centered-cubic case employing nonspherical atoms," *Physical review letters*, vol. 67, no. 17, p. 2295, 1991.

[98] T. Tanabe, M. Notomi, E. Kuramochi, A. Shinya, and H. Taniyama, "Trapping and delaying photons for one nanosecond in an ultrasmall high-q photonic-crystal nanocavity," *Nature Photonics*, vol. 1, no. 1, pp. 49–52, 2007.

[99] L. A. Coldren, S. W. Corzine, and M. L. Mashanovitch, *Diode lasers and photonic integrated circuits*, vol. 218. John Wiley & Sons, 2012.

[100] M. Inoue, K. Arai, T. Fujii, and M. Abe, "Magneto-optical properties of one-dimensional photonic crystals composed of magnetic and dielectric layers," *Journal of applied physics*, vol. 83, pp. 6768–6770, 1998.

[101] M. Inoue, R. Fujikawa, A. Baryshev, A. Khanikaev, P. Lim, H. Uchida, O. Aktsipetrov, A. Fedyanin, T. Murzina, and A. Granovsky, "Magnetophotonic crystals," *Journal of Physics D: Applied Physics*, vol. 39, no. 8, p. R151, 2006.

[102] R. Isogai, N. Sagara, T. Goto, Y. Nakamura, P. B. Lim, and M. Inoue, "Diffraction efficiency of volumetric magnetic holograms with magnetophotonic crystals," *Journal of the Magnetics Society of Japan*, vol. 38, no. 3-2, pp. 119–122, 2014.

[103] J. Park, J. Cho, K. Nishimura, and M. Inoue, "Magnetooptic spatial light modulator for volumetric digital recording system," *Japanese journal of applied physics*, vol. 41, no. 3S, p. 1813, 2002.

[104] U. Efron, *Spatial light modulator technology: materials, devices, and applications*, vol. 47. CRC Press, 1994.

[105] V. Belotelov, I. Akimov, M. Pohl, V. Kotov, S. Kasture, A. Vengurlekar, A. V. Gopal, D. Yakovlev, A. Zvezdin, and M. Bayer, "Enhanced magneto-optical effects in magnetoplasmonic crystals," *Nature Nanotechnology*, vol. 6, no. 6, pp. 370–376, 2011.

[106] G. Armelles, A. Cebollada, A. García-Martín, and M. U. González, "Magnetoplasmonics: combining magnetic and plasmonic functionalities," *Advanced Optical Materials*, vol. 1, no. 1, pp. 10–35, 2013.

[107] C. Elachi, "Magnetic wave propagation in a periodic medium," *IEEE Transactions on Magnetics*, vol. 11, no. 1, pp. 36–39, 1975.

[108] C. Sykes, J. Adam, and J. Collins, "Magnetostatic wave propagation in a periodic structure," *Applied Physics Letters*, vol. 29, no. 6, pp. 388–391, 1976.

[109] J. Owens, C. Smith, S. Lee, and J. Collins, "Magnetostatic wave propagation through periodic metallic gratings," *IEEE Transactions on Magnetics*, vol. 14, no. 5, pp. 820–825, 1978.

[110] 堤誠 and 由木泰紀, "周期的に磁化された yig 棒におけるスピン波の伝搬," **電子情報通信学会論文誌** *B*, vol. 56, no. 7, pp. 320–321, 1973.

[111] M. Tsutsumi and Y. Yuki, "Magnetostatic wave-propagation in periodically magnetized ferrite," *ELECTRONICS & COMMUNICATIONS IN JAPAN*, vol. 58, no. 1, pp. 74–81, 1975.

[112] M. Tsutsumi, T. Bhattacharyya, and N. Kumagai, "Effect of the magnetic perturbation on magnetostatic surface-wave propagation," *IEEE Transactions on Microwave Theory and Techniques*, vol. 24, no. 9, pp. 591–597, 1976.

[113] M. Tsutsumi, Y. Sakaguchi, and N. Kumagai, "Behavior of the magnetostatic wave in a periodically corrugated yig slab (short papers)," *IEEE Transactions on Microwave Theory and Techniques*, vol. 25, no. 3, pp. 224–228, 1977.

[114] 大平孝, 堤誠, and 熊谷信昭, "2 乗余弦状に磁化された yig における表面静磁波の伝搬特性 (技術談話室)," **電子通信学会論文誌** *B*, vol. 62, no. 6, pp. p603–604, 1979.

[115] 大平孝, 湯浅鉄二, 堤誠, and 熊谷信昭, "フェライト周期構造線路からのミリ波の放射," **電子情報通信学会論文誌** *B*, vol. 66, no. 4, pp. 461–468, 1983.

[116] S. Neusser, B. Botters, M. Becherer, D. Schmitt-Landsiedel, and D. Grundler, "Spin-wave localization between nearest and next-nearest neighboring holes in an antidot lattice," *Applied Physics Letters*, vol. 93, no. 12, p. 2501, 2008.

[117] N. Y. Grigorieva and B. Kalinikos, "Dispersion characteristics of spin waves in planar periodic structures based on ferromagnetic films," *Technical Physics*, vol. 54, no. 8, pp. 1196–1203, 2009.

[118] J. Topp, D. Heitmann, M. P. Kostylev, and D. Grundler, "Making a reconfigurable artificial crystal by ordering bistable magnetic nanowires," *Physical review letters*, vol. 104, no. 20, p. 207205, 2010.

[119] M. Krawczyk, S. Mamica, M. Mruczkiewicz, J. Klos, S. Tacchi, M. Madami, G. Gubbiotti, G. Duerr, and D. Grundler, "Magnonic band structures in two-dimensional bi-component magnonic crystals with in-plane magnetization," *Journal of Physics D: Applied Physics*, vol. 46, no. 49, p. 495003, 2013.

[120] M. Dokukin, K. Togo, and M. Inoue, "Propagation of magnetostatic surface waves in a tunable one-dimensional magnonic crystal," *Journal of the Magnetics Society of Japan*, vol. 32, no. 2-2, pp. 103–105, 2008.

[121] A. B. Ustinov, B. A. Kalinikos, V. E. Demidov, and S. O. Demokritov, "Formation of gap solitons in ferromagnetic films with a periodic metal grating," *Physical Review B*, vol. 81, no. 18, p. 180406, 2010.

[122] A. Chumak, P. Pirro, A. Serga, M. Kostylev, R. Stamps, H. Schultheiss, K. Vogt, S. Hermsdoerfer, B. Laegel, P. Beck, *et al.*, "Spin-wave propagation in a microstructured magnonic crystal," *Applied Physics Letters*, vol. 95, no. 26, p. 262508, 2009.

[123] A. Chumak, T. Neumann, A. Serga, B. Hillebrands, and M. Kostylev, "A current-controlled, dynamic magnonic crystal," *Journal of Physics D: Applied Physics*, vol. 42, no. 20, p. 205005, 2009.

[124] M. Vogel, A. V. Chumak, E. H. Waller, T. Langner, V. I. Vasyuchka, B. Hillebrands, and G. von Freymann, "Optically reconfigurable magnetic materials," *Nature Physics*, vol. 11, no. 6, pp. 487–491, 2015.

[125] A. Chumak, A. Serga, S. Wolff, B. Hillebrands, and M. Kostylev, "Design and optimization of one-dimensional ferrite-film based magnonic crystals," *Journal of Applied Physics*, vol. 105, no. 8, p. 083906, 2009.

[126] M. Krawczyk and H. Puszkarski, "Plane-wave theory of three-dimensional magnonic crystals," *Physical Review B*, vol. 77, no. 5, p. 054437, 2008.

[127] D. A. Frickey, "Conversions between s, z, y, h, abcd, and t parameters which are valid for complex source and load impedances," *IEEE Transactions on Microwave Theory Techniques*, vol. 42, pp. 205–211, 1994.

[128] J. Adam, G. Bennett, and J. Wilkinson, "Experimental observation of magnetostatic modes in a y.i.g. slab," *Electronics Letters*, vol. 6, no. 14, pp. 434–436, 1970.

[129] F. Ciubotaru, A. Chumak, N. Y. Grigoryeva, A. Serga, and B. Hillebrands, "Magnonic band gap design by the edge modulation of micro-sized waveguides," *Journal of Physics D: Applied Physics*, vol. 45, no. 25, p. 255002, 2012.

[130] S. Tumanski, *Handbook of magnetic measurements*. CRC Press, 2016.

[131] M. Hämäläinen, R. Hari, R. J. Ilmoniemi, J. Knuutila, and O. V. Lounasmaa, "Magnetoencephalography:theory, instrumentation, and applications to noninvasive studies of the working human brain," *Reviews of modern Physics*, vol. 65, no. 2, p. 413, 1993.

[132] R. C. Knowlton, "The role of fdg-pet, ictal spect, and meg in the epilepsy surgery evaluation," *Epilepsy & Behavior*, vol. 8, no. 1, pp. 91–101, 2006.

[133] G. Bison, R. Wynands, and A. Weis, "A laser-pumped magnetometer for the mapping of human cardiomagnetic fields," *Applied Physics B*, vol. 76, no. 3, pp. 325–328, 2003.

[134] T. Oida, Y. Ito, K. Kamada, and T. Kobayashi, "Detecting rotating magnetic fields using optically pumped atomic magnetometers for measuring ultra-low-field magnetic resonance signals," *Journal of Magnetic Resonance*, vol. 217, pp. 6–9, 2012.

[135] R. Wyllie, M. Kauer, G. Smetana, R. Wakai, and T. Walker, "Magnetocardiography with a modular spin-exchange relaxation-free atomic magnetometer array," *Physics in medicine and biology*, vol. 57, no. 9, p. 2619, 2012.

[136] P. Ripka, "Advances in fluxgate sensors," *Sensors and Actuators A: Physical*, vol. 106, no. 1, pp. 8–14, 2003.

[137] K. Sekiguchi, K. Yamada, S.-M. Seo, K.-J. Lee, D. Chiba, K. Kobayashi, and T. Ono, "Time-domain measurement of current-induced spin wave dynamics," *Physical review letters*, vol. 108, no. 1, p. 017203, 2012.

[138] B. Kalinikos, N. Kovshikov, M. Kostylev, P. Kabos, and C. Patton, "Observation of the amplification of spin-wave envelope solitons in ferromagnetic films by parallel magnetic pumping," *Journal of Experimental and Theoretical Physics Letters*, vol. 66, no. 5, pp. 371–375, 1997.

[139] P. A. Kolodin, P. Kabos, C. E. Patton, B. A. Kalinikos, N. G. Kovshikov, and M. P. Kostylev, "Amplification of microwave magnetic envelope solitons in thin yttrium iron garnet films by parallel pumping," *Physical review letters*, vol. 80, no. 9, p. 1976, 1998.

[140] H. Dürr, E. Dudzik, S. Dhesi, J. Goedkoop, G. Van der Laan, M. Belakhovsky, C. Mocuta, A. Marty, and Y. Samson, "Chiral magnetic domain structures in ultrathin fepd films," *Science*, vol. 284, no. 5423, pp. 2166–2168, 1999.

[141] Y. Ge, O. Heczko, O. Söderberg, and V. Lindroos, "Various magnetic domain structures in a ni–mn–ga martensite exhibiting magnetic shape memory effect," *Journal of Applied Physics*, vol. 96, no. 4, pp. 2159–2163, 2004.

[142] A. Wachowiak, J. Wiebe, M. Bode, O. Pietzsch, M. Morgenstern, and R. Wiesendanger, "Direct observation of internal spin structure of magnetic vortex cores," *Science*, vol. 298, no. 5593, pp. 577–580, 2002.

[143] S.-B. Choe, Y. Acremann, A. Scholl, A. Bauer, A. Doran, J. Stöhr, and H. A. Padmore, "Vortex core-driven magnetization dynamics," *Science*, vol. 304, no. 5669, pp. 420–422, 2004.

[144] A. Khitun, M. Bao, and K. L. Wang, "Magnonic logic circuits," *Journal of Physics D: Applied Physics*, vol. 43, no. 26, p. 264005, 2010.

[145] K. Nanayakkara, A. P. Jacob, and A. Kozhanov, "Spin wave scattering and interference in ferromagnetic cross," *Journal of Applied Physics*, vol. 118, no. 16, p. 163904, 2015.

[146] A. Ustinov and B. Kalinikos, "Nonlinear microwave spin wave interferometer," *Technical Physics Letters*, vol. 27, no. 5, pp. 403–405, 2001.

[147] J. Collins, D. Hastie, J. Owens, and C. Smith Jr, "Magnetostatic wave terminations," *Journal of Applied Physics*, vol. 49, no. 3, pp. 1800–1802, 1978.

[148] J. Adam, "Yig film characterization for msw devices," *Circuits, Systems and Signal Processing*, vol. 4, no. 1-2, pp. 105–113, 1985.

[149] G. Melkov, Y. V. Kobljanskyj, A. Serga, V. Tiberkevich, and A. Slavin, "Reversal of momentum relaxation," *Physical review letters*, vol. 86, no. 21, p. 4918, 2001.

[150] G. Melkov, V. Vasyuchka, Y. V. Kobljanskyj, and A. Slavin, "Wave-front reversal in a medium with inhomogeneities and an anisotropic wave spectrum," *Physical Review B*, vol. 70, no. 22, p. 224407, 2004.

[151] A. Y. Dobin and R. Victora, "Surface roughness induced extrinsic damping in thin magnetic films," *Physical review letters*, vol. 92, no. 25, p. 257204, 2004.

[152] M. Sparks, R. Loudon, and C. Kittel, "Ferromagnetic relaxation. i. theory of the relaxation of the uniform precession and the degenerate spectrum in insulators at low temperatures," *Physical Review*, vol. 122, no. 3, p. 791, 1961.

[153] O. Yalcin, "Ferromagnetic resonance-theory and applications," *Microwave Absorption in Nanostructured Spinel Ferrites*, p. 169, 2013.

[154] C. Bilzer, T. Devolder, P. Crozat, C. Chappert, S. Cardoso, and P. Freitas, "Vector network analyzer ferromagnetic resonance of thin films on coplanar waveguides: Comparison of different evaluation methods," *Journal of applied physics*, vol. 101, no. 7, p. 074505, 2007.

[155] J.-M. Beaujour, W. Chen, K. Krycka, C.-C. Kao, J. Sun, and A. Kent, "Ferromagnetic resonance study of sputtered co— ni multilayers," *The European Physical Journal B*, vol. 59, no. 4, pp. 475–483, 2007.

[156] J. M. Shaw, H. T. Nembach, and T. Silva, "Roughness induced magnetic inhomogeneity in co/ni multilayers: Ferromagnetic resonance and switching properties in nanostructures," *Journal of Applied Physics*, vol. 108, no. 9, p. 093922, 2010.

[157] A. Szaplonczay and H. Quon, "Chemical etching of gadolinium-gallium garnet substrates," *Journal of Materials Science*, vol. 7, no. 11, pp. 1280–1284, 1972.

[158] Z. Qiu, K. Ando, K. Uchida, Y. Kajiwara, R. Takahashi, H. Nakayama, T. An, Y. Fujikawa, and E. Saitoh, "Spin mixing conductance at a well-controlled platinum/yttrium iron garnet interface," *Applied Physics Letters*, vol. 103, no. 9, p. 092404, 2013.

[159] K. Ando, S. Takahashi, J. Ieda, H. Kurebayashi, T. Trypiniotis, C. Barnes, S. Maekawa, and E. Saitoh, "Electrically tunable spin injector free from the impedance mismatch problem," *Nature materials*, vol. 10, no. 9, pp. 655–659, 2011.

[160] Y. Sun, H. Chang, M. Kabatek, Y.-Y. Song, Z. Wang, M. Jantz, W. Schneider, M. Wu, E. Montoya, B. Kardasz, *et al.*, "Damping in yttrium iron garnet nanoscale films capped by platinum," *Physical review letters*, vol. 111, no. 10, p. 106601, 2013.

[161] B. Heinrich, C. Burrowes, E. Montoya, B. Kardasz, E. Girt, Y.-Y. Song, Y. Sun, and M. Wu, "Spin pumping at the magnetic insulator (yig)/normal metal (au) interfaces," *Physical review letters*, vol. 107, no. 6, p. 066604, 2011.

[162] R. De Wames and T. Wolfram, "Characteristics of magnetostatic surface waves for a metalized ferrite slab," *Journal of Applied Physics*, vol. 41, no. 13, pp. 5243–5246, 1970.

[163] J. Adam and S. Bajpai, "Magnetostatic forward volume wave propagation in yig strips," *IEEE Transactions on Magnetics*, vol. 18, no. 6, pp. 1598–1600, 1982.

[164] K. Y. Guslienko, S. Demokritov, B. Hillebrands, and A. Slavin, "Effective dipolar boundary conditions for dynamic magnetization in thin magnetic stripes," *Physical Review B*, vol. 66, no. 13, p. 132402, 2002.

[165] J. Adam, "A temperature stabilized magnetostatic wave device," in *1979 IEEE MTT-S International Microwave Symposium Digest*, pp. 160–161, 1979.

[166] A. De Vos, *Reversible computing: fundamentals, quantum computing, and applications*. John Wiley & Sons, 2011.

[167] E. Goto, "The parametron, a digital computing element which utilizes parametric oscillation," *Proceedings of the IRE*, vol. 47, no. 8, pp. 1304–1316, 1959.

[168] K. Wesolowski, *Introduction to digital communication systems*. John Wiley & Sons, 2009.

[169] W. S. McCulloch and W. Pitts, "A logical calculus of the ideas immanent in nervous activity," *The bulletin of mathematical biophysics*, vol. 5, no. 4, pp. 115–133, 1943.

[170] J. Adam and S. Stitzer, "A magnetostatic wave signal-to-noise enhancer," *Applied Physics Letters*, vol. 36, no. 6, pp. 485–487, 1980.

[171] X. Xing, Y. Yu, S. Li, and X. Huang, "How do spin waves pass through a bend?," *Scientific Reports*, vol. 3, 2013.

[172] D. Sirdeshmukh, L. Sirdeshmukh, K. Subhadra, K. K. Rao, and S. B. Laxman, "Systematic hardness measurements on some rare earth garnet crystal," *Bulletin of Materials Science*, vol. 24, no. 5, pp. 469–473, 2001.

[173] M. Nemiroff, H. J. Yue, and W. R. Schevey, "Yttrium iron garnet disks on gadolinium gallium substrates for microwave applications," Nov. 29 1977. US Patent 4,060,448.

[174] A. Chumak, A. Serga, B. Hillebrands, and M. Kostylev, "Scattering of backward spin waves in a one-dimensional magnonic crystal," *Applied Physics Letters*, vol. 93, no. 2, p. 022508, 2008.

[175] Y. V. Gulyaev, S. A. Nikitov, L. Zhivotovskii, A. Klimov, P. Tailhades, L. Presmanes, C. Bonningue, C. Tsai, S. Vysotskii, and Y. A. Filimonov, "Ferromagnetic films with magnon bandgap periodic structures: magnon crystals," *Journal of Experimental and Theoretical Physics Letters*, vol. 77, no. 10, pp. 567–570, 2003.

[176] E. Belloy, I. Zalunardo, A. Sayah, and M. A. Gijs, "Powder blasting as a three-dimensional microstucturing technology for mems applications," in *Micromachining and Microfabrication*, pp. 467–476, International Society for Optics and Photonics, 2000.

[177] J. P. Castera and P. Hartemann, "Magnetostatic wave magnetometer," July 27 1982. US Patent 4,341,998.

[178] J. Stigloher, M. Decker, H. S. Körner, K. Tanabe, T. Moriyama, T. Taniguchi, H. Hata, M. Madami, G. Gubbiotti, K. Kobayashi, *et al.*, "Snell's law for spin waves," *arXiv preprint arXiv:1606.02895*, 2016.

[179] T. Schwarze, R. Huber, G. Duerr, and D. Grundler, "Complete band gaps for magnetostatic forward volume waves in a two-dimensional magnonic crystal," *Physical Review B*, vol. 85, no. 13, p. 134448, 2012.

[180] T. Schwarze and D. Grundler, "Magnonic crystal wave guide with large spin-wave propagation velocity in cofeb," *Applied Physics Letters*, vol. 102, no. 22, p. 222412, 2013.

[181] K. Chi, Y. Zhu, and C. Tsai, "Confinement of magnetostatic forward volume waves in two-dimensional magnonic crystals with line defects," *Journal of Applied Physics*, vol. 115, no. 17, p. 17D125, 2014.

[182] H. Kosaka, T. Kawashima, A. Tomita, M. Notomi, T. Tamamura, T. Sato, and S. Kawakami, "Photonic crystals for micro lightwave circuits using wavelength-dependent angular beam steering," *Applied Physics Letters*, vol. 74, no. 10, pp. 1370–1372, 1999.

[183] P. Gruszecki, J. Romero-Vivas, Y. S. Dadoenkova, N. Dadoenkova, I. Lyubchanskii, and M. Krawczyk, "Goos-hänchen effect and bending of spin wave beams in thin magnetic films," *Applied Physics Letters*, vol. 105, no. 24, p. 242406, 2014.

[184] I. A. Danilov, M. S. Gorbunov, and A. A. Antonov, "Set tolerance of 65 nm cmos majority voters: a comparative study," *IEEE Transactions on Nuclear Science*, vol. 61, no. 4, pp. 1597–1602, 2014.

[185] P. Balasubramanian and N. Mastorakis, "A standard cell based voter for use in tmr implementation," in *5th European conference of circuits technology and devices, Geneva, Switzerland*, pp. 29–31, 2014.

[186] H. Yu, G. Duerr, R. Huber, M. Bahr, T. Schwarze, F. Brandl, and D. Grundler, "Omnidirectional spin-wave nanograting coupler," *Nature communications*, vol. 4, 2013.

[187] Y. KAWAGUCHI, Y. TAMURA, T. HARUNA, Y. YAMAMOTO, and M. HIRANO, "Ultra low-loss pure silica core fiber," *SEI TECHNICAL REVIEW*, no. 80, p. 51, 2015.

[188] A. V. Chumak, A. A. Serga, and B. Hillebrands, "Magnon transistor for all-magnon data processing," *Nature communications*, vol. 5, 2014.

[189] A. Azevedo and S. M. Rezende, "Controlling chaos in spin-wave instabilities," *Physical review letters*, vol. 66, no. 10, p. 1342, 1991.

[190] P. E. Wigen, *Nonlinear phenomena and chaos in magnetic materials*. World Scientific, 1994.

[191] T. Harayama, S. Sunada, K. Yoshimura, P. Davis, K. Tsuzuki, and A. Uchida, "Fast nondeterministic random-bit generation using on-chip chaos lasers," *Physical Review A*, vol. 83, no. 3, p. 031803, 2011.

[192] A. Khitun, M. Bao, and K. L. Wang, "Spin wave magnetic nanofabric: A new approach to spin-based logic circuitry," *IEEE Transactions on Magnetics*, vol. 44, no. 9, pp. 2141–2152, 2008.

[193] N. Cai, C.-W. Nan, J. Zhai, and Y. Lin, "Large high-frequency magnetoelectric response in laminated composites of piezoelectric ceramics, rare-earth iron alloys and polymer," *Applied physics letters*, vol. 84, no. 18, pp. 3516–3518, 2004.

[194] P. A. Merolla, J. V. Arthur, R. Alvarez-Icaza, A. S. Cassidy, J. Sawada, F. Akopyan, B. L. Jackson, N. Imam, C. Guo, Y. Nakamura, *et al.*, "A million spiking-neuron integrated circuit with a scalable communication network and interface," *Science*, vol. 345, no. 6197, pp. 668–673, 2014.

[195] S. Arora and B. Barak, *Computational complexity: a modern approach*. Cambridge University Press, 2009.

Publications

Articles

- **Spin wave absorber generated by artificial surface anisotropy for spin wave device network**
  Naoki Kanazawa, Taichi Goto, Koji Sekiguchi, Alexander B. Granovsky, Hiroyuki Takagi, Yuichi Nakamura, and Mitsuteru Inoue
  AIP Advances, **6**(6):95204, 2016.
  doi:10.1063/1.4962664

- **Demonstration of a robust magnonic spin wave interferometer**
  Naoki Kanazawa, Taichi Goto, Koji Sekiguchi, Alexander B. Granovsky, Caroline A. Ross, Hiroyuki Takagi, Yuichi Nakamura, and Mitsuteru Inoue
  Scientific reports, **6**(8):30268, 2016.
  doi:10.1038/srep30268

- **Spin wave differential circuit for realization of thermally stable magnonic sensors**
  Taichi Goto, Naoki Kanazawa, Altansargai Buyandalai, Hiroyuki Takagi, Yuichi Nakamura, Shingo Okajima, Takashi Hasegawa, Alexander B. Granovsky, Koji Sekiguchi, Caroline A. Ross, and Mitsuteru Inoue
  Applied Physics Letters, **106**(3):132412, 2015.
  doi:10.1063/1.4916989

- **Metal thickness dependence on spin wave propagation in magnonic crystal using yttrium iron garnet**
  Naoki Kanazawa, Taichi Goto, Jet Wei Hoong, Altansargai Buyandalai, Hiroyuki Takagi, and Mitsuteru Inoue
  Journal of Applied Physics, **117**(3):17E510, 2015.
  doi:10.1063/1.4916815

- **Spin wave isolator based on frequency displacement nonreciprocity in ferromagnetic bilayer**
  Shinsuke Shichi, Naoki Kanazawa, Kenji Matsuda, Shingo Okajima, Takashi Hasegawa, Takekazu Okada, Taichi Goto, Hiroyuki Takagi, and Mitsuteru Inoue

Journal of Applied Physics, **117**(3):17D125, 2015.
doi:10.1063/1.324870

- **Spin wave localization in one-dimensional magnonic microcavity comprising yttrium iron garnet**
  Naoki Kanazawa, Taichi Goto, and Mitsuteru Inoue
  Journal of Applied Physics, **116**(4):83903, 2014.
  doi:10.1063/1.4893936

Presentations

- **Fabrication of three-input spin wave interferometer using yttrium iron garnet**
  Naoki Kanazawa,* Taichi Goto, Koji Sekiguchi, Alexander B. Granovsky, Caroline A. Ross, Hiroyuki Takagi, Yuichi Nakamura, Hironaga Uchida, and Mitsuteru Inoue
  61st Annual Conference on Magnetism and Magnetic Materials (New Orleans, USA, 2nd November 2016).

- **Spin wave logic operation in three-ports yttrium iron garnet waveguide**
  Naoki Kanazawa,* Taichi Goto, Hiroyuki Takagi, Yuichi Nakamura, Caroline A. Ross, Alexander B. Granovsky, Takashi Hasegawa, Shingo Okajima, Koji Sekiguchi, and Mitsuteru Inoue
  Spin Waves (Saint Petersburg, Russia, 9th June 2015).

- **Magnonic Crystals Exciting Localized States with Microcavity**
  Naoki Kanazawa,* Taichi Goto, Shingo Okajima, Takashi Hasegawa, and Mitsuteru Inoue
  the IEEE International Magnetics Conference (Dresden, Germany, 6th May 2015).

Posters

- **Demonstration of XNOR gate using interference of magnetostatic forward volume waves propagating in yttrium iron garnet**
  Naoki Kanazawa,* Taichi Goto, Hiroyuki Takagi, Yuichi Nakamura, Shingo Okajima, Takashi Hasegawa, Alexander B. Granovsky, Caroline A. Ross, Koji Sekiguchi, and Mitsuteru Inoue
  Magnonics 2015 (Seeon Abbey, Germany, 3rd August 2015).

- **Propagation Properties of Forward-Volume Spin Waves in a YIG single Crystal with Roughened Surface for Logic Circuits**
  Jet Wei Hoong, Taichi Goto, Naoki Kanazawa,* Altansargai Buyandalai, Shingo Okajima, Takashi Hasegawa and Mitsuteru Inoue
  The 59th Annual Magnetism and Magnetic Materials (Hawaii, USA, 4th November 2014).

- **Effect of magnetic anisotropy on spectral coherence of spin waves**
  Naoki Kanazawa,* Taichi Goto, and Mitsuteru Inoue
  Moscow International Symposium on Magnetism (Moscow, Russia, 1st July 2014).

- **Spin wave transmission properties with magnonic crystals**
  Naoki Kanazawa,* Taichi Goto, Hiroyuki Takagi, Yuichi Nakamura, and Mitsuteru Inoue
  Magnetics and Optics Research International Symposium (Saitama, Japan, 4th December 2013).

- **Spin Wave on the Periodically Metallized Magnonic Crystals Analyzed with Matrix Approach**
  Naoki Kanazawa,* Taichi Goto, Hiroyuki Takagi, Yuichi Nakamura, and Mitsuteru Inoue
  Irago Conference (Aichi, Japan, 24th October 2013).

- **The Effect of Temperature fluctuation on Transmission Property of Magnetic Garnet Based Magnonic Crystals**
  Naoki Kanazawa, Altansargai Buyandalai, Hiroyuki Takagi,* Yuichi Nakamura, Kazushi Ishiyama and Mitsuteru Inoue
  The 11th International Conference on Ferrites (Okinawa, Japan, 17th April 2013).

- **Magnetic field resolution of the Magnonic Crystal-based Magnetic field sensor**
  Naoki Kanazawa,* Tomomi Ueno, Hiroyuki Takagi, Yuichi Nakamura, Kazushi Ishiyama, and Mitsuteru Inoue
  12th Joint MMM/Intermag Conference (Chicago, USA, 14th January 2013).

Awards

- **講演奨励賞受賞**
  応用物理学会 (2017)

- **Best Poster Award**
  59th Conference on Magnetism and Magnetic Materials (2016)

- **優秀論文発表賞 (基礎・材料・共通部門表彰)**
  電気学会 (2014)

- **電気学会技術委員会奨励賞**
  電気学会 (2014)

- **電気学会東海支部長賞**
  IEEJ 東海支部 (2012)